

UNDERSTANDING THE INTERACTION BETWEEN ENZYMES AND NANOMATERIALS

A Dissertation
Submitted to the Graduate Faculty
of the
North Dakota State University
of Agriculture and Applied Science

By

Sunanda Neupane

In Partial Fulfillment of the Requirements
for the Degree of
DOCTOR OF PHILOSOPHY

Major Department:
Chemistry and Biochemistry

December 2019

Fargo, North Dakota

North Dakota State University
Graduate School

Title

UNDERSTANDING THE INTERACTION BETWEEN ENZYMES AND
NANOMATERIALS

By

Sunanda Neupane

The Supervisory Committee certifies that this *disquisition* complies with North Dakota
State University's regulations and meets the accepted standards for the degree of

DOCTOR OF PHILOSOPHY

SUPERVISORY COMMITTEE:

Dr. Zhongyu Yang

Chair

Dr. Andriy Voronov

Dr. D.K. Srivastava

Dr. Guodong Liu

Approved:

12/02/19

Date

Dr. Gregory Cook

Department Chair

ABSTRACT

The rapid development of nanoparticles (NPs) has impacted many fields including energy efficiency, material science, biosensing, and medical therapeutics. Recently, NPs have been utilized to immobilize enzymes. The so-formed enzyme- NP complex show great potential to increase the reusability of enzymes and catalytic efficiencies. Enzyme-NP complex can also advance enzyme delivery for therapeutics where NPs serve as the enzyme carrier. In all applications, the contact of NPs with biomacromolecules, especially proteins, is either necessary or inevitable, which can lead to alterations in adsorbed enzyme structure and function. In biocatalysis, such changes often reduce the desired catalytic activity; in living organisms these changes can even cause protein malfunction, raising concerns about public health and nanotoxicity. Therefore, understanding the correlation of enzyme structure and activity upon contact with NPs is essential.

While enzyme activities can often be determined, the details of enzyme structural changes caused by NPs are underexplored for most enzyme-NP complexes. Obtaining the structural information is challenging due to the relatively large size of the complexes, high heterogeneity in enzyme binding, and complexities caused by the presence of NPs which limit most structure determination approaches. These challenges were overcome using a set of biophysical techniques especially site-directed spin labeling (SDSL) with Electron Paramagnetic Resonance (EPR). SDSL-EPR can measure site-specific structural information in the native state of enzyme/NP systems, regardless of the complexity, primarily due to its “penetrating” power which is only sensitive to the motion of the spin label.

The focus of this dissertation was on T4 lysozyme (T4L), a representing model enzyme proven useful in many works. Gold Nanoparticles (AuNPs), Gold Nanorods (AuNRs), Silica

Nanoparticles (SiNPs), and Carbon Nanotubes (CNTs) were the studied NPs. The interaction of T4L with each NPs was unique. The local structural information and the orientation of T4L in each NP was revealed based on which the possible docking mechanism for each case was proposed. The ultimate goals to reveal the structure-function relationship of enzymes on NPs and utilize this information to fine-tune enzyme adsorption on various NPs to 1) avoid NPs aggregation and 2) optimize NPs as enzyme carriers were met.

ACKNOWLEDGEMENTS

I am very grateful to everyone who supported my four years-long journey in graduate school. A great thanks to my advisor Dr. Zhongyu Yang for always encouraging me, believing in me and guiding me through. Without your mentorship and timely guidance, my journey would not have been possible. My committee members Dr. Andriy Voronov, Dr. D.K. Srivastava, and Dr. Guodong Liu have been phenomenal. Thank you very much for your suggestions and support.

My family has been my rock. A great shout out to always understanding me and being there for me. My mom, dad, brothers, and grandfathers have compromised a lot, missing a lot of festivals and celebrations with me, to make this journey successful. I am very grateful for their unconditional love and support. My husband has made a lot of sacrifices for my success. Thank you for choosing to commute 2.5 hours every day for the past 1.5 years to be there for me.

A huge shout to all my friends in graduate school; without you guys these four years would not be smooth. Special thanks go to Hashini Herath who has always been there for me through my ups and downs. Thank you so much for doing this journey with me.

I thank all the current members of the Yang group for making work fun and always helping. Great thanks to Dr. Yanxiong Pan for selflessly sharing his scientific expertise and always being open for scientific discussions. He has been a great mentor and has been very helpful in the technical aspects of the progression of my research. Jasmin, thank you very much for always listening to me and sharing your proof-reading skills.

DEDICATION

In memory of my grandfather, Professor Bishnu Prasad Neupane, who has been my inspiration in every stage of my life.

TABLE OF CONTENTS

ABSTRACT	iii
ACKNOWLEDGEMENTS.....	v
DEDICATION.....	vi
LIST OF TABLES	xiii
LIST OF FIGURES	xiv
LIST OF ABBREVIATIONS.....	xxii
LIST OF SYMBOLS	xxv
LIST OF APPENDIX TABLES	xxvi
LIST OF APPENDIX FIGURES.....	xxvii
CHAPTER 1. INTRODUCTION.....	1
Enzyme Immobilization.....	2
Modes of Enzyme Immobilization	4
Matrix for Enzyme Immobilization	6
Types of Nanomaterials	8
Gold Nanoparticles	11
Gold Nanorods.....	13
Silica Nanoparticle.....	14
Carbon Nanotubes.....	17
Characterization of Enzyme-NP Complexes	20
Introduction to SDSL-EPR	24
EPR Signal	25
EPR Line Shape and Hyperfine Interaction	27
CW EPR Spectrometer.....	32
CHAPTER 2. PROBING THE AGGREGATION MECHANISM OF GOLD NANOPARTICLES TRIGGERED BY A GLOBULAR PROTEIN	36

Introduction	36
Experimental Methods	39
Apparatus and Reagents	39
Protein Expression, Purification, and Spin labeling	39
Continuous-Wave EPR Spectroscopy.....	40
Preparation of Gold Nanoparticles	40
Preparation of the AuNP-Protein Mixture	41
Dynamic Light Scattering	41
Time-resolved UV-vis Spectra of AuNP upon Interaction with 44R1 and 65R1 Mutants.....	42
Estimation of the AuNP Diameter	42
Characterization of Protein Secondary Structure Using Circular Dichroism.....	43
Activity Measurements	43
Zeta Potential Measurements	44
TEM Images	44
Results and Discussion	45
Characterization of T4L and AuNPs.....	45
T4L Triggers the Aggregation of AuNP	48
Characterization of Protein upon Aggregate Formation	51
Probing the Interaction Mechanism: Interaction with other Biomolecules	53
Probing the Interaction Mechanism: Interaction of T4L with Larger AuNPs	56
Origins of the color change	58
Possible Mechanistic Processes.....	59
Outlook	63
Conclusions	64

CHAPTER 3. PROBING THE STRUCTURAL BASIS AND ADSORPTION MECHANISM OF AN ENZYME ON NANO-SIZED PROTEIN CARRIERS	66
Introduction	66
Experimental Methods	69
Protein Expression, Purification, Spin Labeling, and Characterization.....	69
Continuous-Wave EPR Spectroscopy.....	70
Preparation of the Hydroxylated Silica Nanoparticles (OH-SiNPs).....	70
Preparation of the Amine-coated Silica Nanoparticles (NH ₂ -SiNPs).....	70
Preparation of the Carboxyl-coated Silica Nanoparticles (COOH-SiNPs).....	71
Fourier Transformation Infrared (FTIR) Spectroscopy	71
Zeta Potential Measurements	71
TEM	72
T4L Adsorption Profile on SiNPs.....	72
Activity.....	73
DEER EPR	73
CD Spectroscopy	74
Desorption	74
AFM Imaging	75
DLS Measurement	75
Results and Discussion	75
Characterization of the Model Protein and SiNPs	76
TEM Images Depict the Adsorption of T4L onto SiNPs	79
Atomic Force Microscopy (AFM) Images Confirm the Enzyme Adsorption	79
Probing the Loading Capacity of the Hard Corona	80
EPR Area Analysis to Estimate the SiNP-carrier Loading Capacity.....	82
Enzymatic Activity Loss upon Adsorption to SiNPs.....	85

Probing the Origins of the Activity Loss: Site-specific Conformational Dynamics of the Adsorbed Enzyme	88
Probing the Origins of the Activity Loss: Intra-protein Structural Changes upon Adsorption to SiNPs	92
Differences in the Structural Basis of Enzyme Adsorption between the two SiNPs.....	95
Desorption of Enzyme: Reversible Adsorption.....	95
Possible Docking Models.....	96
Influence of Ionic Strength.....	100
Conclusions	102
CHAPTER 4. ENGINEERING PROTEIN-GOLD NANOPARTICLE/NANOROD COMPLEXATION VIA SURFACE MODIFICATION FOR PROTEIN IMMOBILIZATION AND POTENTIAL THERAPEUTIC APPLICATIONS	103
Introduction	103
Experimental Methods	106
Protein Expression, Purification, and Spin Labeling	106
Preparation of Gold Nanoparticles (AuNPs) and Gold Nanorods (AuNRs).....	107
Preparation of Thiol-terminated mPEG (mPEG-SH)	107
Preparation of Thiolated Polyacrylic Acid (PAA).....	109
Preparation of Thiolated Polyethylenimine (PEI-(SH) _n)	111
Small Molecular Coating via Ligand Exchange.....	111
Polymer Coating via Ligand Exchange.....	111
Incubation of Protein and AuNPs	112
UV-vis Spectra of AuNP upon Ligand Exchange and Interaction with the Protein	112
TEM Sample Preparation	112
Zeta Potential Measurements	113
Gel Permeation Chromatography (GPC) Measurements	113
EPR Measurements	113

EPR Spectral Simulation	114
Activity of the Protein Adsorbed AuNPs and AuNRs	114
Dynamic Light Scattering (DLS) Measurements	114
Results and Discussions	114
Materials and Methods Selection.....	114
AuNP/AuNR Characterization	116
Protein Mutants and Spin Labeling	117
Coating Compounds.....	117
Positive and Neutral Coatings Prevent T4L Adsorption and Particle Precipitation	121
T4L Induces Agglomeration of Negatively Coated AuNPs.....	126
T4L Forms a Stable Corona on the Negative “Shell” of AuNPs.....	129
T4L Adsorption Behavior on AuNRs	131
Molecular Models of T4L Adsorption	133
Coordination of Coating Molecules with Gold Surface.....	134
Polymer Coatings.....	135
Applications of Engineering Protein-Nanoparticle Complexation.....	135
EPR as a Sensitive Tool to Probe the Local Environment of Proteins in Complex with Nanoparticles	137
Conclusions	139
CHAPTER 5. ENHANCING ENZYME IMMOBILIZATION ON CARBON NANOTUBES (CNTS) VIA METAL-ORGANIC FRAMEWORKS (MOFS) FOR LARGE SUBSTRATE BIOCATALYSIS	141
Introduction	141
Experimental Methods	144
Acidification of Carbon Nanotube.....	144
CNT Characterization	144

Protein Expression, Purification, and Spin Labeling	145
CNT-T4L Complex Preparation	145
EPR Spectroscopy.....	146
CNT-T4L-ZIF Composite Preparation	146
Powder X-ray Diffraction (PXRD).....	147
Activity for T4L in the Complex and the Composite	147
Activity for α -Amylase	147
EPR Spectral Simulation.....	149
Calibration of Enzyme Concentration.....	149
Results and Discussions	149
Enzyme Immobilization on CNTs	151
ZIF Enhances Enzyme Loading Stability and Reduces Leaching	153
Activity of Lysozyme in CNT-T4L-ZIF Composite	157
Application to Amylase on Starch Degradation	159
Structural Basis of large-substrate Enzyme Activity in ZIF Scaffolds.....	161
Future Directions	167
Conclusions	168
CHAPTER 6. CONCLUSION	170
REFERENCES	172
APPENDIX. EPR SPECTRAL SIMULATION	226

LIST OF TABLES

<u>Table</u>	<u>Page</u>
4.1. The Zeta potentials of the involved AuNPs in this study, in the absence and presence of T4L. a: T4L triggered the precipitation of AuNPs; no Zeta potential was measured. b: There was no protein adsorption; the Zeta potentials remained unchanged as in the absence of T4L.	123
4.2. The hydrodynamic radius of particles with various coatings in the absence and presence of protein.	124
5.1. Conditions used to optimize loading capacity of CNT-T4L-ZIF composite.....	154
5.2. Relative probability of each labeled site to be exposed to the solvent in ZIF crystals and CNT-enzyme-ZIF composites. *=data from reference. ³³⁸ Grey=sites with a high chance to be exposed to the solvent.	166

LIST OF FIGURES

<u>Figure</u>	<u>Page</u>
1.1. Traditional methods of enzyme immobilization. ²⁴	4
1.2. Comparison of the size of nanomaterials VS other objects.....	8
1.3. Schematic representation of Surface Plasmon band. ⁶⁴ The absorption band arises from the collective oscillation of conduction electrons across nanoparticle in the electromagnetic field of the incident light.	12
1.4. Tunable optical absorptions of AuNRs at visible and Near-Infrared wavelengths. ⁵⁹ (a) Optical absorption spectra of AuNRs with different aspect ratios. (b) AuNRS labeled (a-e) ave reference to longitudinal and transverse resonance wavelength (λ_{LR} and λ_{TR}) in the colorwheel.....	14
1.5. Schematic representation of tunable physicochemical properties of Silica Nanoparticles. ⁷⁷	16
1.6. Covalently bound enzyme molecules to SWCNT. ⁸⁷ The linker molecule is glutaraldehyde.....	19
1.7. The scheme of SDSL in protein. The nitroxide side chain “R1”, is the free electron that serves as the EPR detectable probe.	25
1.8. The magnetic field dependent energy level splitting for an unpaired electron.....	26
1.9. The hyperfine interaction. The allowed transition for an electron spin bound to a spin =1 nucleus. ¹¹⁶	28
1.10. The time scale at which EPR spectra is sensitive. $\tau = 0.1- 2$ ns represents fast motion, $\tau > 2 - 10$ ns represents weak and moderate immobilization, $\tau > 10 - 100$ ns represents strong immobilization, and $\tau > 100$ ns is the rigid limit.	30
1.11. The principle of CW EPR to probe local dynamics.	32
1.12. Block diagram of CW EPR instrument. The major components of CW EPR are Resonator, magnets, microwave bridge and console electronics. The source and the detector are part of microwave bridge.....	34
2.1. Illustration of the influences of proteins on NPs (A) and the influences of NPs on proteins (B). A (I) Protein molecules coat the surface of NP and keep the NP-protein complexes stably dispersed. (II) The NP-protein complexes form larger agglomerates. (III) Protein triggers the aggregation of NPs while being unfolded and precipitated. B (I) NPs trigger conformational changes of proteins. (II) NPs stimulate or inhibit the formation of protein fibrils. (III) NPs induce conformational reorientation of adsorbed proteins.....	37

2.2. Characterization of T4L and AuNPs. (A) The three regions of T4 lysozyme highlighted with orange, grey, and purple. Each region is spin-labeled with one site (green spheres). (B) The CD spectra of the indicated T4L mutants in the “spin buffer”. (C) The activity assay for water, wild-type T4L, and the mutants of T4L as indicated in the figure inset. (D) The UV absorption spectra of various amount of the AuNP in 1000 μ L water. The absorption at 518 nm indicates the presence of the AuNPs with a diameter of \sim 14 nm. (E) The TEM image of the 14-nm AuNPs. (F) The TEM image of the 40-nm AuNPs.	47
2.3. The CW-EPR spectra of spin labeled protein in buffer with 30% sucrose. These data are consistent with literature. ^{178,184,185} The arrows labeled with “i” and “m” indicate the spectrum of 44R1 contains an immobile and a mobile component, respectively, also consistent with literature. The scan range is 3300-3400 G.....	48
2.4. (A) The color of AuNPs alone (left) and upon addition of 151R1 (right) 5 min after mixing. (B) The time resolved UV spectra after mixing the AuNPs with 151R1. The dotted curve indicates the UV spectrum of the AuNP in water with no protein. A clear shift to the longer wavelength can be observed, indicating a diameter change in AuNP upon interaction of T4L. (C) The estimated particle size and the maximum absorption (see main text) as a function of contact time for the three studied T4L mutants. (D) The estimated number of protein either bound or adsorbed to AuNP pellets as a function of protein-to-AuNP ratio. (E), (F) The TEM image of the 14-nm AuNPs upon interaction with T4L at different resolution.	49
2.5. The time-resolved UV-vis spectra of 44R1 and 65R1 upon interaction with AuNPs.	50
2.6. (A) The CD spectra of the three protein mutants in the supernatants after removing the aggregated AuNPs. (B) The CD spectra of the three protein mutants together with the wild-type protein in water.	51
2.7. The activity assay data of the three protein mutants in the supernatant.	52
2.8. The CW EPR spectra of the three labeled sites, 44R1, 65R1, and 151R1, in water (A), upon interaction with AuNP (B), in the supernatant of the protein/AuNP mixture (C) and on the pellets (D). The pellets were washed with water and the CW EPR spectrum were reacquired for one mutant (E). The adsorbed protein was almost completely removed by washing.....	53

2.9. (A) The time-resolved UV-vis spectra after mixing the AuNPs with BSA. A substantial peak shift to longer wavelengths is visible, indicating a slight diameter increase in AuNPs upon interaction with BSA. (B) The time-resolved UV-vis spectra after mixing the BSA-coated AuNPs with T4L (151R1). A clear shift to longer wavelengths is observed, indicating an increase in the size of AuNPs upon interaction with T4L. (C) The time-resolved UV-vis spectra after mixing the AuNPs with the TBA aptamer. Almost no shift is observed, indicating no change in AuNP diameter upon interaction with aptamer. (D) The time-resolved UV-vis spectra after mixing the aptamer-coated AuNPs with T4L (151R1). Similar to (C), a shift to longer wavelengths is observed, indicating an increase in the size of AuNPs upon interaction with T4L. (E) The change in AuNP particle size in cases (A) to (D) as a function of contact time.	55
2.10. The TEM images of the 70 nm(A) and 90 nm (B) AuNPs. The size is less homogeneous and the reported diameter for each case was the average diameter. (C), (D) The TEM images of the 90-nm AuNPs upon interaction with T4L.	57
2.11. The CW EPR spectra of 44R1 upon interaction with the 40-, 70-, and 90-nm AuNPs. The scan range of each spectrum is 100 G. The line shape of each case is identical for that of 44R1 in water (Figure 2.8A).	58
2.12. The time-resolved UV-Vis absorption spectra of the AuNPs at four difference sizes. The baseline was shifted for clarity.	59
2.13. Schematic illustration of the NP-T4L interaction mechanism. (A) Upon contact of T4L with AuNPs, a portion of AuNPs are decoated by T4L. Some of these decoated AuNPs rapidly form pellets (upper panel). The rest of the decoated AuNPs interact with T4L to rapidly form larger AuNPs dispersed in solution (middle panel). This process is defined as the “fast bridging” mechanism. The non-decoated AuNPs directly interact with T4L to form larger dispersed AuNPs in solution (lower panel). Due to the protection layer, this size increase process is slower than the case of the fast bridging process. We therefore define this process as the “slow bridging” mechanism. The larger AuNPs dispersed in solution are not stable and eventually form pellets over a longer time interval (overnight). During the whole process the protein either remains in the native conformation or refold to the native conformation. (B) In the presence of BSA, the decoating pathway is effectively blocked (upper panel). The bridging mechanism is also substantially slowed down since only the BSA-coated AuNPs are available for T4L to bridge (down panel). No pellets are formed in the presence of BSA. (C) For AuNPs that are large enough (ca. > 90 nm), the decoating pathway is not feasible (upper panel). The bridging mechanism is also slowed down since only the coated AuNPs are available for T4L to bridge (down panel). The larger AuNPs dispersed in solution are not stable and eventually form the pellets over a longer time interval (overnight).....	61
3.1. (A) The FTIR spectra of the OH-SiNPs, the NH ₂ -SiNPs, and the COOH-SiNPs (color-coding see inset); (B) Zeta potential changes of the NH ₂ -SiNPs, and the COOH-SiNPs as a function of pH (color-coding see inset).	77

3.2. TEM images of the OH-SiNPs (A) and the COOH-SiNPs (B) in water. The approximate particles diameter is 30 nm in each case. Upon saturation of the OH-SiNPs (C) and the COOH-SiNPs (D) with the T4L 44R1 mutant, a clear black layer coating each SiNP is evident, indicating the adsorption of enzyme on SiNPs.	79
3.3. (A) AFM images for 1: COOH-SiNP, 2: OH-SiNP, 3: T4L-COOH-SiNP, 4: T4L-OH-SiNP (10 μm x 10 μm). The z scale for 1 and 2 images is 0-30 nm, 3 and 4 images is 0-120 nm. Images 5,6,7,8 are the zoom of images 1,2,3,4, respectively (2 μm x 1.3 μm). The z scale for 1, 2, 5, and 6 images is 0-30 nm; for 3, 4, 7, and 8 images is 0-90 nm. (B) The height image, blue-dotted = 5, red-dotted=6, blue=7, and red=8.	80
3.4. The adsorption profile of 44R1 on the OH-SiNPs. Approximately 3,500-4,000 proteins were found to be able to adsorb onto each OH-SiNP. Note there was no wash done on each protein/SiNP mixture with the protein-to-SiNP ratios indicated by the x-axis.	81
3.5. The CW EPR spectra of the 44R1 adsorbed to the COOH-SiNPs (A) and the OH-SiNPs (B) with a protein-to-SiNP ratio of 15,000:1 and 10,000:1, respectively, before (black) and after wash (red) with water. The gray rectangle is to highlight the loss of the peak intensity. The dotted line is to illustrate the peak position shift between the spectra on different SiNPs.	84
3.6. The control experiments for the activity assay. The value of 1.4 μL was selected because that volume of SiNPs was identical to the SiNPs we used for the protein activity test.	86
3.7. The activity assay of the 44R1 adsorbed to the COOH-SiNPs (A) and the OH-SiNPs (B) with a protein-to-SiNP ratio of 250:1 (green) and when the SiNPs were saturated (red) with the enzyme. The black curve indicates the activity of 44R1 in water without any SiNPs and is reproduced in both figures for comparison.	88
3.8. (A) The crystal structure of the T4L (pdb: 3lzm) and the $\text{C}\alpha$ of the residues that were mutated and spin labeled (red spheres) viewed at two angles. (B) – (I) The CW EPR spectra of each spin labeled mutant when attached to the CNBr-activated sepharose beads (dotted black) and when adsorbed to the OH-SiNPs (black and green) and the COOH-SiNPs (red and blue). The black and red curves indicate the spectra taken from samples when the T4L-to-SiNP ratio was 250:1, while the green and blue curves indicate the spectra of 44R1 when the corresponding SiNPs were saturated. The rectangle in each figure is to highlight the spectral region where the spectral line shape changes are the most evident between different solid supports. The arrows are to help guide the identification of the spectral changes. Specifically, the arrow in (B) indicates that the pointed low field peak was populated on other solids; arrows in (F), and (G) indicate the reduction in peak intensity; arrows in other figures indicate an increase in peak intensity.	90

3.9. (A) The crystal structure of the T4L (pdb: 3lzm) and the C α of the three residue pairs that were mutated and spin labeled (green spheres). Dotted lines indicate the intra-protein distances measured in each DEER experiment. (B) – (D) The distance distribution of each spin-labeled cysteine pair when adsorbed to the COOH-SiNPs (black) and the OH-SiNPs (red). DEER data analysis is provided in the main text and the ESI. The gray areas indicate the distance distribution of the corresponding pair when protein is in the spin buffer. There is a clear broadening upon adsorption to the SiNPs, indicating an increase in protein conformational states.	94
3.10. The CD spectra of T4L mutant 109R1/131R1 in water (black) and adsorbed to the OH- (red) and the COOH- (blue) SiNPs.....	94
3.11. The EPR spectra of T4L mutant 151R1 in water (A), supernatants after T4L desorption from the OH-SiNPs (B) and the COOH-SiNPs (D), and those of the OH-SiNPs (C) and the COOH-SiNPs (E) after desorption.	96
3.12. The surface charge of T4L estimated using PyMOL’s APBF function. Three views from different angles were presented to show the location of each studied mutant. Blue: positively charged surface. Red: negatively charged surface.	97
3.13. The proposed adsorption model for the SiNPs. (A) On the OH-SiNPs when a single layer of T4L is adsorbed. The green dots highlight the preferred contact point, while the magenta ones show the less favored contact point, as judged by CW EPR. (B) When the OH-SiNPs were saturated with T4L, the orientation of each protein is random, and the packing between protein layers is relatively loose. (C) On the COOH-SiNPs, when a single layer of T4L is formed, three sites are favored (green) while another three (magenta) are less favored but still possible to contact the nanoparticle surface. Two sites (65R1 and 151R1) were found to be unlikely to make the contact. The model shows certain preferences in protein orientation relative to the particle surface. (D) When the COOH-SiNPs are saturated with T4L, three sites locating near the N- and the C-terminus were found to face more crowding due to packing (cyan).	99
3.14. The EPR spectra of 44R1 in different NaCl concentrations (A), 44R1 upon adsorption to the COOH-SiNPs (B) and the OH-SiNPs (D) at different NaCl concentrations. After washing with the corresponding solutions, the EPR signal of the COOH-SiNPs (C) and the OH-SiNPs (E) at different NaCl concentrations were also acquired.	101
4.1. The synthetic routes of the 3, 3'- disulfanediyldipropanoyl chloride (A) and PEG-SH (B).....	108
4.2. The synthetic routes of PAA-(SH) _n (A) and PAA-SH (B).	110
4.3. The synthetic route of PEI-(SH) _n	111

4.4. The Transmission Electron Microscopy (TEM) images (A, B) and UV-vis spectra (C) of AuNPs prepared in two sizes in citrates. (D) The Fourier Transformation Infrared (FT-IR) of the involved polymer coatings in the main text. (inset) The characteristic –SH peak of FT-IR is visible after zooming-in.	116
4.5. The Transmission Electron Microscopy (TEM) images (A) and UV-vis spectra (B) of AuNRs prepared with CTAB coating.	117
4.6. The GPC data for PAA-(SH) _n and PAA-SH.	119
4.7. Schematic illustration of our coating strategies: pathways to implant small molecular coatings (A) and polymer coatings (B, C).	120
4.8. The TEM (A), UV-Vis spectrum (B), and CW EPR (C) of the AuNPs coated with a positively charged polymer, PEI. The black trace in (C) indicates the CW EPR spectrum of a representative protein site, 151R1, in water. The red and green traces were the same site on AuNPs before and after wash. The same set of data are also acquired for the PEG coated AuNPs (D=TEM; E=UV-Vis spectrum; F= CW EPR spectra). (Inset) The three labeled sites for site-specific protein backbone dynamics (crowding environment) studies.	122
4.9. The UV-Vis spectra of AuNPs and various coatings. The red curves in (B) and (C) were acquired 30 min after mixing the protein with the associated particles. The UV-Vis spectra do not change much over time. The results show almost no change in particle numbers upon addition of the protein.	125
4.10. The TEM images of AuNPs coated with the negatively charged MSNa in the absence (A) and presence (B) of T4L. The “cloud-like” network indicates particle crosslink by T4L. (C) The CW EPR spectra of a representative site (151R1) before and after wash indicate a very low amount of protein adsorption. The same set of data for the PAA-(SH) _n coated AuNPs are also shown. The TEM images in the absence (D) and presence (E) of T4L indicate the formation of interparticle crosslink. (F) The CW EPR of the same representative site after wash indicates a substantial broadening in the protein network in comparison to the “control” (red VS green). Proteins were dyed before TEM test. The “*” indicates the background signal of our resonator.	126
4.11. Supporting CW EPR data for 44R1 adsorbed to the PAA-(SH) _n and PAA-SH coated AuNPs and AuNRs. The “control” stands for data acquired from the same protein site immobilized to the CNBr-activated sepharose beads, wherein the protein rotational tumbling is known to be restricted but proteins retain the native conformation. Broadening in the low field region indicates “contact” of 44R1 sidechain with other protein molecules or nanoparticle coatings. The asterisk indicates the background signal from our resonator; the blue triangles indicate proteins detached into the solution.	129

4.12. The TEM images of AuNPs coated with PAA-SH in the absence (A) and presence (B) of T4L. Stable protein adsorption is evident as shown by the coronas around the particles. (C, D) The CW EPR spectra of 65R1 (C) and 151R1 (D) show a medium extent of spectral broadening (red) for these two mutants on the PAA-SH coated particles comparing to the control (black) and the PAA-(SH) _n coated ones (green). Proteins were dyed before TEM test. The “*” indicates the background signal of our cavity. The blue triangles could originate from unattached proteins or unfolded proteins adsorbed on the particles.	131
4.13. The TEM images of AuNRs coated with PAA-SH and PAA-(SH) _n in the absence (A, B) and presence (C,D) of T4L. Stable protein adsorption is evident as shown by the coronas around the particles. (E-H) The CW EPR spectra of 65R1 (E, F) and 151R1 (G, H) on AuNRs with different coatings and their comparison to the spectra on AuNPs and the “control”.	132
4.14. The schematic models of T4L adsorption to AuNPs with various surface charges (green=neutral, red=positive, blue=negative). (A) Positive/neutral coatings create isolation of protein and AuNPs. (B) Strong negative coatings based on PAA crosslinks facilitate agglomerates formation. The protein surface charge might be the key for the crosslinked protein network (right). (C) PAA-SH shells adsorb proteins with no aggregation formation. (D) Negative PAA-(SH) _n coatings does not form agglomerates with T4L.	134
4.15. The activity assays of T4L coated on various negatively charged AuNPs and AuNRs. Positive control (black triangles) = T4L; negative control (black squares) = AuNP.	136
4.16. The size distribution from DLS for the AuNPs coated with PAA-(SH) _n . The dominant peak at ~95 nm contains 91 % population and a standard deviation of 25.6 nm.	138
4.17. The size distribution from DLS for the AuNPs coated with PAA-(SH) _n in the presence of protein. The dominant peak at ~307 nm contains 100 % population and a standard deviation of 58.6 nm.	139
5.1. Scheme for CNT-T4L complex formation.	146
5.2. Scheme for CNT-T4L-ZIF composite formation.....	147
5.3. Characterization of CNTs. FTIR spectra of CNTs with (A) no acidification, (B) 1 hour acidification, and (C) 2 hour acidification. (D) TEM image of 1 hour acidified CNT.	150
5.4. TEM images of CNTs (A) and lysozyme adsorbed to CNTs (B). The layer covering the tubes of (B) originates from the stained enzyme.....	151
5.5. Activity assay of free lysozyme (black), lysozyme adsorbed on CNT (red), and CNT alone as a negative control (blue). Uncertainties are indicated by the error bars.	152

5.6. EPR spectra of CNT-T4L complex in PBS Buffer (magenta) and a high salt buffer (black).....	153
5.7. TEM images of CNT-T4L-ZIF composite (A) and CNT-ZIF without any enzyme (B).....	155
5.8. Powder XRD data of CNT (black), ZIF-8 (blue) and CNT-T4L encapsulated ZIF-8 (red) indicate that CNT-lysozyme encapsulation does not affect the crystal scaffold.	155
5.9. CW EPR spectra of the CNT-T4L-ZIF composite in PBS Buffer (magenta), in a high salt buffer (black), and in methanol (cyan).....	156
5.10. TEM images of the CNT-T4L-ZIF composite in (A) PBS Buffer at pH 5.8 and (B) Acetate Buffer at pH 3.8.....	157
5.11. Activity assay of CNT- ZIF as a negative control (blue), free lysozyme (black), and lysozyme on CNT-ZIF composites (red). Uncertainties are indicated by the error bars.	158
5.12. The activity assay of T4L free (blue), on CNT-T4L-ZIF composite high concentration (magenta), medium concentration (black), and low concentration (red).	159
5.13. TEM images of CNT-amylase complex (A) and CNT-amylase-ZIF composite (B). (C) The activity assay of amylase on CNTs (black squares) and in CNT-amylase-ZIF composites (red circles). The control for the activity assay are CNT only (blue triangles) and CNT-ZIF (purple triangles). Uncertainties are indicated by the error bars. (D) Direct visualization of starch digestion using the protocol described in the main text. Free amylase generates more maltose (middle) comparing to amylase in CNT-ZIF composites (right).....	159
5.14. (A) Representative surface sites of T4L spin-labeled with R1. (B) Example spectral simulations of the mobile and immobile components of a labeled site in two matrices. (C–H) CW EPR spectra of six labeled sites in different matrices.	163
5.15. Aromatic residues of T4L from two views. There are more solvent exposable aromatic residues (blue sticks) in the C-terminus than in the N-terminus. Buried aromatic residues are shown in light pink sticks.....	165
5.16. (A) Three sites (44, 72, 131) show a higher chance to make contact with CNT surface, based on which the preferred orientations of enzymes on CNTs are proposed. (B) Proposed enzyme orientations on CNT-ZIF surface. Orientations I and II are more preferred than III.....	167

LIST OF ABBREVIATIONS

μM	Micro molar
AFM	Atomic Force Microscopy
AFM	Atomic Force Microscopy
AuNP.....	Gold Nanoparticle
AuNR	Gold Nanorod
BSA.....	Bovine Serum Albumin
CD.....	Circular Dichroism Spectroscopy
CLE	Cross-Linked Enzyme
CLEA	Cross-Linked Enzyme Aggregates
CLEC.....	Cross-Linked Enzyme Crystals
CNT.....	Carbon Nanotube
CTAB	Cetyl trimethylammonium bromide
CW EPR	Continuous wave Electron Paramagnetic Resonance
DEER	Double Electron - Electron Resonance
DLS	Dynamic Light Scattering measurement
DWCNT	Double-Walled Carbon Nanotube
E. coli	<i>Escherichia coli</i>
EDC.....	1-ethyl-3-(3-dimethylaminopropyl)carbodiimide
EM.....	Electron Microscopy
EPR	Electron Paramagnetic Resonance
FTIR	Fourier Transform Infrared Spectroscopy
GHz	Giga Hertz
GPC.....	Gel Permeation Chromatography
H ₂ SO ₄	Sulfuric Acid

HAuCl ₄	Gold (III) chloride trihydrate
HNO ₃	Nitric Acid
kDa	kilodaltons
KHz	Kilo Hertz
MOF	Metal- Organic Framework
MPNa	Mercaptopropionic acid neutralized with NaOH
ms	mili second
MSNa	Mercaptosuccinic acid neutralized with NaOH
MTSL	Methyl methanesulfonylthioate Spin-Labeling reagent
MWCNT	Multi-Walled Carbon Nanotube
NaBH ₄	Sodium borohydride
NaCl	Sodium Chloride
NaCl	Sodium Chloride
NHS	N-Hydroxysuccinimide sodium salt
nm	nano meter
nM	Nano molar
NMR	Nuclear Magnetic Resonance
NMs	Nanomaterials
NP	Nanoparticle
ns	Nano second
OD	Optical Density
PAA	Poly(acrylic acid)
PBS	Phosphate Buffered Saline
PDI	Polydispersity Index
PEG	Polyethylene glycol

PEI.....	Polyethylenimine
pI.....	Isoelectric point
PVP.....	Polyvinyl pyrrolidone
PXRD.....	Powder X-ray Diffraction
rpm.....	Revolutions per minute
S/N ratio.....	Signal to Noise ratio
SDSL.....	Site-Directed Spin Labeling
SiNP.....	Silica Nanoparticle
SPR.....	Surface Plasmon Resonance
SWCNT.....	Single -Walled Carbon Nanotube
T4L.....	T4 lysozyme
TBA.....	Thrombin Binding Aptamer
TEM.....	Transmission Electron Microscopy
UV-Vis.....	Ultraviolet-visible absorption spectroscopy
ZIF.....	Zeolitic Imidazolate Framework

LIST OF SYMBOLS

ΔE	Energy difference between the two electron spin state
g	Proportionality constant
h	Planck's constant
H	Strength of the magnetic field
I	Nuclear Spin number
β	Bohr magneton
ν	Frequency
τ	Relaxation time

LIST OF APPENDIX TABLES

<u>Table</u>	<u>Page</u>
A1. The fitting parameters for 151R1 on PAA-SH and PAA-(SH) _n coated AuNPs and AuNRs. The restricted component is indicated by “res”; the less restricted component is indicated by “m”. The uncertainties in population is +/-2-4 %	230
A2. The fitting parameters for 65R1 on PAA-SH and PAA-(SH) _n coated AuNPs and AuNRs. The restricted component is indicated by “res”; the less restricted component is indicated by “m”. The uncertainties in population is +/-2-4 %	231
A3. EPR fitting parameters for 4 spin labeled mutants adsorbed to CNTs. Note that 65R1 and 151R1 did not yield converged fitting results due to the high heterogeneity of enzyme binding mode on these two sites.	231
A4. EPR fitting parameters for the 6 spin labeled mutants adsorbed to CNT-ZIF. Grey indicates mutants that have more mobile component and are more exposable to the solvent.	232

LIST OF APPENDIX FIGURES

<u>Figure</u>	<u>Page</u>
A1. Definition of the three coordinate systems (Z_D , Z_R , and Z_M) related to the MOMD model used in our simulations.	227
A2. Simulations of key spectra discussed in Chapter 4.	229

CHAPTER 1. INTRODUCTION

This dissertation is focused on using Site-directed Spin Labeling (SDSL) in combination with Electron Paramagnetic Resonance (EPR) to understand the interaction between enzymes and Nanomaterials (NMs), a new frontier of biomaterials. The rapid development of nanoparticles (NPs) has improved many fields including energy efficiency, material science, biosensing, and medical therapeutics.¹ Recently, NPs have been utilized to immobilize enzymes. Such immobilization provides several advantages:

- **Stability and long-term storage:** Enzyme rotational tumbling and translational motion are restricted upon immobilization, which enhances protein stability (pH and temperature) and advances long-term enzyme storage.
- **Economic convenience:** As unique and biocompatible catalysts, enzymes immobilized on NPs enhance the cost-efficiency and often the catalytic efficiency.²
- **Targeted delivery:** NPs are good enzymes carriers for targeted delivery of enzymes for nutrition or therapeutic purposes.³
- **Reusability:** Enzymes in biocatalyst can be easily separated from the reaction mixture allowing reuse. This is useful in the food and pharmaceutical industries.¹
- **Fundamental studies:** Immobilization helps fundamental studies of protein structure and dynamics as it removes complications caused by protein rotational and translational motion.

Therefore, enzyme-NP complexes have broader applications in food industry, biosensing, biocatalysis, drug delivery, biomedicine, biofuel, and many other areas. A major hurdle in this field is the activity loss of enzymes upon immobilization on Nanoparticles (NPs), which reduces the desired enzyme function. Due to the close structure-function relationships of enzymes, such

loss is presumably believed to be originated from enzyme structural perturbation caused by enzyme-NP interactions. The current knowledge gap is the understanding of such perturbation, which limits understanding of enzyme activity on NP surfaces and rational design of NPs with minimal activity loss. The main hurdle in understanding the interaction of enzyme and nanomaterial at the molecular level is the technical limitation. We need a technique that has minimal perturbation to the nanomaterial-enzyme system, can be useful in a heterogeneous system like the enzyme-Np interface, can give dynamic information, and does not have a size restriction. SDSL-EPR fulfills all this requirement.

Enzyme Immobilization

Enzymes are biomolecules, usually proteins, that accelerate biochemical and chemical reactions with high specificity, selectivity, and efficiency.⁴ Enzymes are found ubiquitously in all plants, animals, and microorganisms where they catalyze biological processes necessary for life. The growth in technology for protein extraction and purification has led to industrial production of many enzymes for research and biotechnological applications. The advantages of purified industrial enzymes are that they permit high volumetric activity and prevent undesired side reactions by contaminant enzymes.⁵ Enzymes can be manufactured in a green way by reducing the consumption of energy and chemicals and reducing waste. Enzymes are biodegradable and are produced from renewable materials. Simple and controlled equipment can be used for the production of enzymes.

Enzymes are used in various industries. In food industries, they are used in baking,⁶ dairy products,^{7,8} beverage processing (beer, wine, fruit, and vegetable juices), starch conversion.⁹ In textiles, pulp, paper, and detergent industries enzymes are used to get high-quality end product.¹⁰⁻¹² They are used in biosensors because of their specificity.¹³ Healthcare and pharmaceuticals,¹⁴

chemical manufacturing,¹⁵ biofuel,¹⁶ and waste treatment¹⁷⁻¹⁹ are other areas where enzymes are used.

The industrial applications of enzymes are challenged by their lack of long-term operational stability, shelf-storage, and difficulty in recovery and re-use. Despite many advantages of using enzymes, there are some limitations in industrial applications of enzymes compared to traditional catalyst. The cost of enzyme isolation and purification is higher than that of ordinary catalyst and they are sensitive to various denaturing conditions and process conditions (pH, temperature, trace amounts of substance/inhibitors) when isolated from their natural environments. These challenges can be overcome by enzyme immobilization to develop stable and robust biocatalysts.²⁰

Immobilization is a process of creating a heterogeneously immobilized enzyme system by fixing enzymes to or within the solid supports. In nature, enzymes are attached to the cellular cytoskeleton, membrane, and organelle structures; therefore, immobilizing enzymes can mimic the cellular conditions as well. Structure and function of enzymes are related to each other. The solid support stabilizes the structure of the enzyme, makes enzyme robust to environmental changes and hence maintains their activities through multiple cycles. Immobilized enzyme systems allow for reuse and recovery of both enzymes and products as well as rapid termination of reactions. Immobilized enzymes commonly show lower activity and generally higher Michaelis constants because of difficulty in accessing the substrate.²¹ To efficiently use immobilized enzymes for industrial applications, the type of support used and the method of immobilization must be considered as they influence the activity and subsequent reuse of the biocatalyst.^{22,23}

Modes of Enzyme Immobilization

There are four traditional methods of enzyme immobilization: i) Physical adsorption, ii) Covalent attachment, iii) Physical entrapment, and iv) Cross-linking (Figure 1.1).

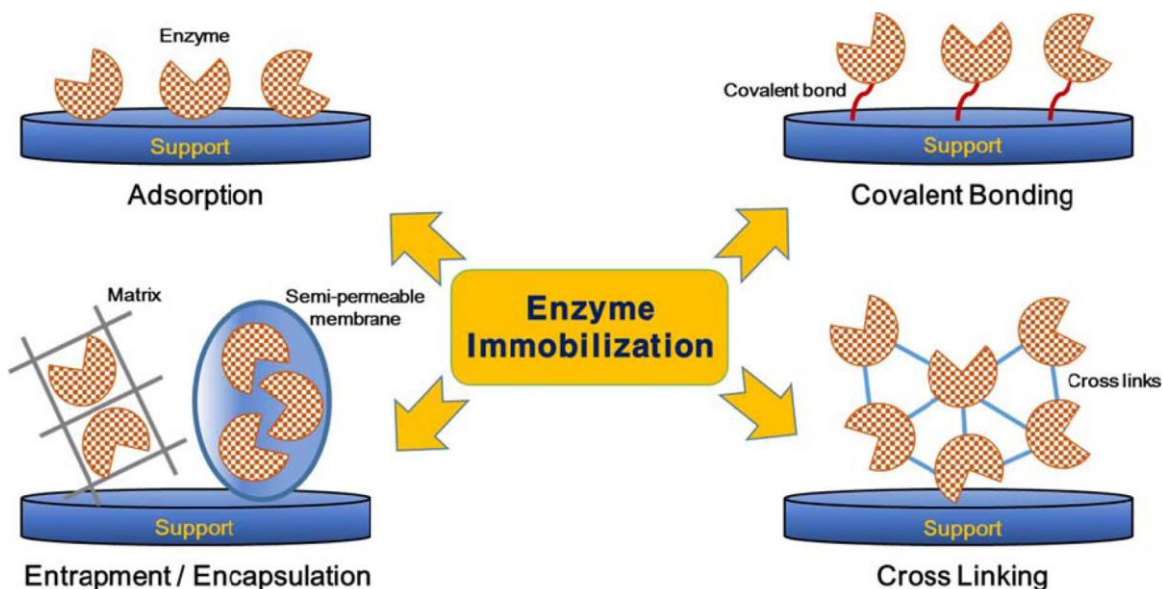


Figure 1.1. Traditional methods of enzyme immobilization.²⁴

- i) **Physical adsorption:** This method involves electrostatic interaction with charged surfaces or passive adsorption onto hydrophobic surfaces. Physical adsorption is simple, low-cost, and effective. Since no modification of the enzyme is needed, there is no perturbation to the enzyme structure. Also, additional coupling reagents are not needed. The only disadvantage of this technique is that the interaction is weak and is often reversible. As a result, enzymes can leach out from the support causing a loss of activity over time. Excessive crowding of enzymes on the support may result in loss of enzyme activity since there is often no control over the packing density of the immobilized enzymes.
- ii) **Covalent attachment:** This method involves the formation of a covalent bond with the functional groups present on the protein surface. The functional groups that

take part in the binding of the enzyme involve lysine (amino group), cysteine (thiol group), aspartic and glutamic acids (carboxylic group), imidazole and phenolic groups which are not essential for the catalytic activity of enzyme.²⁵⁻²⁷ It requires coupling reagents (e.g. NHS/EDC) for faster reactions and may require surface modification of enzyme causing structural perturbation. This method is effective and durable.

- iii) Physical entrapment: Entrapment is the irreversible physical restriction of enzymes within a confined space or network like inside of fibers, the lattice structure of a material or in polymer membranes.^{28,29} Enzymes can be fragile and can be easily denatured by proteases. Encapsulation or entrapment helps minimize leaching, improve stability, and prevent aggression and denaturation by allowing substrates and products to pass through but retaining the enzyme.³⁰ The encapsulating material is tunable to create an optimal microenvironment for the enzyme. Different materials used for entrapment are polymers, sol-gels, polymer/sol-gel composites, and other inorganic materials.³⁰ Sol-gel chemistry method is one of the most common and established methods.¹ The disadvantage of this method is that the kinetic properties of enzymes may be altered during entrapment resulting in changes in enzymes' activity.¹⁴
- iv) Cross-linking: Cross-linking is a carrier-free irreversible enzyme immobilization technique. The enzyme itself acts as its carrier; hence the advantages and disadvantages associated with carriers can be eliminated.^{31,32} Bi-or multifunctional reagents are used to form intermolecular cross-linkages between the dissolved enzymes (Cross-linked enzymes, CLE), crystallized enzymes

(Cross-linked enzyme crystals, CLEC), and aggregated enzymes (Cross-linked enzyme aggregates, CLEA).^{30,33} CLE involves the formation of insoluble protein linkage while CLEC involves linkage between purified enzymes. The requirement of high purity enzyme renders CLEC very expensive. CLEA are prepared by aggregating the enzymes in precipitants such as salts, organic solvents or non-ionic polymers.^{34,35} followed by a cross-linker and linked together by the non-covalent binding. Glutaraldehyde is one of the most commonly used cross-linking reagents as it is economical and easily obtainable in large quantities.^{31,32,36} CLEC and CLEA offer better stability similar to carrier-immobilized enzymes, exhibiting 10 to 1000 times greater activity than the corresponding enzymes attached to a support.^{31,33,37,38} The disadvantages of cross-linking enzyme is that it is difficult to tune its size, flexibility, stability, selectivity, and activity.³³

Matrix for Enzyme Immobilization

The components of an immobilized enzyme system are an enzyme, the matrix and the method of immobilization. Hence, the properties of matrix are an essential component to determine the effectiveness of the immobilized enzyme system. The interaction between the matrix and the enzyme provides the immobilized enzyme with specific mechanical, chemical, biochemical, and kinetic properties.³¹ An ideal matrix must provide an inert and biocompatible environment, provide resistance to microbial attack and compression, and be cost-effective and readily available.^{39,40} The matrix should not interfere in the native structure of the enzyme. There is no one size fits all when it comes to a suitable matrix, but the availability of reactive functional groups, an affinity for the enzyme of choice, mechanical stability, rigidity, the feasibility of

regeneration, non-toxicity, and biodegradability of the matrix must be considered while selecting a matrix.⁴¹

To improve enzyme activity, different matrices with variable physical and chemical properties like pore size, hydrophilic/hydrophobic balance and surface chemistry are available.⁴² Based on the chemical composition, solid supports can be classified into organic and inorganic and can be further subdivided into natural and synthetic polymers. Some of the available supports are carboxymethyl-cellulose, starch, collagen, sepharose, ion exchange resins, acrylic resins, active membranes, aluminum oxide, titanium, active charcoal, silica, clay, diatomaceous earth, hydroxyapatite, ceramic, celite, agarose, treated porous glass, nanomaterials, and certain polymers.³⁰ The porous supports are usually preferred because of higher enzyme loading per unit mass from their high surface area. Silica-based carriers, acrylic and exchange resins, synthetic polymers, and active membranes which are among the most commonly used materials for enzyme immobilization have the disadvantage of increasing the cost of the biocatalyst. These materials are expensive to begin with and need technologies to apply fixation methods.³⁰

Nanomaterials are 1000 times smaller than the width of a human hair. Nanomaterials have one dimension less than or equal to 100 nm. Figure 1.2 compares the size of nanoparticles to the sizes of biologically relevant entities and everyday objects. Nanomaterials such as nanoparticles, nanofibers, nanotubes, and nanocomposites are preferred material for enzyme immobilization because they offer the ideal characteristics for balancing the key factors that determine biocatalysts efficiency. They offer a large surface to volume ratio, high mechanical properties that allow effective enzyme loading with minimum diffusion limitation and mass transfer resistance.⁴³⁻⁴⁶ Nanoparticles possess electronic, magnetic, optical, physical, and chemical properties that are completely different from both the bulk and that constituent atoms or

molecules.⁴⁷ Immobilized enzymes on nanomaterials show high stability in a wide range of temperature and pH, compared to free enzymes.

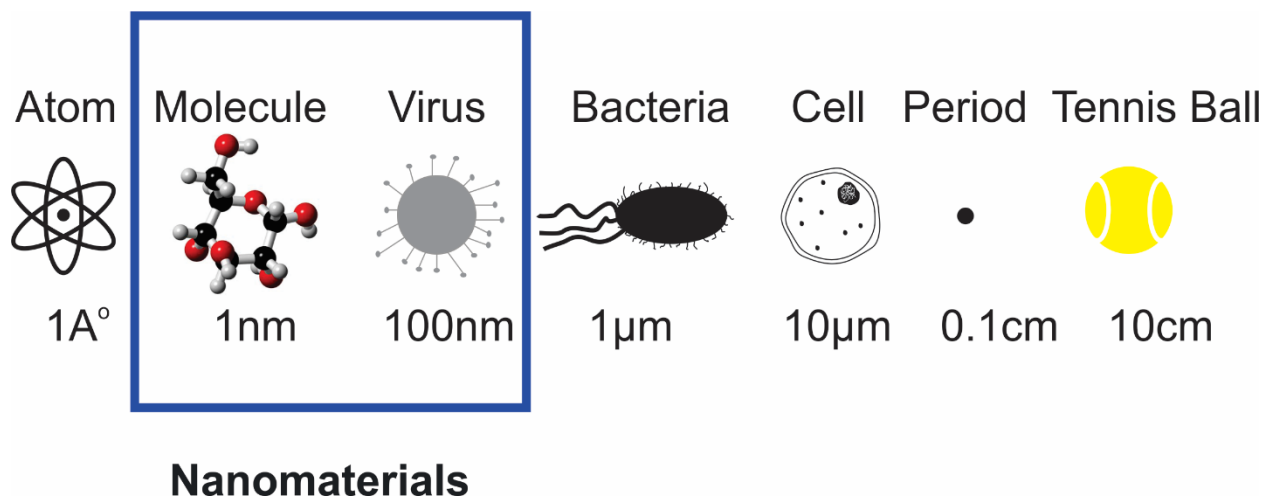


Figure 1.2. Comparison of the size of nanomaterials VS other objects.

Nanomaterial based immobilization techniques shows three characteristics compared to the conventional immobilization technique, i) easy to synthesize without the use of toxic reagents, ii) homogenous coating of the enzyme with homogenous and well-defined core-shell nanoparticles, and iii) possible tailoring of nanoparticle size within effective working limits.⁴⁸ There are certain disadvantages of nano-immobilization such as cost of fabrication, large scale application, and separation of the reaction medium. The cost of nanoparticles depends on the materials involved, some possessing high costs such as nanogold and nanodiamonds while some are not expensive.⁴⁹ Their ideal characteristics out balances the disadvantages which is why they are very popular for immobilization.

Types of Nanomaterials

Nanomaterials can be classified into six categories based on their chemical and physical properties.

- Carbon-based Nanomaterials: The two major classes of carbon-based materials are fullerenes and carbon tube nanotubes (CNTs).⁵⁰ Fullerenes have sp^2 hybridized pentagonal or hexagonal carbon units. CNTs are tubular in structure and resemble a rolled-up graphite sheet. Depending on the number of layers of rolled up graphite sheets they could be Single-walled (SWCNT), double-walled (DWCNT), and Multi-walled (MWCNT). Electrical conductivity, high strength, structure, electron affinity, and versatility are some of the advantages of carbon-based nanomaterials. Some of the applications of carbon nanotubes are as biosensors, electrodes, and filling materials.
- Metal Nanomaterials: As the name suggests, they are made up of metal precursors. For example, gold, silver, copper, titanium, zinc, cerium, iron, thallium, etc. They possess unique optoelectronic properties because of localized surface plasmon resonance. It is comparatively easy to control their size, shape and surface properties. They have applications in a wide range of areas such as imaging, drug delivery, and anticancer agents.⁵¹
- Ceramic Nanomaterials: They are amorphous, polycrystalline, dense, porous or hollow inorganic material (silica, titania, alumina, zirconia, hydroxyapatite, etc.) with a solid core. The nanomaterial core could consist of metals, metal oxides, and metal sulfides.⁵² There are three categories of ceramic nanomaterials: ceramic nanoparticles, ceramic nano-scaffold, and ceramic nanoclays.⁵⁰ They are used in different areas because of high heat resistance and chemical inertness. They find applications in catalysis, photocatalysis, photodegradation of dyes, carriers of drugs, genes, proteins, imaging agents, etc.

- **Semiconductor Nanomaterials:** They possess properties between metals and non-metals and their properties are dependent on their size. These nanomaterials possess wide bandgaps. Thus, it allows for the tuning of nanomaterial property.⁵⁰ They are found in the periodic table in groups II-VI, III-V or IV-VI. Photocatalysis, photo optics, and electronic devices are some of the areas that use semiconductor nanomaterials. Some examples of semiconductor nanomaterials are cadmium selenide (CdSe), Zinc sulfide (ZnS), cadmium telluride (CdTe), Zinc oxide (ZnO), mercuric selenide, Silica Nanoparticles, germanium nanoparticles, among others.
- **Polymeric Nanomaterials:** Polymeric nanomaterials are organic nanomaterial. These could have a spherical shape or capsule shape. In nanosphere the overall mass is solid, and the other molecules are adsorbed at the outer boundary whereas in nanocapsules the other molecule is encapsulated. Because of the ease of functionalization, specific targeting, and controlled release, they find applications in various areas of drug delivery, drug release, and optoelectronics.⁵⁰
- **Lipid-based Nanomaterials:** Lipid-based nanomaterials possess a solid core made up of lipid and a matrix that contains soluble lipophilic molecules. Emulsifiers are often used to stabilize the external core of these NMs.⁵⁰ These are used as drug carrier and delivery vehicles, as RNA releaser in cancer therapy, etc. They provide convenience in tuning and functionalization that is why they are very versatile. Some of the examples of lipid-based nanomaterials are liposomes, solid-core micelles, and hybrid lipid nanoparticle.⁵³

The four projects discussed in this dissertation use four different NPs. The focus is on metal nanoparticles (AuNPs and AuNRs), non-metal nanoparticles (CNTs) and metalloids

(SiNPs) to gain an understanding of enzyme immobilization on different types of materials. The main goals for all the projects were to probe the orientation of the enzyme on NPs and propose the mechanism of interaction of T4L with NPs. The first project used AuNPs (metals), T4L triggered AuNPs aggregation and the original goal of probing the orientation of enzyme on AuNPs could not be achieved. The findings in AuNP-T4L study portrayed the mechanism of T4L triggered AuNP aggregation which led to the second project, changing the charge and coating of AuNP/AuNR to prevent aggregation. The orientation of the enzyme could be probed after the coating on AuNP/AuNR was changed. Silica NPs represented the metalloid category and is well-known in literature for enzyme adsorption. We could probe the orientation of enzyme on SiNP and propose a mechanism. Finally, the understandings from the interactions of AuNP-T4L, AuNR-T4L, and SiNP-T4L provided the basis for the fourth project to develop novel, effective approach to anchor large-substrate enzymes, T4L, and α -amylase on the surface of CNTs (non-metals) using ZIF and one-pot synthesis to reduce leaching and retain catalytic activity. Each of these nanoparticles and their properties are discussed below.

Gold Nanoparticles

The history of gold, its study and applications are estimated to be several thousand years old as it was one of the first metals discovered by humans. Colloidal gold was used for medical purposes as early as in the fifth and fourth century BC according to the tracts by Chinese, Arabic and Indian scientists.⁵⁴ In the middle ages in Europe, colloidal gold was studied and employed in alchemists laboratory. The age of the use of gold particles in biological research began in 1971 when W.P. Faulk and G.M. Taylor published an article titled “An immunocolloid method for the electron microscope.”⁵⁵ From this point on the use of colloidal-gold biospecific conjugates in various fields of biology and medicine became very active. Currently, Gold nanoparticles

(AuNPs) are used in biomedicine, diagnostics and therapeutics area such as genomics, biosensors, immunoassay, clinical chemistry, targeted delivery of drugs, peptides, DNA, and antigens, optical bioimaging, detection and photothermolysis of microorganisms and cancer cells.⁵⁴

Spherical AuNPs are important tool in bionanotechnology because they possess useful attributes such as size-and shape-related optoelectronic properties,^{56,57} large surface-to-volume ratio, excellent biocompatibility, high thermal stability, ease of preparation and functionalization, and low toxicity.^{58,59} Surface plasmon resonance (SPR) and the ability to quench fluorescence are the important physical properties of AuNPs. Spherical AuNPs show a size relative absorption peak from 500 to 550 nm and exhibit a range of colors in aqueous solutions as the core size increases from 1 to 100 nm.⁶⁰⁻⁶² This absorption band arises from the collective oscillation of the conduction electrons due to the resonant excitation by the incident photons called a surface plasmon band (Figure 1.3).⁶³ This band is absent in both small nanoparticles ($d < 2$ nm) and the bulk material.

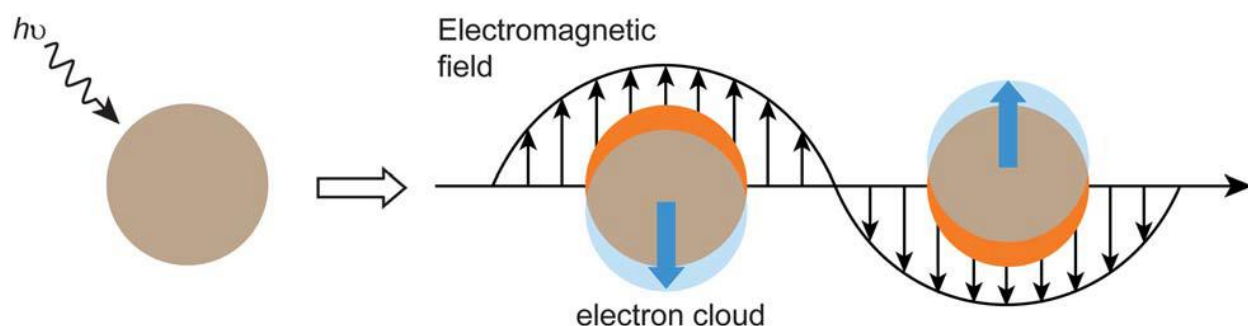


Figure 1.3. Schematic representation of Surface Plasmon band.⁶⁴ The absorption band arises from the collective oscillation of conduction electrons across nanoparticle in the electromagnetic field of the incident light.

Immobilizing the surface of Nanoparticles with proteins can add biofunctionality and increase biocompatibility to enable their use in many biomedical fields and the development of biocompatible materials.⁶⁵ Along with the exciting development and applications, concerns have

been raised about the effects of the biological environment on NP functions. All the effects originate from the molecular interaction of AuNPs and the highly diverse biomolecules, especially proteins. To minimize the aforementioned concerns, it becomes essential to reveal the mechanism of the NP-protein interaction and identify the pathways that cause these concerns at the molecular level.

Gold Nanorods

Gold nanorods have two distinct plasmon bands: one because of light being absorbed transversely (short axis) and the other due to longitudinal (long axis) absorption (Figure 1.4). As the rod length changes the plasmon frequency position changes too.⁵⁹ AuNRs can be tailored to have strong absorptions spanning a wide range of wavelengths (visible to near-infrared), simply by changing rod length. This easy tunability property of AuNRs has gathered lots of interest. Also, controlled assembly of AuNRs is possible as particles having anisotropic shapes may possess different chemical affinities for different crystallographic faces.^{59,66-69} Under appropriate conditions, AuNRs have been shown to link preferably end-end.⁷⁰ This leads to plasmonic coupling resulting in controlled frequency shifts. AuNRs are unique compared to spherical AuNPs in that AuNRs can enhance quantum yields of fluorescent molecules at specific distances from the rod surface.

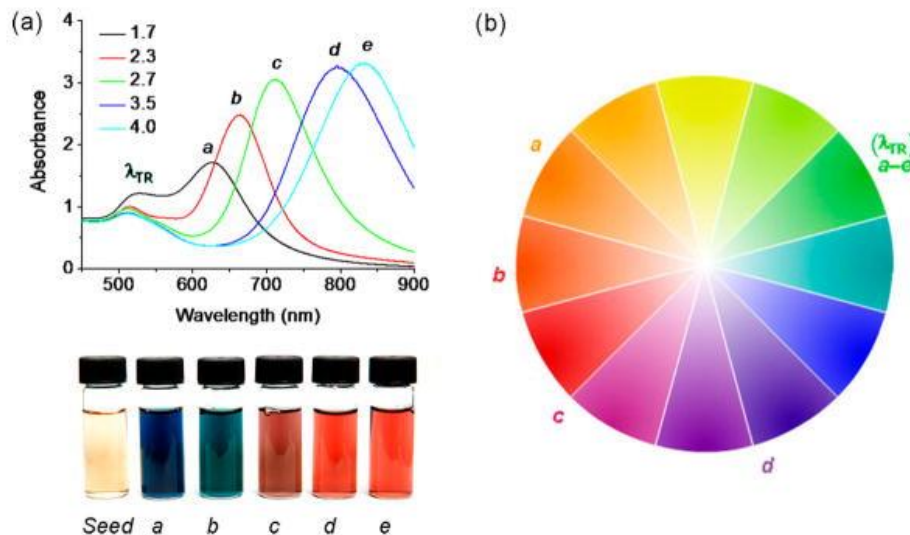


Figure 1.4. Tunable optical absorptions of AuNRs at visible and Near-Infrared wavelengths.⁵⁹ (a) Optical absorption spectra of AuNRs with different aspect ratios. (b) AuNRs labeled (a-e) are reference to longitudinal and transverse resonance wavelength (λ_{LR} and λ_{TR}) in the colorwheel.

AuNRs have applications in different fields such as chemical sensing and imaging,⁶⁹ drug delivery,⁷¹ and photothermal therapy or lysis.^{67,72} All the applications are derived from the properties of the plasmon bands. In biological applications, the contact of AuNPs/AuNRs with proteins is inevitable, resulting in the formation of a “protein corona”, protein–particle agglomerates, or particle precipitation. While nonspecific adsorption or particle precipitation should be avoided, controllable protein adsorption and agglomerate formation via surface modification find applications in protein immobilization and therapeutics. Therefore, it becomes essential to understand the influences of particle surfaces on protein adsorption.

Silica Nanoparticle

Nanomedicine has been increasing rapidly. The goal of nanomedicine is to design and synthesize drug delivery vehicles that can carry sufficient drug loads, efficiently cross physiological barriers to reach target sites, and safely and sustainably cure diseases. There are numerous drug delivery platforms such as liposomes, drug-polymer conjugates, dendrimers, polymeric micelles, and nanoparticles (NPs). Each delivery platform has its advantages and

disadvantages. Silica Nanoparticles (SiNPs) have attracted significant interest because of their unique properties such as hydrophilic surface favoring protracted circulation, versatile silane chemistry for surface functionalization, excellent biocompatibility, ease of large-scale synthesis and low cost of NP production.^{73,74} In 2011, US Food and Drug Administration (FDA) approved an Investigational New Drug Application for exploring an ultra-small nonporous silica NP for targeted molecular imaging of cancer for a first-in-human clinical trial. This highlights the progress of clinical translation of silica NP drug delivery platform.^{75,76}

Silica NPs used for biomedical applications are amorphous silica structure that can be mesoporous or nonporous (solid). Mesoporous and Nonporous silica are different in the way the cargos are loaded and released for delivery. Nonporous silica deliver cargos through encapsulation or conjugation and the release is controlled using chemical linker or by the degradation of silica matrix. The size, surface property, and shape of nonporous silica NPs can be excellently controlled by tuning the composition and concentration of surfactants during synthesis (Figure 1.5).⁷⁷ Our focus is on Nonporous silica. Nonporous SiNPs are extensively used as drug carriers because of their biocompatibility and easy formulation with drugs; they are also used as a host material for other types of functional NPs. Active cargoes delivered by silica NPs are small molecule drugs, proteins, or photosensitizers, gene delivery, and molecular imaging for different contrast agents.⁷⁷ SiNPs are used for biocatalysis or protein delivery because of the many advantages such as the ease of NPs formation, matrix degradability, stability, and tunability of physical properties.⁷⁸

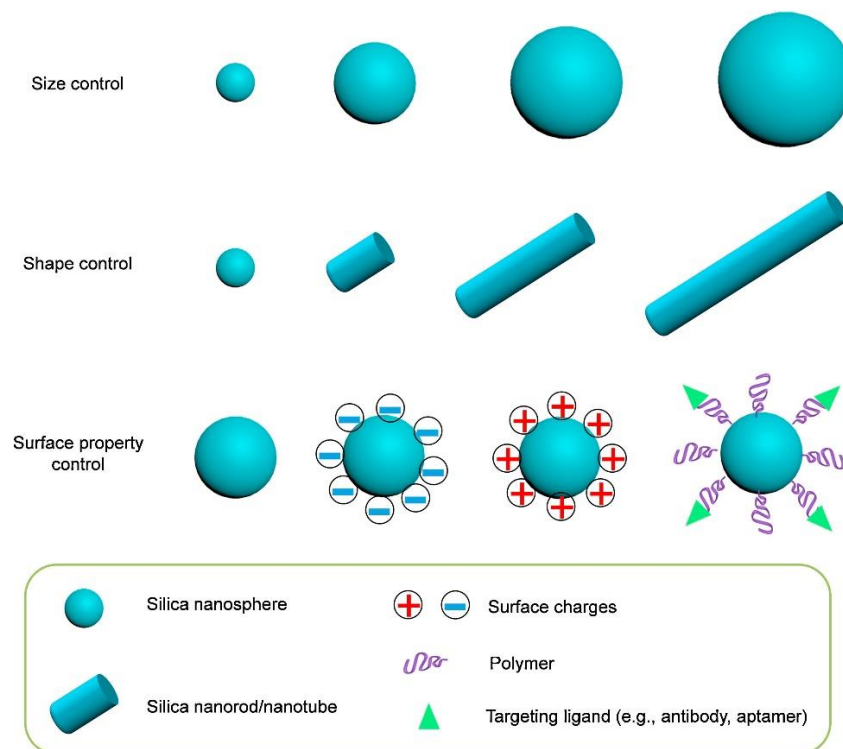


Figure 1.5. Schematic representation of tunable physicochemical properties of Silica Nanoparticles.⁷⁷

Immobilization of enzymes onto non-porous SiNPs is of interest because immobilization of enzymes helps increase the environmental tolerance of enzymes, prevents enzyme aggregation and/or unfolding and allows for the reuse of the host.⁷⁹ Non-covalent attachment of enzymes is of more interest because structural perturbation of enzyme caused by covalently linking enzyme to the solid phase can be minimized. Also, it makes it possible to detach the enzyme from the solid phase when needed. One of the major concerns in utilizing these SiNPs to carry or host enzymes is the possible enzymatic activity loss caused by the molecular interaction between the SiNPs and the cargo enzymes and the interaction between the cargo enzyme and surrounding biomolecules.^{80,81} Therefore, understanding the structure-function relationship of cargo enzyme on SiNP surface in the biological environment becomes an essential task.

Carbon Nanotubes

Carbon nanotube was first synthesized in 1976 as carbon filament.⁸² Some believe, if high powered microscope were available in 1950s, carbon nanotubes would have been observed by Roger Bacon in the 1950s.⁸³ In 1990, Iijima produced CNTs using an arc-discharge evaporation method. He published detailed structural characterization of newly discovered multi-walled carbon nanotube in Nature in 1991.⁸⁴ That publication triggered the new beginnings of the use of Carbon nanotubes.

Carbon nanotubes are graphene sheets which are wound into a seamless cylindrical shape. Their ends may be open or closed. The ends may be closed with caps containing pentagonal rings. In Multi-walled carbon nanotube (MWCNTs) there are multiple layers of CNTs each enclosing each other compared to only single layer of CNT in Single-walled carbon nanotube (SWCNT).⁸⁵ Each carbon is covalently bound to its three adjacent neighbors resulting in a structure with hexagonal honeycomb lattices. Graphite is sp^2 hybridized imparting unique properties like metallic or semi-conducting properties depending on the orientation of graphene lattice with respect to the tube axis (chirality) and amazing tensile strength around 50 times more than steel.⁸⁶ The length of CNT could be hundreds of micron long while the SWCNT are approximately 1-2 nm in diameter and MWCNT are 2-50 nm in diameter with interlayer distance of 0.34 nm.⁸⁷

CNTs have many of the same advantages of AuNPs. They are biocompatible and have a high surface-volume ratio, high electro-catalytic effect and fast electron transfer rate. CNTs are 10 times stronger than any industrial fiber.⁸⁸ This makes CNT very useful as a mechanical property enhancing filler material. Individual MWCNTs have tensile strength of 100 GPa and elastic modulus approaching 1 TPa.⁸⁹ MWCNTs are metallic and can carry current up to 100

times greater than that of Copper wire i.e. up to 10^9 A cm^{-2} .⁹⁰ CNTs are chemically inert and thermally stable up to 2800°C under vacuum.⁹¹ Individual SWCNTs are twice as thermally conductive as diamond; the thermal conductivity is $3500 \text{ W m}^{-1} \text{ K}^{-1}$ at room temperature based on the wall area.⁹² CNTs have commercial applications in the fields of electrochemical biosensors, fluorescent and photoacoustic imaging, engineering plastics, polymers, anti-corrosion paints, thin films and coatings, transparent and non-transparent conducting electrodes, super hydrophobic coatings and anti-static packaging; MWCNTs are used in lithium ion batteries for notebook computers and mobile phones.⁸⁸ CNTs are used in electrochemical biosensors because they tend to have higher sensitivities, lower detection limits, and faster response times compared to conventional carbon electrode sensors.⁹³ CNT sensors have been used for gas and toxin detection in the food industry, military and environmental applications.^{94,95} Active research is ongoing in fields such as batteries, fuel cells, solar cells, advanced devices, optics, water desalination, shape recovery, dry adhesion, high damping, terahertz polarization, large-stroke actuation, near-ideal black-body absorption, thermoacoustic sound emission, and many others.^{96–}
¹⁰² The worldwide CNT production capacity has increased at least 10-fold since 2006 and the CNT-related patents and journal publications continues to grow.

Since CNTS are hollow structures, enzymes can be loaded to the inside and the outside of the tube, thus, increasing the loading capacity. This will also eliminate the enzyme active sites from becoming the limiting reagent in biocatalytic reaction. Surface functionalization of carbon nanotube is necessary for electrostatic interaction of enzymes onto CNTs. Oxidative pretreatment of CNTs introduces carboxylic groups on the ends of sidewalls, or defects.⁸⁷ In CNTs without functionalization, the aromatic structure is quite hydrophobic and electrostatic bonding does not occur but hydrophobic interaction between aromatic residues make physical adsorption possible.

Covalent attachment of an enzyme onto CNT is possible via a linker molecule such as glutaraldehyde (Figure 1.6).⁸⁷ The advantage of cross-linking is that it provides strong attachment and may increase catalytic activity. The disadvantage is that there is potential structure perturbation of enzyme.

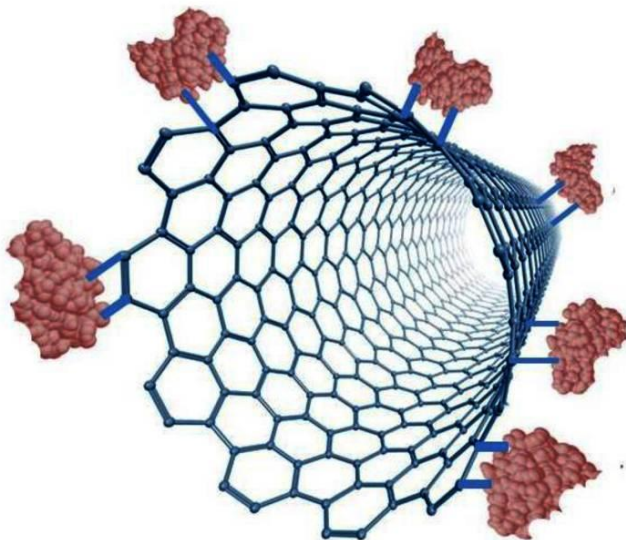


Figure 1.6. Covalently bound enzyme molecules to SWCNT.⁸⁷ The linker molecule is glutaraldehyde.

Carbon nanotubes are better support material for enzyme immobilization because they are more stable under harsh conditions, provide higher loading of enzyme and enhanced catalytic activity of enzyme as compared to flat support and even higher than native enzyme.¹⁰³ Enzymes are more stable in carbon nanotubes as CNTs have highly curved surfaces that are unfavorable for enzyme denaturation in harsh conditions and suppress lateral interactions between adjacent adsorbed proteins.^{103,104} Enzymes can be non-covalently adsorbed to the surface of oxidized carbon nanotubes. However, the immobilized enzyme can be gradually lost through leaching during the use of CNT-enzyme complex. Additional steps of encapsulation may be needed to

overcome this problem. The novel approach of co-precipitating ZIF-8 with CNT-enzyme encapsulates CNT-Enzyme complex and provides stability.¹⁰⁵

Characterization of Enzyme-NP Complexes

From the review presented above, it is clear that enzyme-NP complexes attract interest in a variety of different fields. A major hurdle in this field is the activity loss of enzymes upon immobilization on Nanoparticles (NPs), which reduces the desired enzyme function. Due to the close structure-function relationships of enzymes, such loss is presumably believed to be originated from enzyme structural perturbation caused by enzyme-NP interactions or orientation of enzymes on Nanoparticles. The current knowledge gap is the understanding of such perturbation, which limits the understanding of enzyme activity on NP surfaces and rational design of NPs with minimal activity loss. While the enzyme activity can often be determined, the details of residue-level backbone dynamics change caused by NPs, large-scale conformational flexibility, and orientation of enzyme on NMs are unknown for most enzyme-NM combinations. The study of these structural changes has many technical challenges. The main hurdle in understanding the interaction of enzyme and nanomaterial at the molecular level is the technique. One needs a technique that has minimal perturbation to the Nanomaterial-protein system, can be useful in a heterogeneous system like NM-enzyme interface, can give dynamic information, and does not have a size restriction.

The protein-NMs complexes have been studied by different physico-chemical methods including UV-Vis, Fluorescence spectroscopy, NMR, Calorimetry, Electron microscopy, Atomic Force Microscopy, and Circular Dichroism (CD).¹⁰⁶ The majority of these techniques, however, do not provide dynamic structural details. For example, NMR can probe the sites which are in contact with NMs but is limited to smaller proteins. NMR is also challenged by the slow-motion

upon protein adsorption to NMs (which can cause line broadening) and background signals from NPs. Optical approaches are complicated by NPs scattering light. Fluorescence spectroscopy is limited by the presence of multiple fluorescent amino acids (Tryptophan, Tyrosine, and Phenylalanine) which complicate the data analysis toward binding site detection.¹⁰⁷ Structural determination based on fluorescence labeling suffers from the large label sizes too. Circular Dichroism can reveal changes in protein secondary structure, but it cannot tell the orientation of enzyme on nanoparticle and can be challenged by the background signals from nanoparticles. Electron microscopy (EM) has enough resolving power but cannot resolve to image organic or biological components of protein-NP complexes.¹⁰⁸ Also, Electron microscopy and Atomic Force Microscopy cannot provide dynamic information. Lastly, the large size and high complexity/heterogeneity of protein-NM complex challenge the X-ray crystallography and cryo-EM approaches.

When it comes to probing the orientation of the enzyme on NP surface there are two strategies: 1) Identifying residues/regions of enzyme responsible for contacting NP surface based on backbone dynamics and 2) Measuring the angle between certain enzyme bonds or secondary structures (e.g. a helix) and the surface normal.

Identifying residues/regions of the enzyme responsible for contacting NP surface based on backbone dynamics: Residues/regions of an enzyme have different backbone dynamics, local polarity, and/or solvent accessibility based on whether they contact the NP surface or face towards the solvent. Detecting these differences can indirectly reveal enzyme orientation. One technique is Time-of-flight secondary ion mass spectrometry (TOF-SIMS), which determines protein portions located on the outer 1 nm of the protein-NP complexes. Castner and coworkers utilized TOF-SIMS to reveal the protein segments located in the

outermost layer of various GB1 mutants adsorbed to gold surfaces.¹⁰⁹ Although TOF-SIMS is applicable to protein-NP surfaces the resolution of orientation may be less desirable. Usually other orientation probing methods are combined with TOF-SIMS. Another technique is Site-directed fluorescent probing can report contact protein residues based on protein local polarity changes upon contact with NP surface. Carlsson and coworkers investigated the orientation of human carbonic anhydrase II on silica NPs by labelling different enzyme areas with fluorescent probes.¹¹⁰ This work demonstrates the feasibility of using site-directed fluorescent labelling for probing protein orientation on NP surface.

H/D exchange heteronuclear single quantum coherence (HSQC) Nuclear Magnetic Resonance (NMR), is another approach with a residue-level resolution. This technique is sensitive to the chemical environment of each amino acid. The possible arrangement of protein on NPs can be deduced by comparing the chemical shifts. Rossi and coworkers employed this approach to probe the chemical shift perturbation of ubiquitin upon adsorption to gold nanoparticles and determined residues (2-3 and 15-18) likely responsible for the contact.^{111,112} The higher resolution of NMR methods is advantageous to understand the nano-bio interface. The limitations may be the protein size usually <45 kDa. Also, in highly heterogeneous orientations due to the overlapped chemical environments peak assignment may be challenging.

Measuring the angle between certain enzyme bonds or secondary structures (eg. a helix) and solid surfaces: An example is Dichroic or difference attenuated total reflection (ATR)-Fourier transform infrared (FTIR). By probing the difference between ATR spectra acquired with differently polarized beams, the relative orientation of a helix with respect to a solid surface can be probed.^{113,114} A beam polarized in parallel with the helix would generate a more intense amide I band than a perpendicularly polarized beam. A challenge of this approach

on NPs is that the angle between the incident beam and NP surface can be random which may wash off the orientation dependence of the ATR signal. Also, for proteins with differently oriented helices, it will be difficult to assign amide I and II bands to secondary structures and determine their relative orientations. Overall, ATR-FTIR is a powerful approach for probing enzyme orientation and may be applicable to the nanoscale surface if the barriers can be overcome. A similar approach is polarization modulation infrared reflection-absorption spectroscopy (PM-IRRAS), which also relies on differently polarized beams. A major advantage of this approach is to identify characteristic bonds of specific secondary structures (ca. α -helices or β -sheet) and reveal their orientation. IRRAS/PM-IRRAS is mainly applicable in air-water or protein-membrane interfaces and may face similar challenges on the nano-bio interface as ATR-FTIR.

Sum Frequency Generation (SFG) is another approach free from background vibrations. Varying IR frequency can detect different vibrational motions, while by varying the polarization of the IR beam, the orientation of certain bonds (ca. amides) with respect to the solid surface can be determined. For example, the orientation of the methyl groups in odd layers of fatty acids adsorbed on gold nanoparticles was found to be different from that in even layers.¹¹⁵ This information is an important structural insight for nano-bio materials design. This work also indicates the possibility of using SFG on protein orientation studies on NPs. Combining SFG and ATR-FTIR may be applicable to reveal protein orientation on NP surfaces; however, there has been no report in the literature yet.

For enzyme activity, residue-level backbone dynamics and large-scale conformational flexibility are more relevant to the protein function. The experimental techniques that can perform dynamic measurements are relatively limited. NMR based on paramagnetic relaxation

enhancement (PRE) of nuclei has been used to determine the global dynamics and exchange kinetics of the interaction between ubiquitin and nanoparticles.¹¹⁶ However, the scale of resolved dynamics is often limited to local backbone dynamics. FRET can probe large scale motions and is ultrasensitive (single molecule) but may face challenges of large fluoro-label size and hydrophobicity. CW EPR can probe local dynamics of protein on NP surfaces and even in between NPs crosslinked by proteins.

Site-Directed Spin Labeling (SDSL) along with Electron Paramagnetic Resonance (EPR) offers an opportunity to overcome the challenges of other techniques. SDSL-EPR along with other spectroscopic and imaging techniques provides a better understanding of structure and orientation of enzyme immobilized on nanoparticles.

Introduction to SDSL-EPR

Site-Directed Spin Labeling (SDSL) along with Electron Paramagnetic Resonance (EPR) is a powerful technique to probe the structure and dynamics of an enzyme. EPR is sensitive to local structure and dynamics at the vicinity of the spin-label.^{117,118} In SDSL, a cysteine is generated at the protein site of interest via site-directed mutagenesis. A nitroxide moiety (methanethiosulfonate reagent) is then reacted with the cysteine to form a spin label side chain, R1 (Figure 1.7).^{119,120} The small size of R1 causes negligible changes to protein structure and stability, particularly for solvent-exposed sites like those used in this dissertation,^{119–121} an advantage in comparison to other labeling-techniques. A potential disadvantage of this spin labeling technique is that the native free cysteine(s) in the protein must be mutated to serine or alanine residues prior to SDSL. However, this operation often causes negligible influences for most proteins due to the low natural abundance of cysteine. For cysteine-rich proteins, the alternative strategies for site-specific labeling based on the incorporation of unnatural amino

acids with bio-orthogonal groups are available.¹²² The SDSL-EPR technique is highly sensitive and specific because many biological samples do not normally contain an unpaired electron, allowing a broad range of protein structural features to be investigated.

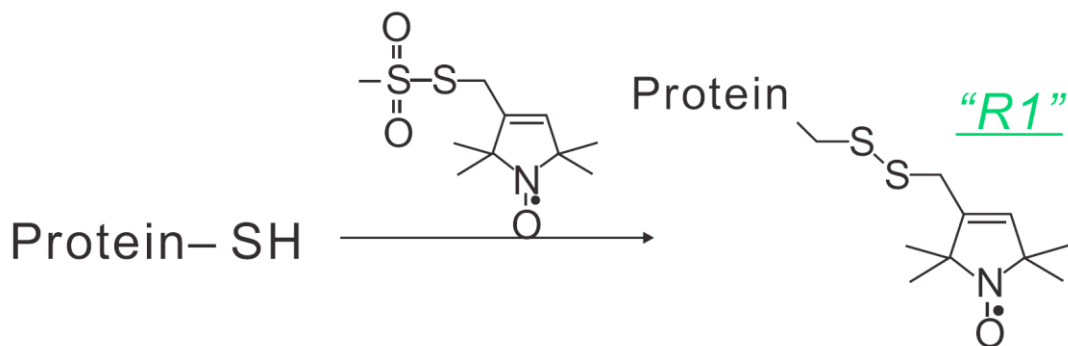


Figure 1.7. The scheme of SDSL in protein. The nitroxide side chain “R1”, is the free electron that serves as the EPR detectable probe.

EPR spectrum is highly sensitive to motion of R1 on the ns time scale and contains contributions from protein rotational tumbling, backbone dynamics, and intrinsic motion of the spin label.¹²³ The work in this dissertation is primarily comprised of using SDSL-EPR to probe the orientation of enzyme T4 Lysozyme (T4L) when immobilized on the nanomaterials discussed above and how the orientation changes based on nanoparticles, and coatings. Therefore, our work makes use of EPR as a technique but is not the work on theory and science behind EPR itself. However, a general understanding of the theory behind EPR is important to understand our work and its significance and is briefly discussed below.

EPR Signal

The measurement and interpretation of the energy difference between atomic or molecular states is spectroscopy which can be carried out by supplying the right amount of electromagnetic radiation to excite the electrons from lower energy state to the higher energy state. According to Plank’s law, electromagnetic radiation will be absorbed following $\Delta E=hf$.

Here ΔE is the energy difference between a lower energy state and a higher energy state, h is Planck's constant and ν is the frequency of the radiation. In traditional spectroscopic techniques, sweeping through the frequency and observing frequencies which result in absorption provides the information on energy differences between two states. However, in EPR the frequency of radiation is held constant (in gigahertz, GHz) while the magnetic field is varied to obtain an absorption spectrum.

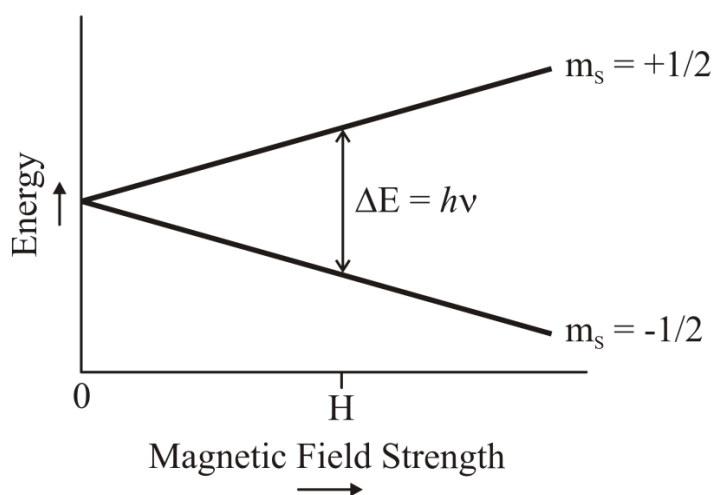


Figure 1.8. The magnetic field dependent energy level splitting for an unpaired electron.

Electrons are like tiny bar magnets and have associated magnetic moments. When an unpaired electron is put in a magnetic field, it can align its magnetic moment in the direction of the field (parallel/low field, $-1/2$) or against the field (anti-parallel/high field, $+1/2$). This creates two energy levels for the unpaired electrons (Figure 1.8) and allows us to measure the gap between them as the electron is driven between the two levels. The energy levels are magnetic field dependent and in the absence of the magnetic field there is no energy difference. The energy difference between the two electron spin states is represented by the equation $\Delta E = g\beta H$, where g is a proportionality constant, β is the Bohr magneton (value of the intrinsic magnetic moment associated with the spin of a free electron), and H is the strength of the magnetic field. This

equation establishes that the difference in energy between electron spin states is linearly dependent on the external magnetic field. Absorption of electromagnetic radiation occurs when sweeping magnetic field tunes the spin states of electron such that their energy level gap matches that of the electromagnetic radiation. The spectrometer then detects the absorption. Radiation in the microwave range is required for electron spin transition to occur. A resonance cavity is needed to create standing waves of the microwaves used to induce electron spin transitions. The resonance cavity would have to be retuned every time the frequency changed if the frequency of the radiation was to be swept and magnetic field was held constant. Thus, keeping microwave frequency constant means tuning resonance cavity to one microwave frequency; this offers better experimental performance and precision.

EPR Line Shape and Hyperfine Interaction

Along with the applied magnetic field, unpaired electrons are also sensitive to their local environments. Nuclei of the atoms in a molecule also have a magnetic moment, which induces a local magnetic field at the electron resulting in either an increase or decrease in the external field strength required to excite a transition. The resulting interaction between the nuclear spin and electron spin is called hyperfine interaction. The hyperfine interaction causes the splitting of the EPR resonance absorption lines referred to as hyperfine splitting. This splitting depends on the nuclear spin number (I)s of nearby nuclei. The number of absorption peaks/splitting increases according to $(2I+1)$ nuclear spin states.

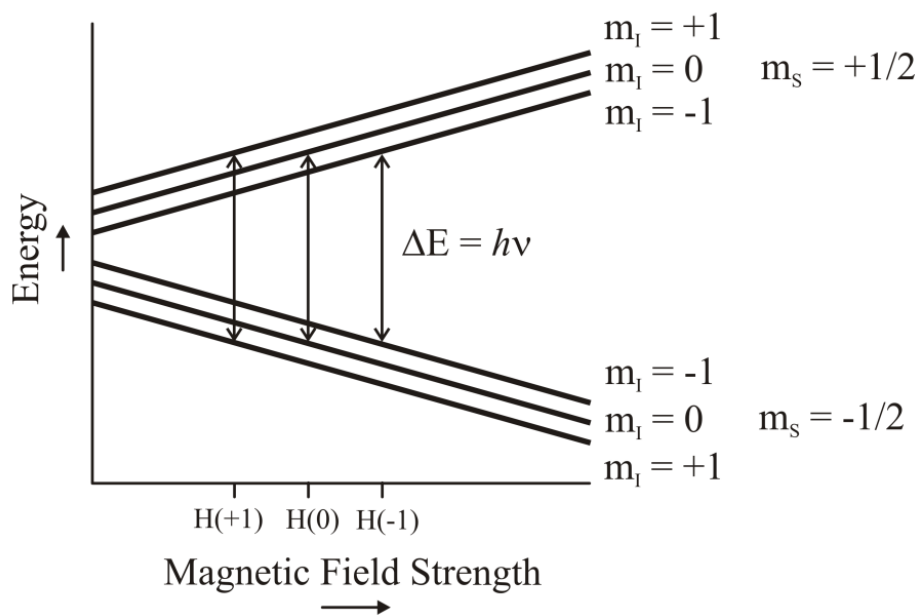


Figure 1.9. The hyperfine interaction. The allowed transition for an electron spin bound to a spin =1 nucleus.¹²⁴

In our work, we have used the nitroxide spin label. In nitroxides the unpaired electron is bound to an ^{14}N nucleus with nuclear spin angular momentum $I = 1$.¹²⁵ The nuclear magnetic moment can have three possible orientations corresponding to the $m_I = +1, 0,$ and -1 state and an electron can have two possible quantum states in the presence of the field $+1/2$ and $-1/2$. Thus, each spin state of an electron is split into three energy levels. The selection rules of quantum mechanics dictate that $\Delta m_s = \pm 1$, and $\Delta m_I = 0$, resulting in the three allowed transitions (Figure 1.9) and hence the three lines in the EPR spectra discussed throughout this dissertation. The EPR signal coming from the cavity is weak due to the small differences in the relative populations of the $+1/2$ and $-1/2$ electronic states. To increase the signal-to-noise ratio it is necessary to selectively amplify the signal. The method known as magnetic field modulation with phase sensitive detection is used. If there is an EPR signal, the field modulation sweeps through part of the signal and the amplitude of the microwaves reflected from the cavity is modulated at the same frequency. The EPR signal will be linear over the set interval if the appropriate modulation

is used, and the EPR signal is transformed into a sine wave with an amplitude that is proportional to the slope of the signal. The phase sensitive detector filters out all signals other than the signal modulated at 100 KHz by comparing the modulated signal with a reference signal having the same frequency and phase as the field modulation. Hence, the EPR spectra is displayed as the first derivative of the actual absorption.

Lineshape Analysis

The mobility of the nitroxide spin label affects the CW EPR spectral lineshape. Protein rotational tumbling, backbone dynamics, and intrinsic motion of the spin label all contribute to the mobility of R1, hence the local protein dynamics is encoded in the spectral lineshape.¹²⁶ The time range where the lineshape of X-band CW-EPR spectra is sensitive to molecular motion is 0.1-100 ns (Figure 1.10). The hyperfine interaction has an orientation independent component (isotropic) and an orientation dependent component (anisotropic). The frequency difference of the anisotropies determines the timescale of motion required to produce averaging of magnetic anisotropies. Simply, if a spin label in solution is not tumbling rapidly enough to average out anisotropic components in the time required to obtain spectral information, resonance occurs over a wide range of applied field, as different net fields are experienced by molecule in each of its various orientations. As a result, considerable broadening of the EPR lineshape with decreased amplitude is observed. When spin label tumbles rapidly the anisotropic component is averaged to zero ($\tau < 0.1$ ns) as a result EPR spectra are orientation independent influenced only by the nuclear spin states of ^{14}N consisting of three sharp lines of equivalent height and width.

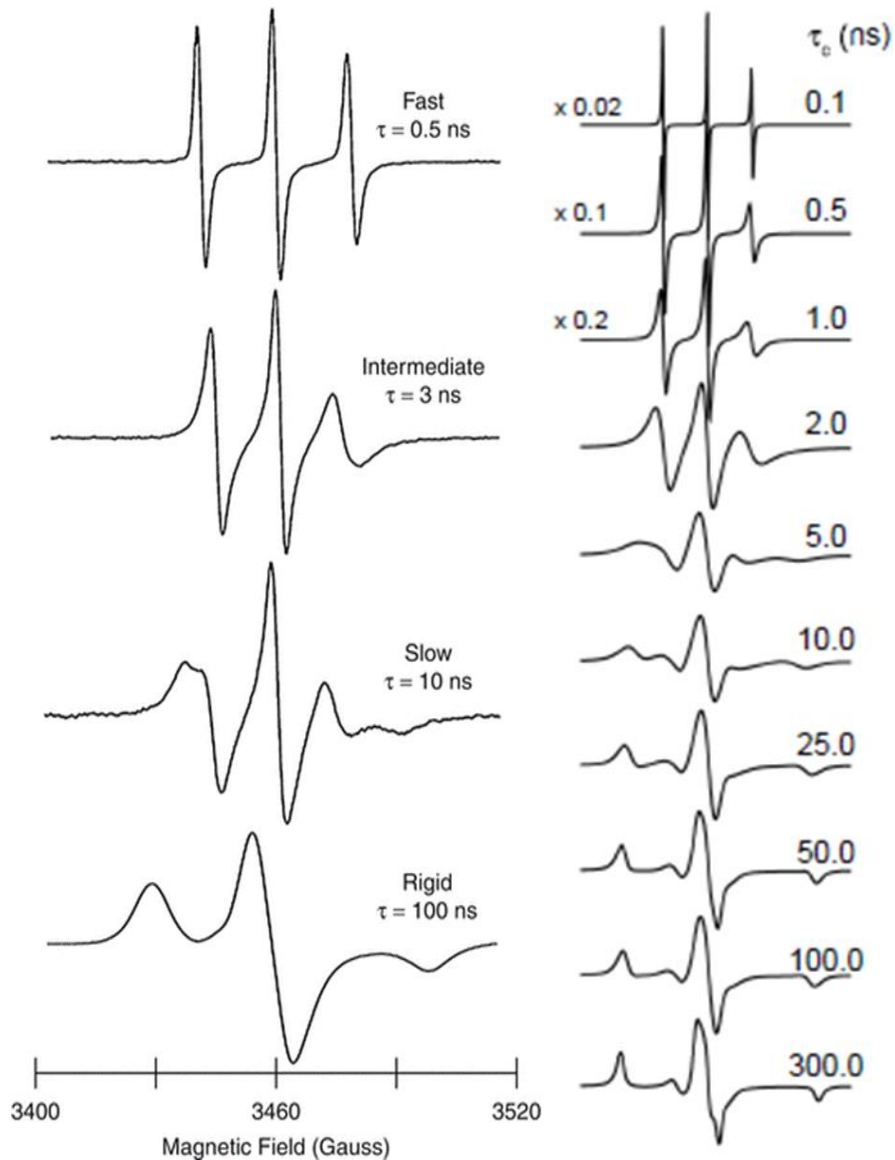


Figure 1.10. The time scale at which EPR spectra is sensitive. $\tau = 0.1- 2$ ns represents fast motion, $\tau > 2 - 10$ ns represents weak and moderate immobilization, $\tau > 10 - 100$ ns represents strong immobilization, and $\tau > 100$ ns is the rigid limit.

Another factor with anisotropy is the g -factor. It determines the point about which the spectrum is centered. This is dependent on the microwave frequency, therefore by operating at a different EPR frequency bands, the time window for motional sensitivity of the lineshape can be shifted. As discussed above $\Delta E = h\nu = g\beta H$, rewriting this equation in terms of $g = h\nu/\beta H$ shows that g , the spectroscopic splitting constant, is important in determining the magnetic field (H)

that corresponds to the resonance at a fixed frequency. Because of the anisotropic components that influence the magnetic field, value of g will vary with the orientation of a molecule with respect to the external magnetic field. If a spin label does not tumble sufficiently rapid to remove these anisotropic effects, the value of g , and thus the field for resonance will be slightly affected.

The SDSL-EPR spectra with T4 Lysozyme are well studied.^{127,128} The spin labels on protein surfaces in α -helix show a high degree of mobility, reflected in the EPR lineshape by sharper lines, and less overall spectral broadening. On the other hand, the spin label that interacts with neighboring side chains or is placed in the subunit interface has lower mobility resulting in a broader spectrum. Mobility of side-chain can help monitor the conformational changes, as relative amounts of motional components indicate a change of protein conformation.

In this work, we have attached spin label to various surface exposed sites of T4 Lysozyme and monitored the EPR spectra after immobilization on NPs. For proteins with a molecular weight (MW) ≤ 45 kDa,^{120,129} these all three motions together narrow the spectral linewidth in buffer solutions (Figure 1.11, black) due to motional averaging. If any of the three motions slow down, the spectrum becomes broadened. For example, in solution, if the protein MW is increased (ca. by conjugating with polymers), the spectrum become broader than that in the buffer (Figure 1.11, blue) because the protein rotational tumbling rate is reduced. If such tumbling is completely restricted (ca. protein is immobilized or has MW > 45 kDa), then the spectrum only reflects the protein backbone and R1 intrinsic motions, resulting in an even broader line shape (Figure 1.11, green). On top of that, if the R1 intrinsic motion is restricted by “contact” with some species, the spectrum becomes the broadest (Figure 1.11, orange and star). This information is helpful for determining protein orientation on a surface. CW EPR can also detect local disordering/disturbances. For example, in solution, if the protein secondary structure

changes to a less ordered state, then the linewidth becomes sharp again (Figure 1.11, red VS blue or green). Most of our signals are broad due to the slowing of rotational tumbling because of immobilization, and some are even broader due to contact of spin label with NP or crowding. The site-specific broadening and the extent of broadening help one identify the orientation of the enzyme on NPs, which then allows one to propose the model of interaction and/or the mechanism of interaction. Furthermore, the broadening of spectra helps monitor the local conformational dynamics of the enzyme at the labeled site.

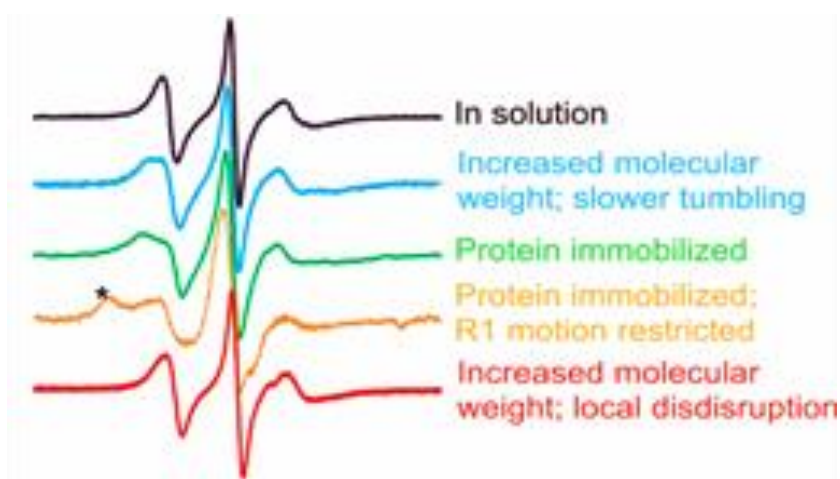


Figure 1.11. The principle of CW EPR to probe local dynamics.

CW EPR Spectrometer

The CW EPR spectrometer has four main components: a magnet, a resonator, a microwave bridge, and the electronics in the console. The source and the detector are in the microwave bridge. Figure 1.12 is a block diagram of the major components of CW EPR spectrometer and key components of the microwave bridge. Vacuum tube called klystron is used to generate microwave radiation of approximately 9.5 GHz. The microwave radiation is then split into two paths, one towards the cavity and the other towards the reference arm. There are attenuators on both paths to control the microwave radiation used. The attenuated radiation towards the cavity is then fed into the circulator. The radiation is traveling along the waveguide.

Circulator directs the microwave radiation from the source to the resonator and directs the reflected microwave radiation (after absorption) by the sample to the detector without mixing the two. The resonator has a set of magnetic field modulation coils. The detector changes the reflected microwave radiation to electrical current, which is then sent to the console for recording and analysis. The signal going to the detector is first combined with a reference signal coming from the reference arm. The reference arm has a phase shifter that sets a defined phase to match that of the signal coming from sample resonator. Hence, permits the phase-sensitive detection and also amplifies only the signal modulated at 100 kHz in phase with the source.

Reference arm has attenuator and phase shifter. The detector is a linear detector because at high power levels greater than 1 mW the diode current is proportional to the square root of the microwave power. The diode should be operating at a linear range for optimal sensitivity and quantitative output. Reference arm ensures that the detector is operating at an optimum level by providing a bias. The magnetic assembly includes the power supply as well as a field sensor or regulator.

Resonator enhances the microwave magnetic field at the sample to induce EPR transition. It is a box that resonates with microwaves. The resonance of the cavity means that the amount of energy reflected from the cavity to the detector remains constant until magnetic resonance occurs within the sample. When resonance occurs, microwave radiation is absorbed by the sample which is detected as a 'dip' in the spectrometer's detector current. Microwave reflection of a resonator is frequency- dependent. Iris is present in the resonator to control how much radiation is reflected to the detector. Adjustment of this quantity is called coupling. Coupling screw is used to adjust iris.

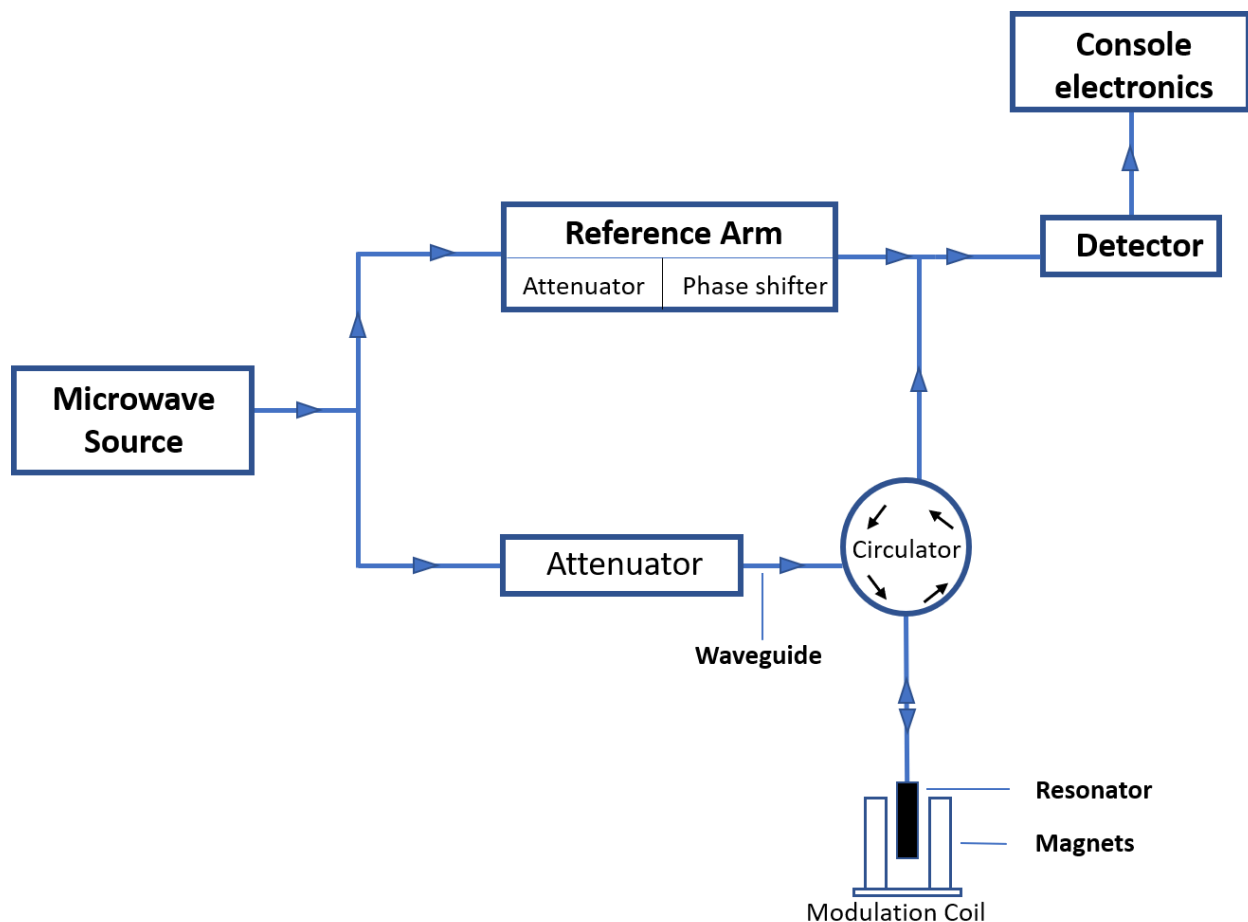


Figure 1.12. Block diagram of CW EPR instrument. The major components of CW EPR are Resonator, magnets, microwave bridge and console electronics. The source and the detector are part of microwave bridge.

Resonator stores microwave energy; energy may be lost to the side walls of the cavity. The energy in the resonator has an electrical component and a magnetic component that are perpendicular. To avoid samples absorbing energy via the electric field, the samples are positioned such that they lie within the magnetic field maximum and the electric field minimum so that the signal is the largest. When absorption occurs, the coupling of the resonator changes and increases the intensity of the reflected microwaves sent back to the bridge which increases the signal sent from the detector to the console.

Field modulation coil is situated around the resonator to modulate the main field. Modulation coil produces a low amplitude oscillating field. Field modulation performed at 100 kHz results in the direct detection of the 1st derivative of absorption. This allows the detection of typically weak signals in EPR spectra.

The console has modules to control microwave frequency, phase, and attenuation. In addition, it has magnetic field control until to regulate and sweep the applied magnetic field. Electronics within the console digitizes the EPR signals into a recordable and analyzable format. The X-band EPR magnet is standard water-cooled copper electromagnet operating at approximately 3400 Gauss but can reach fields greater than 12,000 Gauss without overheating.

CHAPTER 2. PROBING THE AGGREGATION MECHANISM OF GOLD NANOPARTICLES TRIGGERED BY A GLOBULAR PROTEIN[†]

Introduction

The rapidly developing nanomaterials, especially the nanoparticles (NPs), are advancing a number of areas.^{80,130–135} Among the NPs, gold NPs (AuNPs) have found broad applications in optics, bio-sensing, drug delivery, genetics, medical science, and therapeutics,^{133,136–143} due to their small size, high volume-to-mass ratio, high thermal stability, ease of preparation and functionalization, relatively less toxicity, and convenience for detection.^{133,136–140} Meanwhile, along with the exciting development and applications, concerns have been raised about the impacts of AuNPs on public health and environment, as well as the effects of the biological environment on NP functions.^{58,136,144} Fundamentally, all effects originate from the molecular interaction of AuNPs and the highly diverse biomolecules, especially proteins. Therefore, in order to minimize the aforementioned concerns, it becomes essential to reveal the molecular mechanisms of the NP-protein interactions and identify the pathways that cause these concerns.

Due to the large variety of proteins in the biological system, interaction of AuNPs and proteins is often a complex process. Generally, upon exposure to a biological environment (ca. serum), NPs are often coated by a dynamic layer of proteins, known as the protein corona.^{145,146}

[†] The work discussed in this chapter was co-authored by Sunanda Neupane, Yanxiong Pan, Sunitha Takalkar, Kylie Bentz, Jasmin Farmakes, Yi Xu, Bingcan Chen, Steven Y. Qian, and Zhongyu Yang. The work was previously published in the *Journal of Physical Chemistry C*.¹²¹ Sunanda Neupane and Yanxiong Pan had equal contributions in this work. Sunanda Neupane and Yanxiong Pan were the primary developers of the conclusions that are advanced here. Sunanda Neupane collected all the data discussed in this chapter and Yanxiong Pan prepared AuNPs. Sunanda Neupane and Yanxiong Pan drafted previously published versions of this chapter. Sunitha Takalkar, Kylie Bentz, Jasmin Farmakes, Yi Xu, Bingcan Chen, Steven Y. Qian, and Zhongyu Yang proofread the manuscript and helped trouble shoot experimental conditions. Sunanda Neupane, Yanxiong Pan, and Zhongyu Yang revised previously published versions of this chapter.

Such adsorption of protein is usually non-specific and but may assist in the dispersion of NPs in solution (Figure 2.1, case I); the desired NP functions might be disturbed as well.^{144,147,148}

Proteins and NPs could also form large agglomerates (Figure 2.1A, case II), which have found applications in medical research.¹⁴⁹ Lastly, some proteins (i.e. lysozyme) are able to trigger the aggregation of AuNPs, forming both large agglomerates and protein aggregates.^{150,151} Therefore,

to ensure NPs remain functioning as desired, it is essential to minimize the non-specific

adsorption of proteins onto NPs, which can be achieved by identifying the pathways of the protein-AuNP adsorption and developing approaches to block these pathways. On the other

hand, NPs are also able to induce proteins to undergo a complex, heterogeneous conformational change at the NP surface (Figures 2.1A, case I and 2.1B, case I).^{130,147,152,153} One consequence of

this process has been found to either inhibit or trigger the protein/peptide fibril formation (Figure 2.1B, case II).¹⁵⁴⁻¹⁵⁶ Upon specific modification/functionalization, NPs may even be able to

adsorb proteins uniformly on their surface (Figure 2.1B, case III), leading a change (often

enhancement) in protein thermos-stability and enzymatic activity.¹⁵⁷⁻¹⁵⁹ Therefore, understanding

the changes in protein structure and dynamics upon adsorption to AuNPs becomes essential in

designing and optimizing the NP-based protein carriers.^{158,160,161}

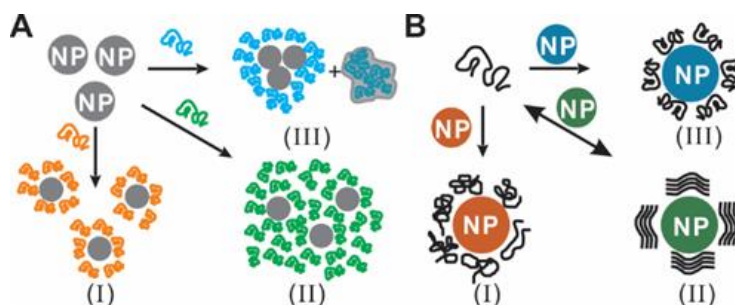


Figure 2.1. Illustration of the influences of proteins on NPs (A) and the influences of NPs on proteins (B). A (I) Protein molecules coat the surface of NP and keep the NP-protein complexes stably dispersed. (II) The NP-protein complexes form larger agglomerates. (III) Protein triggers the aggregation of NPs while being unfolded and precipitated. B (I) NPs trigger conformational changes of proteins. (II) NPs stimulate or inhibit the formation of protein fibrils. (III) NPs induce conformational reorientation of adsorbed proteins.

Due to the aforementioned complexities, understanding the nano-protein interface should be approached in a case-by-case manner. Among the current attempts, the binding kinetics and thermodynamics have been probed for AuNPs and several proteins via various approaches (see recent reviews^{80,81,145,162}). In spite of these exciting findings, the molecular level interaction mechanisms are largely unclear, mostly due to the lack of information on site-specific conformational dynamics and structure changes of proteins upon interaction with AuNPs. The major barriers preventing such efforts include the complexity caused by the molecular interaction as well as the large size and high heterogeneity of the protein-NP complexes.

Our original intention of investigating the inter-molecular interaction of a globular protein, T4 lysozyme (T4L), and the AuNPs was to probe the molecular mechanisms of such an interaction in order to serve as the structural basis to design more biocompatible AuNPs. In addition, we intended to demonstrate the effectiveness and advantages of Electron Paramagnetic Resonance (EPR) spectroscopy in probing the conformational dynamics of the proteins at the residue level regardless of the system complexity and heterogeneity. Before this work, EPR has been applied to probe structural information in many (complex) biological and/or synthetic systems, such as globular proteins, nucleic acids, membrane proteins, protein-DNA complexes, and metalloproteins.¹⁴⁸⁻¹⁶¹ The special advantages of the EPR approach including probing structure and dynamics information of macromolecules in their native states, no size limitation, and no heterogeneity and complexity limitation, guaranteed the success of these studies.¹⁷⁷ In addition, the EPR technique had been applied to study the lateral diffusion of thiol-ligand on the surface of AuNPs,¹⁷⁸ radical formation on the surface of AuNPs,¹⁷⁹ and detection of reactive oxygen species,¹⁸⁰ indicating that the presence of the metallic nano-sized materials does not affect EPR signal. We selected T4L as the model protein for our studies because this hydrolytic

enzyme is an ideal model for several reasons. It has been demonstrated to cleave glycosidic linkages in the peptidoglycan of bacterial cell walls¹⁸¹ and its intrinsic flexibility is known to be closely correlated with its enzymatic activity.^{127,182,183} At physiological pH, T4L is positively charged making it possible to be adsorbed by the negatively charged AuNP surface. The relatively small size makes T4L a good candidate to create short-range molecular interactions.¹⁸⁴ Lastly, the EPR data interpretation of T4L have been documented in literature, making it a good reference protein.¹⁸³

Experimental Methods

Apparatus and Reagents

Bovine serum albumin (BSA) was purchased from Sigma-Aldrich (A9306). The thrombin binding aptamer sequence was custom made by Integrated DNA Technologies, Inc (Coralville, IA). UV spectra were obtained with the NanoDrop UV-Vis Spectrophotometer (Thermo Scientific ND-2000 C) at the Core Biology Facility of Department of Chemistry and Biochemistry, North Dakota State University (NDSU). CD data were obtained with Jasco J-815 spectropolarimeter at the core facility of Department of Pharmaceutical Sciences, NDSU. All CW EPR data were acquired with a Varian E109 and a cavity resonator. The DLS data were obtained by using the Zetasizer (NICOMP 380 ZLS Particle Sizer, Particle Sizing Systems, Inc. USA) at the Department of Coating and Polymeric Materials at NDSU. The Transmission Electron Microscopy (TEM) was conducted at the NDSU Electron Microscopy Center.

Protein Expression, Purification, and Spin labeling

Mutants of 44C, 65C, and 151C were prepared as described before.¹⁸⁵ Briefly, the DNAs of these mutants were generated by QuikChange site-directed mutagenesis of the pET11a-T4L genetic construct containing the pseudo-wild-type mutations C54T and C97A,^{186,187} followed

with verification of each mutation by DNA sequencing.¹⁸⁸ These mutants of T4L were expressed, purified, and then desalted (to remove DTT) into a buffer suitable for spin labeling (the “spin labeling buffer”, containing 50 mM MOPS and 25 mM NaCl at pH 6.8) using previously reported procedure.¹⁸⁶ The desalted protein mutants were then reacted with a 10 fold molar excess of S-(2,2,5,5-tetramethyl-2,5-dihydro-1H-pyrrol-3-yl) methylmethanesulfonylthioate (MTSL, Toronto Research Chemicals, Inc., Toronto) at 4°C overnight (yielding R1). Excess MTSL was removed using the Amicon spin concentrator (Millipore, 10,000 MWCO, 50 ml). The spin labeled protein mutants were stored in this spin buffer at -20 °C for further use.

Continuous-Wave EPR Spectroscopy

To confirm the conformational dynamics of the spin labeled T4L, the stored samples were concentrated to ~100 µM using the Amicon spin concentrator (Millipore, 10,000 MWCO, 50 ml). This stock was diluted by half with a 60% w/w sucrose solution to yield a concentration of ~50 µM in 30% w/w sucrose solution. Approximately 20 µL of sample was loaded into a borosilicate capillary tube (0.70 mm i.d./1.25 mm o.d.; VitroGlass, Inc.), which was mounted in a Varian E-109 spectrometer fitted with a cavity resonator. All continuous wave (CW) EPR spectra were obtained with an observe power of 200 µW. All spectra were obtained with modulation frequency of 100 kHz and a modulation amplitude of 1.0 Gauss.

Preparation of Gold Nanoparticles

The gold nanoparticles (AuNPs) with an average diameter of 14±3.5 nm were prepared using the reported methods with minor modifications.¹⁸⁹ In the first cleansing step, all the glassware were thoroughly cleaned with aqua regia (3 HCl: 1 HNO₃) followed by rinsing with distilled water. In a 500 mL round bottomed flask, 100 mL of 0.01% H₂AuCl₄ was boiled with

continuous heating and stirring. Rapid addition of 4 mL 1% sodium citrate changed the color of this solution from pale yellow to wine red. The heating was continued for another 10 min; the heating mantle was then removed to continue the stirring for additional 15 min. The resulting gold nanoparticle solution was stored at 4°C for future use. Larger AuNPs (40, 70, and 90 nm) were prepared similarly but with decreased sodium citrate addition (2, 0.75, and 0.35 mL, respectively).

Preparation of the AuNP-Protein Mixture

To prepare the protein-AuNP mixtures with different protein-to-AuNP ratio (1:1, 25:1, 50:1, 100:1, and 250:1), the concentration of the AuNPs was first brought up by a factor of 10 via centrifugation (12,000 rpm, 5 min) and resuspension with 1/10 of the original volume (referred as to the “10xAuNP” through the work). In order to generate the desired protein-to-AuNP ratio, various amount of spin labeled T4L mutants were then added to 25 - 50 μ L 10xAuNP via solely pipetting (without extra stirring or turbulence).

To estimate the amount of bound T4L protein, we quantified the protein in the supernatant of each mixture by measuring OD 280 nm. The supernatant in each mixture was obtained by allowing the mixture to settle down for at least 30 minutes (gravimetric separation) or gentle centrifugation (1,000 rpm, 2 min). There was no clear difference in the supernatant created via these two approaches. So, the gentle centrifugation approach was used for most of our studies.

Dynamic Light Scattering

The diameter of AuNPs in the absence and presence of bovine serum albumin (BSA) were determined via dynamic light scattering by using Zetasizer (NICOMP 380 ZLS Particle Sizer, Particle Sizing Systems, Inc. USA). For each measurement, 2 μ L AuNPs solution (\sim 0.01

μM), either with or without BSA, was mixed with 1 mL distilled-deionized (DD) water and transferred into a disposable flint glass tube with plain end. The intensity of the incident laser light was tuned closed to 250 KHz in order to measure the particle size. Details of operation followed the standard user's guide provided by the manufacturer.

Time-resolved UV-vis Spectra of AuNP upon Interaction with 44R1 and 65R1 Mutants

The time-resolved UV-Vis absorption of samples was determined using NanoDrop UV-Vis Spectrophotometer (Thermo Scientific ND-2000 C). To determine the effect of AuNPs concentration on the UV-Vis absorption, various volumes of original AuNPs (0.01 μM), 1, 5, 10, 25 and 50 μL were mixed with 1000 μL DD water and immediately investigated using the UV-Vis Spectrophotometer. To investigate the interaction of AuNPs and T4L, predetermined protein mutants, 44R1, 65R1 and 151R1 ($n_{\text{T4L}}: n_{\text{AuNPs}} = 250:1$), were added into 1050 μL AuNPs medium (1000 μL DD water and 50 μL original AuNPs), one at a time. For each mixture, the UV-Vis absorption was measured at 0, 10, 30, 50, 60 second, and 5, 10, 30 and 60 min.

Estimation of the AuNP Diameter

The sizes of the involved AuNPs were estimated using an established procedure.¹⁹⁰ Specifically, for the AuNPs in the absence of T4L, we obtained an absorbance peak (A_{spr}) at 518 nm. The particle size thus follows:

$$d = \exp(B_1 \frac{A_{spr}}{A_{450}} - B_2)$$

where the B_1 and B_2 is the slope and intercept of the linear fit, respectively. The A_{450} is the absorbance at 450 nm.

Upon contact with T4L, the spectra were shift to larger wavelength indicating the formation of larger AuNPs. The particle size at each contact time was estimated with:

$$d = \frac{\text{Ln}\left(\frac{\lambda_{spr} - \lambda_0}{L_1}\right)}{L_2}$$

where the λ_{spr} is the experimental peak positions whereas the λ_0 , L_1 and L_2 are equal to 512 nm, 6.53 and 0.0216, respectively.

Characterization of Protein Secondary Structure Using Circular Dichroism

For the pseudo-wild type protein and the three involved mutants, 44R1, 65R1 and 151R1, the CD spectrum was obtained (Jasco J-815-15OS, Japan) from 260 to 200 nm using a cylindrical cuvette with 1 mm path length. Typical sample volume and concentration were 300 μL and 10 mM, respectively. For the supernatant study, protein and AuNP mixture samples were prepared as described in the UV-Vis sample preparation section. The supernatant of each sample was obtained via gentle centrifugation (1,000 rpm, 2 min). A 300 μL volume was carefully taken and subjected to CD study. The baseline of each sample was corrected using DD water. Figure 2.6A shows the CD spectra of protein mutants in the supernatant after triggering AuNP aggregation in water; the deviation between different mutants was caused by the uncertainty in estimation of protein concentration in the supernatant. These spectra are very close to those of protein mutants in water shown in Figure 2.6B. The errors in helical content between mutants as estimated based on the mean residue ellipticity at 208 and 222 nm are on the order of ~5 % (or ~1 helical turn).

Activity Measurements

The activity assay was conducted using the kit provided by Sigma-Aldrich (*Micrococcus lysodeikticus* cells, ATCC No. 4698, M3770) as described earlier.^{182,191} Briefly, 10 mg of the cell was suspended in 100 mL 66 mM potassium phosphate buffer (pH 6.2). The active protein degrades the amount of the cell membrane, which was reflected by the reduction of the optical

density at 450 nm. Such reduction in optical density was employed to monitor the amount of active protein.

To prepare sample for the activity assay, predetermined pseudo-wild type protein and the three mutants, 44R1, 65R1 and 151R1 were mixed with 66 mM potassium phosphate buffer (pH 6.24, at 25°C) to prepare 100 μ L (1 μ M) protein solution, one at a time. Then, 40 μ L of the mixture was added into 1 mL of the *Micrococcus* suspension prepared as described above. The density at 450 nm was monitored immediately after the mixture formation for 300 s.

For the supernatant study, the protein nanoparticle sample was prepared as in the UV-vis absorption study. The supernatant of each sample was obtained via centrifugation.

Approximately 40 μ L of the supernatant was added into the 1 mL *Micrococcus* suspension and subjected to the activity assay.

Zeta Potential Measurements

The zeta potential of the involved AuNPs were measured in water using a Nano ZS Zetasizer (Malvern Instrument Ltd.). Approximately 50 μ L as-obtained AuNPs with different particles size were mixed with 1000 μ L water. The mixture was then moved into a disposable folded capillary cell, one at a time, followed by data acquisition. All the experiments were conducted at 25 °C. Each sample was repeated three times.

TEM Images

Copper TEM grids (300-mesh, formvar-carbon coated, Electron Microscopy Sciences, Hatfield, Pennsylvania, USA) were prepared by applying a 5 mL drop of the sample and allowing it to stand for 30 seconds, wicking off the liquid with torn filter paper, then allowing the grids to air dry. Phosphotungstic acid 0.1%, pH adjusted to 7-8, was dropped onto the grid containing the sample, allowed to stand for 2 min, and wicked off. After the grids were dry,

images were obtained using a JEOL JEM-2100 LaB₆ transmission electron microscope (JEOL USA, Peabody, Massachusetts) running at 200 kV. For TEM images shown in Figures 2.4E, 2.4F, 2.10C, and 2.10D, the AuNPs were mixed with T4L (protein-to-AuNP ratio of 250:1) for ~2 min, immediately followed by the drying process mentioned above.

Results and Discussion

To employ EPR in our investigation, a paramagnetic spin label has to be attached to the desired site of the target protein. We employed site-directed spin labeling (SDSL) to do so, where a cysteine residue is generated using site-directed mutagenesis, followed by reaction with a methanethiosulfonate spin labeling (MTSL) reagent to form a disulfide bond with the cysteine.^{119,186} The so-generated protein side chain is often named as “R1”.¹¹⁹ It has been demonstrated that attaching an R1 sidechain at most sites of T4L did not alter the function or conformation of the protein.^{120,186,192,193} Since it is the first time we expressed this protein in our laboratory, we carried out a full characterization of the protein using the Circular Dichroism (CD) spectroscopy and an activity assay.¹⁸² The particle size of AuNPs plays an important role in their properties. Our studies therefore involve AuNPs with a few diameters.

Characterization of T4L and AuNPs

A total of three T4L mutants were spin labeled (Figure 2.2A, green spheres) for our study, the 44C, 65C, and 151C (the spin labeled mutants: 44R1, 65R1, and 151R1). These mutants essentially serve as the representatives of the three major regions of the protein, the N-terminus, the inter-domain helix,¹⁹⁴ and the C-terminus (Figure 2.2A). To confirm that each of the spin labeled proteins retain the native secondary structure and activity, we obtained CD data and performed an activity assay for the three mutants as well as the “pseudo-wild type” protein. The two native cysteine residues of the “pseudo-wild type” protein were mutated to serines.¹²²

This protein will be referred as to the “wild-type” protein through the rest of this work. Note that such spin labeled pseudo-wild type proteins do not contain free cysteine. Thus, unlike some other proteins,^{195–197} the molecular interaction between our T4L and AuNPs is a non-bonding, electrostatic interaction. The CD data presented in Figure 2.2B clearly illustrate that the wild-type and the spin-labeled T4L mutants expressed in our laboratory were in the native secondary structure.¹²⁷ The activity assay of T4L was performed according to a published procedure.¹⁸² The principle is to monitor the optical density (OD) at 450 nm of the *Micrococcus lysodeikticus* cells as T4L is added. A decrease in OD₄₅₀ is related to the amount of substrate being degraded by T4L and can be used to determine the T4L activity. Since a visual comparison of data from the wild-type and the mutant proteins is sufficient to demonstrate the protein activity, only qualitative analysis is presented here. As shown in Figure 2.2C, both the wild-type protein and the three mutants showed a rapid decay of the OD 450 nm within ~ 1 min, indicating the presence of active protein in the sample. The slope of the decay is comparable among the wild-type protein and the mutants, indicating the mutation and spin labeling did not alter the protein enzymatic activity of T4L. A negative control assay, wherein only water was used to interact with the substrate, showed essentially no activity (Figure 2.2C, purple triangles). To confirm the backbone dynamics of the spin labeled sites, we have obtained the Continuous Wave (CW) EPR data in 30% (w/v) sucrose. The purpose of sucrose in each sample is to slow down the protein molecular tumbling, so that the CW EPR signal only originates from the local backbone dynamics of the labeled sites and the intrinsic motion of the spin label.^{186,192} As shown in Figure 2.3, for each of the three studied sites, the resultant spectra were consistent with literature.^{186,192,193}

To characterize the AuNP, we obtained the UV-vis absorption spectrum of the AuNPs dispersed in water. The absorption at 518 nm (Figure 2.2D) indicates the presence of AuNPs. Using a previously reported procedure (see Experimental Methods), the diameter of the AuNPs was estimated to be ~14 nm.¹⁹⁰ This value was confirmed with the Dynamic Light Scattering (DLS), the Zeta potential measurements, as well as the Transmission Electron Microscopy (TEM) as shown in Figure 2.2E. TEM was also employed to characterize AuNPs with larger sizes involved in this work (Figure 2.2F for example).

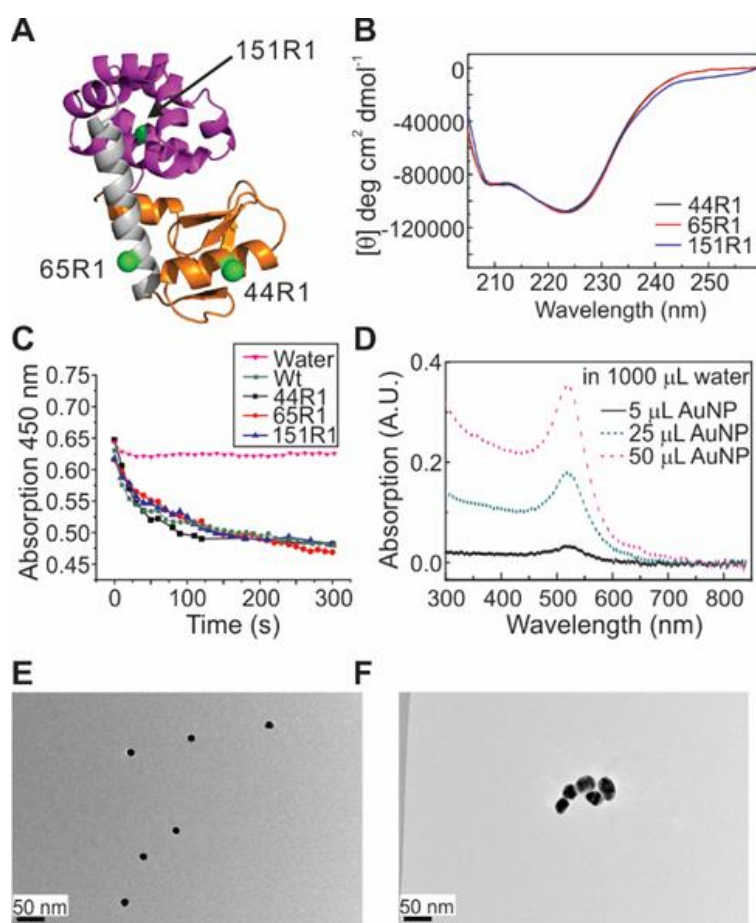


Figure 2.2. Characterization of T4L and AuNPs. (A) The three regions of T4 lysozyme highlighted with orange, grey, and purple. Each region is spin-labeled with one site (green spheres). (B) The CD spectra of the indicated T4L mutants in the “spin buffer”. (C) The activity assay for water, wild-type T4L, and the mutants of T4L as indicated in the figure inset. (D) The UV absorption spectra of various amount of the AuNP in 1000 μ L water. The absorption at 518 nm indicates the presence of the AuNPs with a diameter of ~ 14 nm. (E) The TEM image of the 14-nm AuNPs. (F) The TEM image of the 40-nm AuNPs.



Figure 2.3. The CW-EPR spectra of spin labeled protein in buffer with 30% sucrose. These data are consistent with literature.^{186,192,193} The arrows labeled with “i” and “m” indicate the spectrum of 44R1 contains an immobile and a mobile component, respectively, also consistent with literature. The scan range is 3300-3400 G.

T4L Triggers the Aggregation of AuNP

To probe the interaction of the AuNPs and T4L, a series of protein-AuNPs mixtures were prepared for each of the three mutants, with a protein-to-AuNPs ratio of 1:1, 25:1, 50:1, 100:1, and 250:1, respectively. In each mixture, we observed two phenomena occurring simultaneously. First, the color of each mixture solution turned from pink to violet-purple within 1 to 20 min upon addition of protein, depending on the amount of added protein. The change in color, as shown in Figure 2.4A, has been attributed to the size increase of AuNPs due to aggregation.¹⁹⁸ Note that the color change is not caused by the protein storage buffer¹²² since AuNPs were well-dispersed in the buffer. Meanwhile, we also observed the formation of visible, dark pellets precipitating out from the sample solutions. For simplicity in future discussions, from now on we will designate these two processes as pathway 1 and pathway 2:

Immediate formation of pellets (Pathway 2) \leftarrow T4L + AuNPs \rightarrow size increase of dispersed AuNPs (Pathway 1)

In pathway 1, the color change can be quantified via time-resolved UV-vis absorption. As shown in Figures 2.4B and 2.5, a clear shift of the absorption peak from 518 nm to 580 nm was observed for each of the three spin labeled mutants (T4L: AuNPs=250:1) within ~60 min,

indicating a time-dependent particle size increase. To quantify the kinetics, we estimated the diameter of the AuNPs at different contact times (Figure 2.4C).¹⁹⁰

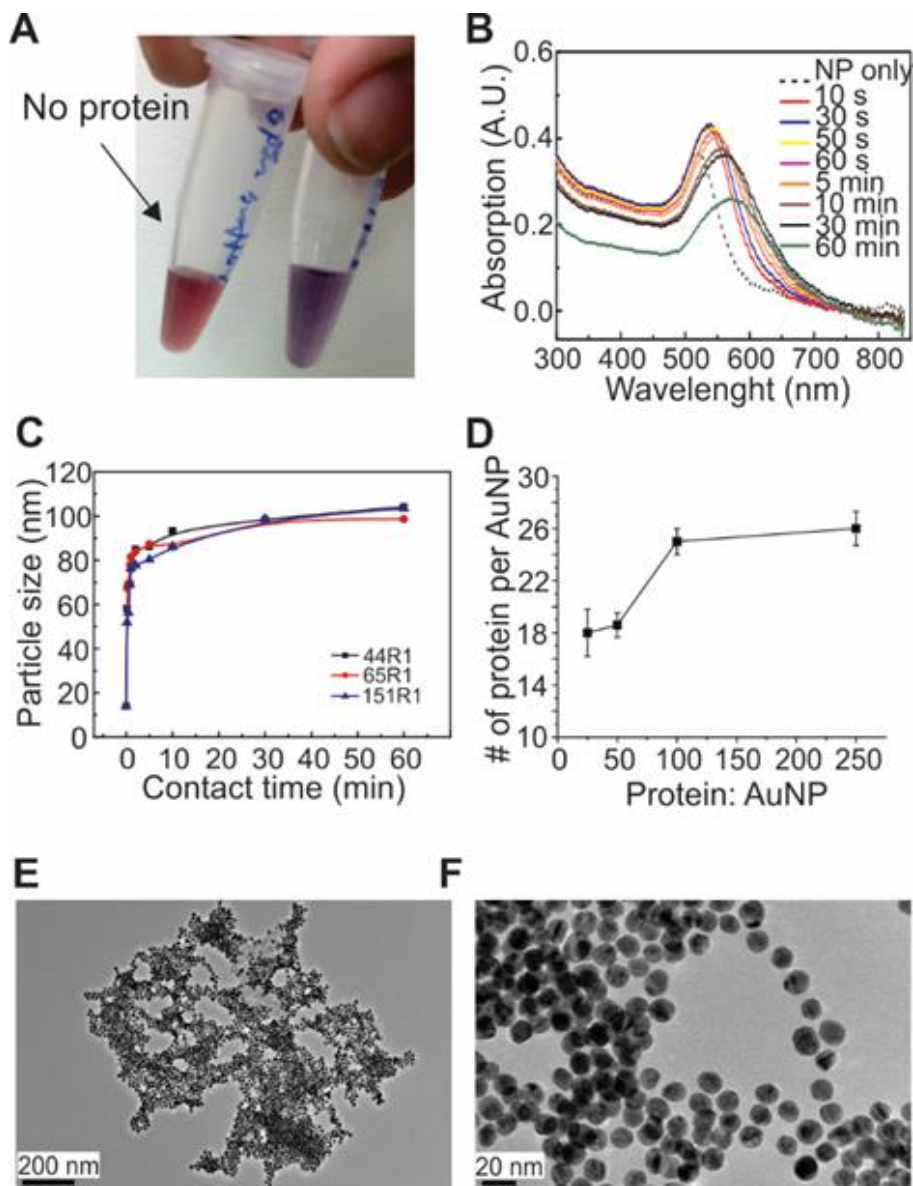


Figure 2.4. (A) The color of AuNPs alone (left) and upon addition of 151R1 (right) 5 min after mixing. (B) The time resolved UV spectra after mixing the AuNPs with 151R1. The dotted curve indicates the UV spectrum of the AuNP in water with no protein. A clear shift to the longer wavelength can be observed, indicating a diameter change in AuNP upon interaction of T4L. (C) The estimated particle size and the maximum absorption (see main text) as a function of contact time for the three studied T4L mutants. (D) The estimated number of protein either bound or adsorbed to AuNP pellets as a function of protein-to-AuNP ratio. (E), (F) The TEM image of the 14-nm AuNPs upon interaction with T4L at different resolution.

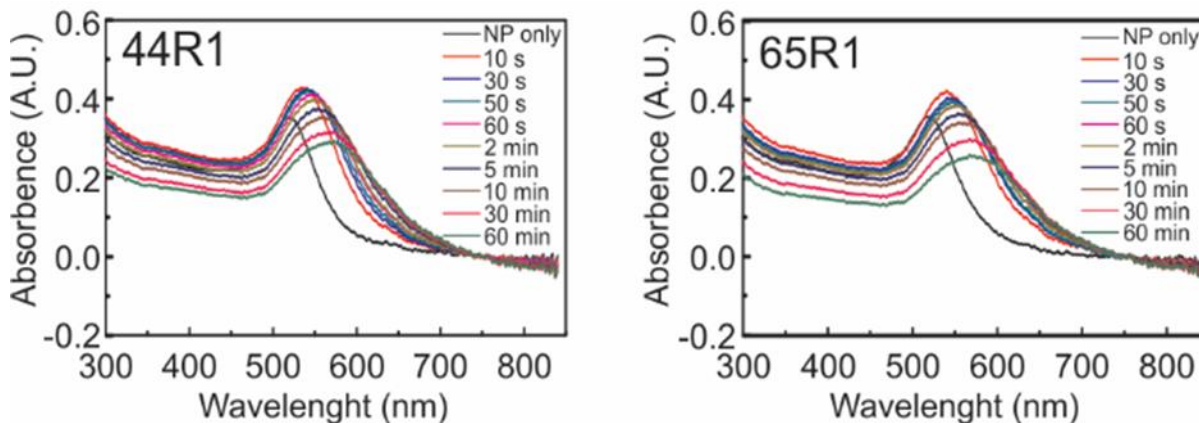


Figure 2.5. The time-resolved UV-vis spectra of 44R1 and 65R1 upon interaction with AuNPs.

The data indicates a two-phase particle size change, a rapid increase from ~14 nm to ~90 nm completed within ~5 min and a slow increase from ~90 nm to ~110 nm taking ~one hour. We speculated that such two-phase transition was due to two different aggregation processes: 1) a rapid aggregation of AuNPs triggered by T4L to form aggregates with a diameter of ~90 nm (named as “AuNP-90”) and 2) further aggregation of AuNP-90 to form larger aggregates (~110 nm, named as “AuNP-110”). The possible mechanism of each process was probed with later experiments (see below). It has to be noted that, the AuNP-110 continued aggregating slowly (usually overnight) to eventually form the visible dark pellets which were also precipitated out from the solution.

To estimate the amount of “bound” T4L protein in the pellets, we quantified the protein in the supernatant of each mixture for the protein-to-AuNP ratios, 25:1, 50:1, 100:1, and 250:1, were selected for such study. The amount of “bound” protein in the pellets was obtained by subtracting the amount of protein in the supernatant from the total protein added. The number of “bound” protein per AuNP was plotted as a function of protein-to-AuNP ratio and shown in Figure 2.4D. While at high ratios ($\geq 100:1$) ~25-26 protein per AuNP seemed to be “saturating” the AuNPs, as the ratio was decreased, less number of protein molecules were involved in

forming the pellets (e.g. at 25:1 protein-to-AuNP ratio, 18 protein molecules were bound to one AuNP and 7 proteins were released to the supernatant). This finding indicates that possibly only a small amount of free protein is sufficient to trigger the aggregation. This is supported by our finding wherein AuNP pellets were observed even with a 1:1 protein-to-AuNP ratio. The aggregation of the AuNPs was visualized by TEM (Figures 2.4E and 2.4F), wherein clustered particles were clearly observed upon interaction with T4L, in comparison to the isolated particles in the absence of T4L (Figure 2.2E), indicating T4L triggered the aggregation of the 14-nm AuNPs. In addition, since the TEM samples were taken during the color change (pink to purple) process, the TEM images confirmed that the color change is associated with nanoparticle aggregation.

Characterization of Protein upon Aggregate Formation

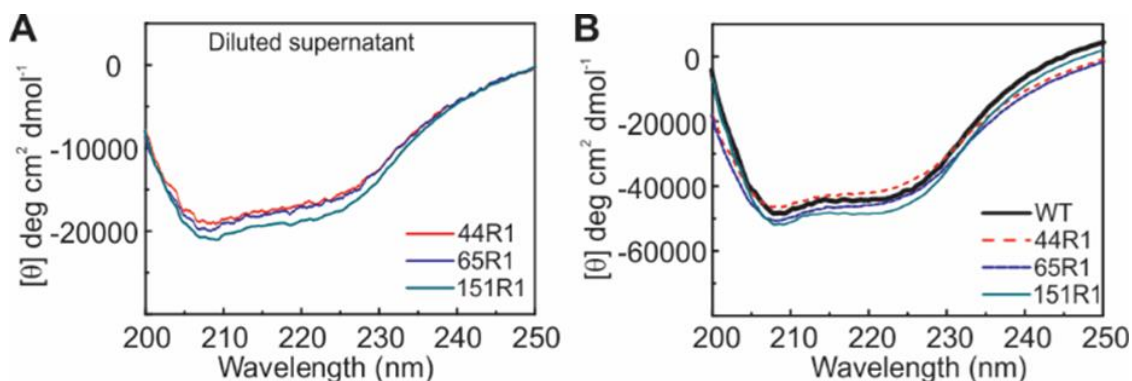


Figure 2.6. (A) The CD spectra of the three protein mutants in the supernatants after removing the aggregated AuNPs. (B) The CD spectra of the three protein mutants together with the wild-type protein in water.

To probe more details of the protein-NP interaction, we characterized three properties of T4L upon interaction with AuNPs: the secondary structure, the enzymatic activity, and the local backbone dynamics. In the supernatant of each mutant, the CD spectra and the activity assay were similar to those obtained in water (Figures 2.6A VS 2.6B), indicating proteins in the

supernatant have similar secondary structure and enzymatic activity as those in the native state (Figures 2.7A VS 2.7B).

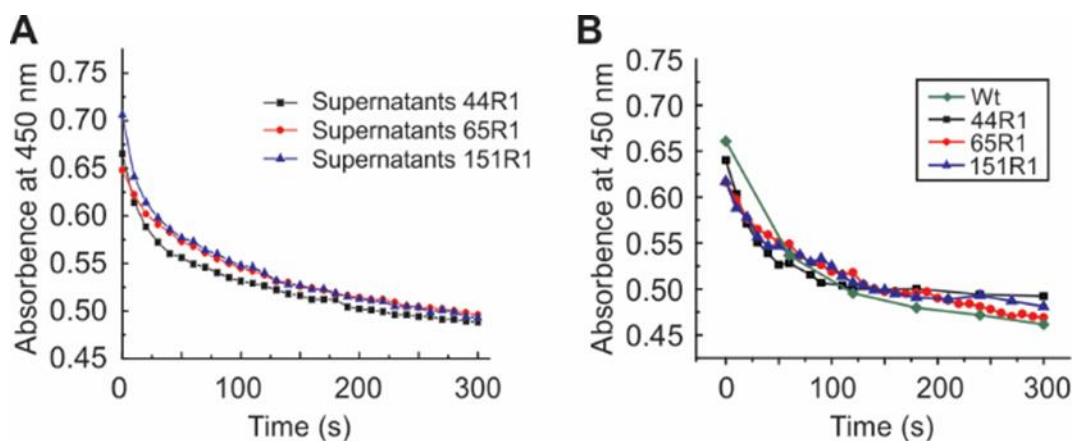


Figure 2.7. The activity assay data of the three protein mutants in the supernatant.

To probe the protein local conformational dynamics, CW EPR spectra were acquired on the mixture of AuNPs and the three mutants, one at a time. The recorded data of each labeled site is almost identical to that of protein in water with no AuNPs (Figures 2.8A VS 2.8B), indicating the local dynamics of the protein in the mixture are close to that of the protein in water at the three labeled sites. The protein-to-AuNP ratio for each mutant/AuNP mixture studied by EPR was 250:1. Note the sharper line shape shown in Figure 2.8A (VS Figure 2.3) is caused by protein rotational tumbling which adds additional motion to the R1 side chain.^{120,186,192} The CW EPR data on the supernatant of each mixture after centrifugation was identical to that of the native protein (Figure 2.8C), indicating the protein in the supernatant is also in the native conformation. When proteins bound to the large visible AuNP pellets were tested, the signal intensity was very weak, meaning that there was only a small amount of proteins on the aggregates. However, the EPR signal of the pellets showed that the linewidth of the central peak for each studied mutant was close to that of the protein in water, indicating that the protein mutants were mostly in their native protein conformation (Figure 2.8D). Note that such local

structural information is not available from the CD spectroscopy and the activity assay. Also it is difficult to measure the secondary structure and the activity of protein in the pellets, due to the low solubility of these aggregates. This information is only available from EPR measurements. Lastly, washing the aggregates with water almost completely eliminated all EPR signal (Figure 2.8E). It has to be noted that lowering the protein-to-AuNP ratio to 100:1 or even 50:1 did not alter the spectral line shape. Only the signal-to-noise ratio was decreased (data not shown). These EPR findings clearly indicated that there was a small amount of protein in the native conformation adsorbed to the surface of the aggregates. Such adsorption is likely to be weak, as the EPR signal was removed by washing the aggregates with water.

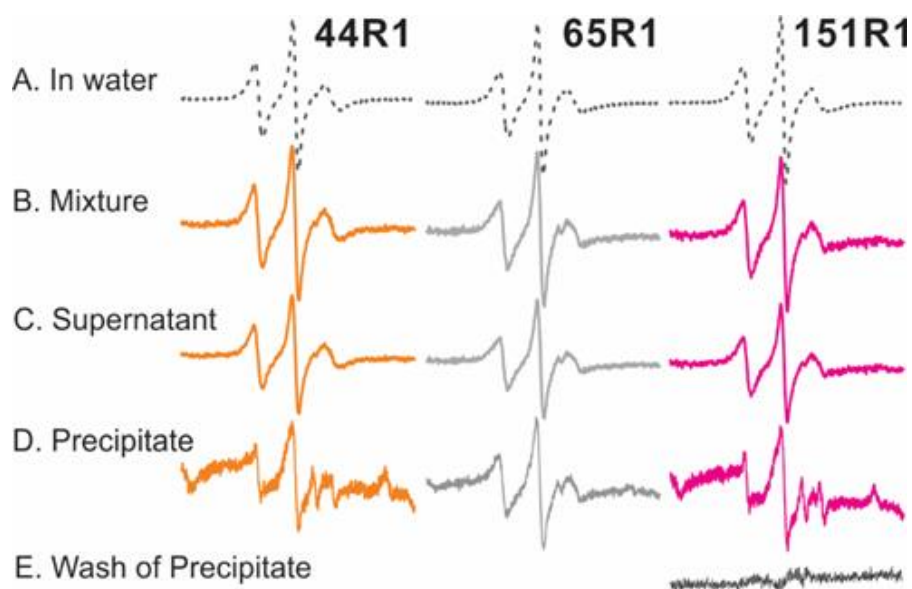


Figure 2.8. The CW EPR spectra of the three labeled sites, 44R1, 65R1, and 151R1, in water (A), upon interaction with AuNP (B), in the supernatant of the protein/AuNP mixture (C) and on the pellets (D). The pellets were washed with water and the CW EPR spectrum were reacquired for one mutant (E). The adsorbed protein was almost completely removed by washing.

Probing the Interaction Mechanism: Interaction with other Biomolecules

To confirm T4L is really the cause of the AuNP aggregation, we went on to investigate the interaction of AuNPs with other biomolecules, a serum protein and a single strand DNA. We started with Bovine serum albumin (BSA) because it has been utilized to stabilize AuNPs.^{199,200}

A mixture of BSA and AuNPs (BSA-to-AuNP ratio ~ 200:1) was prepared and subjected for study using time-resolved UV-vis spectroscopy. The spectra showed a noticeable shift in absorption occurring in ~10-20 min (Figure 2.9A), indicating that the introduction of BSA triggered the AuNPs to aggregate. The resulting particle size however, is much smaller (~30 nm as estimated with the published procedure,¹⁹⁰ Figure 2.9E). This indicated that BSA formed a corona on AuNP surface which stabilized these AuNPs at a diameter of ~30 nm. We then added T4L to the premixed BSA-coated AuNPs and found a similar trend in the time-resolved UV-vis spectra as observed before (Figures 2.9A VS 2.9B), except that the aggregation kinetics were much slower (Figure 2.9E, squares). The AuNP aggregation stopped when the particle size reached a diameter of ~ 90 nm. A possible explanation of this observation is that T4L was able to access AuNP surface via an exchange with BSA (dynamic corona),^{130,146,201} initiating the AuNP aggregation in a similar fashion as in the case without BSA. The slower kinetics is possibly due to the BSA coating which reduced the efficiency for T4L to trigger AuNP aggregation (see “slow bridging mechanism” below). Such aggregation yielded the AuNP-90 (definition see above), which can most likely be stabilized by BSA. There were no visible pellets formed immediately or overnight during this experiment, indicating BSA was able to effectively block the pathway 2 (rapid pellets formation). The EPR spectra of T4L in the BSA-coated AuNPs are identical to T4L in water. (data not shown), indicating T4L remains in its native conformation when interacting with the BSA/AuNP corona.

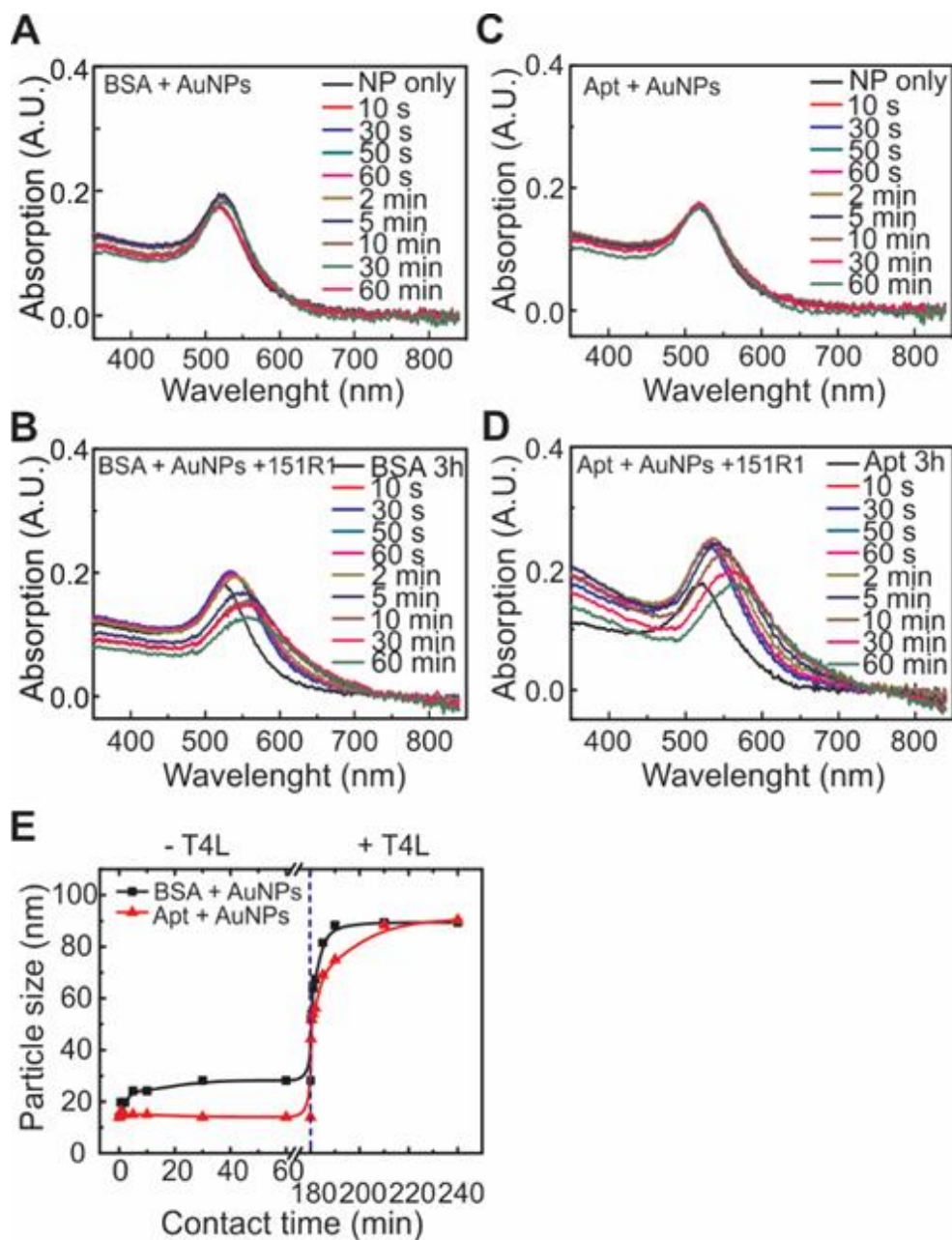


Figure 2.9. (A) The time-resolved UV-vis spectra after mixing the AuNPs with BSA. A substantial peak shift to longer wavelengths is visible, indicating a slight diameter increase in AuNPs upon interaction with BSA. (B) The time-resolved UV-vis spectra after mixing the BSA-coated AuNPs with T4L (151R1). A clear shift to longer wavelengths is observed, indicating an increase in the size of AuNPs upon interaction with T4L. (C) The time-resolved UV-vis spectra after mixing the AuNPs with the TBA aptamer. Almost no shift is observed, indicating no change in AuNP diameter upon interaction with aptamer. (D) The time-resolved UV-vis spectra after mixing the aptamer-coated AuNPs with T4L (151R1). Similar to (C), a shift to longer wavelengths is observed, indicating an increase in the size of AuNPs upon interaction with T4L. (E) The change in AuNP particle size in cases (A) to (D) as a function of contact time.

Another control experiment was to utilize the negatively charged, single-strand DNAs (also known as aptamers) to coat the AuNPs. We selected the Thrombin binding aptamer (TBA) sequence: GGT TGG TGT GGT TGG (the “TBA aptamer”), for our study.^{202,203} The TBA aptamers were mixed with AuNPs at room temperature. We found that the TBA aptamer can stabilize AuNPs for a few days at 4 C° (no color change; no UV spectrum change; example data shown in Figure 2.9C). We then mixed the aptamer-coated AuNPs with T4L mutants at room temperature. We again observed both pathways 1 and 2, except a smaller amount of visible pellets formed through pathway 2 were observed. Our time-resolved UV-vis spectra once again showed a shift in absorption (Figure 2.9D). Most likely T4L can also exchange with the bound aptamer to access the AuNP surface, triggering the AuNP aggregation. The aggregates thus formed also have a diameter of 90 nm similar to aggregates mentioned above. It was observed that the AuNP-90nm were only partially stable in aptamers, forming relatively less amount of pellets. Similar to the case of BSA coated AuNPs the aggregation rate is much slower, indicating the aptamer is also effective in slowing down the AuNP aggregation triggered by T4L (see “slow bridging” mechanism below).

Probing the Interaction Mechanism: Interaction of T4L with Larger AuNPs

To probe the effect of AuNP size on the interaction, we investigated the interaction of T4L and AuNPs with three different sizes: 40, 70, and 90 nm. Our selection of these three sizes was based on the fact that the particle size increase shown in Figure 2.4C reached a plateau at 90 nm. We would like to investigate the effect of T4L on AuNPs with sizes on the pathway of the 14-nm AuNP aggregation, which may serve as valuable information for probing the aggregation mechanism. The preparation of these AuNPs is described in the Experimental Methods. The UV-vis spectroscopy, the Zeta potential measurements, and the TEM (Figures 2.2F, 2.10A, and

2.10B) were used to confirm the size. For AuNPs smaller than 90 nm (ca. the 40 and 70 nm AuNPs) we observed that T4L triggered AuNP aggregation via both pathways. For 90 nm, no pellets were immediately formed, meaning only pathway 1 took place. However, the visible pellets were again observed after being left overnight. These findings indicated that the aggregation of the 90-nm AuNPs triggered by T4L was most likely a slow and heterogeneous process. This speculation was consistent with the TEM images of the 90-nm AuNPs upon interaction with T4L (Figures 2.10C and 2.10D), wherein only partial aggregation (clustered particles) was observed (Figure 2.10C), while most particles remained isolated (Figure 2.10D). It has to be noted that the protein remained in their native conformation after interaction with these larger AuNPs as judged by EPR. The CW EPR spectra of a representative T4L mutant upon interaction with larger AuNPs were presented in Figure 2.11. The general conclusion is that after triggering the 40- and 70-nm AuNP aggregation, T4L remained in its native conformational dynamics. Since T4L triggered 90-nm AuNP aggregation is very slow, it is not surprising that the CW EPR spectrum is unchanged.

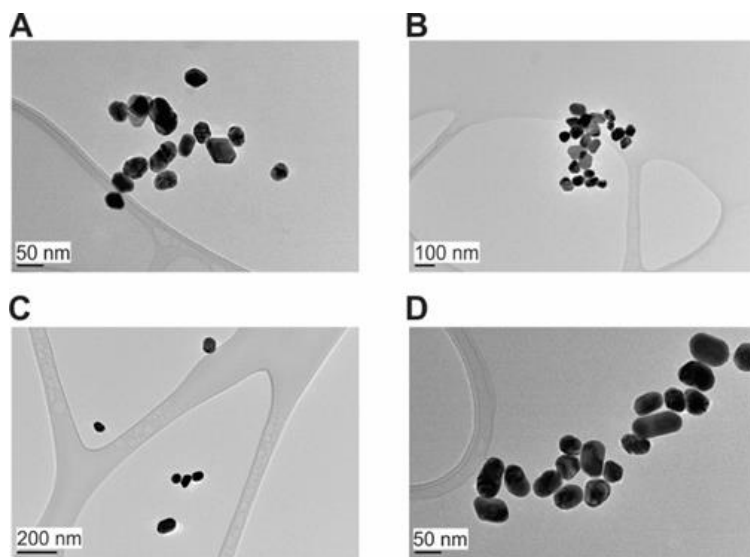


Figure 2.10. The TEM images of the 70 nm(A) and 90 nm (B) AuNPs. The size is less homogeneous and the reported diameter for each case was the average diameter. (C), (D) The TEM images of the 90-nm AuNPs upon interaction with T4L.

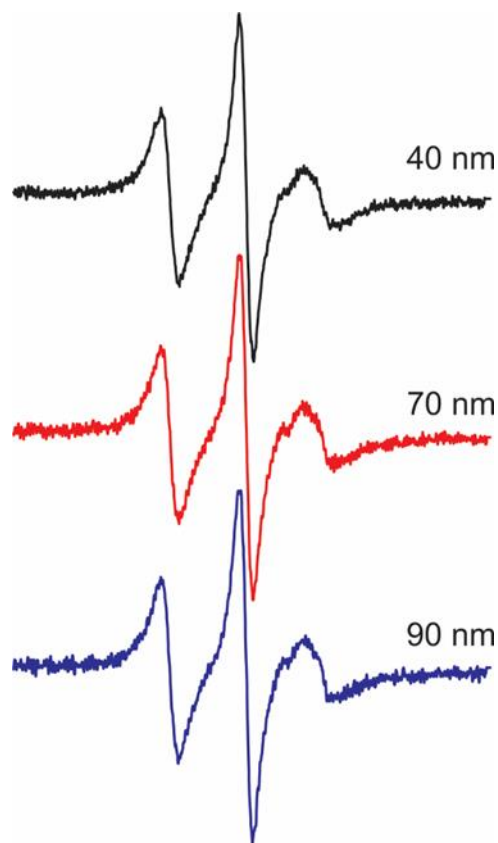


Figure 2.11. The CW EPR spectra of 44R1 upon interaction with the 40-, 70-, and 90-nm AuNPs. The scan range of each spectrum is 100 G. The line shape of each case is identical for that of 44R1 in water (Figure 2.8A).

Origins of the color change

We attributed the color change and UV-Vis absorption shift to the aggregation of AuNPs caused by T4L. First, our control experiment wherein the protein storage buffer was used to disperse the AuNPs showed that the ionic strength and pH of the solution is not the reason we observe AuNP aggregation (Figure 2.12). As shown in Figure 2.12, over a time period of ~1 hr, there was almost no change in the spectra for each AuNPs. Next, the color change (from pink to purple) was found to be irreversible, indicating that most likely the color change is on the pathway to the final pellets of AuNPs. Lastly but most importantly, the TEM images (Figures 2.4E and 2.4F) acquired during the color change/UV shift clearly demonstrated that the color change is associated with aggregation.

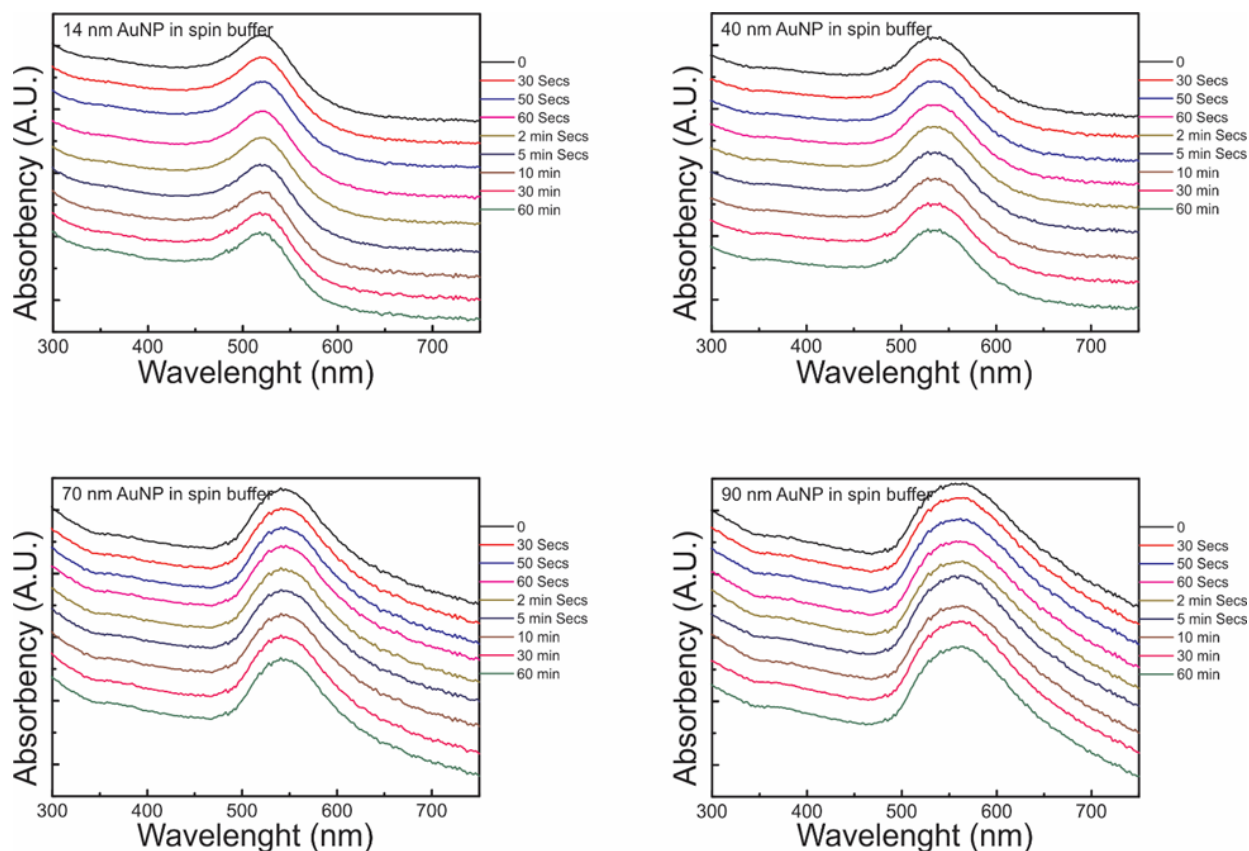


Figure 2.12. The time-resolved UV-Vis absorption spectra of the AuNPs at four different sizes. The baseline was shifted for clarity.

Possible Mechanistic Processes

Proteins have been found to not only coat the surface of NPs by forming a protein corona, but also trigger NPs to aggregate.^{204,205} In the latter case proteins were often (partially or completely) unfolded, aggregated, or even co-aggregated with the NPs. Consequently, the NP function can be severely affected. We hereby observed a slightly different phenomenon: while triggering the AuNP aggregation, T4L remained mostly in their native conformation and functionally active. By combining several analytical techniques, we had an opportunity to speculate the T4L-AuNP interaction mechanism and probe the role(s) T4L plays based on our experimental findings summarized as follows. 1) T4L making direct contact with AuNPs seems to be critical in triggering the aggregation of AuNPs. 2) T4L is capable to rapidly trigger the

AuNP-90 formation but further aggregation is much slower. 3) During and after aggregating AuNPs, T4L either remained in their native conformation or underwent a conformational transition to “refold” to its native conformation. 4) T4L was able to be (loosely) adsorbed to the surface of the pellets. 5) The BSA and aptamer test indicated that the protein corona was dynamic and again direct contact of T4L with the surface of the AuNPs was critical for aggregate formation. 6) T4L was unable to trigger the rapid formation of the pellets if the particle sizes were larger than 90 nm. Combining all above, a possible mechanism accounting for all our findings are described as follows.

It is known that AuNPs are only stable under surface protection (citrate ions in our case). De-protection or de-coating of the AuNP surface often leads to the formation of the visible black pellets. We, therefore, attribute pathway 2 to the decoating of the citrate ions on the AuNPs, most likely caused by the positive net charge of T4L under our pH. The unprotected AuNPs then become unstable and begin rapidly aggregating in solution, yielding the visible pellets (Figure 2.13A, upper panel). The surface of these large aggregates is able to adsorb T4L, which can then be washed off, consistent with our EPR finding (Figure 2.8). Pathway 1 is attributed to the previously reported, “bridging mechanism”,^{204,205} wherein T4L serves as a bridge to bring two AuNPs into close proximity (Figure 2.13A, middle and lower panels). Specifically, one T4L molecule binds to one AuNP with a positively charged region, and another with a different region. Due to the relatively small size of T4L (3-4 nm), once such protein bridge is formed, the two AuNPs are brought together to form a dimer. After the dimer is formed, T4L is released to the liquid phase. The protein might undergo some conformational change when serving as the bridge but eventually refolds to its native conformation (Figure 2.13A). It has to be noted that, after bridging two AuNPs, one T4L may leave the newly formed dimer and trigger the

aggregation of another pair of AuNPs. The bridging mechanism helps save the amount of protein needed to trigger AuNP aggregation, which is consistent with our finding that only a small amount of T4L is needed to trigger the aggregation.

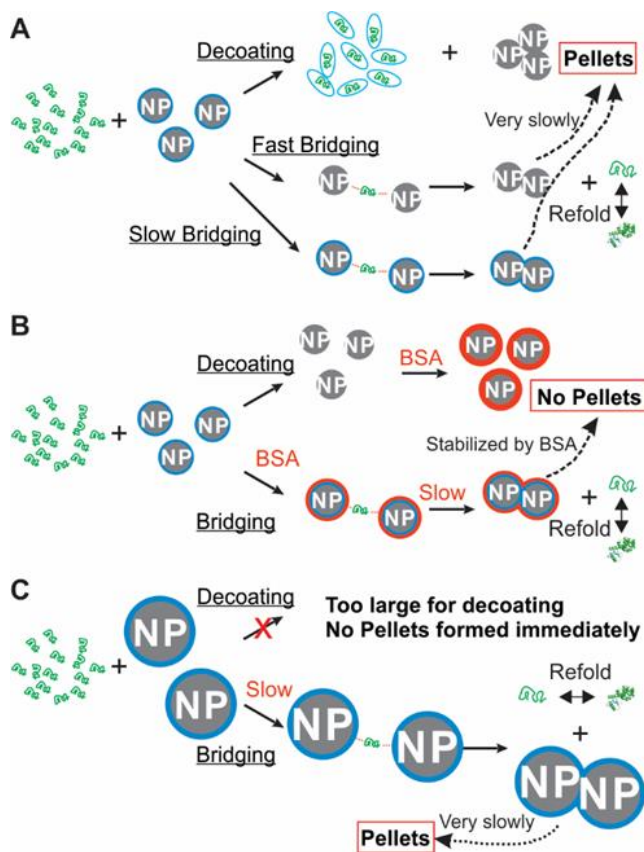


Figure 2.13. Schematic illustration of the NP-T4L interaction mechanism. (A) Upon contact of T4L with AuNPs, a portion of AuNPs are decoated by T4L. Some of these decoated AuNPs rapidly form pellets (upper panel). The rest of the decoated AuNPs interact with T4L to rapidly form larger AuNPs dispersed in solution (middle panel). This process is defined as the “fast bridging” mechanism. The non-decoated AuNPs directly interact with T4L to form larger dispersed AuNPs in solution (lower panel). Due to the protection layer, this size increase process is slower than the case of the fast bridging process. We therefore define this process as the “slow bridging” mechanism. The larger AuNPs dispersed in solution are not stable and eventually form pellets over a longer time interval (overnight). During the whole process the protein either remains in the native conformation or refold to the native conformation. (B) In the presence of BSA, the decoating pathway is effectively blocked (upper panel). The bridging mechanism is also substantially slowed down since only the BSA-coated AuNPs are available for T4L to bridge (down panel). No pellets are formed in the presence of BSA. (C) For AuNPs that are large enough (ca. > 90 nm), the decoating pathway is not feasible (upper panel). The bridging mechanism is also slowed down since only the coated AuNPs are available for T4L to bridge (down panel). The larger AuNPs dispersed in solution are not stable and eventually form the pellets over a longer time interval (overnight).

We have discovered a clear difference in the kinetics of size increase in pathway 1 (Figure 2.13C), wherein the formation of AuNP-90 was much faster than further aggregation. Here we propose a “slow bridging mechanism” and a “fast bridging mechanism”. In the fast bridging mechanism, a T4L molecule bridges two decoated AuNPs together (Figure 2.13A middle panel), which would form AuNP dimers in a faster rate than one T4L bridging two coated AuNPs together (Figure 2.13A lower panel). This speculation is supported by further evidence (see below). In the presence of BSA, the overall surface charge of BSA is negative at our pH. Without T4L, BSA is able to coat the AuNPs and stabilize them in water due to charge repulsion and the good hydrophilicity of BSA. The large size of BSA may create long-range molecular interactions¹⁸⁴ between AuNPs, which potentially result in aggregation of AuNP to ~30 nm (see Figure 2.9E). Upon interaction with T4L, pathway 2 is effectively blocked, possibly due to the fact that the moment an AuNP is decoated, one or a few BSA will quickly recoat it (Figure 2.13B upper panel). Only pathway 1 proceeds in the presence of BSA, wherein the process to form the AuNP-90 is similar, except the presence of BSA slows down the rate of size increase (kinetics see Figure 2.9E). Pathway 1 is possible because the positively charged T4L can be attracted to the BSA layer of AuNPs. The exchange of T4L with BSA is slower though, possibly due to the large size of BSA, in comparison with the exchange of T4L with citrate ions. This finding supports the proposed “slow bridging” mechanism—herein BSA serves as the coating and triggering coated AuNPs to aggregate. Once the aggregates were formed, BSA was able to stabilize the AuNP-90. During the whole process, T4L remains in their native conformation. Aptamers also have negative net charges. Without T4L, the charge, the good hydrophilicity, and the intrinsic flexibility of aptamers stabilize AuNPs. Similar to BSA, in the presence of T4L, pathway 2 is effectively blocked due to the high efficiency of the smaller aptamers in filling the

decoated surface area of AuNPs. Pathway 1 is slowed down too. The only difference is, once AuNP-90 is formed, aptamer cannot effectively stabilize AuNP-90, perhaps due to their small sizes. Our AuNP size study also supports the proposed slow and fast bridging mechanisms. For AuNPs smaller than 90 nm (ca. 14, 40, or 70 nm) T4L is able to decoat them and trigger the rapid formation of the visible pellets, as well as the rapid size increase of soluble NPs. For larger NPs (ca. AuNP-90), the NPs were too large for T4L to effectively decoat. The size of these AuNPs was increased very slowly though, possibly triggered by T4L as a bridge. The “bridging” rate however is much slower than decoated AuNPs (Figure 2.13C).

Outlook

As mentioned earlier, the “negative” impacts, especially the toxicity, of AuNPs on the surrounding environment have become one of the major concerns of AuNP application. The size of either the dispersed or the aggregated AuNPs has been realized to play an important role in the toxicity.^{206,207} However, there is no convincing evidence to definitively clarify a specific size of range of sizes wherein AuNPs are toxic. This is because there is no standard assessment to evaluate the toxicity of AuNPs, which seriously depends on factors like the cell line employed for the toxicity studies and the dose of AuNPs applied to the target system.^{208,209} Furthermore, a certain size of AuNPs may not affect the cell viability, but instead cause a serious deposition in a certain organ (ca. lung), which might lead to long term “toxicity”.²⁰⁹ A slightly larger aggregated AuNP might even be easier for cellular uptake than smaller ones.²⁰⁷ Nevertheless, the general consensus is that whenever the particle size is <400 nm, there is a toxicity concern. Particles larger than 400 nm often are believed to be less toxic.^{210,211} Therefore, our findings indicate that T4L might be potentially useful in some areas. T4L could be applied to remove the small sized AuNPs (ca. 14 nm) by forming the less-toxic, large-sized pellets. The key advantage for using

T4L is that no malfunctioned or unfolded proteins are generated during the whole process, causing minimal biological perturbation to the host. Accordingly, in mammalian cells lysozyme proteins, in addition to preventing bacterial infections, might help prevent infection caused by external, invading AuNPs, indicating lysozymes might have more immunological responsibilities.²¹²⁻²¹⁴ In addition, T4L might be used as a bio-sensor for detection of small AuNPs.

Our results revealed the pathways for T4L to trigger AuNP aggregation. In the meanwhile, there are unknown areas that remain to be explored. For example, what is the physical nature governing the 90 nm as the “magic” particle size which prevents decoating of the protection layer by T4L? We had probed the surface charge of our AuNPs in four different sizes (14, 40, 70, and 90 nm) via Zeta potential measurement and found no major difference between AuNP-90 and other AuNPs. Exploring this area is one of our on-going research directions. In addition to reporting a new phenomenon on protein interaction with AuNPs, we intended to generate some excitement of using the EPR spectroscopy to probe the site-specific dynamics of proteins in complexes composed of biological and synthetic materials. Particular power of EPR lies on the fact that the EPR spectra can probe structural information even for the otherwise inaccessible aggregated NP precipitates. The methods presented here can be applied to investigate general protein-NP interaction systems. Such information is not only of fundamental importance in understanding the impact of the synthetic materials on public health and environment, but also can guide rational design of novel NPs with desirable biocompatibility.

Conclusions

We found that T4L was able to trigger AuNP aggregation while maintaining its native structure and activity. The interaction mechanism involves two pathways, a rapid pellet

formation and a size increase of soluble AuNPs facilitated by T4L. The particle size increase was found to be a two-phase process, which had been attributed to a fast and a slow bridging mechanism. In either pathway, the protein was able to somehow maintain its native structure and function. Our results indicate that to prevent NP aggregation caused by non-specific interaction with proteins, ca. T4L, one needs to avoid both decoating of AuNPs and the protein-NP non-specific, short range interaction (both the fast and the slow bridging interaction). These findings serve as the fundamentals to develop novel AuNPs so that the AuNP aggregation can eventually be prevented. Although BSA might be a good choice to stabilize larger AuNPs (ca. 30 nm diameter), as demonstrated by our size studies, BSA itself is not sufficient to prevent AuNP aggregation caused by other proteins (e.g., T4L). Coating with aptamers might be good alternative approach, if an optimized sequence can be determined. Chemical modification is also a possible route.

CHAPTER 3. PROBING THE STRUCTURAL BASIS AND ADSORPTION MECHANISM OF AN ENZYME ON NANO-SIZED PROTEIN CARRIERS[†]

Introduction

Nanotechnology has advanced many areas of life over the past few decades. The involved nanomaterials, especially nanoparticles (NPs), often have unique chemical, electrical, optical, and magnetic properties, depending on the chemical composition, such as metals, inorganics, organic molecules, or block polymers, as well as their particle sizes and surface functional groups. An attractive area for the use of NPs, especially the nonporous silica nanoparticles (SiNPs), is to house enzymes for enhancing catalysis efficiency^{43,79,215} as well as to carry and deliver genes, and even prodrug molecules.^{77,216,217} Of particular interest is to immobilize enzymes onto the nonporous SiNPs. Immobilization of enzymes helps increase the environmental tolerance of enzymes, prevents enzyme aggregation and/or unfolding, and allows for the reuse of the host.⁷⁹ Compared to other NP hosts/carriers, SiNPs have straightforward preparation, relatively low-cost, and good biocompatibility.²¹⁸ While most enzyme immobilization were realized via covalent bonding of the enzyme to the nonporous SiNPs, it is also promising to attach enzymes via non-covalent interactions (ca. charge-charge interaction). In doing so, the potential enzyme structural restriction caused by covalently linking one site of

[†] The work discussed in this chapter was co-authored by Yanxiong Pan, Sunanda Neupane, Jasmin Farmakes, Michael Bridges, James Froberg, Jiajia Rao, Steven Y. Qian, Guodong Liu, Yongki Choi, and Zhongyu Yang. The work was previously published in *Nanoscale*.²⁹¹ Sunanda Neupane and Yanxiong Pan had equal contributions in this work. Sunanda Neupane and Yanxiong Pan were the primary developers of the conclusions that are advanced here. Sunanda Neupane performed majority of the experiments discussed in this chapter and Yanxiong Pan synthesized all the Silica Nanoparticles discussed here. AFM data was collected by James Froberg and Yongki Choi. Michael Bridges helped collect DEER EPR spectra. Sunanda Neupane and Yanxiong Pan drafted and revised the previously published versions of this chapter. Jasmin Farmakes, Jiajia Rao, Steven Y. Qian, Guodong Liu, and Zhongyu Yang proofread the manuscript and helped trouble shoot experimental conditions.

the enzyme to the solid phase can be minimized. It also makes it possible to detach the enzyme from the solid support.

Another potential application of SiNPs is to serve as hosts to immobilize proteins to probe protein structure and dynamics information at the molecular level. This area has important potential to be explored because the complications caused by the protein rotational tumbling can be effectively removed.^{120,186} For example, the continuous wave (CW) electron paramagnetic resonance (EPR) in combination with Site-Directed Spin Labelling (SDSL)¹²⁰ probes protein backbone dynamics in a site-specific manner. This approach relies on the close relationship between the EPR line shape and the spin label motion, which includes both protein rotational tumbling and backbone dynamics. For smaller proteins (<45 kDa), the rotational tumbling dominates the line shape and washes off its sensitivity to backbone motion. An effective approach to avoid protein rotational tumbling is to immobilize the target protein onto a solid support. A common approach to immobilize proteins is via the CNBr-activated sepharose beads,^{126,219} The surface charges of SiNPs are often tunable, making it possible to immobilize proteins via non-covalent bonding and the adsorption reversible. Taken together, SiNPs as hosts and/or carriers are important in both nanotechnology and protein science.

One of the major concerns in utilizing these SiNPs to carry or host enzymes is the possible enzymatic activity loss caused by the molecular interaction between the SiNPs and the cargo enzymes. A common consequence when an enzyme is adsorbed to a carrier is the structural and/or conformational changes upon adsorption, the scale of which are often associated with the activity loss at various levels.^{130,146,147,220} In addition, the surrounding biomolecules may also reduce the enzymatic activity of the cargo enzyme, by either blocking the access of substrates or replacing the adsorbed enzyme molecules.^{80,81} Therefore, understanding

the structure-function relationship of cargo enzyme on SiNP surface in the biological environment becomes an essential task in nanobiotechnology.

When adsorbed to the SiNP surface, the enzyme molecules usually form two layers of the well-known protein corona: the hard corona and the soft corona.^{81,144,145,221–224} While the soft corona contains protein loosely adsorbed, the hard corona is formed by proteins tightly adsorbed to the SiNP, which is, therefore, the corona layer where the enzymes function and the focus of most studies on enzyme-carrier complexes. While exciting progress has been made to help understand the hard corona, the structural basis of the enzymatic activity loss and the relative orientations of the enzymes upon adsorption to their SiNP carriers still need to be elucidated. Full understanding of these interactions are challenging to obtain, mainly due to the large size of and the difficulty to co-crystallize the protein/SiNP complexes as well as the high heterogeneity and dynamics of the protein-SiNP interaction (“dynamic corona”).

Reported here is a comprehensive study to probe the structure, dynamics, and function of a model enzyme, T4 lysozyme (T4L), upon adsorption to a few surface-modified SiNPs using the EPR spectroscopy in combination with several other analytical techniques. Prior to this work, EPR has been mainly applied to probe structure information in complex biological and/or synthetic systems.^{148,149, 150-161} The technical advantage of EPR in these studies is the capability to probe structure and dynamics information of macromolecules in their native states, regardless of the size and complexity.¹⁷⁷ Particular information EPR provides are long-range (a few nm) intra-macromolecular distance distributions^{225,226} and site-specific conformational dynamics in a broad time window (ns to ms).^{120,227} Comparing to other experimental techniques, EPR has some unique advantages which make it a good complimentary approach. For example, the size limitation of NMR-based structural determination can be removed by EPR. In comparison to the

large fluoro-labels, the small EPR spin label causes minimal structural perturbation to the target macromolecules and results in smaller uncertainties in distance measurements.¹⁷⁷ EPR is able to probe macromolecules in their native states, which is particularly helpful for systems that are difficult to crystallize. Based on two EPR techniques, the CW¹²⁰ and the Double Electron-Electron Resonance (DEER)²²⁶ EPR, the dynamic and structural changes of T4L enzyme upon adsorption to these surface-modified SiNPs were characterized. The average number of adsorbed proteins per SiNP was estimated and the residues that are responsible for making contact with each SiNP surface and other enzymes (when the SiNPs were fully loaded) were identified via CW EPR. Then, the extent of structural changes was probed via DEER. Interestingly, it was found that the adsorbed enzyme can be released via pH adjustment, highlighting the possibility of using SiNPs with different surface modifications to perform controlled release of cargo enzymes. Lastly, possible structural models for enzyme adsorption to different SiNPs are proposed.

Experimental Methods

Protein Expression, Purification, Spin Labeling, and Characterization

Eight T4L mutants, 44C, 65C, 72C, 89C, 115C, 118C, 131C, and 151C, were created via site-directed mutagenesis as described in the literature.¹⁸⁵ These mutants were expressed, purified, and spin labeled using procedures described in our recent work.¹²¹ The spin-labeled mutants were confirmed to have the correct secondary structure and activity via CD spectroscopy and an activity assay, respectively, both of which were described in our recent work (also see chapter 2).¹²¹ A few representative sites were characterized via CW EPR to confirm the local conformational dynamics.

Continuous-Wave EPR Spectroscopy

The typical sample concentration for our CW EPR studies was $\sim 100 \mu\text{M}$. Approximately 20 μL of sample was utilized in each measurement. A Varian E-109 spectrometer fitted with a cavity resonator was used for all CW EPR studies. All continuous wave (CW) EPR spectra were obtained with an observe power of 200 μW . All spectra were obtained with a modulation frequency of 100 kHz and a modulation amplitude of 1.0 G.

Preparation of the Hydroxylated Silica Nanoparticles (OH-SiNPs)

The classic Stöber method was employed to prepare the OH-SiNPs.²²⁸ Particularly, ~ 7.5 mL ammonia hydroxide (48 mmol) was mixed with 130 mL anhydrous ethanol in a 250 mL three-necked flask. The mixture was stirred vigorously at 50 °C for ~ 1 hr. Then 3.75 mL TEOS (16 mmol, tetraethyl orthosilicate, reagent grade, Sigma) was mixed with 30 mL anhydrous ethanol and dropped into a pre-heated (ammonia-ethanol) mixture with a stirring speed of 1500 rpm. After reaction of ~ 24 hrs, the suspension solution was washed with anhydrous ethanol for at least three times via centrifugation at 13,000 rpm for 30 min to remove unreacted reagents. The obtained OH-SiNPs were then redistributed in 35 mL anhydrous ethanol and stored at 4 °C for further use. The original OH-SiNPs particle size was ~ 30 nm as judged by TEM (see below).

Preparation of the Amine-coated Silica Nanoparticles (NH₂-SiNPs)

The NH₂-SiNPs were prepared based on the modification of the OH-SiNPs. Approximately 17.5 mL (~ 0.51 mmol) OH-SiNPs suspension and 100 μL ammonia hydroxide were charged into a dried 100 mL two-necked flask with magnetic stirring, followed by addition of 1.88 mL 3-(Trimethoxysilyl) propylamine (10.7 mmol, Sigma, 97%) into the suspension and reaction for 24 hrs at 60 °C. The suspension was washed with anhydrous ethanol for at least three

times to remove unreacted reagents and then redistributed in 17.5 mL anhydrous ethanol for further use. A severe aggregation was observed for NH₂-SiNPs.

Preparation of the Carboxyl-coated Silica Nanoparticles (COOH-SiNPs)

The COOH-SiNPs were prepared via further modification of the NH₂-SiNPs. Before modification, ~8.8 mL (~ 0.25 mmol) suspension of NH₂-SiNPs was washed with anhydrous DMF for three times via centrifugation at 13,000 rpm for 15 mins to eliminate ethanol. The final volume of the NH₂-SiNPs in DMF was 10 mL. Next, 1 g succinic hydride (9.9 mmol) and 0.5 mL triethylamine were charged into the NH₂-SiNPs suspension and stirred at room temperature for 24 hrs. The suspension was washed with anhydrous ethanol for at least three times and stored in ethanol at 4 °C for further use. The final COOH-SiNPs have better dispersity.

Fourier Transformation Infrared (FTIR) Spectroscopy

FTIR spectra of the OH-SiNPs, the NH₂-SiNPs, and the COOH-SiNPs were acquired with an FTIR spectrometer (Thermo Scientific Nicolet 8700) on potassium bromide (KBr) disk. The broad absorption peak at 3300-3600 cm⁻¹ and the peak at 2980 cm⁻¹ indicated the presence of the OH-SiNPs. The absorption peak at 1486 cm⁻¹ indicates the existence of -NH₂ group on NH₂-SiNPs. The absorption peaks at 1557 cm⁻¹ and 1722 cm⁻¹ are consistent with the COOH groups on SiNPs.

Zeta Potential Measurements

All Zeta potential measurements were carried out with a Nano ZS Zetasizer (Malvern Instrument Ltd.). Typically, 5 μL 5 X SiNPs (~0.029 μM, suspended in ddH₂O) was mixed with 1000 μL solution at the desired pH value, one at a time, and then subjected to measurement. The pH of each medium solution was adjusted from 2.0 to 12.55 with 0.01M HCl and 0.01 M NaOH wherein the ionic strength was fixed at 0.01 M (final NaCl concentration). At pH 7.0, the OH-

SiNPs and the COOH-SiNPs were found to have negative surface charges, while the NH₂-SiNPs were found to have positive surface charges.

TEM

A drop of the sample was placed on a 300-mesh formvar-carbon coated copper TEM grid (Electron Microscopy Sciences, Hatfield, Pennsylvania, USA) for 30 seconds and wicked off. Phosphotungstic acid 0.1%, pH adjusted to 7-8, was dropped onto the grid, allowed to stand for 2 minutes and then wicked off. After the grids were dry, images were obtained using a JEOL JEM-2100 LaB₆ transmission electron microscope (JEOL USA, Peabody, Massachusetts) running at 200 kV. Phosphotungstic acid is a negative stain that stains the outside of the particles. This gives the particles contrast when subjected to the electron beam in the TEM.

T4L Adsorption Profile on SiNPs

The OH-SiNPs, the NH₂-SiNPs, and the COOH-SiNPs were washed with water via centrifuging at 13000 rpm for 5 min (at least three times) to replace the ethanol with water. These samples were then re-suspended to 5-fold (5X SiNPs). To determine adsorption profile, a representative protein mutant, 44R1, was added to 50 μL 5X OH-SiNPs with various protein-to-SiNP ratios. The amount of adsorbed protein was computed by subtraction of the amount of protein in the supernatant of each mixture from the total protein added (the initial protein/OH-SiNP; c.f. Figure 3.4). The protein concentrations in stock and in the supernatant of each mixture were determined by measuring the protein optical density at 280 nm (OD₂₈₀).

To perform the EPR area analysis, the OH- or COOH-SiNPs with a concentration of ~ 0.05 μM was mixed with T4L and incubated at room temperature under gentle nutation. The EPR spectrum did not change after the mixture was incubated for >30 min. We, therefore, performed all of our binding experiments following such timeline. When washing the samples,

after centrifugation and removal of the supernatant, we added ~0.5 mL water and varied the incubation time under gentle nutation at room temperature. The EPR spectra did not change after the mixture was incubated for > 5 min. We, therefore, performed all our unbinding experiments following such time line. Taken together, all our EPR measurements were performed on samples under equilibrium state, and the spectral area analysis could be considered as a close approach to estimate the amount of unbound protein.

Activity

The activity assay was tested using the kit purchased from Sigma-Aldrich (*Micrococcus lysodeikticus* cells, ATCC No. 4698, M3770) as described earlier in previous reports was used,¹²¹ except that the protein-SiNPs mixtures were used to interact with the *Micrococcus* suspension. Typically, to prepare samples for the activity assay, the OH- and the COOH-SiNPs were mixed with a representative mutant, 44R1, at a protein-to-SiNP ratio of 250:1. The second set of samples were prepared by saturating each of the OH- and the COOH-SiNPs with 44R1. These enzyme adsorbed SiNPs were then mixed with 66 mM potassium phosphate buffer (pH = 6.24, at 25°C) to prepare 100 µL (1 µM) protein solution, one at a time. Lastly, 40 µL of the SiNP/protein mixture was added into ~1 mL (960 µL, precisely) of the *Micrococcus* suspension prepared as described above. The final volume of SiNPs added to the substrate was ~1.4 µL. The OD at 450 nm was monitored immediately using Nanodrop after the mixture formation for 300 s. To eliminate the possibility of SiNPs affecting OD@450 nm, a series of control experiments were conducted.

DEER EPR

Four-pulse DEER data at 80K were obtained on an ELEXSYS 580 spectrometer operated at Q-band. Typical final protein concentration is <~ 200 µM, with a typical sample volume of ~

20 μL in water in a glass capillary (1.4 i.d. \times 1.7 o.d.; VitroCom, Inc.). All samples were flash frozen in liquid nitrogen. A 36-ns π -pump pulse was set at the maximum absorption spectra, and the observer $\pi/2$ (16 ns) and π (32 ns) pulses were positioned 50 MHz (17.8 G) upfield, which corresponds to the absorption maxima of the center-field line. Distance distributions were obtained from the raw dipolar evolution data using the program “LongDistances” (www.chemistry.ucla.edu/directory/hubbell-wayne-l).

CD Spectroscopy

To further probe the secondary structural changes of enzyme adsorption and to confirm the conformational perturbation indicated by DEER EPR, we conducted the Circular Dichroism spectroscopy for the protein attached to the OH- and the COOH-SiNPs. A doubly labeled mutant of T4L used for the DEER studies, the 109R1/131R1, was used in CD. Our positive control was the same sample dissolved in water.

The CD spectra were obtained (Jasco J-815- 15OS, Japan) from 260 to 200 nm using a cylindrical cuvette with 1 mm path length. Typical sample volume and concentration were 300 μL and 10 mM, respectively. The baseline of each sample was corrected using DD-water.

Desorption

Desorption experiments were conducted for both saturated OH- and COOH-SiNPs. A representative mutant, 151R1, was adsorbed to both SiNPs and washed with $2 \times 200 \mu\text{L}$ HCl (pH = 3, 0.01 M NaCl) via centrifugation at 13,000 rpm for 5 min. The supernatants after each wash were combined and concentrated using the Amicon Ultra-0.5 mL Centrifugal Filters (10 K cut-off).

AFM Imaging

The four nanoparticle solutions (1. COOH-SiNPs, 2. OH-SiNPs, 3. T4L-COOH-SiNPs, 4. T4L-OH-SiNPs) were prepared in a water solution (~5 μM). The samples were prepared by incubating 10- μL of each solution on silicon substrates (University Wafer) for 10 min in a sealed compartment to protect evaporation at room temperature. The samples were then washed with de-ionized water (Millipore), and dried under purified air flow. The imaging measurements were performed using a commercial atomic force microscope (NT-MDT NTEGRA AFM). The samples were imaged under ambient conditions in semi-contact mode with a resonant frequency of 190 kHz AFM probes (Budget sensors).

DLS Measurement

The hydrodynamic diameter of SiNPs in the absence and presence of T4L were determined via dynamic light scattering by using the Zetasizer (NICOMP 380 ZLS Particle Sizer, Particle Sizing Systems, Inc. USA). For each measurement, 2 μL solution (~ 0.05 μM), either with or without T4L, was mixed with 1 mL distilled-deionized (DD) water and transferred into a disposable flint glass tube with plain end. The intensity of the incident laser light was tuned closed to 250 KHz in order to measure the particle size. Details of operation followed the standard user's guide provided by the manufacturer.

Results and Discussion

T4L is a good model enzyme for our study for several reasons. It cleaves glycosidic linkages in the peptidoglycan of bacterial cell walls.¹⁸¹ The intrinsic flexibility of T4L is closely correlated to its enzymatic activity, which serves as a good model to investigate the structure-function relationship of enzymes.^{127,182} In addition, T4L has been investigated with EPR in solution and other medium with data well-interpreted in literature, making it a good reference

protein for EPR study.¹⁸³ Due to its relatively small size (18.7 kDa), the CW EPR spectrum of spin-labeled T4L is dependent on the intrinsic motion of the spin label, the local backbone dynamics of the labeled site, and the rotational tumbling of the protein molecule.^{120,126,177} Upon adsorption onto the SiNPs, the rotational tumbling of the enzyme molecules is severely restricted, causing a significant change (broadening) in CW EPR line shape. This change can be used to indicate and monitor the behavior of the protein in the protein-SiNP complex.¹⁸⁶ Lastly, T4L has a positive net charge at the pH 7, making it possible for SiNPs to adsorb T4L. To employ EPR, the SDSL is often employed to implant a paramagnetic spin label to the desired site of the target protein.^{170,229} In SDSL, a cysteine residue is generated via site-directed mutagenesis, followed by reaction with a methanethiosulfonate spin labeling (MTSL) reagent to form a disulfide bond with the cysteine.^{119,186} The so-generated protein side chain is often named as “R1”.¹¹⁹ It has been demonstrated that attaching an R1 sidechain at a number of sites in T4L does not alter the function or the secondary structure of the protein.^{120,186,192,193} In order to evaluate the effects of surface charge and functional groups on enzyme adsorption, three SiNPs were prepared, the amine-, the hydroxyl- and the carboxyl-coated SiNPs, the net charge of which is positive, negative, and negative at pH 7, respectively (from now on we designate them as NH₂-SiNPs, OH-SiNPs, and COOH-SiNPs, respectively, for simplicity).

Characterization of the Model Protein and SiNPs

A total of eight T4L mutants were spin labeled for study (the spin-labeled mutants were named as xR1 where x is the residue being mutated). These mutants essentially scan through the whole protein. The enzyme mutants expressed and spin-labeled in our laboratory were confirmed to have native secondary structure and activity using the Circular Dichroism (CD) spectroscopy and an activity assay, respectively.¹²¹ In addition, the CW-EPR spectra of the spin-labeled

mutants were acquired to confirm the local conformational dynamics of the labeled sites to be identical to those reported in the literature.^{121,186} The involved SiNPs were prepared as described in the Experimental Methods and characterized using the Fourier Transformation Infrared (FTIR) spectroscopy (Figure 3.1A), the Zeta potential measurements (Figure 3.1B), and the Transmission Electron Microscopy (TEM). As shown in Figure 3.1A, for the OH-SiNPs, the broad absorption peak at 3300-3600 cm^{-1} and the peak at 2980 cm^{-1} are attributed to the O–H stretching vibration on the SiNPs surface and C–H stretching vibrations of the alkyl groups, respectively. The absorption peaks at 1095, 952 and 801 cm^{-1} were attributed to the asymmetric vibration of Si–O, the asymmetric vibration of Si–OH, and the symmetric vibration of Si–O, respectively. On NH_2 -SiNPs, the appearance of a new peak at 1486 cm^{-1} , which is attributed to the formation of $-\text{NH}_2$, indicates the existence of $-\text{NH}_2$ group on the surface of NH_2 -SiNPs. The COOH -SiNPs were confirmed by the appearance of new peaks at 1557 cm^{-1} and 1722 cm^{-1} , which are attributed to the amide and carboxyl stretching vibration, respectively.

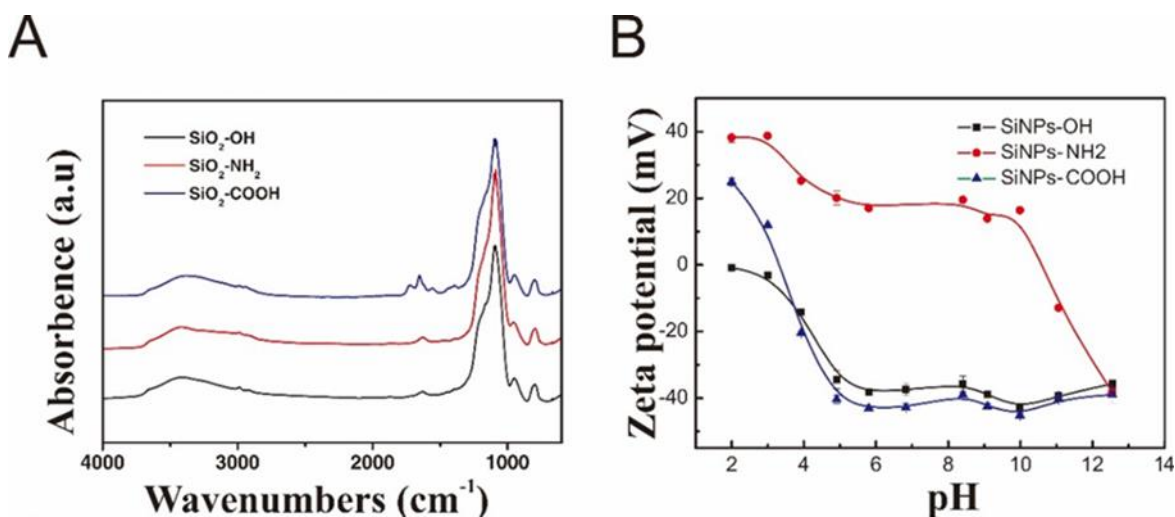


Figure 3.1. (A) The FTIR spectra of the OH-SiNPs, the NH_2 -SiNPs, and the COOH -SiNPs (color-coding see inset); (B) Zeta potential changes of the NH_2 -SiNPs, and the COOH -SiNPs as a function of pH (color-coding see inset).

The surface charge of each SiNP was as expected as determined by the Zeta potential measurements (Figure 3.1B). Since the isoelectric point of the OH-SiNPs is close to a pH of 2.0, we observed a potential of zero at pH 2.0. As the pH was increased, the Zeta potential was decreased until reaching a plateau (~ -38 mV) when $\text{pH} > 5.8$ (Figure 3.1B black squares). This confirmed that at pH 7.0 the surface charge of the OH-SiNPs was negative. The NH_2 -SiNPs displayed a positive potential in a wide range of pH (~ 2 to ~ 10.5 , Figure 3.1B red dots), confirming that the surface charge of the NH_2 -SiNPs at pH 7.0 was positive. This also confirmed our rationalization of the negligible adsorption of T4L onto NH_2 -SiNPs at pH 7.0. It has to be noted that we observed strong aggregation and therefore low dispersibility of NH_2 -SiNPs at most pHs. The COOH-SiNPs with an isoelectric point at $\text{pH}=2.7$ showed a similar trend as the OH-SiNPs (Figure 3.1B triangles). This again confirmed that at pH 7.0 the surface charge of the COOH-SiNPs was negative. Taken together, the findings in zeta potential further confirmed the successful surface-modification of the three SiNPs.

As shown in Figure 1, the TEM indicated that the average diameters of the OH-SiNPs and the COOH-SiNPs were ~ 30 nm. The NH_2 -SiNPs, however, were severely aggregated. Therefore, no TEM image was attempted for the NH_2 -SiNPs.

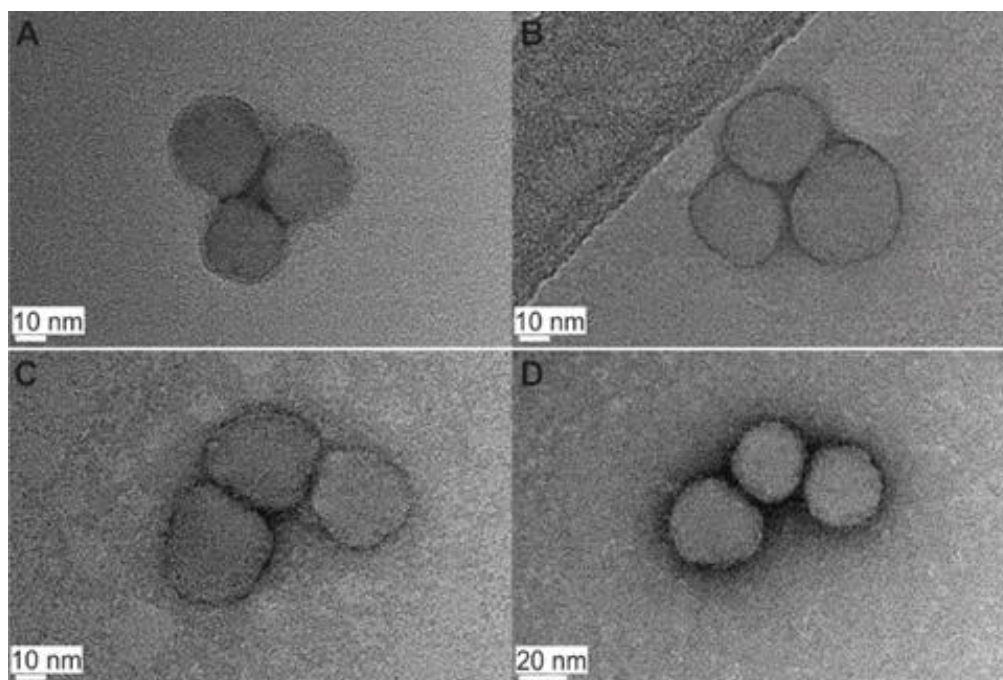


Figure 3.2. TEM images of the OH-SiNPs (A) and the COOH-SiNPs (B) in water. The approximate particles diameter is 30 nm in each case. Upon saturation of the OH-SiNPs (C) and the COOH-SiNPs (D) with the T4L 44R1 mutant, a clear black layer coating each SiNP is evident, indicating the adsorption of enzyme on SiNPs.

TEM Images Depict the Adsorption of T4L onto SiNPs

The best way to depict and confirm enzyme adsorption to SiNPs is to visualize the change in TEM upon enzyme adsorption. Therefore, the TEM images of T4L adsorbed to the OH- and the COOH-SiNPs (enzyme-to-SiNP ratio ~10,000:1) after incubation for ~30 min were acquired. The resultant mixtures were washed extensively to remove non-adsorbed enzymes (the SiNPs were “fully saturated” with T4L). The phosphotungstic acid was used to stain molecules outside of the nanoparticles. As shown in Figures 3.2C and 3.2D, the dark areas surrounding each particle clearly indicate the adsorption of T4L onto SiNPs.

Atomic Force Microscopy (AFM) Images Confirm the Enzyme Adsorption

AFM imaging provides direct visualization of enzyme adsorption with higher resolutions. The AFM images of the COOH- and the OH-SiNPs in the absence and presence of T4L

adsorption (enzyme-to-SiNP ratio $\sim 10,000:1$) were acquired. As shown in Figure 3.3A (images 1, 2, 5, & 6), without enzyme the images of the two SiNPs are indistinguishable. Upon enzyme adsorption, the particle sizes are clearly increased (Figure 3.3A). Furthermore, the overall size of the COOH-SiNPs (Figure 3.3A, images 3&7) is larger than that of the OH-SiNPs (Figure 3.3A, images 4&8), indicating more enzymes were adsorbed to the COOH-SiNPs. The height image (Figure 3.3B) shows a better view, wherein protein adsorption increases the size of the particle, and there is apparently more proteins adsorbed to the COOH-SiNPs (Figure 3.3B, red VS blue).

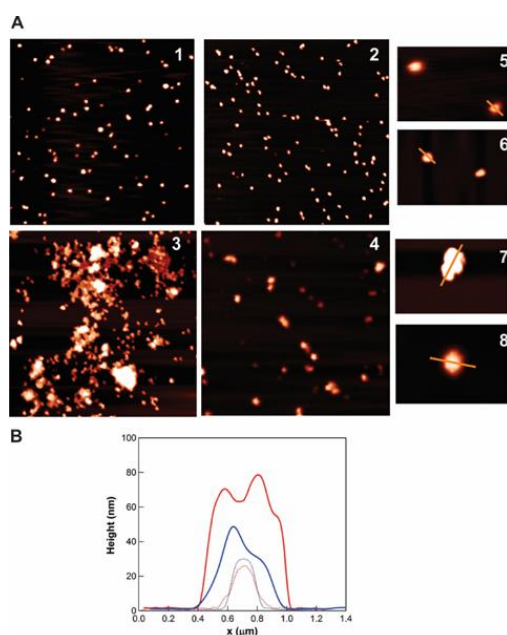


Figure 3.3. (A) AFM images for 1: COOH-SiNP, 2: OH-SiNP, 3: T4L-COOH-SiNP, 4: T4L-OH-SiNP ($10 \mu\text{m} \times 10 \mu\text{m}$). The z scale for 1 and 2 images is 0-30 nm, 3 and 4 images is 0-120 nm. Images 5,6,7,8 are the zoom of images 1,2,3,4, respectively ($2 \mu\text{m} \times 1.3 \mu\text{m}$). The z scale for 1, 2, 5, and 6 images is 0-30 nm; for 3, 4, 7, and 8 images is 0-90 nm. (B) The height image, blue-dotted = 5, red-dotted=6, blue=7, and red=8.

Probing the Loading Capacity of the Hard Corona

A key character of the SiNP-based enzyme carriers is the loading capacity. To probe this, we prepared a series of mixtures with increasing T4L-to-SiNP ratio for the OH- and the COOH-SiNPs. After an incubation of at least 30 min, the supernatant of each sample was separated from the mixture via centrifugation (2,000 rpm, 5 min). The amount of adsorbed protein at each ratio

can be computed by subtracting the amount of protein in the supernatant from the total added protein. The adsorption profile was then obtained by plotting the amount of adsorbed protein as a function of added T4L-to-SiNP ratio. There was essentially no adsorption on the NH₂-SiNPs, as most added proteins remained in the supernatant. This is expected since, at pH 7.0, T4L and NH₂-SiNPs repel each other due to their positive surface charges. Both the OH- and the COOH-SiNPs showed a clear indication of T4L adsorption. The adsorption profile of the OH-SiNPs, as shown in Figure 3.4, indicates that as the T4L-to-SiNP ratio is increased, the amount of bound protein is increased. A plateau is reached with ~ 3,500-4,000 protein per SiNP. Such adsorption is most likely due to the opposite surface charges of T4L and the OH-SiNPs. Interestingly, the COOH-SiNPs were so well-separated and dispersed that, our attempts to separate the supernatant from the mixture failed. The small amount of remaining COOH-SiNPs in the supernatant contributed to the UV absorption and complicated our measurements. We, therefore, did not obtain any reproducible, convincing adsorption profile for the COOH-SiNPs. A technique which is not so sensitive to the dispersed COOH-SiNPs should be used.

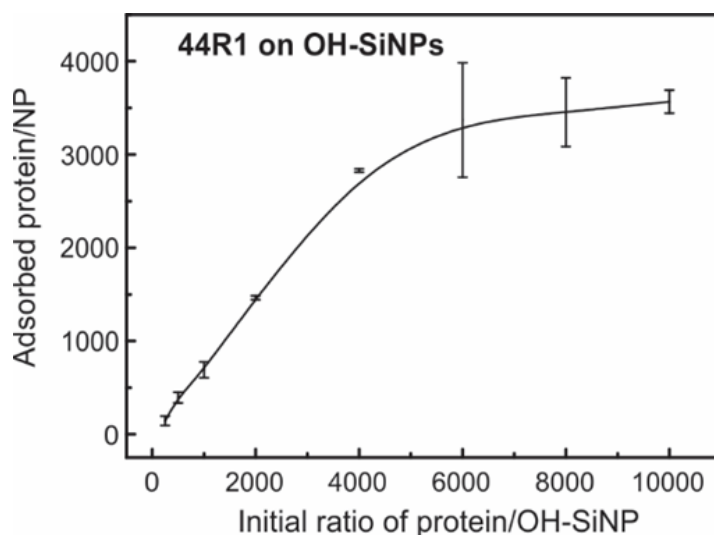


Figure 3.4. The adsorption profile of 44R1 on the OH-SiNPs. Approximately 3,500-4,000 proteins were found to be able to adsorb onto each OH-SiNP. Note there was no wash done on each protein/SiNP mixture with the protein-to-SiNP ratios indicated by the x-axis.

EPR Area Analysis to Estimate the SiNP-carrier Loading Capacity

The principle of using EPR area analysis to probe the amount of adsorbed proteins is based on the fact that the amount of (spin-labeled) protein is proportional to the CW EPR spectral area. The CW EPR spectra of a mutant before and after washing with water can be compared. The percentage of the adsorbed proteins can be estimated by computing the loss in the spectral area due to washing. It is worth noting that the EPR samples were washed via the same procedure as in the previous section. However, the small amount of suspended COOH-SiNPs in the supernatant did not present to be a major problem because the majority of the COOH-SiNPs were settled to the pellet; the uncertainty in loading capacity estimation caused by these suspended particles is negligible. This EPR approach is less sensitive to the presence of SiNPs, therefore, providing a close estimation of the enzyme loading capacity. In addition, as mentioned above, the restriction of enzyme rotational tumbling due to adsorption on SiNPs results in a broadened EPR spectrum, while the unbound enzymes often show a relative sharper spectrum.

The mutant we selected for such study was 44R1 since the “broad” spectral component of its spectrum is well-separated from its sharp component (see data below). We started with 10,000:1 and 15,000:1 protein-to-NP ratio for the OH- and COOH-SiNPs, respectively. After mixing and incubation, ~20 μ L sample was loaded to the EPR capillary. This volume is the effective volume of our cavity resonator. It is important to use this sample volume so that both the adsorbed and the unbound proteins are being detected. Loading a sample with a larger volume will result in missing the detection of the unbound enzyme since the SiNPs tend to settle down to the bottom of the capillary. As shown in Figure 3.5, both the 44R1/OH-SiNP and the 44R1/COOH-SiNP sample showed a broad and a sharp peak in the low field region before wash (black curves). Upon washing, the unbound or loosely bound proteins were removed as judged

by the disappearance of the sharp peak in Figure 3.5. For the COOH-SiNPs, washing only removed the sharp component; both the intensity and the line shape of the broad component are almost unaffected (Figure 3.5A). This indicates that most likely washing did not remove the enzymes already adsorbed. The area loss due to wash is ~43 %, corresponding to ~6400 protein molecules adsorbed onto each COOH-SiNP. For the OH-SiNPs, the first round of wash not only removed the sharp spectral component but also reduced the intensity of the broad component by ~50% (c.f. black rectangle of Figure 3.5B). This indicated that the adsorption of the enzyme to the OH-SiNPs was most likely labile and could be easily disturbed. Further wash, however, did not decrease the intensity of the broad component. The area analysis indicated that ~1750 proteins were adsorbed onto each OH-SiNP. Note that this number is less than that estimated by the adsorption profile (Figure 3.4). The discrepancy is caused by the fact that there was no wash in the adsorption profile (Figure 3.4). In fact, given the 50% loss in the intensity of the broad peak, we anticipated ~3500 protein per OH-SiNP if no wash was carried out in the EPR study, which is close to that estimated by the adsorption profile (Figure 3.4). Given the relatively small diameter of SiNPs (~30 nm), the large number of bound enzymes indicates a multiplex adsorption scheme (see later discussions). The enzyme washed off during the experiments was found to be functionally active (data not shown). There was essentially no EPR signal from the NH₂-SiNPs after washing, consistent with the fact that all proteins remained in the supernatant upon mixing with the NH₂-SiNPs.

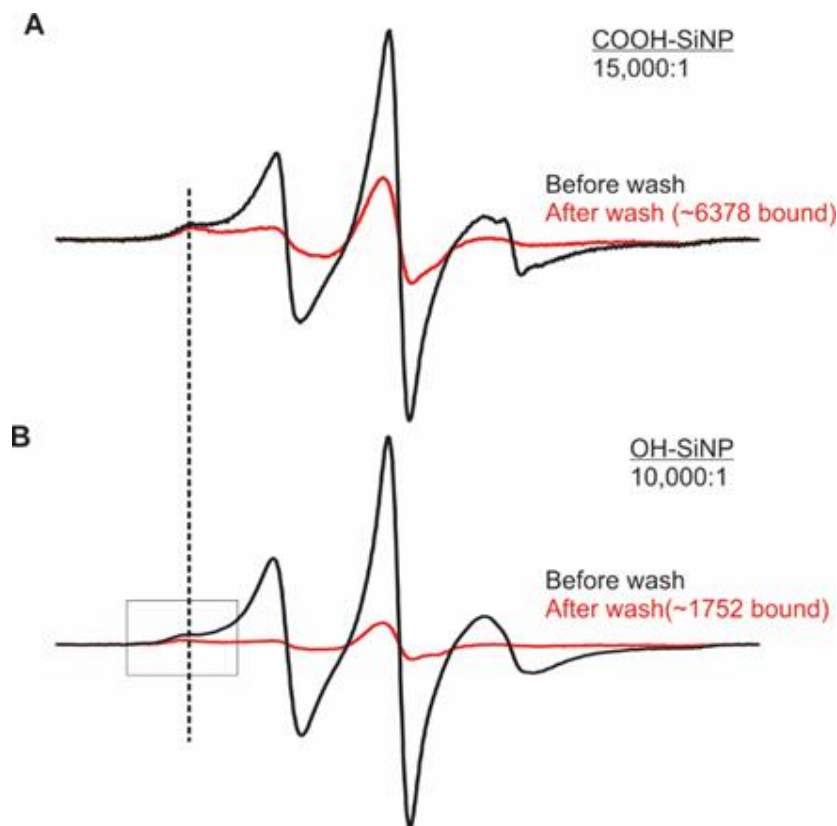


Figure 3.5. The CW EPR spectra of the 44R1 adsorbed to the COOH-SiNPs (A) and the OH-SiNPs (B) with a protein-to-SiNP ratio of 15,000:1 and 10,000:1, respectively, before (black) and after wash (red) with water. The gray rectangle is to highlight the loss of the peak intensity. The dotted line is to illustrate the peak position shift between the spectra on different SiNPs.

In principle, the relative population of the adsorbed protein can be estimated with EPR spectral analysis.¹²⁰ However, we were not successful in such an attempt because the adsorbed protein might very likely be in a very heterogeneous conformation, and it is difficult to account for the broadened spectral component with theoretical models/simulations. Note that the line width of the 44R1 on OH-SiNPs is slightly broader than on the COOH-SiNPs (Figure 3.5 dotted vertical line). This indicates that the enzymes on the OH-SiNPs might have higher conformational heterogeneity than those on the COOH-SiNPs (more discussions see below).

Caution is needed when measuring the adsorption capacity, given the low dispersity of the OH-SiNPs. In fact, partial aggregation of the SiNPs might lead to uncertainties in the estimated loading capacity. Specifically, the gaps between particles may trap enzyme molecules,

yielding a larger capacity. Meanwhile, the aggregation may decrease the surface area, leading to a lower capacity. Therefore, before loading enzyme, we sonicated the SiNPs to ensure dispersion. After adsorption, prior to EPR measurements, the samples were always mechanically vibrated. Even so, our dynamic light scattering (DLS) measurements still indicated a polydispersity in the hydrodynamic radii of SiNPs. In general, the hydrodynamic radii determined by DLS are larger than the radii determined by TEM. DLS offers an opportunity to probe the polydispersity of the COOH- and the OH-SiNPs. Specifically, for the COOH-SiNPs, DLS indicated a dominant diameter at 154 nm (70%) and a minor diameter at 572 nm (30%), the latter of which was possibly originated from minor/local aggregation of the particles. For the OH-SiNPs, the dominant diameter was 123 nm (74%) while the minor diameter was 480 nm (26%). Upon saturation with T4L enzyme, the COOH-SiNPs showed a dominant diameter at 903 nm (90%) and a minor diameter at 282 nm (10%). Such enhancement in size is consistent to the multiple-layer protein adsorption. The OH-SiNPs show a dominant diameter at 711 nm (88%) and a minor diameter at 103 nm (12%). The smaller hydrodynamic radius of the OH-SiNPs is consistent with the findings that a COOH-SiNPs is able to adsorb more proteins than an OH-SiNP. Therefore, the adsorption capacity reported here is only the average number of adsorbed proteins per SiNP.

Enzymatic Activity Loss upon Adsorption to SiNPs

To probe the enzymatic activity of T4L upon adsorption, we selected the 44R1 to be consistent with the previous adsorption capacity studies. Only the OH- and the COOH-SiNPs were involved since the NH₂-SiNPs showed no adsorption. The T4L-to-SiNP ratios were selected with some extra caution. Due to the high loading capacity of enzymes on both SiNPs (see above), it is very likely the enzymes pack to form multiple layers of enzymes on the SiNP

surface (calculations see below). The enzymes in the inner layer(s) are likely to lose activity due to the shielding of substrates caused by the outer layer enzymes. In addition, even if only a single layer of enzymes is coated on SiNP surface, the contact of T4L with the surface might induce conformational changes of the enzyme, possibly causing activity loss. Therefore, it was decided to investigate these two extreme conditions for both the OH- and the COOH-SiNPs. Given the average diameter of ~30 nm, the surface area of a SiNP was estimated to be ~2800 nm². Considering the average area that a T4L molecule could occupy (~10-12 nm²), ~250 proteins adsorbed to the SiNP should form a single layer of protein. Therefore, we selected 250:1 as the protein-to-SiNP ratio for all our single layer studies. Another case was the multiple layer studies wherein the SiNPs were saturated with T4L. The positive control was to determine the activity of 44R1 in water with no SiNPs. Our negative control experiments were to measure the interaction of the substrates with solely SiNPs.

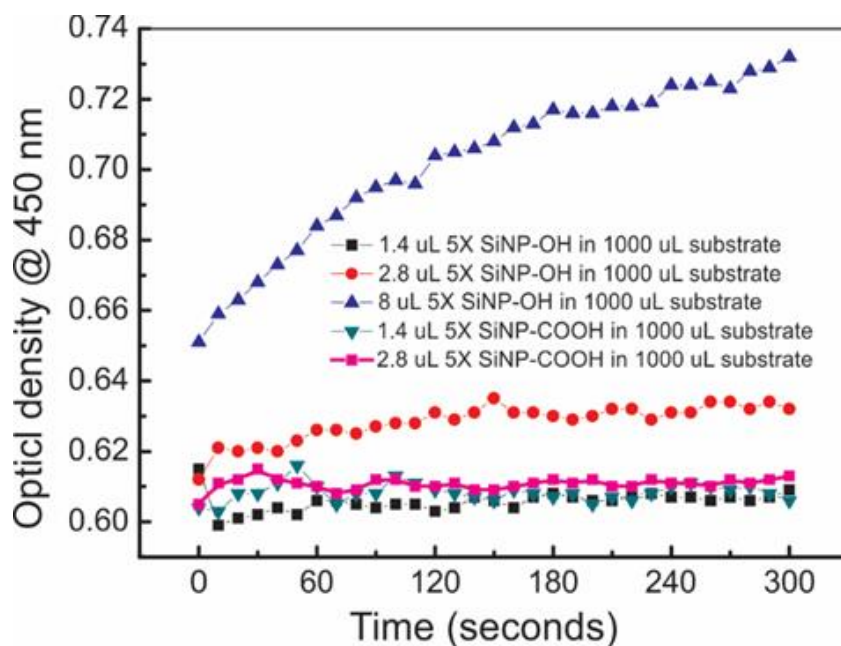


Figure 3.6. The control experiments for the activity assay. The value of 1.4 uL was selected because that volume of SiNPs was identical to the SiNPs we used for the protein activity test.

First it was confirmed that presence of either SiNPs did not affect the OD at 450 nm as shown by our negative controls (See Experimental Methods and Figure 3.6). To quantitatively evaluate T4L activity upon adsorption to SiNPs, we followed the procedure reported by Bower *et al.*, wherein the activity was characterized by the slope of the initial decay of OD at 450 nm (Figure 3.7).¹⁸² In our case, we performed a linear fit to the beginning 40 s of each data set (and converted the slope unit to mA/min as indicated by Bower *et al.*). When the T4L-to-SiNP ratio was 250:1 and the final protein concentration was adjusted to be the same as in the positive control experiments (Figures 3.7A and 3.7B black curves) for the COOH-SiNPs, the slope of the decrease of OD at 450 nm (green; 90 +/- 6 mA/min; the value after the “+/-“ represents the standard deviation from the fitting) is significantly slower than that of protein in water (black; 204 +/- 66 mA/min), indicating when the enzyme formed a single layer on COOH-SiNPs, there was a significant activity loss. This indicated the single-layer adsorption very likely caused a structural change in T4L. On the OH-SiNPs with the same ratio, the activity loss (blue triangles of Figure 3.7B) was even higher, possibly indicating an even larger extent of structural changes. When both SiNPs were saturated with T4L, the concentration of the SiNPs was adjusted to be the same as that in the case of 250:1, meaning the adsorbed, final protein concentration was ~6 and ~17 times higher on the OH- and the COOH-SiNPs, respectively. Interestingly, for both SiNPs, we did not observe a decrease in OD at 450 nm (102 +/- 6 mA/min for COOH-SiNPs and 186 +/- 6 mA/min for OH-SiNPs) that was consistent with the protein concentration increase. This indicated that when multiple layers of enzymes were formed on SiNPs, the enzymes in the inner layer(s) were inactive, most likely due to the conformational change caused by adsorption/ crowding and/or the limited access to the substrates. However, it is unclear why for the enzyme saturated COOH-SiNPs (Figure 3.7A, red), the enhancement in activity was only slightly higher

than in the case of the single layer protein (and the activity is less than the positive control). A higher mixture viscosity when T4L saturated the COOH-SiNPs was observed, which severely limited the access of substrates. Nevertheless, it is clear that adsorption to SiNPs caused a loss in T4L enzymatic activity.

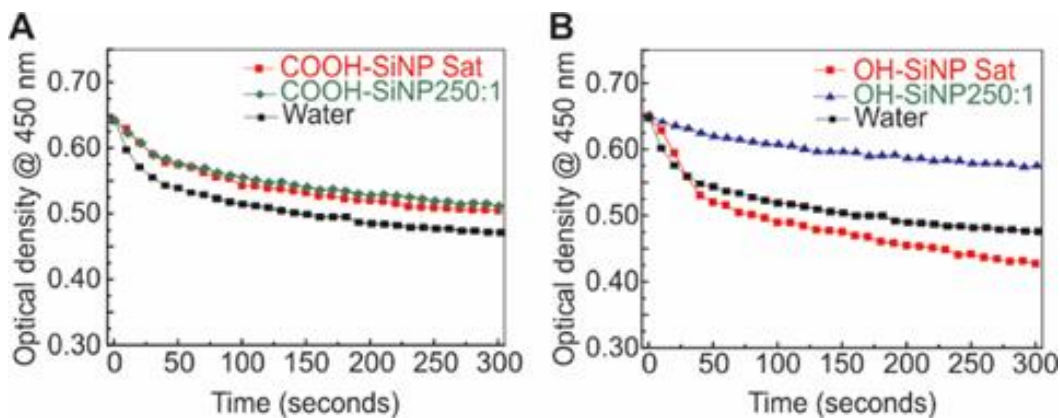


Figure 3.7. The activity assay of the 44R1 adsorbed to the COOH-SiNPs (A) and the OH-SiNPs (B) with a protein-to-SiNP ratio of 250:1 (green) and when the SiNPs were saturated (red) with the enzyme. The black curve indicates the activity of 44R1 in water without any SiNPs and is reproduced in both figures for comparison.

Probing the Origins of the Activity Loss: Site-specific Conformational Dynamics of the Adsorbed Enzyme

Due to the close correlation of structure, dynamics, and activity of enzymes, it is speculated that the loss in activity was related to structural and conformational changes. To probe the conformational dynamics of T4L on SiNPs, the EPR spin label was introduced onto eight sites of T4L (including 44R1; c.f. Figure 3.8A). The CW EPR spectra of these eight mutants upon adsorption to SiNPs were found to be broadened in comparison to the same mutants in solution (Figures 3.8B-3.8I VS Figure 2.3), for both the single-layer enzyme coated and saturated SiNPs. Since the CW EPR line shape is known to be sensitive to motion of the spin label, probing the origins of such broadening on each site might lead to important structural information of enzyme adsorption.

When an enzyme is adsorbed onto the SiNP surface, three factors are anticipated to cause CW EPR line broadening: 1) contact of the enzyme with the SiNP surface, 2) crowding caused by nearby adsorbed enzymes when multiple layers are formed, and 3) restriction of protein rotational tumbling caused by adsorption and/or crowding. To evaluate the contribution of each factor, a series of control experiments are included wherein T4L mutants were immobilized onto the CNBr-activated sepharose beads. Such attachment completely restricted the protein rotational tumbling due to the formation of covalent bonds between the -CN groups on the sepharose surface and the protein amines (lysines). In this case, if there were any line broadening, it must be contributed by the factor 3 (see above). Contributions from factors 1 and/or 2 were removed.

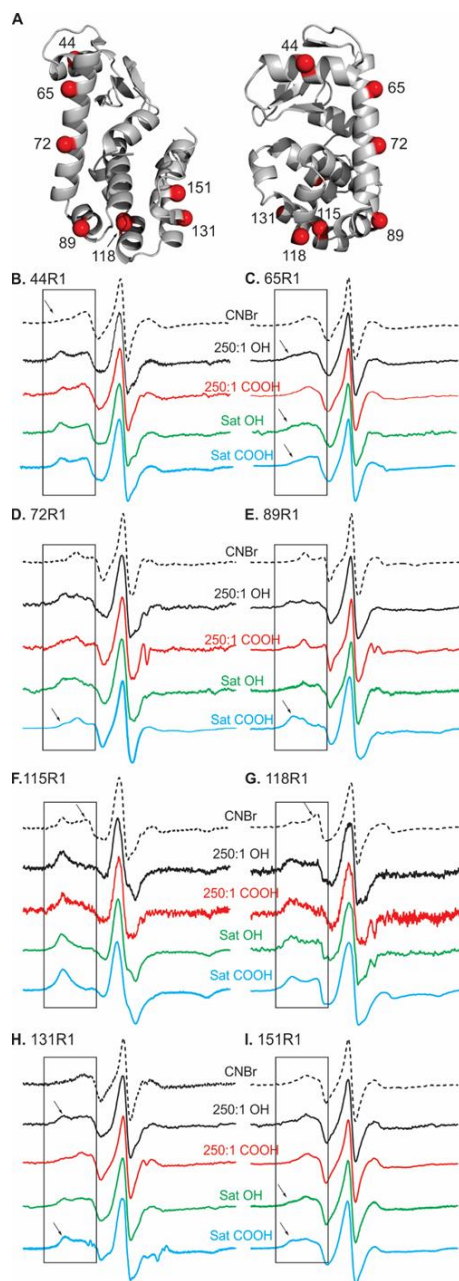


Figure 3.8. (A) The crystal structure of the T4L (pdb: 3lzm) and the C α of the residues that were mutated and spin labeled (red spheres) viewed at two angles. (B) – (I) The CW EPR spectra of each spin labeled mutant when attached to the CNBr-activated sepharose beads (dotted black) and when adsorbed to the OH-SiNPs (black and green) and the COOH-SiNPs (red and blue). The black and red curves indicate the spectra taken from samples when the T4L-to-SiNP ratio was 250:1, while the green and blue curves indicate the spectra of 44R1 when the corresponding SiNPs were saturated. The rectangle in each figure is to highlight the spectral region where the spectral line shape changes are the most evident between different solid supports. The arrows are to help guide the identification of the spectral changes. Specifically, the arrow in (B) indicates that the pointed low field peak was populated on other solids; arrows in (F), and (G) indicate the reduction in peak intensity; arrows in other figures indicate an increase in peak intensity.

When a single enzyme layer was formed on SiNPs, by comparing the spectra of T4L mutants on SiNPs with those of the same sites on the sepharose, all sites were identified that show additional broadening. Sites showing additional broadening must be those making contact with the SiNP surface since factor 3 did not exist in this case. As shown in Figure 3.8 (B-I), a comparison of the black and the dotted curves in the low field region (rectangle) of each mutant yields that almost every studied site shows an additional peak (e.g. arrows in Figures 3.8C and 3.8H), with 151R1 exhibiting the least low-field peak intensity (as comparing to arrows in Figure 3.8I). This indicates that when forming a single layer on the OH-SiNPs, T4L are adsorbed to the SiNP in a random orientation wherein any residues with positive surface charges could be contacting the SiNPs. In contrast, on the COOH-SiNPs (red curves in Figures 3.8B-3.8I), there is almost no additional peak shown in the spectra of 65R1 and 151R1 (solid red VS dotted black). The broadening in 72R1, 89R1, and 131R1 are also much less in extent as compared to the cases when the same mutants are adsorbed to the OH-SiNPs. The spectra of 44R1, 115R1, and 118R1 show strong broadening, which indicates that likely on the COOH-SiNPs T4L has a preference to contact SiNP surface via regions close to residues 44 and 115/118 and via regions close to residues 72, 89, and 131 with a lower preference. When both SiNPs were saturated with T4L, a comparison was conducted of the CW EPR spectra of spin-labeled mutants with those when a single protein layer was formed on the same SiNPs. Sites showing additional broadening indicate regions of T4L that are facing more restriction in motion, most likely due to crowding. For the OH-SiNPs, we found almost no additional broadening (green VS black curves in Figure 3.8) for all studied sites, meaning the crowding effects on the OH-SiNPs were not significant. This means the interaction between multiple protein layers is not strong enough to cause additional restriction to the motion of the spin labeled sites. This is a reasonable finding because proteins in

the first layer are randomly orientated so adsorption of proteins to the next layers is also expected to be non-specific. Such non-specific adsorption is often not enough to create strong inter-enzyme interactions (to generate additional crowding effects). For the COOH-SiNPs, when comparing the red and the green curves (Figures 3.8B-3.8I), additional broadening is observed on sites 44R1, 65R1, 89R1, 131R1, and 151R1, indicating that these sites are affected by strong crowding effects when multiple layers of proteins are formed. This finding indicates that, since proteins in the first layer are adsorbed with certain preferred orientations, the adsorption of proteins to the next layers is also likely to have a preference in terms of contact sites and orientation. These specific intermolecular interactions are possibly strong enough to create additional packing/crowding between proteins in the multiple enzyme layers. The stronger inter-enzyme interaction also helps increase the loading capacity of the enzyme on the COOH-SiNPs (see above discussions of Figure 3.5).

Probing the Origins of the Activity Loss: Intra-protein Structural Changes upon Adsorption to SiNPs

In addition to the local conformational dynamics of T4L upon adsorption, the DEER experiments were also conducted to probe the intra-protein structural changes. DEER EPR spectroscopy is a pulsed EPR technique which relies on probing the magnetic dipolar interaction between two electron spin centers and extracting the distance distribution probability between the two centers.²³⁰ A great advantage of such pulsed dipolar spectroscopy^{225,231} is that the distance distribution profile not only reflects the average intra-protein distance but also the conformational ensemble of the studied protein. In our case, the more conformations the protein spans, the broader the distance distribution is detected. To conduct DEER measurement, we created two cysteine mutations on one protein and spin labeled both. A total of three cysteine

pairs (Figure 6A) were selected to probe the effects of adsorption to SiNPs on the global structure of T4L. For all DEER samples, both SiNPs were saturated by T4L. As shown in Figures 3.9B-3.9D, for each spin pair, the distance distribution of protein on SiNPs (Figure 3.9, black and red curves) is much broader than that of the same pair in buffer (see grey shades of Figure 3.9).²³² This indicates a significant amount of extra protein conformations are induced by adsorption. This is not surprising since the crowding is very likely to change the protein conformation when SiNPs are saturated with T4L. A more careful look at the differences between the black and the red curves leads to the trend that proteins on OH-SiNPs have slightly broader distribution, and therefore, slightly more conformations than proteins on the COOH-SiNPs. This is consistent with the CW EPR results wherein the low field peak of 44R1 on the OH-SiNPs is broader than that of 44R1 on the COOH-SiNPs (Figure 3.5, dotted line).

The structural perturbation caused by adsorption to the SiNPs was also observed from the Circular Dichroism (CD) measurement, wherein the secondary structure of the enzyme upon adsorption to the SiNPs was found to be perturbed as well. As shown in Figure 3.10, the data of the enzymes adsorbed to the SiNPs are relatively noisier, even though the final protein concentration for all of the three involved samples was adjusted to be identical (50 μ M). We rationalized the higher noise level to the scattering effects of particles. Nevertheless, a significant reduction in the peak of 208 nm, which is the characteristic peak for helical structures, for protein adsorbed to the OH- and the COOH-SiNPs indicate a significant secondary structural change in the protein upon adsorption. This conclusion is consistent with findings from DEER.

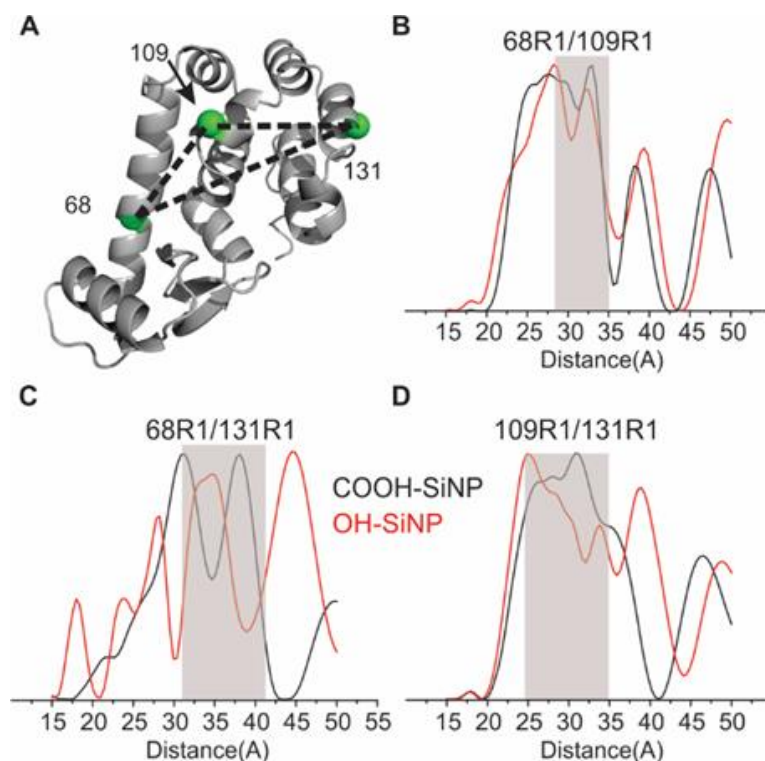


Figure 3.9. (A) The crystal structure of the T4L (pdb: 3lzm) and the C α of the three residue pairs that were mutated, and spin labeled (green spheres). Dotted lines indicate the intra-protein distances measured in each DEER experiment. (B) – (D) The distance distribution of each spin-labeled cysteine pair when adsorbed to the COOH-SiNPs (black) and the OH-SiNPs (red). DEER data analysis is provided in the main text and the ESI. The gray areas indicate the distance distribution of the corresponding pair when protein is in the spin buffer. There is a clear broadening upon adsorption to the SiNPs, indicating an increase in protein conformational states.

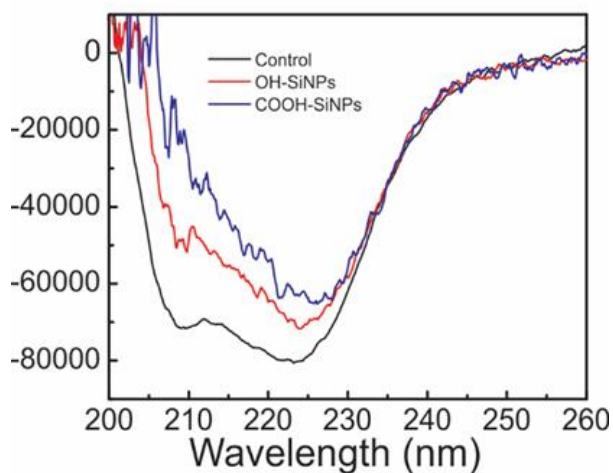


Figure 3.10. The CD spectra of T4L mutant 109R1/131R1 in water (black) and adsorbed to the OH- (red) and the COOH- (blue) SiNPs.

Differences in the Structural Basis of Enzyme Adsorption between the two SiNPs

The discussion above indicates T4L has a broader range of conformation caused by contacting with the OH-SiNP surface and/or crowding, while on the COOH-SiNPs T4L has relatively more uniform conformation. Such finding can be rationalized to the fact that, in addition to the electrostatic interaction between COOH-SiNP and T4L, the additional C=O bonds may serve as proton acceptors to help establish and stabilize hydrogen bonding, which helps stabilize the protein and regulate the protein conformation alignment on the surface of the COOH-SiNPs. The longer linker between the COOH and SiNP surface (see Experimental Methods for SiNP preparation) also possibly provides additional flexibilities to regulate protein conformation.

Desorption of Enzyme: Reversible Adsorption

Since the adsorption of T4L enzyme on these SiNPs was due to the charge-charge interaction, it must be possible to desorb the enzyme from the SiNPs via adjusting the SiNP surface charge. Based on the Zeta potential measurements at various pH (See Figure 3.1B), the wash solution was selected to have a pH of 3.0 in 0.01 M NaCl. Under this condition, the surface charge of the OH- and the COOH-SiNPs were ~ zero and slightly positive, respectively, which should cause desorption of enzyme. Indeed, for both SiNPs, we found almost all adsorbed proteins were detached, as judged by the complete loss in CW EPR intensity and the enzymatic activity when the SiNPs were studied after wash. The eluted enzymes after switching to water medium were found to have identical CW EPR spectra as the same mutants in water (Figure 3.11). The eluted enzymes were also found to be functionally active as judged by the activity assay. The recovery rate was close to 100% after two rounds of wash. Lastly, the washed SiNPs

were able to be “reloaded” with fresh T4L; the conformation and activity of the reloaded protein were found to be identical as those discussed before, indicating the SiNPs can be reused.

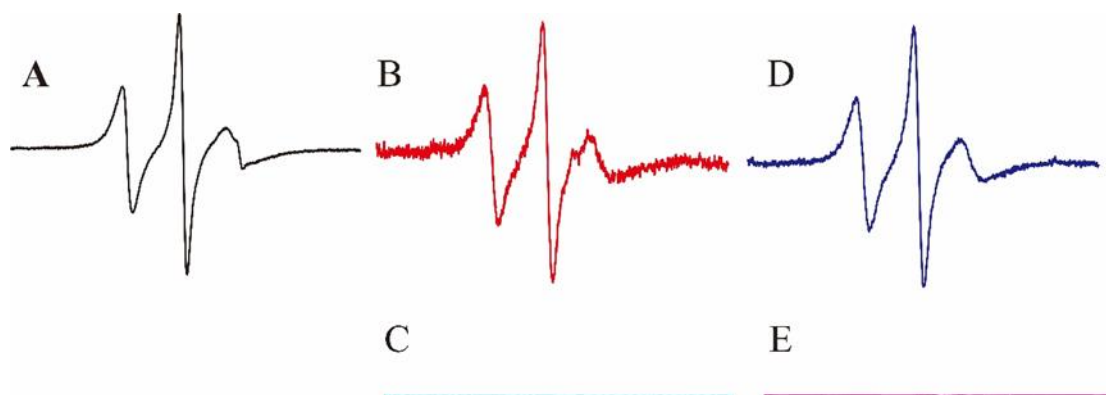


Figure 3.11. The EPR spectra of T4L mutant 151R1 in water (A), supernatants after T4L desorption from the OH-SiNPs (B) and the COOH-SiNPs (D), and those of the OH-SiNPs (C) and the COOH-SiNPs (E) after desorption.

Possible Docking Models

At pH 7.0, the surface charge of T4L was estimated via the APBS function of PyMOL and shown in Figure 3.12. As expected, positive surface charges dominate the protein (see blue VS red). For the OH-SiNPs, although the spin labeled sites (Figure 3.12) are close to either negatively or positively charged areas, the local charges of the protein most likely did not form strong electrostatic interactions with the surface of the OH-SiNP, since no specific sites were found to make contact with the SiNP (Figure 3.8 and discussion above). This might be due to the relatively less negative surface charge and relatively short linker length (comparing to the COOH-SiNPs) between the $-OH$ groups and the Si on the surface, the latter of which may present some hindrance for protein adsorption. It is also possible that other molecular interactions (e.g. the van der Waals force) contribute to the adsorption. Nevertheless, we propose the docking model of a single protein layer on the OH-SiNPs to be as shown in Figure 3.13A, wherein the relative orientation of the protein and the SiNP surface is random. When multiple

layers of proteins are formed, since there is no additional broadening detected in the EPR spectra of all studies sites, a random orientation of proteins loosely adsorbed to the first protein layer of the OH-SiNP surface (Figure 3.13B) is again proposed.

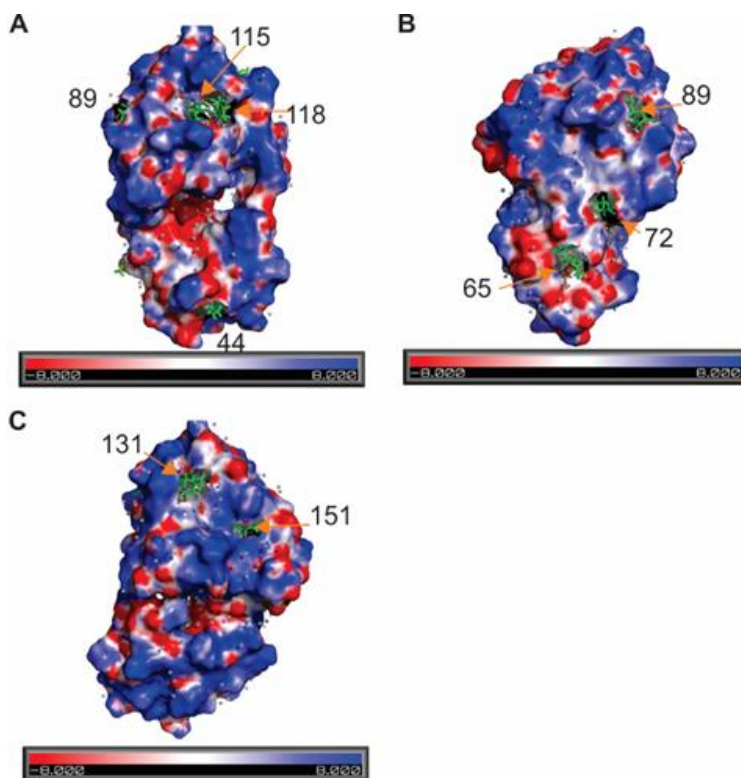


Figure 3.12. The surface charge of T4L estimated using PyMOL's APBF function. Three views from different angles were presented to show the location of each studies mutant. Blue: positively charged surface. Red: negatively charged surface.

For the COOH-SiNPs, at pH 7.0, the surface charge is more negative than that of the OH-SiNPs. The charge-charge interaction might be the dominant driving force for protein adsorption (and the associated EPR spectral broadening). For example, we observed strong broadening in the CW EPR spectra of 44R1, 115R1, and 118R1 because these residues are close to positively charged regions with large areas (Figure 3.12A). The 72R1, 89R1, and 131R1 are also in close proximity to positively charged regions (Figures 3.12B and 3.12C) and therefore, showed some broadening. The site of 65R1 is surrounded by negatively charged residues (Figure 3.12B), and therefore, showed the least possibility to make contact with COOH-SiNP surface (and the least

broadening). The 151R1 is close to the C-terminus of the protein, wherein the mobility is intrinsically higher. It is likely that when single enzyme layers are formed on the COOH-SiNPs, T4L tends to make contact with the regions close to residues 44 and 115/118 (Figure 3.13C, green spheres). It is also possible for a small amount of T4L to interact with COOH-SiNPs via the other few residues (Figure 3.13C, magenta spheres). When multiple layers of proteins are formed on the COOH-SiNPs, it is more likely for sites 44R1, 65R1, 89R1, 131R1, and 151R1 to face crowding (cyan spheres of Figure 3.13D), meaning these regions are more likely to make contact with other proteins.

The multiplex adsorption scheme is possible because of the special surface charge distribution of T4L (Figure 3.12). For example, upon adsorption to the SiNP surface with the positively charged N-terminus (Figure 3.12C) to form the first adsorption layer, a T4L molecule likely positions its regionally negatively charged C-terminus away from the particle, forming a secondary negatively charged surface. This surface facilitates adsorption of the next layer of enzymes.

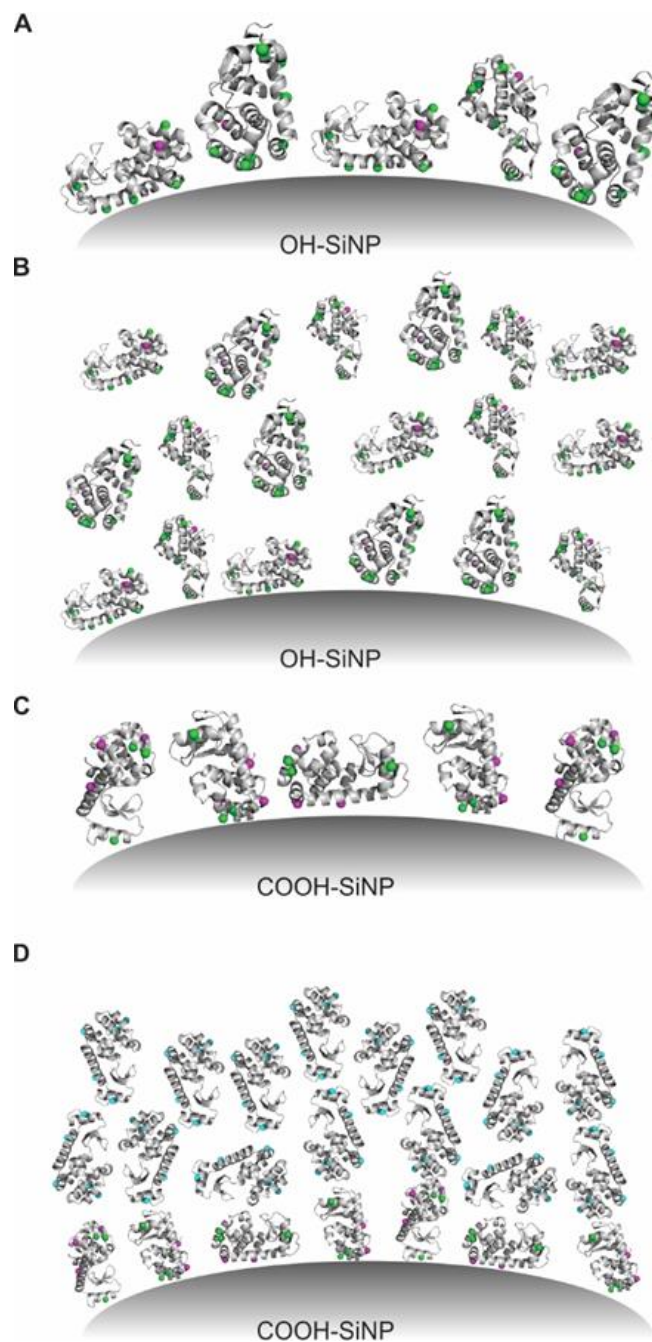


Figure 3.13. The proposed adsorption model for the SiNPs. (A) On the OH-SiNPs when a single layer of T4L is adsorbed. The green dots highlight the preferred contact point, while the magenta ones show the less favored contact point, as judged by CW EPR. (B) When the OH-SiNPs were saturated with T4L, the orientation of each protein is random, and the packing between protein layers is relatively loose. (C) On the COOH-SiNPs, when a single layer of T4L is formed, three sites are favored (green) while another three (magenta) are less favored but still possible to contact the nanoparticle surface. Two sites (65R1 and 151R1) were found to be unlikely to make the contact. The model shows certain preferences in protein orientation relative to the particle surface. (D) When the COOH-SiNPs are saturated with T4L, three sites locating near the N- and the C-terminus were found to face more crowding due to packing (cyan).

Influence of Ionic Strength

The charge-charge interaction is expected to be influenced by the ionic strength of the medium. To probe such influence, we prepared water medium with different NaCl concentrations (300, 100, and 25 mM; see Figure 3.14). First, we confirmed via CW EPR that, for the site of 44R1, the conformational dynamics in water with no salt remains unchanged as compared to that in 100 and 300 mM NaCl (Figure 3.14A).¹²¹ This is reasonable given the stability of the protein.

Next, prior to loading enzymes under different ionic strength, ~20 μ L of each SiNP was washed with ~500 μ L of the corresponding solution for at least three times, in order to ensure complete medium-switch. The protein was also switched to the corresponding medium before loading. Then, the protein-to-SiNP ratios of 10,000:1 and 15,000:1 was loaded for the OH- and the COOH-SiNPs, respectively, for each ionic strength. After incubation for at least 30 mins, the CW EPR spectrum for each sample were acquired (Figure 3.14). For the COOH-SiNPs, at higher salt concentrations (100 and 300 mM), there was almost no adsorption since there was no additional broadening observed (Figures 3.14A VS 3.14B). Washing with the corresponding solution resulted in almost no EPR signal, indicating complete desorption (Figure 3.14C). At 25 mM NaCl, the additional broadening (arrow of Figure 3.14B) is noticeable, indicating adsorption occurs. Washing with the same solution resulted in a small amount of broadened EPR signal (arrow of Figure 3.14C), indicating that at this low salt concentration, the adsorption of enzyme to the COOH-SiNP surface is effective, although the loading capacity is low.

Lastly, for the OH-SiNPs, even at 100 mM salt concentration, noticeable broadening (arrows of Figure 3.14D) can be observed, and washing did not completely diminish the

adsorption. As the salt concentration was decreased to 25 mM, the amount of enzyme adsorption was increased.

The overall findings are that increasing the ionic strength decreases the adsorption and the ionic strength has a bigger impact on the adsorption of T4L enzyme on the COOH-SiNPs than on the OH-SiNPs. The latter is rationalized to the fact that at pH of 7, the surface of the OH-SiNPs is relatively more neutral than that of the COOH-SiNPs.

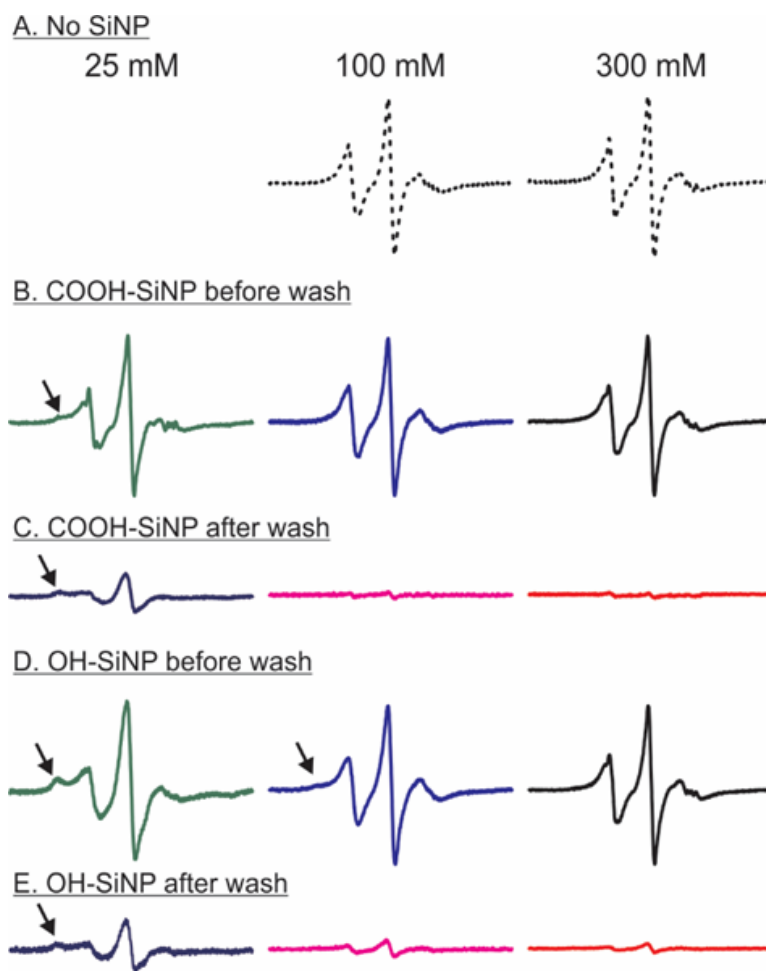


Figure 3.14. The EPR spectra of 44R1 in different NaCl concentrations (A), 44R1 upon adsorption to the COOH-SiNPs (B) and the OH-SiNPs (D) at different NaCl concentrations. After washing with the corresponding solutions, the EPR signal of the COOH-SiNPs (C) and the OH-SiNPs (E) at different NaCl concentrations were also acquired.

Conclusions

A comprehensive study of the structure, dynamics, and activity of a model enzyme upon adsorption to a few surface-modified SiNPs using EPR spectroscopy in combination with several other experimental techniques is reported here. The TEM demonstrated the adsorption of T4L onto two of the prepared SiNPs. The activity assay indicated a significant loss in enzyme activity. To probe the structural basis of such activity loss, the EPR spectroscopy was employed, which overcomes the challenges in probing structural information at the complex and dynamic nano-bio interface. It was found possible to estimate the amount of proteins in the hard corona of the SiNPs via the CW EPR area analysis. The COOH-SiNPs have a higher loading capacity of T4L enzyme than that of the OH-SiNPs. By comparing the CW EPR spectra of eight studied sites when the mutants were adsorbed to larger sepharose beads and when different protein-to-SiNP ratios were adsorbed to different SiNPs, the residues responsible for making contact with SiNPs and/or facing more crowding under various protein-to-SiNP ratios were identified. Based on this a structural model to depict the docking of T4L onto the SiNPs with different surfaces was proposed. Also, the global structural changes caused by adsorption via DEER EPR was probed, which served as a second view of the structural basis of the activity loss. Lastly, it was found that the adsorbed enzyme could be desorbed via pH adjustment, which showed the potential to use SiNPs for enzyme/protein delivery or storage due to the high capacity. Future work will be directed to tune the properties of SiNPs so that the activity loss can be minimized and SiNPs can be used as enzyme hosts. Our results also highlight the use of EPR in probing structural information on the complex and dynamic inorganic/nano and biological interface.

CHAPTER 4. ENGINEERING PROTEIN-GOLD NANOPARTICLE/NANOROD COMPLEXATION VIA SURFACE MODIFICATION FOR PROTEIN IMMOBILIZATION AND POTENTIAL THERAPEUTIC APPLICATIONS[†]

Introduction

Gold nanoparticles (AuNPs) and nanorods (AuNRs) have been applied to advance many fields such as biosensing, biomedical therapeutics, and catalysis, due to their unique optical/chemical properties and thermo-stability.^{55,58,219–229} The possibility of controlling particle size, shape, and surface properties makes AuNPs/AuNRs popular nanostructures.^{244,245} In spite of these exciting features, a concern in biosensing and biomedicine^{246–253} is the inevitable contact of AuNPs/AuNRs with biomacromolecules, especially proteins. Such contact may yield various and often uncontrollable outcomes. For example, in most cases, the AuNPs/AuNRs are rapidly coated with a “protein corona” upon contact.^{146,207,254–257} The protein corona often suppresses or reduces the original functionalities of the particles and should be avoided in most biosensing applications.^{258,259} However, if the protein adsorption can be controlled, then AuNPs/AuNRs may serve as protein immobilizers or delivery vehicles for biocatalysis or molecule/drug delivery applications.^{239,260–263} Recently, proteins have been utilized as the media to crosslink AuNPs/AuNRs and form larger aggregates (also referred as to “agglomerates”).^{246,256,264–269}

[†] The work discussed in this chapter was co-authored by Sunanda Neupane, Yanxiong Pan, Hui Li, Kristen Patnode, Jasmin Farmakes, Guodong Liu, and Zhongyu Yang. The work was previously published in ACS Applied Nano Materials.³⁴⁸ Sunanda Neupane and Yanxiong Pan had equal contributions in this work. Sunanda Neupane was the primary developer of the conclusions that are advanced here. Sunanda Neupane collected all the data discussed in this chapter and Yanxiong Pan synthesized all the polymers discussed here. Sunanda Neupane drafted all versions of this chapter. Sunanda Neupane and Yanxiong Pan revised previously published versions of this chapter. Hui Li, Kristen Patnode, Jasmin Farmakes, Guodong Liu, and Zhongyu Yang proofread the manuscript and helped trouble shoot experimental conditions.

These agglomerates find applications in photothermal therapy,^{250,256} bio-imaging,²⁵⁸ drug delivery,^{246,249} and biosensing.^{270–273} A troubling outcome is that certain proteins trigger the precipitation of AuNPs, which completely demolishes AuNPs' functions and should be avoided.^{121,150,151} Taken together, protein adsorption should be avoided (no adsorption; no aggregation) in biosensing/biomedical applications, while fine-tuned in biocatalysis, delivery, and therapeutic applications. This requires a deeper understanding of the nano-bio interface for improved engineering of protein-nanoparticle complexation. Since the nature of adsorption depends on the protein as well as the particle's surface, protein adsorption studies are often done in a case-by-case manner.

Most protein corona studies are focused on the adsorption of plasma proteins to AuNPs/AuNRs. The corona composition and thermodynamics of the adsorption has been investigated using various experimental tools.^{80,81,145,162} To reduce nonspecific protein adsorption, a common approach is to replace the original protectants, citrate ions,^{274,275} with hydrophilic thiol-containing molecules, such as mercaptoacetic acid,^{276,277} mercaptocarboxylic acids,^{278,279} and mercaptosuccinic acid.²⁸⁰ Herein the strong thiol-gold coordination substitutes the citrate-gold network and creates stable coatings. Prion protein,²⁸¹ bovine serum albumin (BSA),²⁸² and transferrin²⁸³ were found to have a reduced adsorption upon these coating changes. Polymers containing thiol groups also help enhance the AuNP stability and reduce nonspecific protein adsorption,^{207,237,245,284} as demonstrated in serum protein adsorption studies.^{254,285,286} Protein immobilization on and/or delivery via AuNPs were shown on chitosan-stabilized AuNPs,²⁸⁷ nanogold-polyurethane composites,²⁸⁸ and nanoparticles embedded in cellulose nanocrystals,²⁸⁹ wherein AuNPs served as a high-density solid support. Strategies for controlling the agglomerate size via protein adsorption were also reported, wherein inter-particle bio-

reorganization forces were found to play a key role.^{241,264,267,268,270} In regard to the applications of AuNR-protein complexation, hereceptin immobilized on AuNRs can effectively recognize the antigens related to breast tumors.²⁶⁹ AuNRs conjugated with antibody against alpha-fetoprotein has been recognized as an effective sensor of the protein.²⁷³ Protein conformational changes induced by AuNRs have been reported as well.²⁹⁰ Lastly, several groups have probed the protein-triggered AuNP precipitation mechanisms at the molecular and/or cellular level.^{121,150,151} The consensus by far is that the involved proteins approach the AuNPs via electrostatic interactions and/or Au-cysteine coordination and serve as a bridge to bring two AuNPs to a close proximity. A globular protein, T4 lysozyme (T4L), is one of these “problematic” proteins. Our recent work revealed that even the cysteine-free T4L protein could trigger the precipitation of AuNPs. Furthermore, we demonstrated that the removal of the AuNP coating by T4L was essential for the bridging process and highlighted the importance of AuNP coating.¹²¹

In this work, we investigated the effects of surface charge and thickness on the adsorption of T4L. Our original purpose was to avoid the T4L-triggered AuNP precipitation by engineering AuNPs/AuNRs with different surface properties. Coatings with positive or neutral charges and/or steric repulsions were found to be effective. In addition, on negatively coated AuNPs, we observed T4L forming protein corona as well as the protein-AuNP agglomerates, depending on the composition of the coating. On AuNRs, we observed that positive coatings prevent the aggregation of AuNRs while the negative surfaces resulted in protein coronas regardless of coating thickness. Using a combination of Transmission Electron Microscopy (TEM), Zeta potential measurements, Ultraviolet-visible (UV-Vis) absorption spectroscopy, and Electron Paramagnetic Resonance (EPR) spectroscopy, we depicted the molecular model for each adsorption case. Our investigations demonstrated the importance of surface properties on

AuNP/AuNR stability and function in biological environments and we discovered effective approaches to control the T4L adsorption behavior on gold nanostructures. Our findings also suggested that the “problematic” T4L could complex with AuNPs/AuNRs and find good potential applications (as protein carriers or thermotherapeutic targets) if properly coated. Our work is generally informative for AuNP/AuNR functionalization for applications in biosensing, therapeutics, and protein immobilization.

Experimental Methods

Protein Expression, Purification, and Spin Labeling

Mutants of 44C, 65C, and 151C were prepared as described before.²⁹¹ Briefly, the DNAs of these mutants were generated by QuikChange site-directed mutagenesis of the pET11a-T4L genetic construct containing the pseudo-wild-type mutations C54T and C97A,^{186,188} followed with verification of each mutation by DNA sequencing. These mutants of T4L were expressed, purified, and then desalted (to remove DTT) into a buffer suitable for spin labeling (the “spin buffer”, containing 50 mM MOPS and 25 mM NaCl at pH 6.8). The desalted protein mutants were then reacted with a 10-fold molar excess of S-(2,2,5,5-tetramethyl-2,5-dihydro -1-Hpyrrol-3-yl) methyl methanesulfonothioate (MTSL, Toronto Research Chemicals, Inc., Toronto) at 4 °C overnight (yielding R1). Excess MTSL was removed using the Amicon spin concentrator (Millipore, 10,000 MWCO, 50 mL). The spin-labeled protein mutants were stored in the spin buffer at -20 °C for further use.

The spin-labeled mutants were confirmed to have the correct secondary structure and activity via CD spectroscopy and an activity assay, respectively, both of which were described in our recent work.¹²¹ A few representative sites were characterized via CW EPR to confirm the local conformational dynamics.

Preparation of Gold Nanoparticles (AuNPs) and Gold Nanorods (AuNRs)

1-Hexadecyltrimethylammoniumbromide (CTAB) (98%) was purchased from Alfa Aesar(A15235). L-Ascorbic acid (99%) (A92902), Sodium borohydride (NaBH_4) (99%) (213462), and Gold III chloride trihydrate (HAuCl_4) (99.9% metal basis) (520918) were purchased from Sigma-Aldrich. Silver Nitrate (AgNO_3) was purchased from VWR (VW6030).

The typical AuNP preparation procedure reported in our previous work was employed.¹²¹ In detail, 100 ml of 0.01% HAuCl_4 was heated to boil under vigorously stirring for 10 mins. Sodium citrate was added to the HAuCl_4 solution and stirred at boiling temperature for another 15 mins. The obtained AuNPs were stored at 4 °C for further use. In this work, two particle sizes (~14 nm and 56 nm) were prepared by adjusting the amount of added sodium citrate.

The AuNRs were prepared using a known seed mediated procedure with minor modifications.²⁹² In detail, CTAB solution (5 mL, 0.20 M) was mixed with 25 μL of 0.1 M HAuCl_4 . Ice-cold NaBH_4 (600 μL , 10 mM) was added to the mixture and was stirred vigorously for 2 minutes. The solution was kept at 27°C. To AgNO_3 (300 μL ,0.01M) solution, CTAB solution (5mL, 0.20 M) was added at room temperature. The solution was gently mixed after addition of HAuCl_4 (500 μL , 0.01 M). Ascorbic acid (55 μL , 0.1 M) was added to the solution and the growth solution turned from yellow to colorless. The growth solution was kept at room temperature and 6 μL of seed was added to it. AuNRs were characterized using TEM and UV-Vis.

Preparation of Thiol-terminated mPEG (mPEG-SH)

The 3-mercaptopropionic acid (MPA, Sigma-Aldrich; 4.1 ml, 47.2 mmol) was mixed with 50 mL DMSO and stirred at 80 °C for 12 hours. The mixture was precipitated in excess cold water and filtered using a cold Buchner funnel. The solids were then washed with the cold water

for at least three times and dried in vacuum oven at 50 °C for 24 hours. ^1H NMR (400 MHz, DMSO- d_6) 2.89 (t, 2H), 2.62 (t, 2H).

The prepared bis(2-carboxylethyl) disulfide (0.4 g, 1.9 mmol) was mixed with oxalyl chloride (1.37 ml, ~8 mmol) in 5 mL anhydrous CH_2Cl_2 and reacted at room temperature for 6 hours. Excess oxalyl chloride was removed via vacuum pumping (the product is a brown oil). Approximately 1.9 ml (11 mmol) of the “brown oil” was dissolved in 20 ml anhydrous CH_2Cl_2 and mixed with the commercial mPEG-OH (Sigma-Aldrich; $M_n = 5000$, 5 g, 1 mmol). The mixture was stirred at ambient temperature for 12 hours and precipitated with 200 ml ether for three times. This step prepared the PEG-(CO)-(CH $_2$) $_2$ -S-S-(CH $_2$) $_2$ -COCl which was dried under vacuum at ambient temperature. ^1H NMR (400 MHz, DMSO- d_6) δ 3.58 (s, 456H, -CH $_2$ CH $_2$ O-), δ 2.87 (t, 2H), 2.60 (t, 1H).

Next, the PEG-(CO)-(CH $_2$) $_2$ -S-S-(CH $_2$) $_2$ -Cl (1 g, ~0.2 mmol) was dissolved in a DDT solution (0.308 g, 2 mmol) and vibrated overnight. The excess DTT was removed via dialysis (cut-off = 1 kDa) against 3 \times 1000 ml of ddH $_2$ O for 48 hr. The solution was extracted with 3 \times 30 ml CH_2Cl_2 and concentrated to 10 ml, which was then precipitated in 150 ml ether. The final mixture was dried under vacuum at ambient temperature for 24 h. ^1H NMR (400 MHz, Chloroform- d) δ 3.58 (s, 456H, -CH $_2$ CH $_2$ O-), 2.88 (d, 2H, -CH $_2$ CH $_2$ -SH).

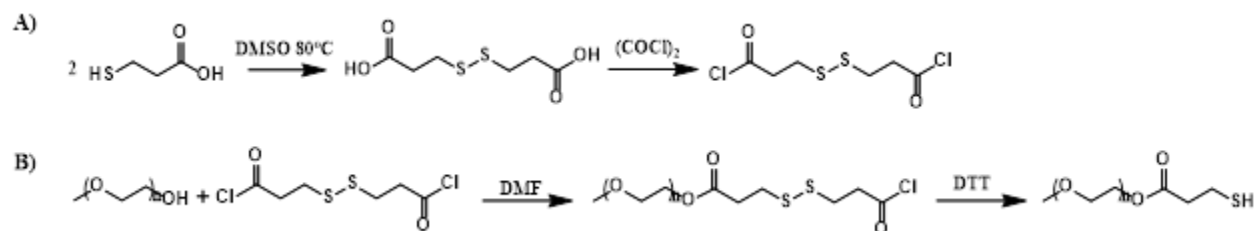


Figure 4.1. The synthetic routes of the 3, 3'- disulfanediyldipropionyl chloride (A) and PEG-SH (B).

Preparation of Thiolated Polyacrylic Acid (PAA)

MPA (65 μ L, 0.75 mmol), tert-Butyl acrylate (t-BA, 5.5 mL, 38 mmol), and azobisisobutyronitrile (AIBN, 14 mg, 0.085 mmol) was dissolved in 20 ml dimethylformamide (DMF). The mixture was degassed with nitrogen under stirring for 30 mins. After that, the mixture was sealed and reacted at 70 °C for 24 hr. The prepared P(t-BA) was precipitated with 500 ml methanol/water mixture (30/70) for at least three times and dried in vacuum oven at 50 °C for 24 hr.

Next, HOOC-P-t-BA (1 g, 13.8 mmol) was dissolved in 20 ml dichloromethane (DCM), followed by addition of trifluoroacetic acid (TFA, 2 mL, ~26 mmol) dropwise into the mixture under vigorously stirring at room temperature for 24 hr. The DCM and residual TFA were removed via rotary evaporation. The solids were then dissolved in ddH₂O and dialyzed (cut-off = 1 kDa) against 5 \times 1000 ml of ddH₂O for 48 h. This hydrolyzed P(t-BA), or, PAA (~0.017 mmol), was mixed with cysteamine (0.05 g, 0.69 mmol), EDC (0.11 g, 0.69 mmol) and N-hydroxysuccinimide (NHS, 0.079g, 0.69 mmol). The mixture was vibrated (160 rpm) overnight and dialyzed (cut-off = 1 kDa) against 3 \times 1000 ml of ddH₂O for 48 h. A white solid, PAA-(SH)_n, was obtained after lyophilization which was stored for further use. ¹H NMR (400 MHz, Deuterium Oxide) δ 2.75 (s, 2H, -CH₂CH₂-SH), 2.64 (s, 2H, -CH₂CH₂-SH), 2.33 (s, 50H, -CH₂CH-), 1.69 (d, 97H, -CH₂CH-).

For preparation PAA-SH, cysteamine (20.3 mg, 0.26 mmol), t-butyl alcohol (t-BA, 5.5 mL, 38 mmol), and azobisisobutyronitrile (AIBN, 2.8 mg, 0.017 mmol) were dissolved in 10 ml dimethylformamide (DMF). The mixture was degassed with nitrogen under stirring for 30 mins. After that, the mixture was sealed and reacted at 70 °C for 24 hr. The prepared P(t-BA) was

precipitated with 500 ml methanol/water mixture (30/70) for at least three times and dried in vacuum oven at 50 °C for 24 hr.

The prepared NH₂-P-t-BA (1 g), 3, 3'- disulfaneyldipropionyl chloride (0.5 mL, 2.9 mmol), and 1 drop of DMF was dissolved in 10 mL CH₂Cl₂. After stirring at room temperature for 24 hr, the mixture was deposited in the methanol/water mixture and dried in vacuum oven at 50 °C for 24 hr. This sample was hydrolyzed in TFA (2 mL, ~26 mmol) at room temperature for 24 hr under vigorous stirring, reduced to cleave the disulfide bonds, and dialyzed via aforementioned procedures. ¹H NMR (400 MHz, Deuterium Oxide) δ 2.76 (s, 2H, -CH₂CH₂-SH), 2.20 (s, 265H, -CH₂CH-), 1.65 (d, 490H, -CH₂CH-).

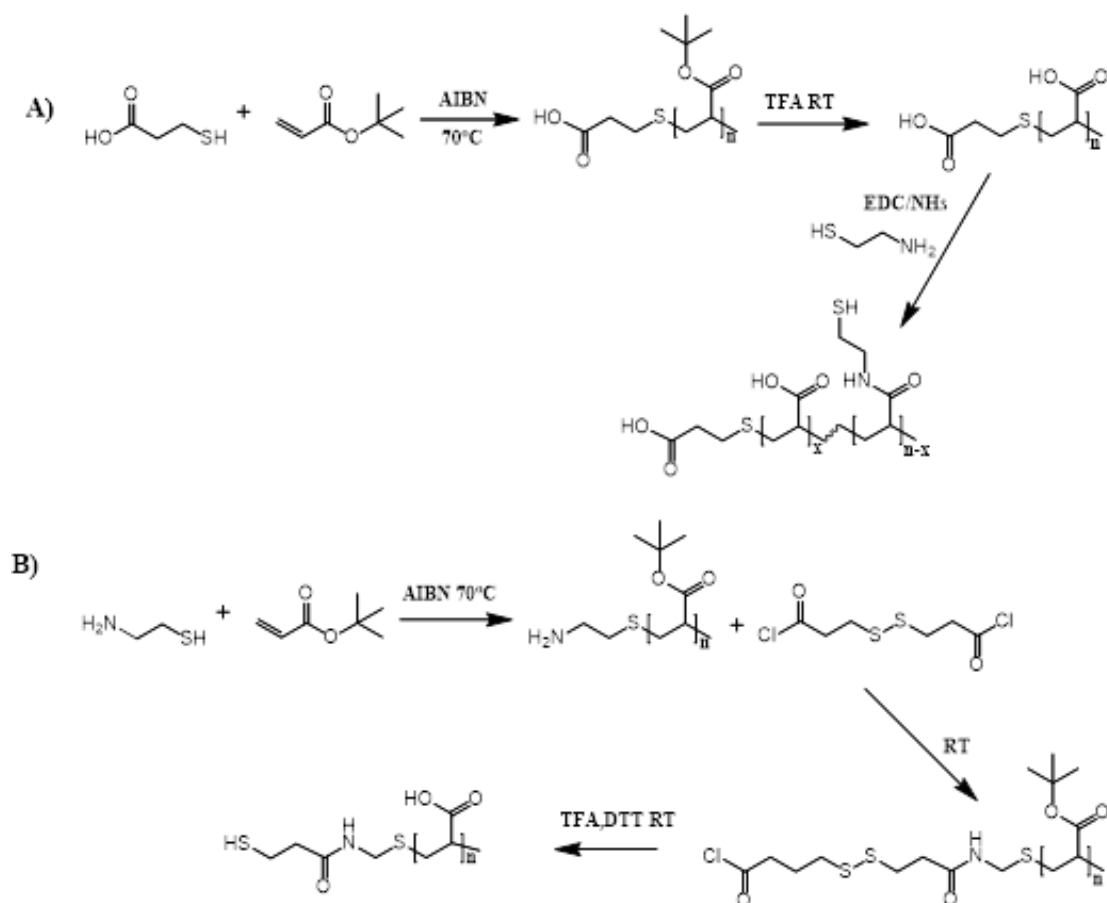


Figure 4.2. The synthetic routes of PAA-(SH)_n (A) and PAA-SH (B).

Preparation of Thiolated Polyethylenimine (PEI-(SH)_n)

The commercial PEI (Sigma-Aldrich; 1 g, 0.1 mmol) was mixed with the 3-mercaptopropionic acid (MPA, 0.059 mL, 0.69 mmol), EDC (0.11 g, 0.69 mmol) and NHS (0.079g, 0.69 mmol). The mixture was vibrated (160 rpm) overnight and further dialyzed (cut-off = 1 kDa) against 3×1000 ml of ddH₂O for 48 hr. A white solid was obtained after lyophilization and stored for further application. The characteristic peaks of -CH₂CH₂SH were overlapped with the N(H)-CH₂CH₂-N(H)-.

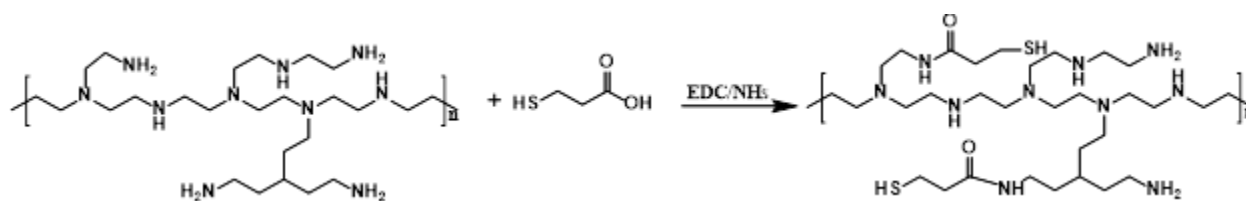


Figure 4.3. The synthetic route of PEI-(SH)_n.

Small Molecular Coating via Ligand Exchange

The MPA and MSA coating at 1.0 M concentration were neutralized with NaOH and diluted to 0.25 M as the stock solution. The neutralized MPA and MSA were named as MPNa and MSNa. The ligand-to-AuNP ratio of 5,000,000:1 was applied for each size of AuNPs. Practically, 200 μL MSNa were added into 1 mL AuNPs and sonicated for 30 mins. Next, the mixture was vibrated (160 rpm) at ambient temperature for >12 hr. Then, each coated AuNPs was washed with ddH₂O for 3 times to remove free unreacted coating species.

Polymer Coating via Ligand Exchange

All involved polymers were dissolved in ddH₂O and diluted to 20 mM as the stock solution. The typical ratio of polymer to AuNPs is 10,000 to 1. Specifically, PAA-(SH)_n (5 μL) were added into AuNPs (1 mL, 0.01 μM) and vibrated at ambient temperature for >12 hr. The

mixture was then washed via centrifugation at 10,000 rpm for 3 times to remove the unreacted PAA-(SH)_n. Similar methods were applied to conduct the ligand exchange for other polymers.

All involved polymers were dissolved in miliQ water and diluted to 1 mM as the stock solution. The typical ratio of polymer to AuNRs is 14,000 to 1. Specifically, PAA-(SH)_n (200 μL) were added into AuNRs (1 mL, 0.014 μM) and vibrated at ambient temperature for >12 hr. The mixture was then washed via centrifugation at 14,000 rpm to remove the unreacted PAA-(SH)_n. Similar methods were applied to conduct the ligand exchange for other polymers.

Incubation of Protein and AuNPs

Typically ~1 nmol of protein mutants was mixed with the ligand-coated AuNPs (mutants/AuNPs = 100/1) and incubated at ambient temperature for 0.5 hr. The unattached protein was removed via centrifugation. Continuous Wave (CW) Electron Paramagnetic Resonance (EPR) was conducted (see below) on samples before and after the removal of unattached protein.

UV-vis Spectra of AuNP upon Ligand Exchange and Interaction with the Protein

All UV-Vis absorption spectra were measured using a NanoDrop UV-Vis Spectrophotometer (Thermo Scientific ND-2000 C). Typically, AuNPs (50 μL, 0.01 μM), before and after the ligand exchange, were diluted to 1000 μL with ddH₂O for the measurements.

TEM Sample Preparation

A drop of the sample was placed on a 300-mesh formvar-carbon coated copper TEM grid (Electron Microscopy Sciences, Hatfield, Pennsylvania, USA) for 30 seconds and wicked off with filter paper. protein-containing samples were stained by adding 1% phosphotungstic acid, adjusted to pH 7-8, to the grid for 2 minutes, then wicked off and allowed to air dry. Images were

obtained using a JEOL JEM-2100 LaB₆ transmission electron microscope (JEOL USA, Peabody, Massachusetts) running at 200 kV.

Zeta Potential Measurements

The zeta potential measurements were carried out with a Nano ZS Zetasizer (Malvern Instrument Ltd.). Typically, 10 μ L AuNPs/AuNRs (\sim 0.01 μ M, suspended in ddH₂O) was diluted to 1000 μ L then subjected to measurement.

Gel Permeation Chromatography (GPC) Measurements

All Samples were analyzed using a Waters GPC system (515 HPLC Pump) with a differential refractometer (2410) detector. Separations were performed using two connected Ultrahydrogel Columns (500 and 120; 7.8 mm ID \times 30 cm) with an eluent flow rate of 0.5 mL/min. The columns and detectors were thermostated at 35 $^{\circ}$ C. The eluent used is 0.1M sodium nitrate solution. Samples were prepared at nominally 2 mg/mL in an aliquot of the eluent and allowed to dissolve at ambient temperature for several hours and the injection volume was 200 μ L for each sample. Calibration was conducted using Polyethylene oxide (Agilent PL2080-0101) and Polyethylene glycol (Agilent PL2070-0100) standards.

EPR Measurements

Approximately 20 μ L of sample was loaded into a borosilicate capillary tube (0.70 mm i.d./1.25 mm o.d.; VitroGlass, Inc.), which was mounted in a Varian E-109 spectrometer fitted with a cavity resonator. All continuous wave (CW) EPR spectra were obtained with an observe power of 12.5 mW. All spectra were obtained with a modulation frequency of 100 kHz and a modulation amplitude of 1.0 G.

EPR Spectral Simulation

The CW EPR spectra were fit using the software developed by Dr. Altenbach and Prof. Hubbell at UCLA (<http://www.biochemistry.ucla.edu/biochem/Faculty/Hubbell/>). This program was essentially the MOMD model of the NSLS program established by Freed and co-workers.²⁹³ See Appendix for details.

Activity of the Protein Adsorbed AuNPs and AuNRs.

For all our activity assays, the amount of adsorbed protein on a particle = the total amount of added protein – the protein amount in the supernatant once the adsorption was completed (both determined by UV absorption and volume). We then strived our best to adjust the loading volume of the protein-particle complex to add the same amount of protein for all samples. Activity assay was performed as previously reported.^{121,291}

Dynamic Light Scattering (DLS) Measurements.

The DLS measurements were conducted on a Nano ZS Zetasizer (Malvern Instrument Ltd.). The intensity of scattered light was detected at 90° to an incident beam. Typically, AuNPs (10 μ L, 0.01 μ M) were diluted to 1000 μ L with ddH₂O for the measurements. Details of operation followed the standard user's guide provided by the manufacture. All data analysis was based on intensity calculations.

Results and Discussions

Materials and Methods Selection

We only focus on the stable, –SH based Au coatings in this work. To understand the impacts of AuNP surface charge and thickness on T4L adsorption, we employed coating molecules with different charge and flexibility (see below). AuNP size was also varied to probe its effect. The involved coatings were implanted on the AuNPs or AuNRs by replacing the

original coating via ligand exchange.^{244,294,295} For conciseness, we only focus on the ligand exchange approach to switch coatings; other coating approaches will be explored in our future work.

For each coated AuNP/AuNR, TEM, UV-vis absorption, Dynamic Light Scattering (DLS) and Zeta potential measurements were employed to characterize the particle morphology, size/shape, and surface charge, in the absence and presence of T4L. All T4L-particle TEM, DLS and Zeta potential measurements were acquired by incubating the particles with excess T4L and washing off the unattached protein. The obtained information, however, is not sufficient to depict the state of the protein at the molecular level. Therefore, we employed Site-Directed Spin Labeling (SDSL) and Electron Paramagnetic Resonance (EPR) spectroscopy. SDSL-EPR is especially powerful in probing protein dynamics at the residue level, wherein the site of interest is mutated to a cysteine residue followed by reaction with a methanethiosulfonate nitroxyl radical derivative to create a spin label sidechain (designated as R1).^{119,120} Once labeled, the Continuous Wave (CW) EPR spectrum reflects the net effect of three motions, the protein rotational tumbling, protein backbone fluctuation, and the internal flexibility of the R1. Knowing these three motions of a protein at a specific site of interest is informative in two folds. First, CW EPR can sense whether protein adsorption occurs on particles because adsorption restricts protein rotational tumbling and yields a broadened linewidth.²⁹¹ Second, if a specific site of protein is in contact with the particle surface or adjacent proteins, the backbone fluctuation and/or R1 internal flexibility are restricted, leading to an even broader spectrum. This fact has been used to characterize protein orientation and crowding conditions on the surface of nanoparticles.²⁹¹ Combining information from TEM, Zeta potential measurements, UV-vis

absorption, and EPR leads to a molecular level understanding of the adsorption behavior of T4L on AuNPs/AuNRs.

AuNP/AuNR Characterization

AuNPs with diameters of 14 and 56 nm with the citrate coating were prepared as described in our recent work.¹²¹ The morphology and size of each particle were confirmed by TEM (Figures 4.4A-4.4B). UV-vis spectra (Figure 4.4C) revealed a dominant peak at 518 and 526 nm for each particle. A rough estimation of particle size using these values yielded consistent findings with TEM.¹⁹⁰ The surface charge was determined via Zeta potential measurements as -26.7 ± 1.9 and -22.3 ± 0.3 mV for the 14 and 56 nm AuNPs, respectively. These values are close to expectation for the negative citrate coatings. AuNRs were prepared according to the literature²⁹² and confirmed with TEM and UV-Vis (Figure 4.5). TEM image was used to calculate aspect ratio of Gold Nanorods to yield an aspect Ratio (Length/Width)= 2.76 ± 0.273 .²⁹⁶

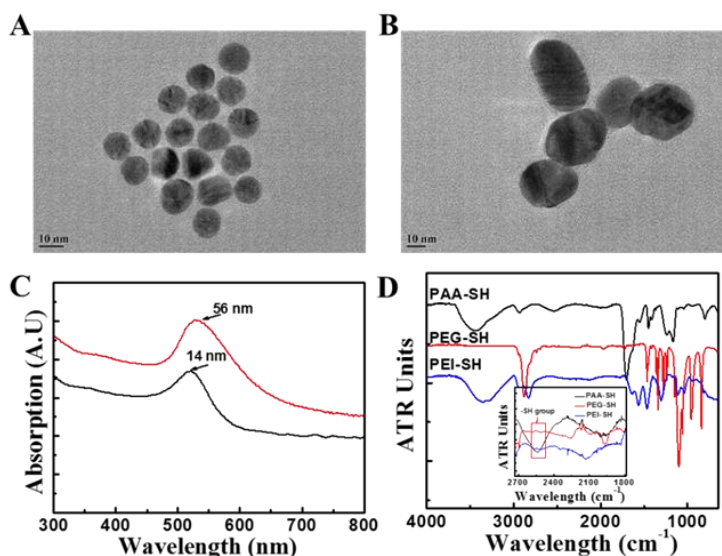


Figure 4.4. The Transmission Electron Microscopy (TEM) images (A, B) and UV-vis spectra (C) of AuNPs prepared in two sizes in citrates. (D) The Fourier Transformation Infrared (FT-IR) of the involved polymer coatings in the main text. (inset) The characteristic -SH peak of FT-IR is visible after zooming-in.

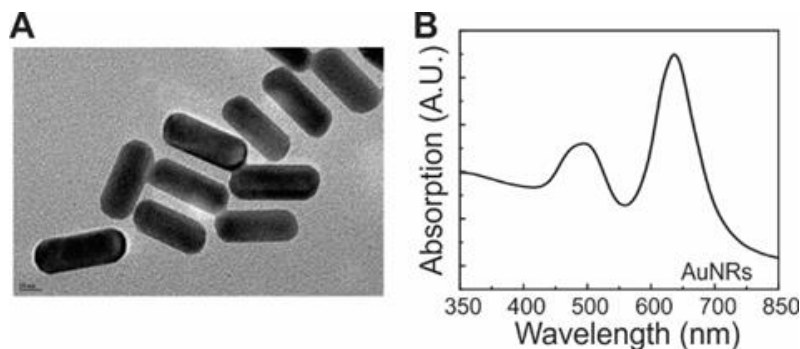


Figure 4.5. The Transmission Electron Microscopy (TEM) images (A) and UV-vis spectra (B) of AuNRs prepared with CTAB coating.

Protein Mutants and Spin Labeling

A total three T4L mutants were spin labeled for our study: 44C, 65C, and 151C (the yielded sidechains are 44R1, 65R1, and 151R1, respectively). These mutants essentially represent the three major regions of the protein, the N-terminus, the inter-domain helix, and the C-terminus. The mutants expressed and spin-labeled in our laboratory were confirmed to have the native secondary structure and activity based on Circular Dichroism (CD) and an activity assay.¹²¹ The purity of the expressed protein mutants was determined to be > 98% using gel-electrophoresis for the studied mutants. The labeling efficiency of the studied mutants was determined to be >95% using previously reported approach.¹²² The CW-EPR spectra of the mutants were also consistent with those reported in the literature.^{186,192,193}

Coating Compounds

The neutral polyethylene glycol (PEG)-SH was generated by reacting the –OH of the commercial PEG-OH with excess 3, 3'- disulfanediyldipropionyl chloride (Figure 4.1A) followed by cleaving the disulfide bond with Dithiothreitol (DTT; Figure 4.1B).²⁹⁷ The negatively charged polyacrylic acid (PAA) was prepared by the polymerization of tert-butyl acrylate (t-(BA)) followed by hydrolysis using TFA (Figure 4.2A). Partial (and random) reaction of the –COOH with cysteamine yielded PAA-(SH)_n, wherein the “n” indicates multiple –SH

groups per PAA chain. PAA-SH was prepared via scheme in Figure 4.2B wherein the end $-NH_2$ group of PAA was connected with excess 3, 3'- disulfanediyldipropionyl chloride followed by cleavage of the disulfide bond to form $-SH$. The $-NH_2$ groups of the positive polyethylenimine (PEI) were partially substituted with $-SH$ groups by reaction with MPA under the catalysis of EDC/NHS (Figure 4.3). The polymers were coordinated to AuNPs via Figure 4.7 pathways B or C. In general, the polymer-to-protein ratio was 10,000:1 and the vibration time was ~ 12 hrs. The PEI-(SH)_n, PEG-SH, and PAA-(SH)_n were characterized using Fourier Transformation Infrared (FTIR) (Figure 4.4D), wherein the three new peaks at ~ 2530 - 2560 cm^{-1} demonstrate the presence of thiol groups. The peak intensities of PEI-(SH)_n and PAA-(SH)_n are higher than that of PEG-SH, in line with the number of $-SH$ groups in these polymers. The molecular weight of PAA-SH and PAA-(SH)_n were characterized with the Gel Permeation Chromatography (GPC; Figure 4.6). Similarly, the CTAB coating of AuNRs was exchanged to PAA-SH and PAA-(SH)_n. The chemical shifts at 2.6-2.8 ppm corresponding to the methylene protons ($-CH_2CH_2-SH$) next to the thiol group confirm the presence of thiols. Integrated intensity of these peaks indicates that 75-85 % of PAA was modified with one thiol group in PAA-SH (only an estimated range is given because of the presence of the broad polymer peaks). For PAA-(SH)_n, NMR indicates that for every PAA ~ 17.7 thiols were attached. According to GPC, for PAA-SH, the Mn is 58.1 kDa, the Mw is 107.7 kDa, and the PDI is 1.86. For PAA-(SH)_n, the Mn is 16.6 kDa, the Mw is 31.2 kDa, and the PDI is 1.88.

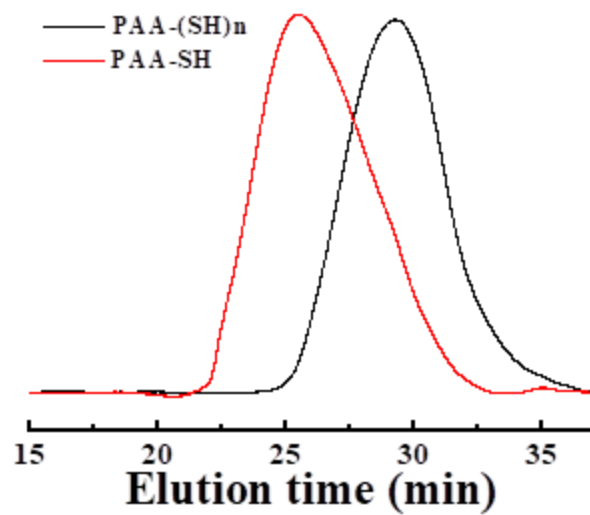


Figure 4.6. The GPC data for PAA-(SH)_n and PAA-SH.

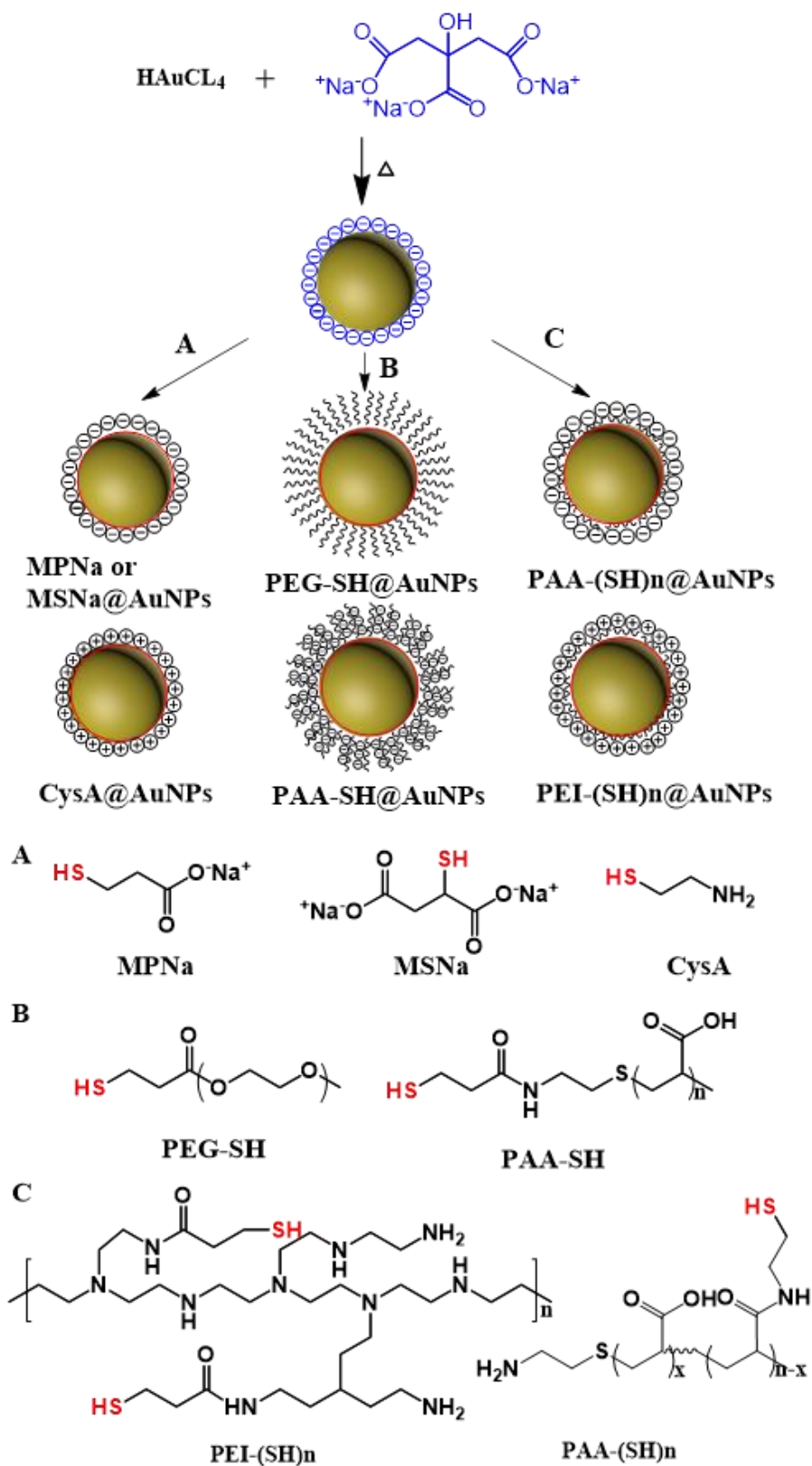


Figure 4.7. Schematic illustration of our coating strategies: pathways to implant small molecular coatings (A) and polymer coatings (B, C).

Positive and Neutral Coatings Prevent T4L Adsorption and Particle Precipitation

In principle, replacing the citrate with a layer of positively charged compounds should prevent the T4L-triggered AuNP precipitation since T4L has a positive net charge at neutral pH (pI 9.2). However, our attempts with cysteamine, which is often used as a positive coating in AuNP studies, produced a clear precipitation in the absence of T4L. Time-resolved UV-vis spectra also showed a rapid decrease in particle concentration regardless. We rationalized this to the electrostatic interaction between the citrates and the positive cysteamine during ligand exchange. This interaction must disrupt the original citrate coating and lead to particle aggregation. Meanwhile, the citrates may cap the $-\text{NH}_3^+$ end of the cysteamine (Figure 4.7) and create the steric hindrance for S-Au coordination, which prevents the effective coating of AuNPs with cysteamine, leading to particle precipitation. Indeed, current reports on cysteamine coating of AuNPs were directly prepared by reducing the HAuCl_4 with NaBH_4 in the presence of cysteamine, instead of through ligand exchange.^{298–300} Note that most of our observations in this work are independent of AuNP sizes (14 and 56 nm). Therefore, for conciseness, our discussion will not specify AuNP size unless particularly stated.

To create effective S-Au coordination, we switched to the $-\text{NH}_2$ based polymer coating, the PEI-(SH)_n (positively charged at pH 7) and conducted ligand exchange. Although the citrates were still able to cap the amines of PEI, the relatively large molecular size of PEI allowed for the spatial availability of $-\text{SH}$ groups and ensured the successful S-Au coordination on the surface. The resultant Zeta potential was on the order of $\sim +40$ mV (see Table 4.1), proving the success of coating exchange. TEM also confirmed the presence of stably dispersed AuNPs (Figure 4.8A). The UV-vis spectrum showed the characteristic absorption at 526 nm for the 56 nm AuNPs (Figure 4.8B), indicating that the AuNP size was retained upon PEI coating. DLS measurements

show a slight increase in the hydrodynamic radius compared to the original AuNPs (from 50 to 75 nm;). This may be caused by the crosslink between PEI molecules which formed multiple layers of PEI coating. Upon incubating with T4L for ~30 min, we acquired CW EPR spectra. As shown in Figure 4.8C, the spectrum of 151R1 (Figure 4.8 inset) on the PEI-(SH)_n coated AuNPs was identical to that in solution, indicating no protein adsorption (because of no change in protein rotational tumbling rates; see above). After removal of the protein via washing, the Zeta potential, TEM, and UV-vis spectra remained; there was no EPR signal retained. Other mutants yielded the same outcomes. PEI, therefore, can serve as a stable AuNP coating to prevent T4L-triggered aggregation.

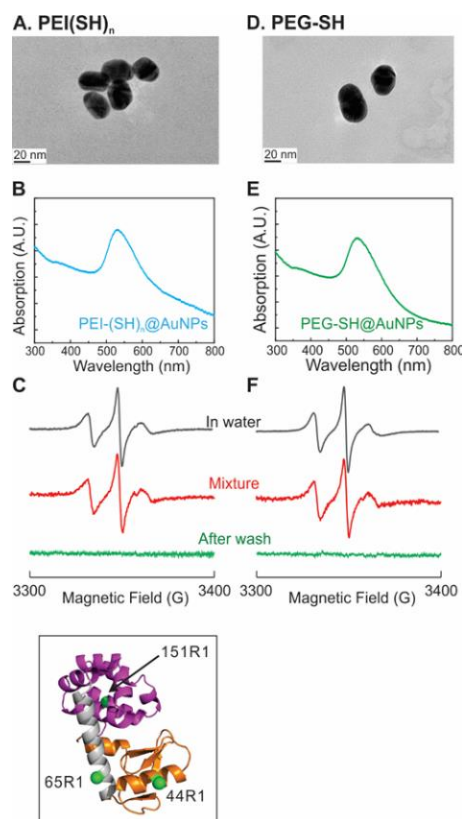


Figure 4.8. The TEM (A), UV-Vis spectrum (B), and CW EPR (C) of the AuNPs coated with a positively charged polymer, PEI. The black trace in (C) indicates the CW EPR spectrum of a representative protein site, 151R1, in water. The red and green traces were the same site on AuNPs before and after wash. The same set of data are also acquired for the PEG coated AuNPs (D=TEM; E=UV-Vis spectrum; F= CW EPR spectra). (Inset) The three labeled sites for site-specific protein backbone dynamics (crowding environment) studies.

Table 4.1. The Zeta potentials of the involved AuNPs in this study, in the absence and presence of T4L. a: T4L triggered the precipitation of AuNPs; no Zeta potential was measured. b: There was no protein adsorption; the Zeta potentials remained unchanged as in the absence of T4L.

Particle Name	- T4L (mV)	+T4L (mV)
14 nm AuNPs	-26.7+/-1.9	N/A ^a
56 nm AuNPs	-22.3+/-0.3	N/A ^a
PEI-(SH) _n 14 nm	+40.8+/-3.8	Unchanged ^b
PEI-(SH) _n 56 nm	+37.8+/-3.1	Unchanged ^b
PEG-SH 14 nm	-30.8+/-3.1	Unchanged ^b
PEG-SH 56 nm	-29.9+/-2.6	Unchanged ^b
MSNa 14 nm	-24.2+/-2.7	4.9+/-1.8
MSNa 56 nm	-21.5+/-1.2	3.6+/-1.6
PAA-(SH) _n 14 nm	-26.2+/-3.6	-18.2+/-2.2
PAA-(SH) _n 56 nm	-34.1+/-2.9	6.0+/-0.6
PAA-SH 14 nm	-39.1+/-3.6	-22.1+/-1.0
PAA-SH 56 nm	-38.7+/-3.7	9.6+/-0.3

We also probed the effect of neutral polymers on T4L-AuNP complexation. We selected the end-modified PEG-SH to conduct this study because the -SH can anchor PEG to the AuNP surface and the PEG chain can effectively create steric hindrance/shielding to prevent AuNPs aggregation.³⁰¹ The TEM and UV-vis spectrum shown in Figures 4.8D and 4.8E confirmed the size and morphology of the PEG-SH coated AuNPs. CW EPR confirmed no protein adsorption (representative data see Figure 4.8F). DLS measurements with and without protein show similar hydrodynamic radii, indicating PEG places no influence on AuNP size (Table 4.2). Particle size stability was judged based on UV-Vis spectra and DLS. The UV-Vis spectra were stable after mixing with protein over time (Figure 4.9), indicating that the particle number was unchanged. Similar finding was true from DLS results. PEG, therefore, can serve as a stable AuNP coating but does not bring extra charges into the system. Indeed, PEG can prevent the adsorption of most proteins with either positive or negative net surface charges due to the steric hindrance.³⁰¹

Table 4.2. The hydrodynamic radius of particles with various coatings in the absence and presence of protein.

Particle Name	- T4L (nm)	+T4L (nm)
AuNPs	50.2+/-16.3	N/A ^a
PEI-(SH) _n	76.9+/-15.3	82.4+/-26.8
PEG-SH	57.8+/-17.4	57.5+/-14.5
PAA-(SH) _n	94.7+/-25.6	307.6+/-58.6
PAA-SH	58.0+/-23.1	282.1+/-44.9

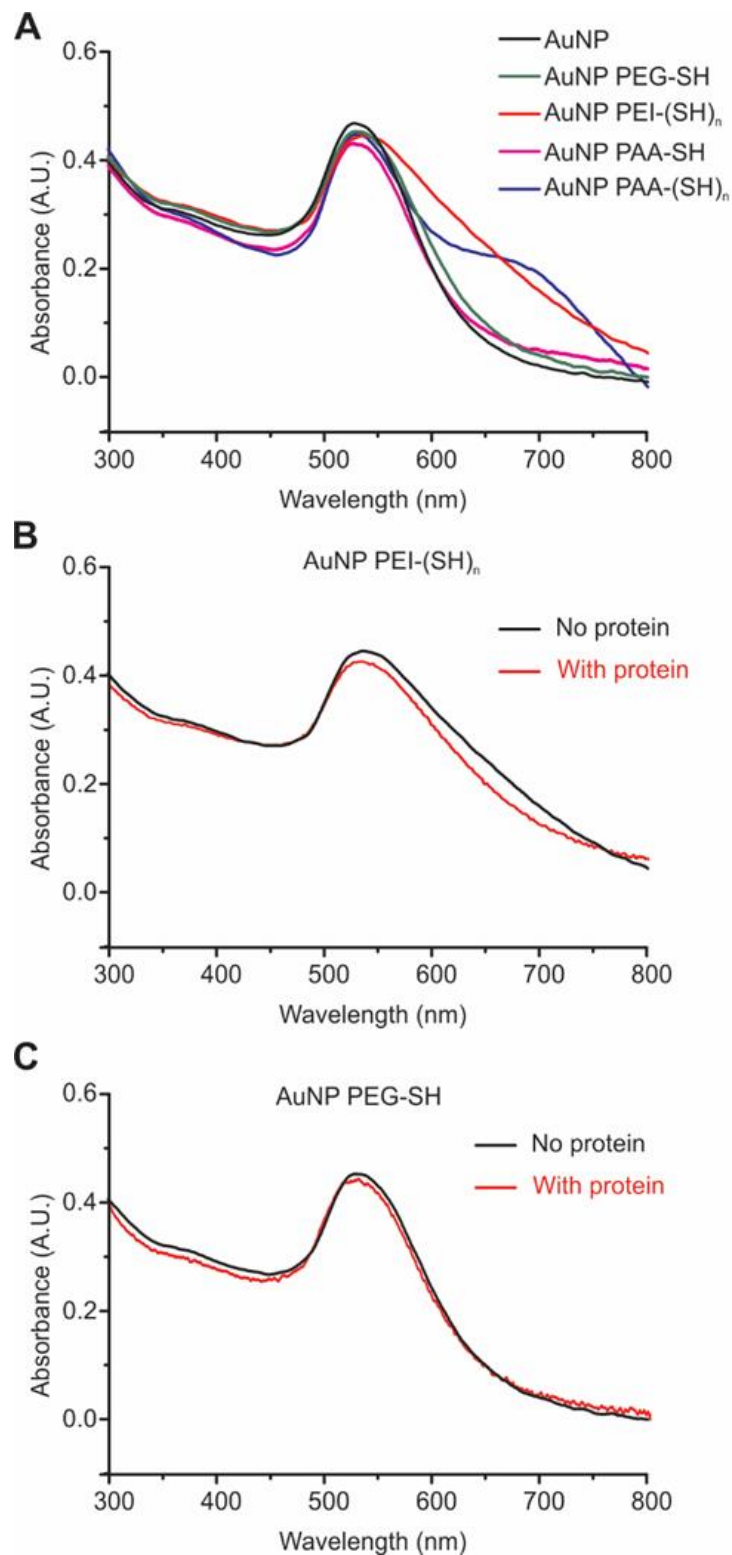


Figure 4.9. The UV-Vis spectra of AuNPs and various coatings. The red curves in (B) and (C) were acquired 30 min after mixing the protein with the associated particles. The UV-Vis spectra do not change much over time. The results show almost no change in particle numbers upon addition of the protein.

T4L Induces Agglomeration of Negatively Coated AuNPs

We have shown that the weak citrate-Au coordination could be disrupted by T4L resulting in precipitation.¹²¹ In this section, we intend to probe the effects of stronger negative coatings on T4L adsorption. We again started with small molecular coatings, MSNa and MPNa. Since our findings are identical for both, our discussion will only be focused on MSNa. Upon ligand exchange, the Zeta potentials were on the order of -20 mV (Table 4.1). There was no precipitation or pellets as judged by visual observation and TEM (Figure 4.10A). The particles tended to settle down to the bottom of the test tube if left static for a few days. However, these particles could be re-dispersed via sonication.

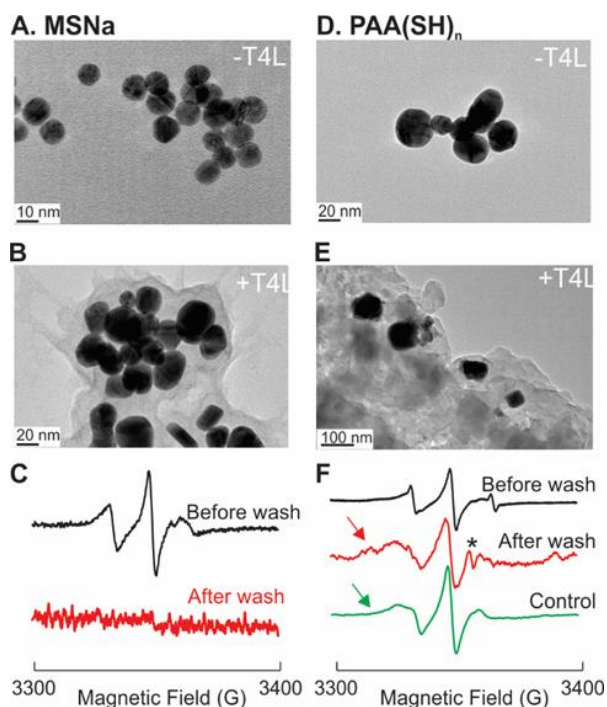


Figure 4.10. The TEM images of AuNPs coated with the negatively charged MSNa in the absence (A) and presence (B) of T4L. The “cloud-like” network indicates particle crosslink by T4L. (C) The CW EPR spectra of a representative site (151R1) before and after wash indicate a very low amount of protein adsorption. The same set of data for the PAA-(SH)_n coated AuNPs are also shown. The TEM images in the absence (D) and presence (E) of T4L indicate the formation of interparticle crosslink. (F) The CW EPR of the same representative site after wash indicates a substantial broadening in the protein network in comparison to the “control” (red VS green). Proteins were dyed before TEM test. The “*” indicates the background signal of our resonator.

Upon addition of T4L, there was no precipitation either. The Zeta potential also became positive (3-5 mV, see Table 4.1), confirming the adsorption of protein. The TEM of the stained protein adsorbed to AuNPs showed agglomeration of particles (Figure 4.10B), wherein the particle sizes were retained but the protein becomes the medium to crosslink AuNPs. This is not a complete surprise because T4L can bridge negatively surfaced particles and the stable, strong coatings prevent the previously observed “decoating” by T4L.¹²¹ Our EPR test, however, did not show indication of protein adsorption (see above). As shown in Figure 4.10C, upon mixing with T4L, the spectrum was identical to that in solution. After washing off the unattached proteins, the remaining EPR spectrum showed almost no signal. This may be caused by the low amount of protein adsorption (ca. lower than our EPR detection limit, ~5-10 μM). It is also possible that T4L adsorption to the MSNa coated AuNPs was labile and the adsorbed proteins were in constant exchange with those in solution. An evidence supporting the possibility of labile interaction between proteins and AuNPs is the fact that the more rounds of washes we carried out, the more the EPR signal reduced. Nevertheless, the TEM and Zeta potential proved the presence of T4L.

Next, we coated AuNPs with PAA-(SH)_n in order to create a higher amount of negative charges for T4L adsorption. Here the index “n” stands for multiple –SH groups per PAA. The Zeta potential became slightly more negative (~ -30 mV; see Table 4.1) indicating the successful replacement of citrate with PAA-(SH)_n. The TEM (Figure 4.10D) confirmed that the core size of AuNPs was unchanged upon the PAA-(SH)_n coating. DLS measurements, however, indicated an increase in the hydrodynamic radius (50 to 95 nm). This could be caused by the inter-PAA molecular crosslinks between thiols which may generate multiple layers of PAAs and/or create AuNP aggregation (to yield a larger hydrodynamic radius). Upon mixing with T4L, the TEM

indicates a more intense inter-particle crosslink between AuNPs (Figure 4.10E), while DLS indicates a significantly increased particle size. We also added excess proteins in order to saturate the AuNPs. The resultant spectrum (Figure 4.10F black) shows the free protein signal (the sharper lines) and some broadened signal, indicating that only a portion of the protein was adsorbed to AuNPs and sensed the local environment change. This change was clearer after removal of the unattached protein (Figure 4.10F after wash), which showed a significantly increased spectral linewidth. The broadening observed in Figure 4.10F (red) is wider than the same protein site immobilized on a solid sepharose surface but with no additional restriction at the labeled site (see “control”, Figure 4.10F green).²⁹¹ We rationalize this finding to the fact that the inter-particle crosslink was so intense that the protein backbone fluctuation and the spin label’s internal motion were both restricted. Same findings held for two other labeled sites (data see below and Figure 4.11). EPR spectral simulations resolve two major contributions to the spectra, a highly restricted component and a less restricted one, indicating some proteins make direct contact with others at the labeled site while others do not. The relative population of the restricted component is 10-20% depending on mutants (see Appendix Tables A1 and A2). The data shown in Figure 4.10F (before wash, black trace) was obtained with a protein-to-particle ratio of 100:1, and the adsorbed protein (the broader component of the spectrum) is ~40-50 % which means each AuNP can adsorb 40-50 proteins on average. Given the AuNP concentration of 0.1 μM , the adsorbed protein concentration is ~5 μM . EPR results, therefore, suggest that the inter-particle crosslink by T4L protein was indeed an intensely crowded protein network. Also, T4L might be a good medium to crosslink negatively charged AuNPs and create gold nano-agglomerates.²⁶⁴⁻²⁶⁶

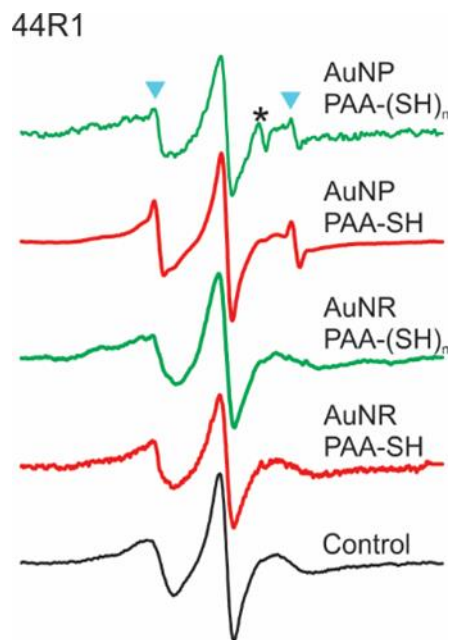


Figure 4.11. Supporting CW EPR data for 44R1 adsorbed to the PAA-(SH)_n and PAA-SH coated AuNPs and AuNRs. The “control” stands for data acquired from the same protein site immobilized to the CNBr-activated sepharose beads, wherein the protein rotational tumbling is known to be restricted but proteins retain the native conformation. Broadening in the low field region indicates “contact” of 44R1 sidechain with other protein molecules or nanoparticle coatings. The asterisk indicates the background signal from our resonator; the blue triangles indicate proteins detached into the solution.

T4L Forms a Stable Corona on the Negative “Shell” of AuNPs

One reason the PAA-(SH)_n coating was able to form the agglomerates is the strong coordination of the multiple thiol groups of PAA-(SH)_n with the AuNP surface as well as the potential crosslinks between PAAs. This strong interaction not only prevented the “decoating” of AuNPs by T4L but also helped the formation of the relatively stable, crosslinked protein network. If the strong crosslinks between thiol groups can be reduced and some steric shielding can be introduced, it is possible to create protein adsorption without aggregation or precipitation. To test this hypothesis, we utilized the PAA-SH to coat the AuNP surface wherein the -SH was anchored on the surface while the rest of PAA was extended to the solution to form a “shell”. The Zeta potential was dropped to ~-40 mV. The TEM shown in Figure 4.12A indicates good dispersity of the PAA-SH coated particle. DLS results indicate a small but noticeable increase in

the hydrodynamic radius (50 to 58 nm). Upon mixing with T4L, instead of the “cloud-like” protein crosslink networks shown in Figure 4.10E, we observed the pattern shown in Figure 4.10B wherein each AuNP was surrounded by a number of (stained) proteins. This indicates that the single point attachment effectively prevents the formation of inter-particle crosslinks and creates a T4L corona. DLS also indicates a significantly increased particle size. A closer look at the EPR data on the three labeled sites indicates that additional “contacts” or broadening are present in comparison to the “control” (described before; red *VS* black curves of Figures 4.12C and 4.12D).²⁹¹ As discussed in our recent work, such broadening indicates the contact of T4L and the shell. Interestingly, the broadening extent in the CW spectra of both 65R1 and 151R1 adsorbed on the PAA-SH coated AuNPs was not as high as that on the PAA-(SH)_n coated AuNPs (green *VS* red curves of Figures 4.12C and 4.12D). This indicates that the local crowding/restriction at the labeled sites in the protein-mediated agglomerates is higher than that in the protein corona. This finding is reasonable because to prevent the disassembly of the agglomerates, stronger protein-protein interaction is needed. EPR spectral simulations using two components show similar findings, a highly restricted component and a less restricted one. The relative population of the restricted component, however, drops to 5-10 % (see Appendix Tables A1 and A2), consistent with our argument above.

Our further tests indicated that the adsorbed proteins can be desorbed via washing with higher ionic strength buffers. Therefore, the PAA-SH coated AuNPs can be used for protein storage. In order to retain the function of T4L on these AuNPs, however, the “additional” protein-surface contact should be avoided. This could be done by introducing some hydrophobic interactions in the shell, which will be explored in our future work. Once achieved, the PAA-SH

coated AuNPs could be used as protein carriers for biocatalysis, protein delivery, enzyme storage, and fundamental protein structure/dynamics studies.

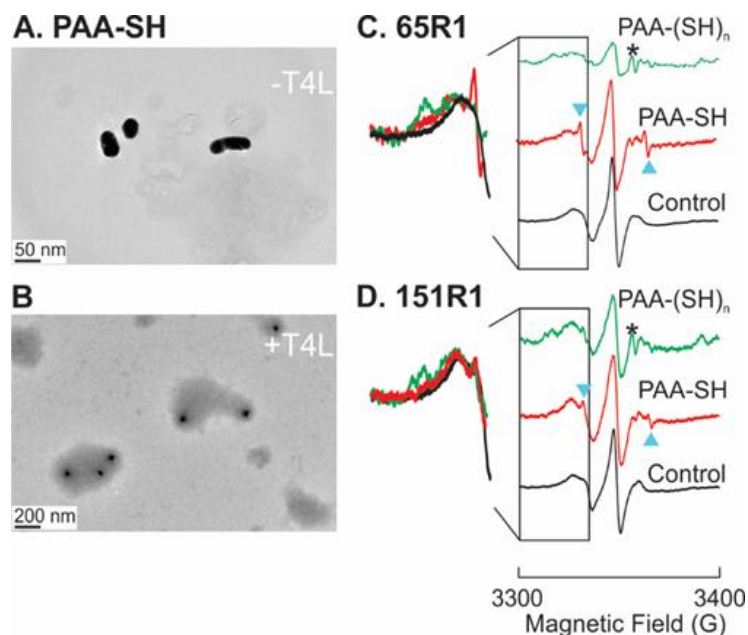


Figure 4.12. The TEM images of AuNPs coated with PAA-SH in the absence (A) and presence (B) of T4L. Stable protein adsorption is evident as shown by the coronas around the particles. (C, D) The CW EPR spectra of 65R1 (C) and 151R1 (D) show a medium extent of spectral broadening (red) for these two mutants on the PAA-SH coated particles comparing to the control (black) and the PAA-(SH)_n coated ones (green). Proteins were dyed before TEM test. The “*” indicates the background signal of our cavity. The blue triangles could originate from unattached proteins or unfolded proteins adsorbed on the particles.

T4L Adsorption Behavior on AuNRs

To probe the influence of geometry on protein adsorption behavior, we went on to investigate the mixture of T4L and AuNRs. With CTAB coating, the addition of T4L did not change the morphology of AuNRs due to the charge repulsion. Next, we utilized the PAA-SH and PAA-(SH)_n to coat the AuNRs and the resultant AuNRs were found to retain their shapes (TEM images shown in Figures 4.13A and 4.13B). Upon addition of T4L, interestingly, we observed a layer of protein corona on both AuNRs, regardless of the coating (Figures 4.13C and 4.13D). The EPR measurements of protein backbone dynamics (Figures 4.13E-4.13H) indicate crowded local environments at the three labeled sites for both PAA coats. In particular, for PAA-

SH coating, the extent of crowding in the AuNRs coronas is higher than that in the AuNPs coronas (see Figures 4.13E and 4.13G, arrows). This may be caused by the flat portion of the AuNR surface which creates additional tension in order to adsorb the protein. For PAA-(SH)_n coating, it is a bit surprise that we did not observe the agglomerates as in the case of AuNPs. The extent of broadening (crowding) is similar in both AuNPs and AuNRs for all studied sites (Figures 4.13F and 4.13H). EPR spectral simulations (see Appendix) using two-component fitting result in similar rates and order of motions, although the populations of the restricted components are slightly higher than those on AuNPs (see Appendix Tables A1 and A2). This may also be rationalized to the flat portion of the AuNR surface, so that although no protein crosslink is formed, the strong interaction between the highly intensive negative charges on the AuNR surface in combination with the flat surface creates the additional crowding.

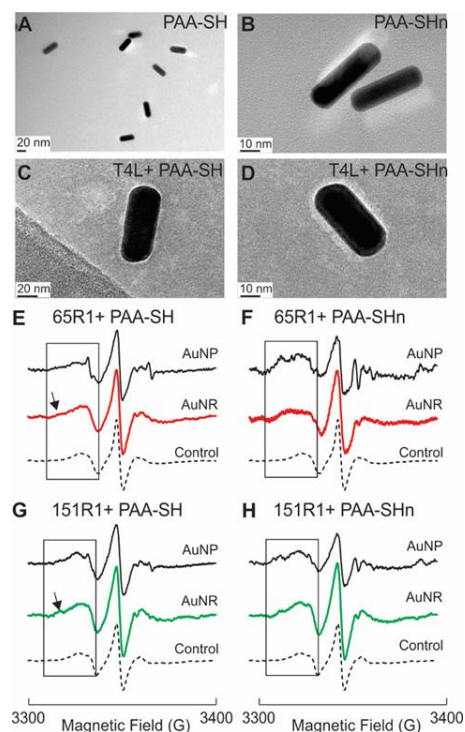


Figure 4.13. The TEM images of AuNRs coated with PAA-SH and PAA-(SH)_n in the absence (A, B) and presence (C,D) of T4L. Stable protein adsorption is evident as shown by the coronas around the particles. (E-H) The CW EPR spectra of 65R1 (E, F) and 151R1 (G, H) on AuNRs with different coatings and their comparison to the spectra on AuNPs and the “control”.

Molecular Models of T4L Adsorption

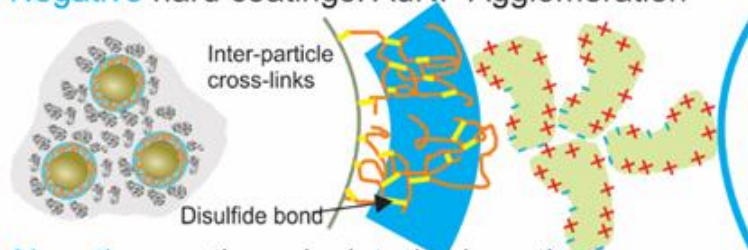
Combining findings from several biophysical and analytical techniques, we propose the following molecular models. As shown in Figure 4.14A, with positive or neutral coatings, T4L was either repulsed or spatially shielded from the particle surface, preventing their capability of bridging particles and triggering particle aggregation/precipitation. With negative coatings, if the coating is stable enough to prevent “decoating”, AuNP precipitation was also prevented. However, depending on the charge distribution and thickness of the coating, the outcomes of T4L adsorption are different. Upon adsorption to the AuNP surface with strong crosslinks between polymers (ca. PAA-(SH)_n coating; Figure 4.14B, left and middle panels), a T4L molecule is able to attract the second one via electrostatic interactions (Figure 4.14B, right panel) to form a protein network. Furthermore, the outer layer of PAAs could crosslink inner layer ones to help form the T4L-PAA (outer)-PAA (inner) network. The so-formed coating layers are thick and stable, which facilitate the formation of the agglomerates. If the number of –SH is reduced (ca. PAA-SH coated AuNPs/AuNRs; Figure 4.14C), the charges are distributed along the shell (with no crosslink). T4L is still able to adsorb to the network of the PAA. However, the relatively low charge density and the intrinsic PAA flexibility as well as the steric shielding (due to the thickness of the shell) together reduces the chance of forming agglomerates. Instead, only protein coronas are formed on AuNPs with good dispersity. Same is true for PAA-SH coated AuNRs. The puzzle here is why AuNRs with PAA-(SH)_n coating does not form the agglomerates. We speculated that this is related to particle geometry and protein size. To form agglomerates, the protein has to serve as the bridge or “cross-linker” to adhere the particles together. Adhering AuNRs with heterogeneous orientation is unstable especially for a small

protein like T4L (Figure 4.14D). A potential direction of generating AuNR based agglomerates using T4L is to orient all AuNRs (Figure 4.14D).

A. Neutral/Positive coatings: Isolation; No adsorption



B. Negative hard coatings: AuNP Agglomeration



C. Negative coatings: Isolated Adsorption;



D. Negative coatings of AuNRs

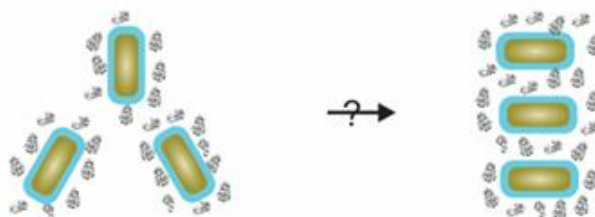


Figure 4.14. The schematic models of T4L adsorption to AuNPs with various surface charges (green=neutral, red=positive, blue=negative). (A) Positive/neutral coatings create isolation of protein and AuNPs. (B) Strong negative coatings based on PAA crosslinks facilitate agglomerates formation. The protein surface charge might be the key for the crosslinked protein network (right). (C) PAA-SH shells adsorb proteins with no aggregation formation. (D) Negative PAA-(SH)_n coatings does not form agglomerates with T4L.

Coordination of Coating Molecules with Gold Surface

Most AuNPs were prepared by reducing the H₂AuCl₄ to AuNPs in the presence of citrate sodium as the reducing agent;³⁰² the resultant citrates were anchored on the GNPs surface through the coordination of η-COO⁻ to gold atoms.^{207,253} The coordination was not so stable (bonding energies are 33.4 -41.8 kJ/mol), creating serious stability issues of AuNPs in biological

and medical applications. The coordination of –SH to gold atoms, on the other hand, has a bonding energy of 184 kJ/mol.^{274,303,304} Such enhanced coordination is essential for the formation of stronger coatings.

Polymer Coatings

In comparison to the small molecular coatings, polymers are able to create a layer of steric shielding to separate AuNPs from aggregation or precipitation. PEG-SH is perhaps the best in this context wherein no new charges are brought to the system. The biocompatibility of PEG coating is also excellent. In addition, the polymer conformation affects the protein adsorption. For example, in PAA-(SH)_n coated AuNPs, the multiple –SH coordination sites likely overcome the charge-charge repulsion between PAA chains, resulting in a PAA conformation which wraps the AuNPs surface. This facilitates the formation of a multi-layer PAA coating stabilized by extensive crosslinking, which helps the inter-particle crosslink mediated by T4L. On the other hand, the conformation of PAA-SH on AuNPs must be extending away from the particle surface toward the solution. This creates steric shielding which weakens the crosslink significantly. The protein is only adsorbed, creating neither inter-particle crosslinks and nor agglomeration. An interesting phenomenon is the PAA-(SH)_n coated AuNPs agglomerates do not continue aggregation or precipitate out. This is likely because the protein becomes the coating of the agglomerates once reached to at a certain size. Of course, we stayed below the 10x concentration of AuNPs (0.01 μM); the agglomerates would be unstable at higher concentrations.

Applications of Engineering Protein-Nanoparticle Complexation

Our negative coating studies are particularly interesting because they imply the potential use of T4L in AuNP/AuNR-based materials design. For example, T4L may be used as the media to crosslink AuNPs/AuNRs to form agglomerates to facilitate therapeutics. The use of T4L may

provide antibacterial functions to the agglomerates as well.^{305–307} One of our future directions is to fine-tune the amount of –SH groups on PAA-(SH)_n, polymer-to-AuNP/AuNR ratio, PAA length, and buffer conditions to control the size and morphology of the T4L-induced AuNPs agglomeration. For the PAA-SH coated AuNPs/AuNRs, the PAA shell can be used to immobilize T4L or other positively charged proteins/enzymes. The major advantage of the PAA shell is the intrinsic flexibility of the polymer chain which creates “soft” contact of the shell with the target protein. It is also possible to co-polymerize other functional polymers with PAA to bring diverse functions to the shell. Immobilization of proteins is important for enzyme storage, biocatalysis, and protein delivery. Indeed, proteins adsorbed to AuNPs or AuNRs showed potential activity as compared to free protein in solution (see Figure 4.15), indicating that both particles can retain some protein function. In comparison to other solid phase immobilizers, AuNPs/AuNRs have the characteristics of high thermal stability, bioinert nature, and higher contrast (for imaging applications).

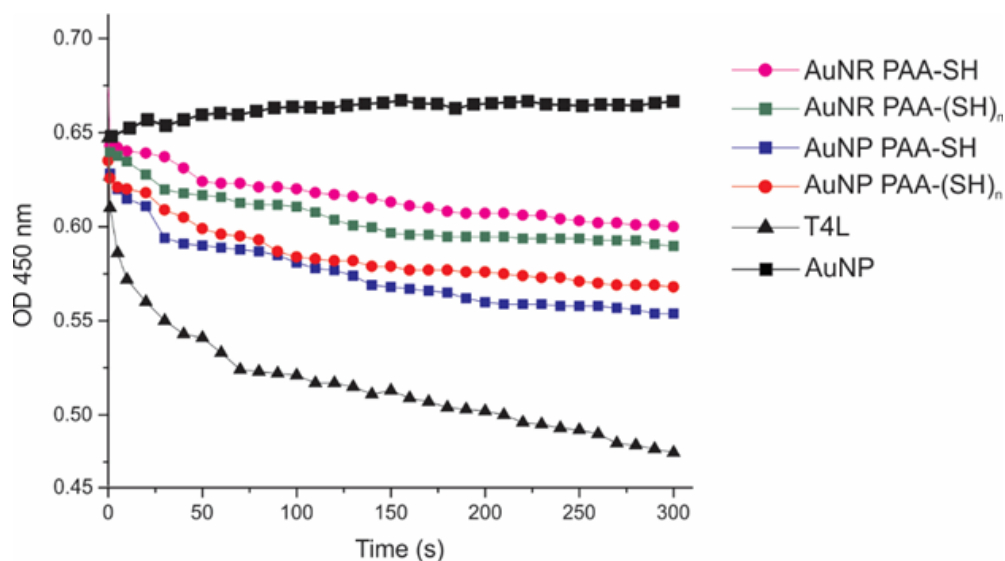


Figure 4.15. The activity assays of T4L coated on various negatively charged AuNPs and AuNRs. Positive control (black triangles) = T4L; negative control (black squares) = AuNP.

EPR as a Sensitive Tool to Probe the Local Environment of Proteins in Complex with Nanoparticles

Knowing the local environment of protein at the nano-bio interface is important for preparation of agglomerates because the strength of inter-protein crosslink (or the crowding) is closely related to the stability of the formed agglomerates. In addition, if the protein biological function is needed in the agglomerates (ca. the antimicrobial function of T4L), the crowding should be reduced in order to retain protein function. The local environment of proteins in coronas is also important when AuNPs/AuNRs are applied in protein immobilization and delivery. This is because if the crowding suppresses the protein biological function, then it becomes meaningless to immobilize or deliver a dysfunctional protein. Determining protein environment at the nano-bio interface is challenging for most techniques due to the complexities caused by the presence of gold and the molecular interaction between protein and the particles. EPR is a unique technique to probe the protein adsorption behavior on nanoparticles, due to its sensitivity to protein rotational tumbling and local spatial restrictions (see before).^{120,291} The “penetrating power” of magnetic resonance allows for structure and dynamics measurements in complex systems regardless of the presence of AuNPs/AuNRs. In this work, we relied on EPR to rapidly sense the presence of protein adsorption by simply checking if there is any line broadening. In addition, we utilized EPR lineshapes to evaluate the relative crowding effects of T4L at three representative sites on various particle surfaces. Lastly, EPR offers an opportunity to probe the relative orientation of proteins on nanoparticles (see “Materials and Methods Selection”). In the PAA-(SH)_n coated AuNPs, our results showed that all sites were able to make the contact, indicating a random protein orientation in the crosslinked network. Similar findings hold for the PAA-SH coated AuNPs and AuNRs.

DLS traces are important in revealing the fine details of the particle size distribution upon coating. For example, in the absence of protein, the PAA-(SH)_n coating shows a dominant mono-modal size distribution at 95 nm (Figure 4.16). However, the relatively large standard deviation (~25.6 nm) may indicate some extent of aggregation, consistent with the findings from UV. In addition, upon adsorption of protein, the average particle size becomes much larger (307 nm). However, the size distribution is still mono-modal according to DLS traces (Figure 4.17). This indicates that relatively uniform agglomerates were generated when T4L was a medium to crosslink AuNPs with PAA-(SH)_n. Note that in some traces, there exists a minor peak (<25%) consistent with small particles (<20 nm). These particles may be caused by irregularities in the synthesis of AuNPs or polymer aggregation.

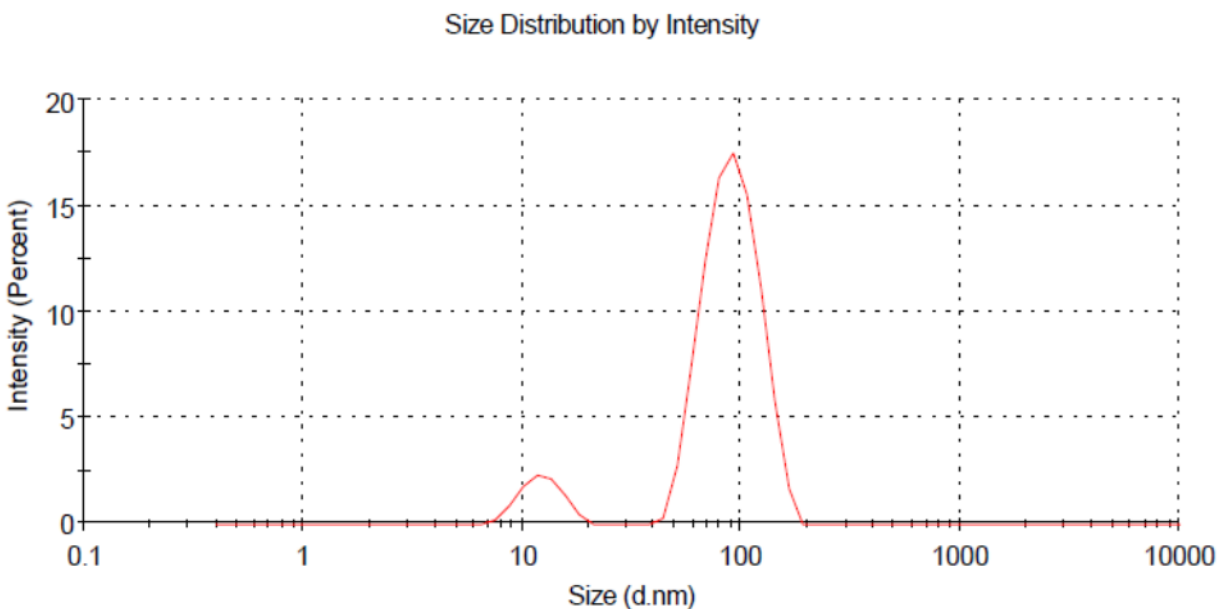


Figure 4.16. The size distribution from DLS for the AuNPs coated with PAA-(SH)_n. The dominant peak at ~95 nm contains 91 % population and a standard deviation of 25.6 nm.

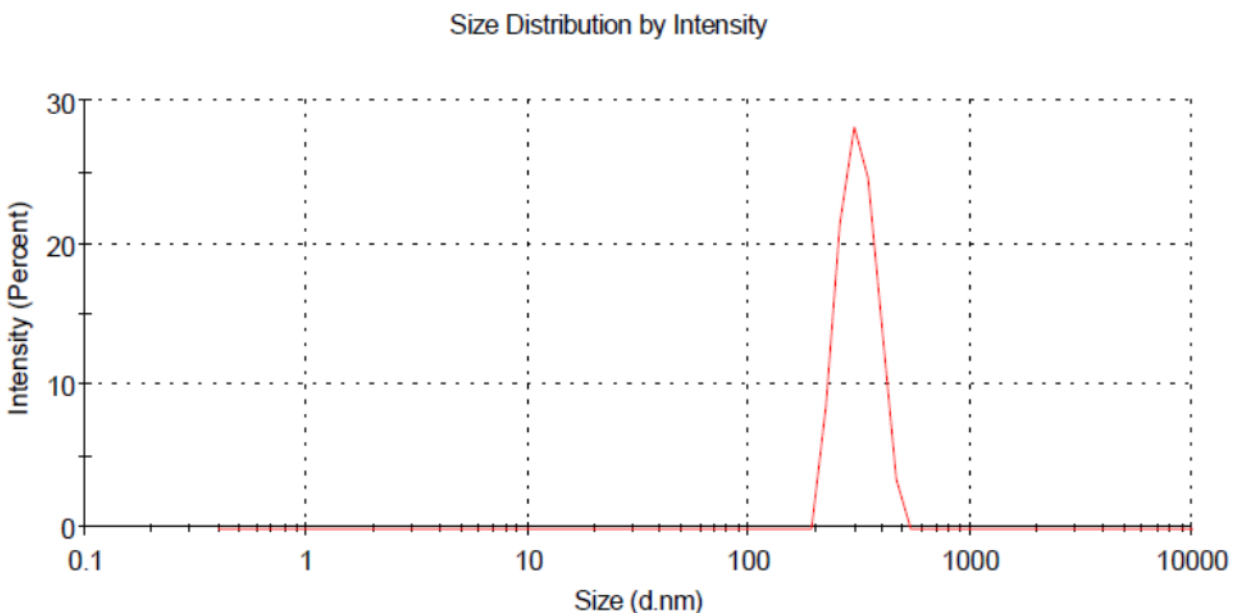


Figure 4.17. The size distribution from DLS for the AuNPs coated with PAA-(SH)_n in the presence of protein. The dominant peak at ~307 nm contains 100 % population and a standard deviation of 58.6 nm.

Conclusions

Reported here is a systematic investigation of the effects of charge and thickness of the AuNP coating on the adsorption behavior of a “problematic” globular protein, T4L. These findings are in line with the literature where polymers were used to avoid protein adsorption. Furthermore, we discovered that negative coatings with stronger coordination to the AuNP surface were also able to avoid the T4L-triggered AuNP precipitation. However, T4L was clearly adsorbed to these AuNPs. Interestingly, depending on the charge distribution and layer thickness, the resultant complexes have different morphology. On AuNPs with strong negative coatings, substantial T4L adsorption was observed which led to particle aggregation to form the agglomerates. With PAA-SH shells, the AuNPs were able to adsorb T4L to form the protein corona which showed good dispersity in solution. This result suggests that AuNPs with proper coatings can be used as protein immobilizers or carriers if the coating can help retain the structure and activity of the protein. When mixed with AuNRs, only protein corona is formed.

Lastly, we proposed molecular models to account for each case of T4L adsorption. Our findings demonstrated/highlighted the importance of surface properties on AuNP functions and effective approaches to control T4L adsorption behavior on AuNPs. With negative coatings, AuNPs/AuNRs can serve as immobilizers for carrying positively charged proteins. On the other hand, with proper coating T4L can be potentially a good biocompatible candidate to facilitate the formation of AuNP-based agglomerates which find thermotherapeutic applications.

CHAPTER 5. ENHANCING ENZYME IMMOBILIZATION ON CARBON NANOTUBES (CNTS) VIA METAL-ORGANIC FRAMEWORKS (MOFS) FOR LARGE SUBSTRATE BIOCATALYSIS[†]

Introduction

Large-substrate biocatalysis finds wide applications in the food industry, antimicrobial materials, as well as biomedicine, and, therefore, attracts great attention.^{308–310} Immobilizing the needed enzymes on solid supports improves biocatalysis by enhancing enzyme stability and cost-efficiency.^{4,311,312} It also improves enzyme storage and delivery, biosensing, and biomedicine.^{313–317} Nanoparticulates (NPs) are promising immobilization platforms due to the increased effective surface area which enhances the enzyme-substrate contact.^{161,318} The nanoscale size also makes NPs effective enzyme delivery vehicles^{317,319–321} to artificially bring in enzyme physiological functions or activate prodrugs in targeted tissues.³²² A unique NP, Carbon Nanotube (CNT), has also been applied in biocatalysis,^{323–326} molecular delivery, and biosensors.^{327,328} In addition, the weak lateral interaction between adjacent CNTs suppresses the contact of the immobilized enzymes, further enhancing enzyme stability (especially when protease enzymes are immobilized).^{103,104} Therefore, CNTs are attractive platforms for enzyme immobilization.

Anchoring enzymes to CNTs, however, faces many challenges. While most works rely on covalent bonding to provide stable attachment, this approach is challenged by the enzyme chemical modification which can perturb enzyme function.^{35,329,330} It can also be difficult to

[†] The material in this chapter was co-authored by Sunanda Neupane, Kristen Patnode, Hui Li, Kwaku Baryeh, Guodong Liu, Jinlian Hu, Bingcan Chen, Yanxiong Pan, and Zhongyu Yang. The work was previously published in ACS Applied Materials & Interfaces.¹⁰⁵ Sunanda Neupane was the primary developer of the conclusions that are advanced here. Sunanda Neupane drafted and revised all versions of this chapter. Kristen Patnode, Hui Li, Kwaku Baryeh, Guodong Liu, Jinlian Hu, Bingcan Chen, Yanxiong Pan, and Zhongyu Yang, proofread the manuscript and helped trouble shoot experimental conditions.

release the attached enzyme, limiting delivery applications and enzyme reuse/reloading for biocatalysis.^{35,329,330} Physical adsorption relying on the electrostatic, π - π stacking, and/or other hydrophobic interactions avoids chemical modifications and allows enzyme release.^{331–334} However, the weak interactions cannot prevent leaching.^{32,335}

Metal-Organic Frameworks (MOFs) offer promising potentials to immobilize enzymes without chemical modifications.^{315–317,336–341} Additional advantages include enhanced stability, reduced leaching, and retained enzyme activity.^{342–345} Thus far, most enzyme-MOF works are focused on relatively small enzymes that can fit into MOF cages; the substrate size is also small due to the small pore/window sizes of MOFs (nm). Recently, we found that large-substrate enzymes can be immobilized on the surface of a special MOF, Zeolitic Imidazolate Framework (ZIF), via “one-pot synthesis”.³⁴⁶ The immobilized enzymes were able to catalyze the degradation of bacterial cell walls (μm).³⁴⁶ However, a large number of enzymes were buried under ZIF surfaces which cannot participate in catalysis, reducing the cost-efficiency.³⁴⁶ In addition, since ZIF is pH-sensitive,³⁴⁷ it is challenging to use this approach for biocatalysis under acidic conditions. An approach which can simultaneously avoid leaching/chemical modification, enable biocatalysis under varied conditions (including acidic cases), and localize enzymes at the surface of the immobilization platform is needed.

In this work, we show an effective approach to meet all aforementioned requirements using ZIFs and one-pot synthesis. We demonstrate this approach on anchoring two model enzymes (one large and one small in size), α -amylase (typical substrate: starch) and lysozyme (typical substrate: bacterial cell walls) on CNT surfaces. By optimizing experimental conditions to form enzyme-ZIF composites on CNT surfaces (CNT-enzyme-ZIF composites), we obtained composites with negligible leaching and substantial catalytic activity using native enzymes

without any chemical modification. Both composites are stable under acidic conditions. To evaluate the amount of enzymes on CNT-ZIF surfaces and better understand the catalytic behavior of enzymes, we characterized enzyme orientation on CNTs and the exposed area of enzymes on CNT-ZIF using site-directed spin labeling (SDSL)- Electron Paramagnetic Resonance (EPR). In comparison to other biophysical techniques, SDSL-EPR is immune to the complexities caused by CNT and ZIF background signals as well as the enzyme-matrix interactions.^{177,291,346,348} SDSL-EPR reports site-specific backbone dynamics of the enzyme,^{170,177} which can depict enzyme areas that contact CNT surfaces and those exposed above or buried under the ZIF surface. This information can help assess the effectiveness of using CNT-ZIF to localize enzymes on composite surfaces which has shown an enhanced amount of enzyme on the surface comparing to pure ZIF; orientation of enzymes itself is important because it is directly related to substrate accessibility and catalytic efficiency.

To the best of our knowledge, this is the first time ZIF and one-pot synthesis are employed to anchor large-substrate enzymes on CNTs for biocatalysis. In comparison to loading enzymes to the pores of or adsorbing to the surface of pre-formed MOF-CNT composites,³⁴⁹ our approach is advantageous for stably immobilizing enzymes with arbitrary sizes. It is also the first report of enzyme orientation and structural insights on CNT and CNT-ZIF surfaces. This information is important for understanding the structure-function relationship of immobilized enzymes and guiding the rational design of CNT-ZIF composites to improve the stability, loading capacity, and catalytic efficiency of the immobilized enzymes. Our approach can be generalized to other large-substrate enzymes with arbitrary sizes and can potentially improve many fields such as antimicrobial materials' development and food processing.

Experimental Methods

Acidification of Carbon Nanotube

Multi-Walled Carbon Nanotube (MW-CNTs, 0.05 Wt/Vol %) purchased from Sigma-Aldrich (No. 755125) was mixed with 1:3 HNO₃/H₂SO₄ under sonication for a few minutes, followed by refluxing for up to 2 hr. An equal volume of mixture was taken out every hr to obtain CNTs with different acidification degrees. The acidified CNTs were then dialyzed in dd-water until the pH reached 7. These CNTs were poured into a glass plate to dry in the hood for 2 days to obtain CNTs in the powder form.

CNT Characterization

Fourier Transformation Infrared (FTIR) spectroscopy

To confirm the acidification of CNTs, FTIR spectra of the acidified CNT treated for 1 and 2 hr as well as the as-purchased CNTs were acquired with an FTIR spectrometer (Thermo Scientific Nicolet is-10) equipped with Attenuated Total Reflection (ATR) element of Smart iTX AR Diamond and an Omnic 5.1 software. CNTs were pressed tightly against the crystal plate. Both the acidified and the non-acidified CNT samples were analyzed, with each spectrum averaged for 32 scans collected from 400 to 4000 cm⁻¹. Air was run as the background for each sample and no baseline or ATR corrections were applied.

TEM sample preparation

A drop of sample was placed on a 300-mesh formvar-carbon coated copper TEM grid or lacey carbon grid (Electron Microscopy Sciences, Hatfield, Pennsylvania, USA) for 30 s and wicked off with a filter paper. Enzyme-containing samples were stained by adding 1% phosphotungstic acid (pH 7-8) to the grid for 2 minutes, then wicked off and allowed for air dry.

Images were obtained using a JEOL JEM-2100 LaB6 transmission electron microscope (JEOL USA, Peabody, Massachusetts) running at 200 kV.

Protein Expression, Purification, and Spin Labeling

Mutants of 44C, 65C, 72C, 118C and 151C were prepared as described before.²⁹¹ Briefly, the DNAs of these mutants were generated by QuikChange site-directed mutagenesis of the pET11a-T4L genetic construct containing the pseudo-wild-type mutations C54T and C97A^{186,188} followed with verification of each mutation by DNA sequencing. These mutants of T4L were expressed, purified, and then desalted (to remove DTT) into a buffer suitable for spin labeling (the “spin buffer”, containing 50 mM MOPS and 25 mM NaCl at pH 6.8). The desalted protein mutants were then reacted with a 10-fold molar excess of S-(2,2,5,5-tetramethyl-2,5-dihydro -1-Hpyrrol-3-yl) methyl methanesulfonothioate (MTSL, Toronto Research Chemicals, Inc., Toronto) at 4 °C overnight (yielding R1). Excess MTSL was removed using the Amicon spin concentrator (Millipore, 10,000 MWCO, 50 mL). The spin-labeled protein mutants were stored in the spin buffer at -20 °C for further use.

The spin-labeled mutants were confirmed to have the correct secondary structure and activity via CD spectroscopy and an activity assay, both of which were described in chapter 2 and our recent work.¹²¹ A few representative sites were characterized via CW EPR to confirm the local conformational dynamics.

CNT-T4L Complex Preparation

Typically, ~2.5 nmol of protein mutants was mixed with the acidified CNT (1mg/mL) (mutants/MWCNTs = 1.2/1) and incubated at ambient temperature in a shaker for 0.5 hr (Figure 5.1). The unattached protein was removed via centrifugation. CW EPR was conducted on the samples before and after the removal of unattached protein.



Figure 5.1. Scheme for CNT-T4L complex formation.

EPR Spectroscopy

Approximately 20 μL of the complex/composite sample was loaded into a borosilicate capillary tube (0.70 mm i.d./1.25 mm o.d.; VitroGlass, Inc.), which was mounted in a Varian E-109 spectrometer fitted with a cavity resonator. An observe power of 200 μW , modulation frequency of 100 kHz and a modulation amplitude of 1.0 G was used for the collection of all CW EPR spectra.

CNT-T4L-ZIF Composite Preparation

Dry acidified MWCNT was dispersed in 67% Methanol and 33% ddH₂O to get 0.067% CNT solution. In one-pot synthesis (Figure 5.2), 5 μL of T4L (23.5 mg/mL) was mixed with 5.5 μL Polyvinylpyrrolidone (PVP, 15 mg/mL in water) to prepare the PVP protected T4L. The complex was added to the CNT solution (100 μL , 0.067% w/v) and gently mixed. 2-methylimidazole (2.5 mL, 25 mM) and Zn(NO₃)₂ (2.5 mL, 25 mM) in methanol (MeOH) were added to the CNT solution. The mixture was vigorously stirred for 1 min, sonicated for another minute, and placed at ambient temperature for 24 hr. The opaque mixture was washed with PBS buffer (pH 7.4) for three times via centrifugation (14500 rpm for 4 min each time); the obtained pellets were dispersed in 70 μL PBS buffer and stored at 4 $^{\circ}\text{C}$.

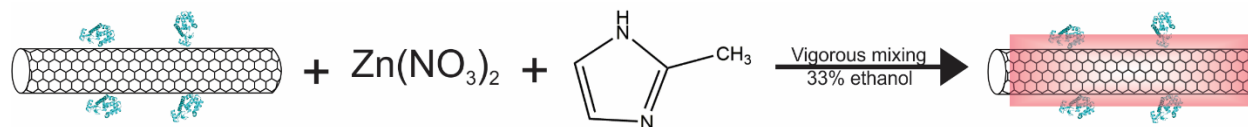


Figure 5.2. Scheme for CNT-T4L-ZIF composite formation.

Powder X-ray Diffraction (PXRD)

Single Crystal Bruker's Diffractometer, Apex II Duo with Cu $I\mu$ S X-ray source was used for Powder XRD experiment. Detector resolution was set to 1024 x 1024 pixels. Data collection strategy is shown in the table below. Apex3 v. 2017.3-0 was used to unwrap, convert and integrate the images. The final phase analysis was done on Panalytical X'Pert HighScore software.

Activity for T4L in the Complex and the Composite

The activity assay was tested using the kit purchased from Sigma-Aldrich (*Micrococcus lysodeikticus* cells, ATCC No. 4698, M3770) as described earlier.³⁴⁸ Briefly, 10 mg of the cell was suspended in 100 mL 66 mM potassium phosphate Buffer (pH = 6.2) to obtain *Micrococcus* suspension (0.01% "substrate"). Reduction in OD at 450 nm was employed to monitor the amount of active protein. Both enzyme-CNT and CNT-enzyme-ZIF samples were mixed with 66 mM potassium phosphate buffer (pH = 6.24, at 25 °C) to prepare 100 μ L (1 μ M) protein solution, one at a time. Lastly, 40 μ L of the sample mixture was added into ~1 mL of the *Micrococcus* suspension prepared as described above. The OD at 450 nm was monitored immediately using Nanodrop after the mixture formation for up to 2 hr.

Activity for α -Amylase

The activity of α -Amylase (EC 3.2.1.1) was determined using the established protocol.³⁵⁰ Soluble Starch solution (1.0% w/v) was prepared using a PBS buffer containing 20 mM sodium phosphate and 6.7 mM NaCl (pH 6.9). Color reagent solution was prepared by mixing potassium

sodium tartrate tetrahydrate solution (5.3 M) and 3,5-dinitrosalicylic acid solution (96 mM) with 12.0 mL warm water. CNT-Amylase mixture was mixed with a representative mutant at a protein-to-CNT ratio of 1.2:1. The CNT-Amylase-ZIF composite was prepared as discussed above. Both sets of samples were then diluted with ultrapure water so that protein concentration was 0.1 mg/mL in each sample. Eight samples were prepared. To 1 mL of starch solution (1.0% w/v), 1 mL of diluted CNT-Amylase or CNT-Amylase-ZIF was added and incubated for 10 min, 30 min, 1 hr, 2 hr, 3hr, 4 hr, 5 hr, and 6 hr. The color reagent solution was then added to stop the reaction at the desired time and the sample tubes were placed in boiling water bath for 15 mins. The tubes were then cooled on ice to room temperature. Ultrapure water was added to get the final volume of each sample solution to 12 mL. Absorbance of each sample was measured using NanoDrop UV-Vis Spectrophotometer (Thermo Scientific ND-2000 C) with absorbance set to 540 nm. The blank sample was prepared in the same way without adding α -Amylase.

The amount of maltose released was calculated by using the standard curve, which was prepared using the established protocol. Specifically, 1.0 mL of color reagent was added to different volumes of maltose (0.2% w/v) and water to prepare a 3 mL solution. The solution was then boiled for 15 mins and cooled on ice to room temperature. Ultrapure water (9.0 mL) was added to each solution. Absorbance of each sample was measured using NanoDrop UV-Vis Spectrophotometer (Thermo Scientific ND-2000 C) with absorbance set to 540 nm.

The amount of maltose was calculated as follow:

$$\Delta A_{540} (\text{Standard}) = A_{540} (\text{Standard}) - A_{540} (\text{Standard Blank})$$

$$\Delta A_{540} (\text{Sample}) = A_{540} (\text{Sample}) - A_{540} (\text{Sample})$$

The amount of maltose ($\mu\text{g/mL}$) released from the starch for each sample was calculated using the standard curve. Equation from the standard curve is $y = 0.00224x - 0.0148$, where y is the ΔA_{540} (Sample) and x is the concentration of maltose.

EPR Spectral Simulation

The CW EPR spectra were fit using the software developed by Dr. Altenbach and Prof. Hubbell at UCLA (<http://www.biochemistry.ucla.edu/biochem/Faculty/Hubbell/>). See Appendix for details.

Calibration of Enzyme Concentration

To perform the external standard calibration, we carried out EPR measurements on a standard TEMPO radical with three concentrations, 25, 50, and 100 μM and conducted a double-integration to each spectrum. This value is proportional to spin concentration. We then plotted the double-integration as a function of initial protein concentration and established a linear calibration curve ($R^2 \sim 0.99976$). The equation of the curve was $y = 14.37914x - 43.21$. The concentration of each hybrid sample was then estimated based on this curve.

Results and Discussions

CNT Preparation: The commercial multi-walled Carbon Nanotubes (MWCNTs) do not disperse well in water. We, therefore, acidified MWCNTs via refluxing with HNO_3 and H_2SO_4 for ~ 2 hr (see experimental methods section). Such acidification introduces carboxyl ($-\text{COOH}$) groups on CNT surfaces thus, making its surface negatively charged under neutral pH. Direct lysozyme adsorption on the acidified CNT is possible via electrostatic interactions due to the high protein isoelectric point (pI of 9.2) which makes T4L positively charged on the surface under neutral pH. Acidification of CNTs was confirmed via Fourier Transformation Infrared (FTIR) spectroscopy. The FTIR of as-purchased MWCNTs (Figure 5.3A) shows peaks at 1690

cm^{-1} , 1033 cm^{-1} , and 3790 cm^{-1} , which are assigned to the C=O, C-O, and O-H stretching, respectively.³⁵¹ The acidified CNTs show increased intensity in the O-H stretching (3678 cm^{-1} ; Figure 5.3B,C). The broad peak at $2894 \text{ cm}^{-1} - 2994 \text{ cm}^{-1}$ belongs to the O-H stretching from carboxyl groups ($\text{O}=\text{C}-\text{OH}$). The peak at 2317 cm^{-1} originates from the O-H stretching from strongly hydrogen-bonded $-\text{COOH}$. The peaks at 1730 cm^{-1} and 1044 cm^{-1} are related to C=O and C-O stretching. These data confirmed the acidification of MWCNTs. The estimated average CNT diameter is $7.2 \pm 1.5 \text{ nm}$ as judged by the Transmission Electron Microscopy (TEM) image (Figure 5.3D) using ImageJ software.³⁵²

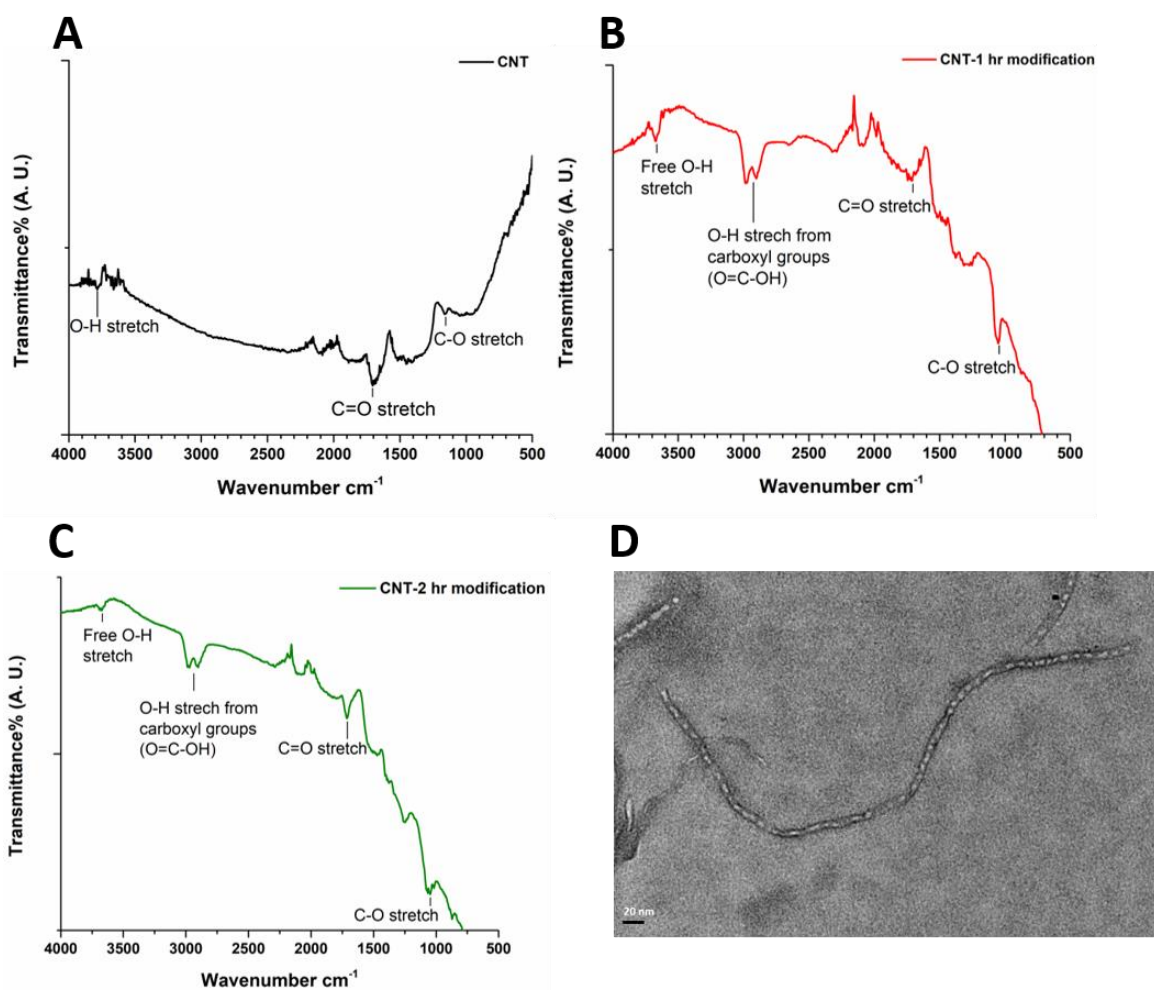


Figure 5.3. Characterization of CNTs. FTIR spectra of CNTs with (A) no acidification, (B) 1 hour acidification, and (C) 2 hour acidification. (D) TEM image of 1 hour acidified CNT.

Enzyme Immobilization on CNTs

T4 Lysozyme (T4L) is selected as a model enzyme because of its widely studied structure-function relationship using various techniques including SDSL-EPR.^{127,183,291,348} In addition, the substrate of T4L is bacterial cell walls, making T4L a good pilot enzyme for developing immobilization platforms for large-substrate enzymes.²⁹¹ The driving forces of T4L adsorption on CNT include electrostatic interaction, π - π interactions, and hydrophobic interactions.^{331,353,354}

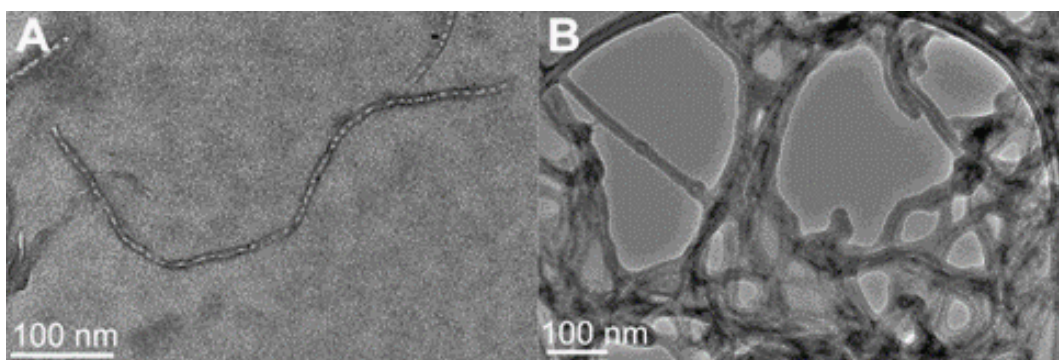


Figure 5.4. TEM images of CNTs (A) and lysozyme adsorbed to CNTs (B). The layer covering the tubes of (B) originates from the stained enzyme.

T4L mutants were prepared and characterized using established procedures. We then mixed T4L with the acidified CNTs in water at room temperature for 0.5 hrs. Upon extensive wash, the TEM image of CNT-T4L complex is shown in Figure 5.4B, wherein the presence of a dark fuzzy layer on the outside of the tube indicates the presence of the stained proteins. The diameter of the CNT-T4L complex is estimated to be 20.4 ± 0.7 nm from TEM using ImageJ software,³⁵² indicating a layer of enzymes was coated on CNTs (diameter of 7.2 nm). The activity of the enzymes adsorbed on the CNTs was measured using the commercial lysozyme activity kit (*Micrococcus lysodeikticus*, ATCC No. 4698, Sigma-Aldrich; see Experimental Section). The principle is to monitor the optical density (OD) at 450 nm of the *Micrococcus lysodeikticus* cells as T4L is added.^{355,356} A decrease in OD₄₅₀ is related to the amount of

substrate being degraded by T4L and can be used to assess T4L activity. To ensure that the same enzyme concentration was used in all activity test, we determined enzyme concentration on CNT based on the spin density determined from the EPR spectrum after a standard calibration and adjusted the final concentration of enzyme to be $\sim 5 \mu\text{M}$ for all activity assays. Our activity results (Figure 5.5) show that the complex is active (CNTs only as shown in Figure 5.5 blue triangles do not show a drop in OD at 450 nm). Although the best attempt was made to match the protein concentrations, the CNT-T4L complex still shows a lower activity. Presumably, such difference (Figure 5.5 red spheres VS black squares) is attributed to enzyme structural perturbation due to the physical contact and/or the improper orientation which blocks bacterial cell walls access to T4L active site (which will be probed below). It is also possible that nonspecific leaching occurs during sample handling in activity measurements because of the weak and nonspecific interactions between T4L and CNTs.

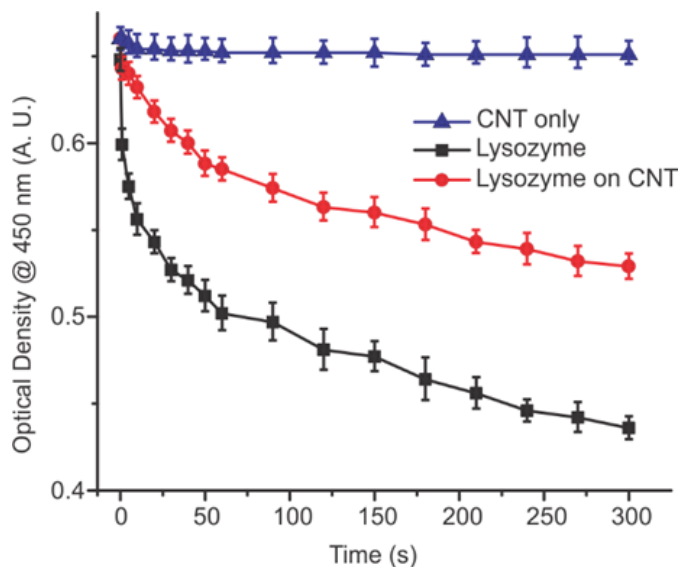


Figure 5.5. Activity assay of free lysozyme (black), lysozyme adsorbed on CNT (red), and CNT alone as a negative control (blue). Uncertainties are indicated by the error bars.

Another evidence of the weak CNT-T4L interaction is that T4L can be easily leached under “harsh” conditions. For examples, we washed CNT-T4L complex with high salt buffer

(PBS buffer with 1 M NaCl) and observed a negligible amount of adsorbed enzyme as evidenced by the low signal in CW EPR spectra (Figure 5.6 black trace) and non-detectable activity (data not shown). Herein, a representative site of T4L, 44, was spin labeled and studied using CW EPR. This result indicates that CNT-T4L complex is prone to enzyme leaching when subjected to harsh conditions.

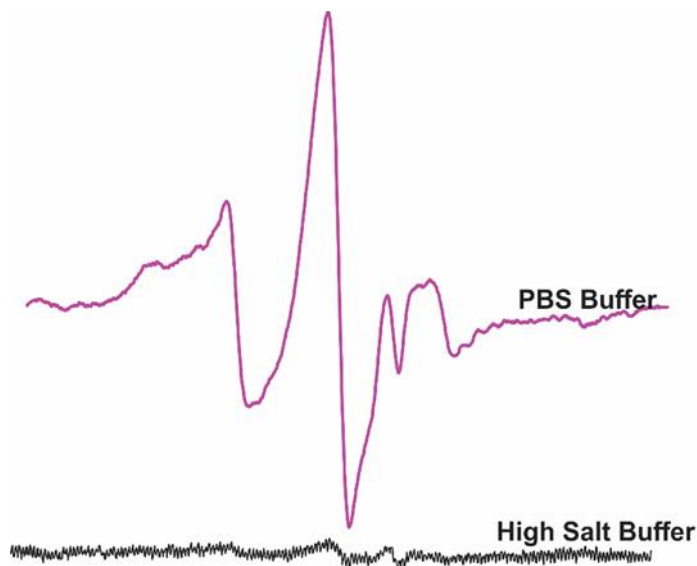


Figure 5.6. EPR spectra of CNT-T4L complex in PBS Buffer (magenta) and a high salt buffer (black).

ZIF Enhances Enzyme Loading Stability and Reduces Leaching

To enhance the stability of enzyme adsorption, we attempted the ZIF-based “one-pot” synthesis to co-crystallize T4L on CNTs with ZIF as the protection layer. The classic ZIF-8 was used in all the samples in this investigation.^{338,345,357–359} The traditional one-pot synthesis procedure,³⁴⁵ however, failed our initial attempts. For example, in MeOH, we found poor dispersity of the acidified CNTs which prevented the formation of any co-crystals, whereas in water, the amount of co-crystal formation was low. We, therefore, decided to mix water and MeOH with various ratios to improve the yield of co-crystals. A series of solvents with different water/MeOH ratios as listed in Table 5.1 were prepared. A T4L site spin-labeled with R1 (44R1)

was incubated with linear polyvinylpyrrolidone (PVP; Mw = 10000) to protect the protein from MeOH and then the enzyme/PVP was co-crystallized in each solvent. The relative loading capacity was estimated based on the signal-to-noise ratio (SNR) of the CW EPR spectrum. The principle is that the SNR of the EPR spectrum of a spin labeled CNT-enzyme-ZIF composite (after removing the unreacted enzyme) is proportional to the amount of trapped enzyme and, therefore, the loading capacity. As is evident from Table 5.1, the composites prepared in (20 - 33%) H₂O showed the highest EPR signal and loading capacity. We, therefore, utilized 33% water in the mixed solvent for all our composite sample preparation.

Table 5.1. Conditions used to optimize loading capacity of CNT-T4L-ZIF composite.

% H₂O to disperse CNT	% MeOH to disperse CNT	S/N ratio
100%	0	4
70%	30%	6
50%	50%	3
33%	67%	18
25%	75%	18
20%	80%	18

The TEM image of the CNT-T4L-ZIF composite is shown in Figure 5.7A. The enzyme was not stained because it would be difficult to differentiate ZIF from enzyme; so, the layer encapsulating CNT is ZIF. The diameter of CNT-T4L-ZIF is estimated to be 51.1 ± 28 nm from TEM using ImageJ software.³⁵² The CNT-ZIF composite without protein is shown in Figure 5.7B, wherein the layer encapsulating CNT is ZIF. The estimated average diameter for CNT-ZIF composite is 16.3 ± 1.6 nm. As the diameter of CNT-T4L-ZIF is much larger than that of CNT-ZIF only and CNT-T4L (20.4 ± 0.7 nm) only, we infer that the ZIF has encapsulated the CNT-T4L complex. EPR and later activity assay also confirmed this (see below). Powder X-ray diffraction (XRD) (Figure 5.8) results indicate that the presence of enzyme did not influence the crystal scaffold for ZIF coated on the CNT-enzyme. The diffraction patterns of the CNT-T4L-

ZIF-8 composite (red) is in agreement with that of pure ZIF-8 (blue), indicating the existence of the well-defined framework units in the synthesized composite. This confirms that CNT-T4L incorporation does not affect the formation of the ZIF-8 crystal scaffold. Also, no obvious peak of CNTs in the composite can be observed.

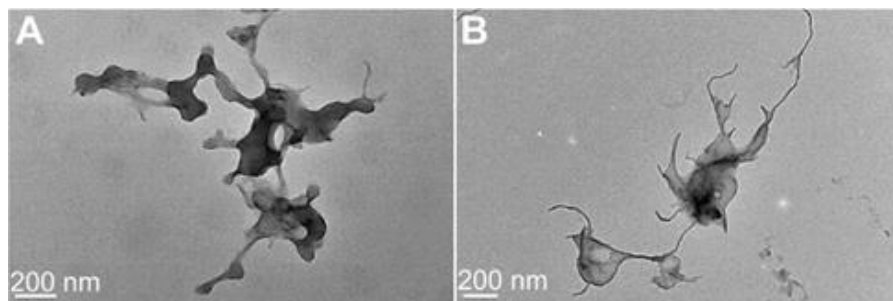


Figure 5.7. TEM images of CNT-T4L-ZIF composite (A) and CNT-ZIF without any enzyme (B).

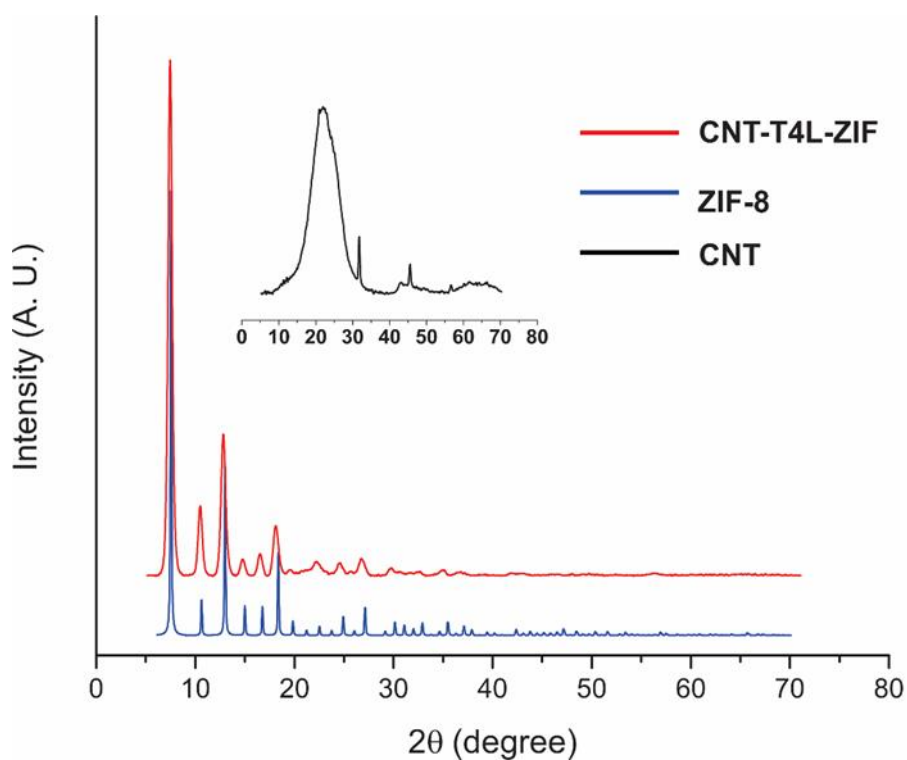


Figure 5.8. Powder XRD data of CNT (black), ZIF-8 (blue) and CNT-T4L encapsulated ZIF-8 (red) indicate that CNT-lysozyme encapsulation does not affect the crystal scaffold.

The CNT-T4L-ZIF composite is stable under harsh conditions. For example, the EPR signal of spin-labeled T4L in the composite was retained in a high salt buffer (1M NaCl) and an

organic solvent (MeOH; see Figure 5.9). The CW EPR spectrum of the composite in MeOH (Figure 5.9 cyan trace) is slightly different from that in the PBS buffer. This indicates that the spin-labeled site encounters a slightly different microenvironment upon switching the solvent to 100 % MeOH. Nevertheless, the ZIF stabilized adsorbed enzymes on CNTs in harsh conditions.

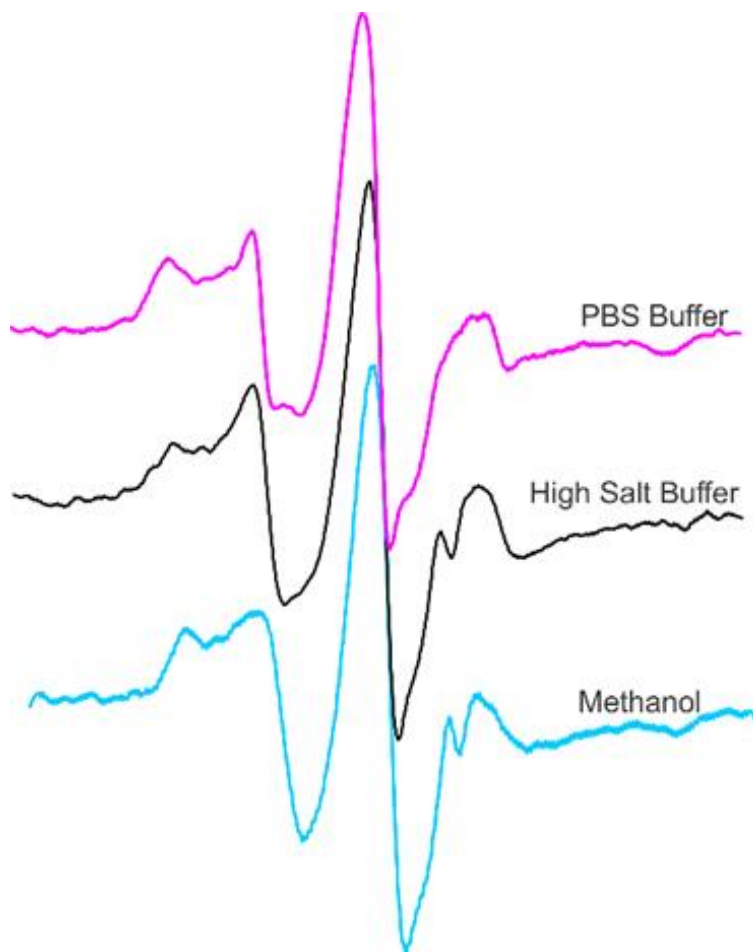


Figure 5.9. CW EPR spectra of the CNT-T4L-ZIF composite in PBS Buffer (magenta), in a high salt buffer (black), and in methanol (cyan).

To evaluate the stability of the CNT-T4L-ZIF composite under acidic conditions, we lowered the pH of the CNT-T4L-ZIF composite using acetate buffer. Interestingly, as shown in the TEM image (Figure 5.10 A and B), in low pH buffers (pH 5.5 and 3.8) only a small portion of ZIF was disassembled. CW EPR data under low pHs also showed negligible EPR signal loss (data not shown). This could be caused by the strong π - π stacking interactions between CNT and

ZIF network, which essentially enhance the stability of the ZIF network. Therefore, immobilizing enzymes on CNTs with the ZIF can overcome the weak stability of ZIF crystals under acidic conditions, which is exciting to observe and can greatly expand the applications of ZIFs to immobilize enzymes for biocatalysis applications. This property limits the release of the immobilized enzymes from CNTs, which leads to our on-going research direction of enzyme release from CNT-ZIF composites (see below discussions).

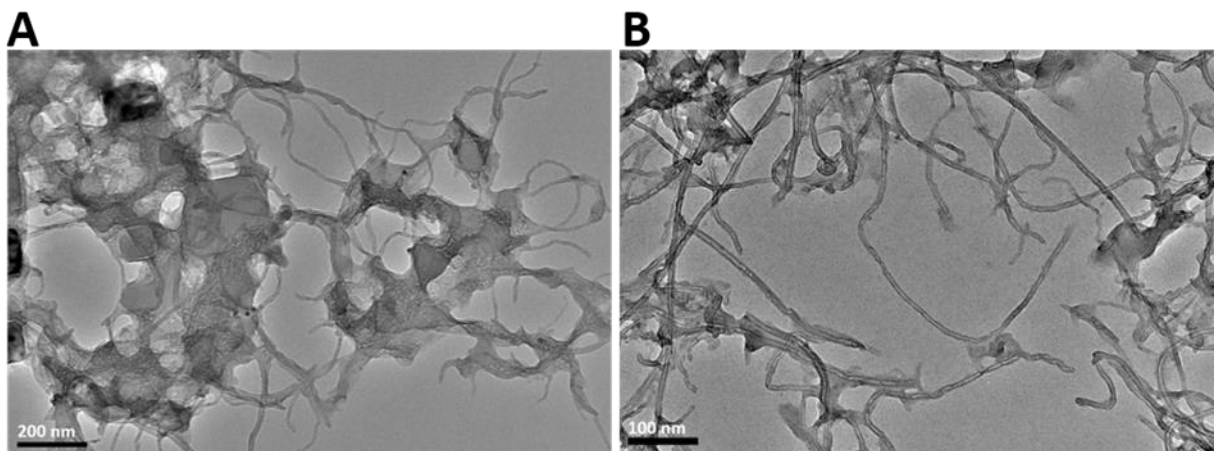


Figure 5.10. TEM images of the CNT-T4L-ZIF composite in (A) PBS Buffer at pH 5.8 and (B) Acetate Buffer at pH 3.8.

Activity of Lysozyme in CNT-T4L-ZIF Composite

Lysozyme in the CNT-T4L-ZIF composite has activity (Figure 5.11) as depicted by the decline in optical density @ 450 nm in ~ 2 hr in comparison to the CNT-ZIF composite alone (Figure 5.11 green squares) which does not show such decline. In comparison to T4L in a buffer, the significantly reduced activity is possibly because only a small portion of active sites were exposed to the surface of CNT-ZIF (with the rest buried under the surface). This is essentially why it took ~ 2 hr for T4L to break the cell walls compared to 5 mins for T4L alone. The activity of the CNT-T4L-ZIF composites shows a concentration dependence, wherein more composites showed more OD 450 drop (see Figures 5.11 and 5.12; magenta = 6X concentration; blue =

1.5X; red =1X; 1X= $\sim 1 \mu\text{M}$ enzyme concentration). Our attempts to further increase the composite concentration failed because high CNT concentrations caused strong scattering effects in our OD measurements. Nevertheless, our results show that the CNT-enzyme-ZIF composites are functionally active.

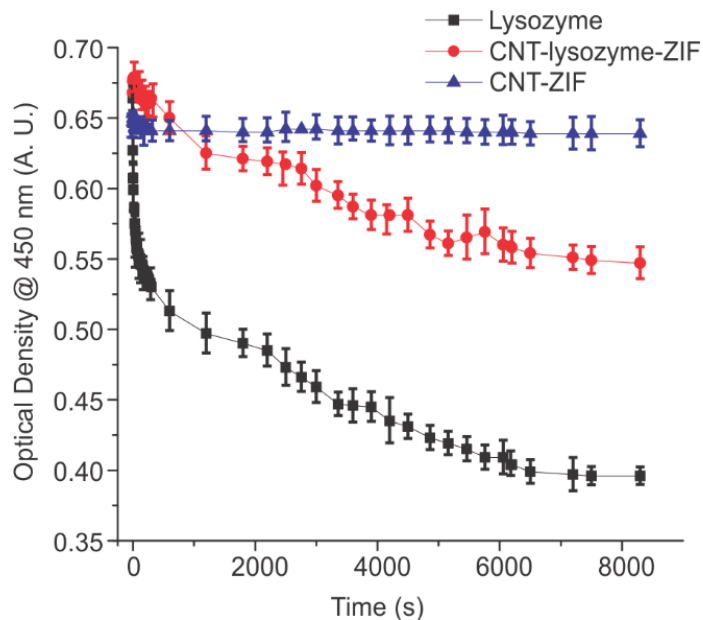


Figure 5.11. Activity assay of CNT- ZIF as a negative control (blue), free lysozyme (black), and lysozyme on CNT-ZIF composites (red). Uncertainties are indicated by the error bars.

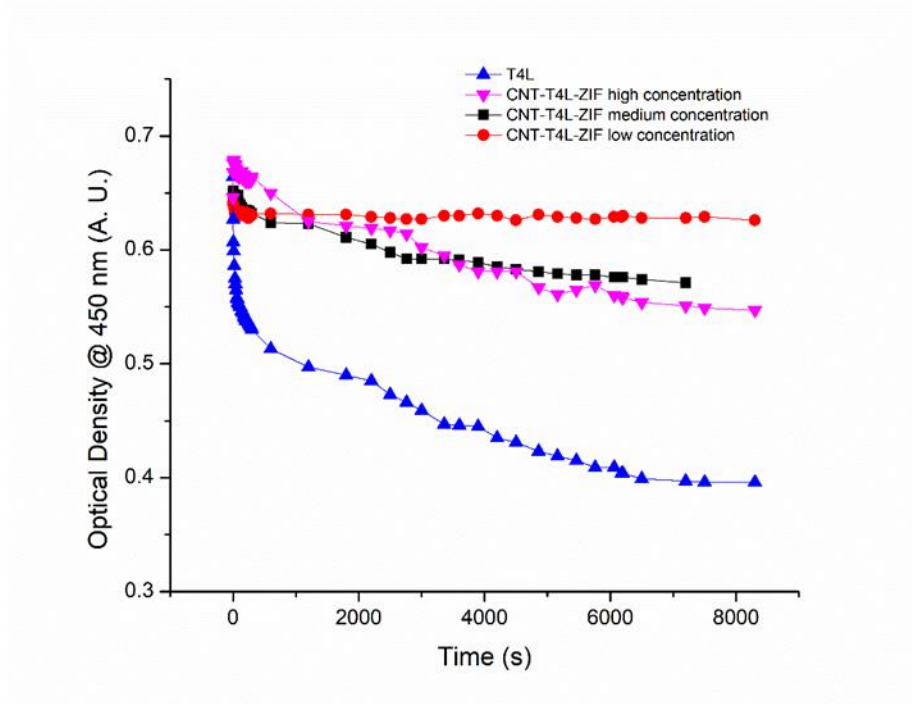


Figure 5.12. The activity assay of T4L free (blue), on CNT-T4L-ZIF composite high concentration (magenta), medium concentration (black), and low concentration (red).

Application to Amylase on Starch Degradation

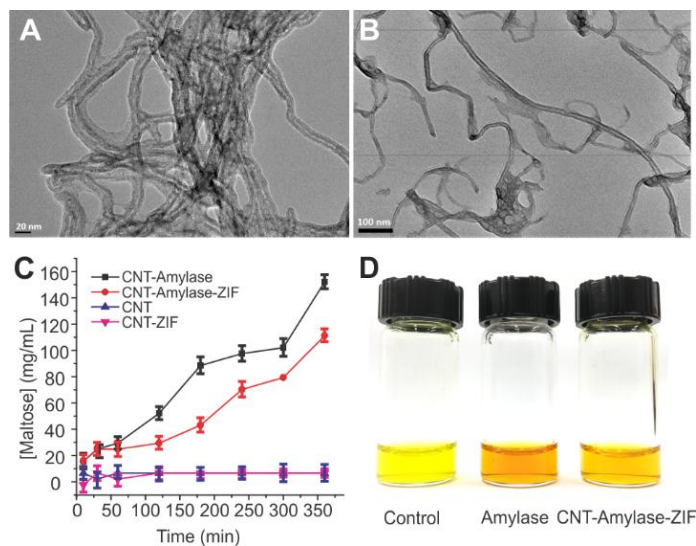


Figure 5.13. TEM images of CNT-amylose complex (A) and CNT-amylose-ZIF composite (B). (C) The activity assay of amylase on CNTs (black squares) and in CNT-amylose-ZIF composites (red circles). The controls for the activity assay are CNT only (blue triangles) and CNT-ZIF (purple triangles). Uncertainties are indicated by the error bars. (D) Direct visualization of starch digestion using the protocol described in the main text. Free amylase generates more maltose (middle) comparing to amylase in CNT-ZIF composites (right).

Upon successful encapsulation of T4L on CNT with ZIF, we intended to generalize this approach to a different enzyme (still with large substrates). To do so, we formed the CNT- α -amylase-ZIF composite. α -Amylase (51 kDa; pI \sim 5.25) was selected because of its opposite surface charge (compared to T4L) and a wide range of application in food, fermentation, and pharmaceutical industries.³⁶⁰⁻³⁶³ The TEM image of the CNT- α -amylase complex (with enzyme stained) shows the fuzzy layer (Figure 5.13A), indicating enzyme adsorption on CNTs. On CNT- α -Amylase -ZIF composites, spots of ZIF formation are visible (Figure 5.13B) indicating the success in coating CNT with ZIF. Here, the enzyme was not stained due to the reasons discussed above. The CNT-amylase-ZIF composite was stable under high-salt and low-pH conditions as judged by TEM images (data not shown), further confirming the effectiveness of using ZIF to stabilize enzymes on CNTs. The presence of α -amylase was also confirmed with the activity assay.

For the activity assay, we utilized the commercial α -amylase activity kit following the principles reported earlier.³⁵⁰ In brief, α -Amylase degrades starch to maltose and dextrin. 3,5-dinitrosalicylic acid (DNS) was then used to react with the formed maltose which reduces the pale-yellow colored alkaline DNS to the orange-red colored, 3-Amino-5-nitrosalicylic acid, the latter of which has an absorbance at 540 nm. By monitoring the intensity of the 540 nm absorption over time, one is able to probe the amount of active α -amylase in a sample. We found active α -amylase in the both CNT-amylase complex and the CNT-amylase-ZIF over a 6 hr period (Figure 5.13C). The amount of maltose produced in CNT-amylase-ZIF (red trace Figure 5.13C) is less than that of CNT-amylase complex (black trace Figure 5.13C), likely because only a portion of α -amylase can be exposed on the surface of the CNT-ZIF while the rest is buried under the ZIF surface. In the absence of amylase, no activity can be detected for CNT and CNT-

ZIF (blue and magenta trace Figure 5.13C). An interesting finding is that the CNT-amylase complexes precipitate overtime but no such precipitation for the CNT-ZIF composites was observed. The same is true for lysozyme complexes. This may indicate that ZIF can help improve the dispersity of the composites, which can help practical applications wherein precipitation needs to be avoided.

Structural Basis of Large-substrate Enzyme Activity in ZIF Scaffolds

To probe site-specific enzyme dynamics and obtain molecular-level information on the behavior of enzyme on the CNT and in the CNT-ZIF composites, we created 6 cysteine mutants on T4L scanning most of its solvent accessible surfaces (Figure 5.14A) and confirmed that all mutants were functionally active and have the native secondary structure after spin-labeling. Then, the CNT-T4L complex and CNT-T4L-ZIF composite for each mutant were prepared as described and characterized before. Continuous Wave (CW) EPR measurements on each complex and composite in PBS buffer at pH 7.4 were carried out and the results are shown in Figure 5.14. For all sites, we see three major regions in the first derivative format, the low-, mid-, and high-field spectrum, due to the hyperfine splitting. The high-field peaks are too wide with a low signal-to-noise ratio (SNR), while the mid-field peaks lose fine details of splitting due to its narrow linewidth. We, therefore, focus our discussion on the low-field region, wherein we categorize the peak into two components, the mobile and the immobile component (see “m” and “im” shades of Figure 5.14). Each component reports the net effect of three motions, protein rotational tumbling, backbone dynamics, and intrinsic motion of the spin label.^{120,177} Both the medium (temperature, buffer pH, viscosity) and the surrounding environment (nearby residues, synthetic materials) can influence these three factors, leading to useful structural insights. In detail, the “im” component, which is often consistent with a highly restricted spin label motion,

originates from a label in contact with surrounding species (ca. CNT surfaces or ZIF scaffolds). The “m” component, on the other hand, often results from the labeled site not in contact with any species. Therefore, measuring the relative contribution of each component in a spectrum can detect the chance for each labeled site to make contact with CNT surfaces, which can be used to derive enzyme orientation on CNTs, or the possibility for each labeled site not in contact with any species (exposed to the solvent), which can report regions of enzyme exposed to reaction medium.

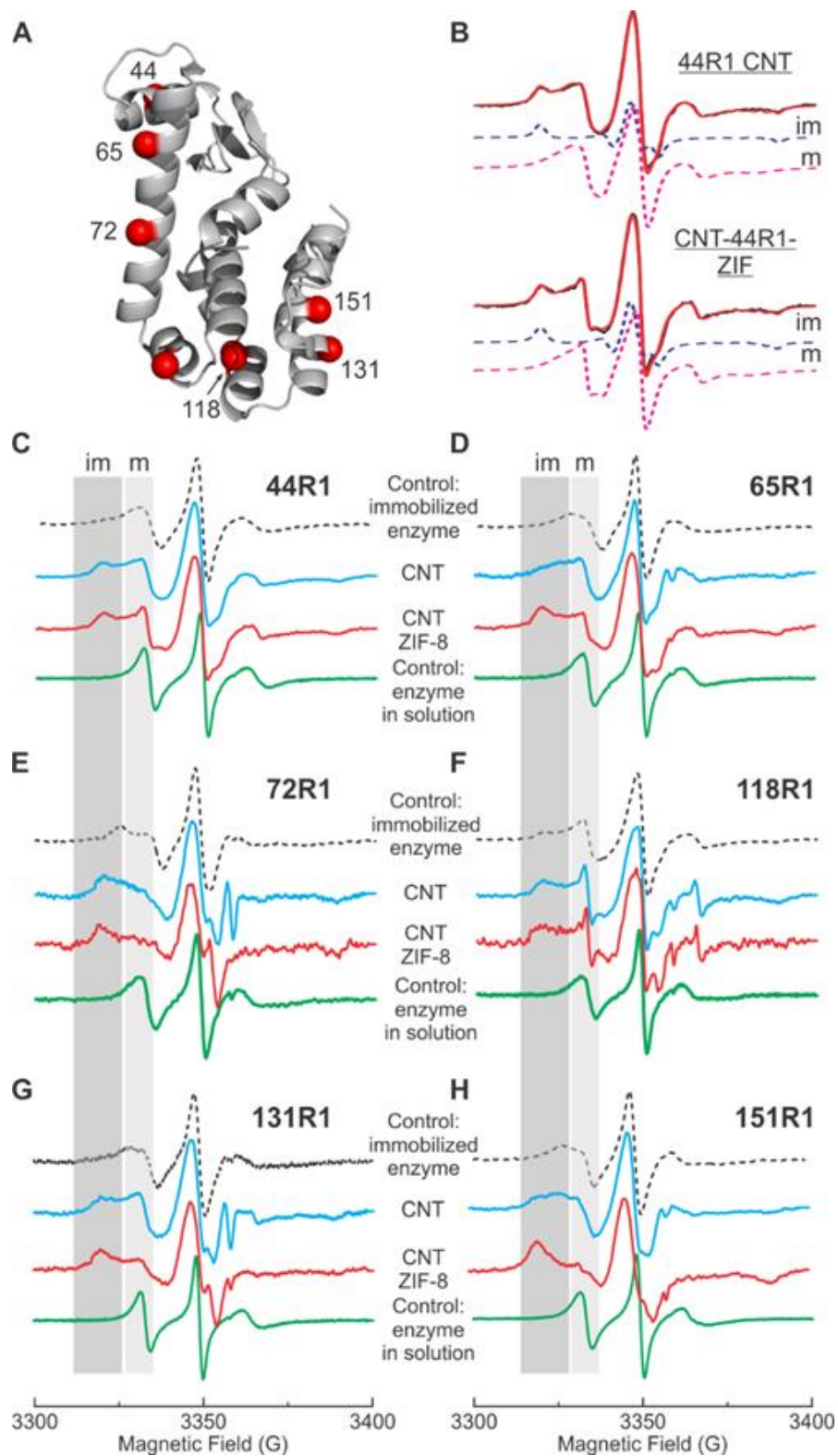


Figure 5.14. (A) Representative surface sites of T4L spin-labeled with R1. (B) Example spectral simulations of the mobile and immobile components of a labeled site in two matrices. (C–H) CW EPR spectra of six labeled sites in different matrices.

The EPR spectra of all mutants (44R1, 65R1, 72R1, 118R1, 131R1, and 151R1) upon adsorption to CNT are shown in blue curves of Figure 5.14C-H. In comparison to the same mutants in buffer (Figure 5.14 green traces), all mutants on CNTs show broadening, consistent with the restriction of the rotational tumbling due to physical adsorption. In comparison to the same mutants attached to a solid surface (but no direct enzyme-surface contact; Figure 5.14 dotted traces), the mutants on CNTs also show various extents of broadening, indicating the presence of additional contact of the labeled sites with the surface of CNTs, as indicated by the “im” peaks. The “im” may also be caused by crowding, although we believe this possibility is low due to the low sample concentrations as judged by the low SNR of most spectra. In comparison to the dotted curves, 44R1, 72R1, and 131R1 (blue *VS* dots) show additional broadening, indicating that these sites are responsible for making contact with CNT surfaces. Therefore, the orientation of the enzyme on CNTs is proposed as shown in Figure 5.16A. These orientations are likely caused by π - π stacking and other hydrophobic interactions as well as electrostatic interactions (herein, the CNT surface is negatively charged). Specifically, 131R1 is located near the C-terminus, where more aromatic rings exist which tend to form more π - π stacking interactions with CNT (Figure 5.15).³³²⁻³³⁴ 44R1 and 72R1 have less number of aromatic rings nearby but are surrounded by some positively charged residues (see Figure 3.12).²⁹¹ All signals can be washed off with the high salt buffer, consistent with the weak physical adsorption of the enzyme to CNTs.

To quantify the relative population of the “im” component, or the amount of enzyme making contact with CNT surfaces, we attempted spectral simulations based on algorithms established by Freed and coworkers (for details see Appendix).²⁹³ Our best attempts showed that the two-component fitting (“im” and “m”, corresponding to the labeled site in contact or hanging

in solution, respectively) were successful for only four sites (44R1, 72R1, 118R1, and 131R1). The other two sites (65R1 and 151R1) showed heterogeneous spectra, indicating these two sites can contact the CNT in multiple ways. This is reasonable since the contact of the enzyme with CNTs is mostly non-specific. The best-fit parameters are provided in Table A3 in Appendix.

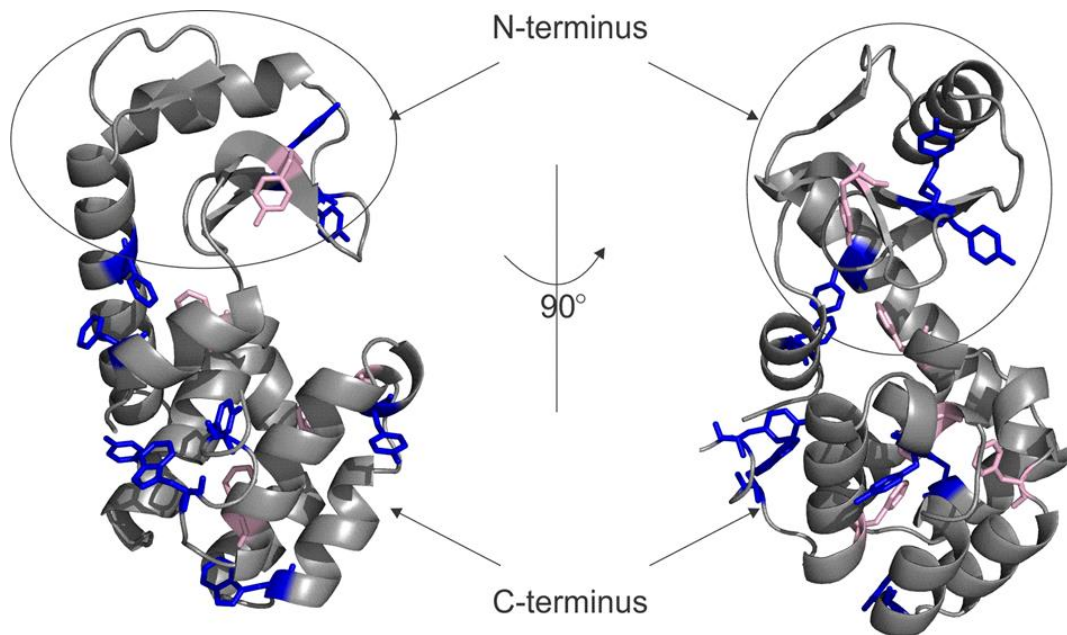


Figure 5.15. Aromatic residues of T4L from two views. There are more solvent-exposed aromatic residues (blue sticks) in the C-terminus than in the N-terminus. Buried aromatic residues are shown in light pink sticks.

In the case of CNT-T4L-ZIF composite, we found that 44R1, 65R1, and 118R1 showed a high mobile component as judged by spectral simulations (see Table A4 of the Appendix), indicating these sites have a higher chance to be exposed to the solvent while other sites are more preferred to be buried under ZIF surfaces. The proposed orientation model is shown in Figure 5.16B. The higher chance of exposure of 44R1, 65R1, and 118R1 is consistent with our recent findings on enzyme trapped on ZIF-8 surfaces.³⁴⁶ The rationalization of our finding is also similar, wherein steric hindrance and π - π stacking interactions play a major role in orientation preference. 151R1 and 131R1 are located near the C-terminus, where more aromatic rings exist

which tend to form more π - π stacking interactions with ZIF imidazole rings and bury the nearby regions. 44R1 is located near the N-terminus and tends to be exposed more to the solvent. 118R1 is also exposed more to the solvent; this orientation preference tends to bury more aromatic residues. Remarkably, in comparison to the 30-40% chance of exposing the same three sites (44R1, 65R1, and 118R1) on pure ZIF crystal surfaces,³⁴⁶ encapsulating the same enzyme mutants on CNT-ZIF exposes ~60 % of the three sites. Furthermore, the rest of the labeled sites also showed an enhanced chance of exposure (from 12-30% to ~40%; see Table 5.2). These findings indicate that CNTs can serve as effective seeds on which ZIF crystals can grow so that enzymes are more likely to be localized on materials surfaces. This approach reduces the number of enzymes buried inside of pure ZIF crystals,³⁴⁶ and has, therefore, promising potential to optimize enzyme positions in solid supports for active site exposure, which is especially useful for large-substrate biocatalysis.

Table 5.2. Relative probability of each labeled site to be exposed to the solvent in ZIF crystals and CNT-enzyme-ZIF composites. *=data from reference.³⁴⁶ Grey=sites with a high chance to be exposed to the solvent.

	44R1	65R1	72R1	118R1	131R1	151R1
ZIF*	35%	41%	29%	44%	25%	12%
CNT-ZIF	61.3%	59.4%	37.9%	57.3%	44.8%	45.2%

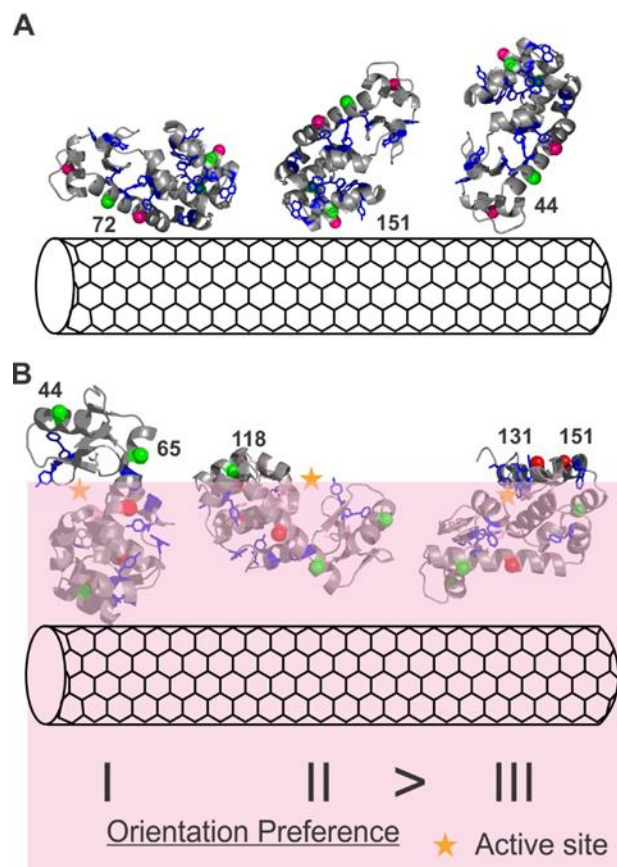


Figure 5.16. (A) Three sites (44, 72, 131) show a higher chance to make contact with CNT surface, based on which the preferred orientations of enzymes on CNTs are proposed. (B) Proposed enzyme orientations on CNT-ZIF surface. Orientations I and II are more preferred than III.

Future Directions

In principle, encapsulating enzymes on the surface of other NPs can also help increase the number of enzymes exposed to solid support surfaces. However, most NPs do not have the extensive aromatic ring network to help stabilize ZIF scaffolds under acidic conditions. Therefore, we will focus our future work mostly on CNTs. While our findings provide evidence that combining ZIF and CNT is effective in simultaneously enhancing enzyme stability under harsh conditions (high salt and acidic conditions), reducing leaching, reducing enzyme waste (when buried below solid surfaces), and retaining activity, there are still a few more steps required to broaden the application of this approach. For example, although enzyme leaching can

be prevented even under acidic conditions, if the enzyme needs to be released for reloading/reuse or delivery applications, it is necessary to modify the ZIF composition so that controlled release of enzymes can be achieved. This is one of our on-going research directions. In addition, the loading capacity at this preliminary stage is relatively low. As judged by the spin density of the spectra of the same mutant on the two platforms, the enzyme concentration was reduced from $\sim 45 \mu\text{M}$ on CNT to $\sim 29 \mu\text{M}$ in CNT-ZIF, confirming the low loading capacity. Approaches to improve the amount of encapsulated enzymes are needed. Lastly, being able to reveal the enzyme orientation is not the end of the story. Knowing this information is the first step to optimize enzyme orientation so that more trapped enzyme molecules can expose their active sites to the CNT-ZIF surfaces, in order to improve the catalytic activity. The system can be applied to encapsulate small-substrate enzyme as well since the one-pot synthesis can be applied to enzymes regardless of their size, surface charge, and substrate size. In fact, the catalytic efficiency may be higher for small-substrate enzymes encapsulated on our CNT-ZIF system as the enzymes partially buried below ZIF surface can participate in interaction with the small substrates which can diffuse into the ZIF pores. The advantage of having CNT is to stably host small-substrate enzymes even under acidic conditions

Conclusions

In this work, we show an effective approach to anchor large-substrate enzymes on the surface of CNTs using ZIF and one-pot synthesis. This method was proved using two model enzymes, T4L and α -amylase, both of which showed enhanced stability, reduced leaching, and retained catalytic activity. This effort essentially solves the leaching problem of physically adsorbing enzymes to CNTs. The CNT-enzyme-ZIF is stable even under acidic pHs, which overcomes the low pH-stability of ZIF alone. Both enzymes on CNT-ZIF composites were

catalytically active, indicating that a portion of the enzyme is exposed to the solvent as both enzymes have large substrates. To better depict the enzyme structural basis of activity and enzyme orientation, we employed SDSL-EPR to probe the enzyme-exposed area and site-specific backbone dynamics on CNT-T4L complexes and CNT-T4L-ZIF composites. Our results show that on CNT-ZIF, three sites, 44R1, 65R1, and 118R1, were more likely to be exposed to the solvent above the surface of ZIF. In comparison to the ZIF crystal alone, all labeled enzyme sites on our CNT-ZIF composites show a higher chance of exposure to the solvent, indicating that encapsulating enzymes on CNTs via ZIF is an effective approach to localize enzymes on crystal surfaces to improve large-substrate contact and, therefore, catalytic efficiency. Based on this, a few preferred enzyme orientations on the CNT-ZIF surface were proposed. Our enzyme immobilization method can be generalized to other enzymes with arbitrary sizes. Our approach to probe enzyme orientation and key structural insights of CNT-enzyme-ZIF composites regardless of the complexities of the matrices will guide the rational design of CNT/ZIF combinations to improve enzyme stabilization, loading capacity, and catalytic efficiency.

CHAPTER 6. CONCLUSION

This dissertation aims to use SDSL-EPR to reveal the structure-function relationship of enzymes immobilized on NPs. This information can be utilized to fine-tune enzyme-NP complexes as the enzyme carrier for biocatalysis, therapeutics, and industrial uses. EPR was successfully used to probe the structure and orientation of enzyme in different nanoparticle-enzyme complex and in the nanoparticle-enzyme-ZIF composite. The study of the interaction of enzyme, T4L, with different nanoparticles, showed that the nanoparticle-enzyme interaction is nanoparticle/enzymes dependent and varies with nanoparticles and enzymes. The goals of understanding the structure-function relationship of the enzymes to 1) avoid NP aggregation and 2) optimize NPs as enzyme carrier were met.

The findings in AuNP-T4L study portrayed the mechanism of T4L triggered AuNP aggregation which led to changing the charge and coating of AuNP/AuNR to prevent aggregation. This change in coating demonstrated that AuNPs with proper coatings can be used as protein immobilizer or carriers if the coating can help retain the structure and the activity of the protein. In addition, the SiNP-T4L study elucidated the structural basis of activity loss of T4L on SiNPs. The enzyme activity loss upon adsorption to SiNPs needs to be reduced to use SiNPs as the enzyme hosts; the obtained structural information helps guide the process of optimizing SiNPs as the enzyme carrier. Finally, all these findings provided the basis to develop novel, effective approach to anchor large-substrate enzymes, T4L, and α -amylase on the surface of CNTs using ZIF and one-pot synthesis. Both enzymes showed, reduced leaching and retained catalytic activity. CNT was successfully optimized as an enzyme carrier.

Overall the results and fundamental studies discussed in this dissertation demonstrate the usefulness of the EPR spectroscopy in probing the complexes formed by nanomaterials and

macromolecules, emphasizing an approach to probe the nano-bio interface in the native state. Also, the methods and approaches discussed here can be applied to other enzymes and nanomaterials. Likewise, the results in this dissertation will guide the rational development of enzyme-NP complexes to improve catalytic efficiency, cost efficiency, loading capacity, enzyme reusability, and enzyme stability. Enzyme-NP complexes have broader applications in food industry, biosensing, biocatalysis, drug delivery, biomedicine, biodiesel, and many other areas.

REFERENCES

- (1) Homaei, A. A.; Sariri, R.; Vianello, F.; Stevanato, R. Enzyme Immobilization: An Update. *J. Chem. Biol.* **2013**, *6* (4), 185–205. <https://doi.org/10.1007/s12154-013-0102-9>.
- (2) Hartmann, M.; Jung, D. Biocatalysis with Enzymes Immobilized on Mesoporous Hosts: The Status Quo and Future Trends. *J. Mater. Chem.* **2010**, *20* (5), 844–857. <https://doi.org/10.1039/B907869J>.
- (3) Barry, J. N.; Vertegel, A. A. Nanomaterials for Protein-Mediated Therapy and Delivery. *Nano Life* **2013**, *03* (04), 1343001. <https://doi.org/10.1142/s1793984413430010>.
- (4) Ding, S.; Cargill, A. A.; Claussen, J. C.; Medintz, I. L.; Claussen, J. C. Increasing the Activity of Immobilized Enzymes with Nanoparticle Conjugation. *Curr. Opin. Biotechnol.* **2015**, *34*, 242–250. <https://doi.org/http://dx.doi.org/10.1016/j.copbio.2015.04.005>.
- (5) Garcia-Galan, C.; Berenguer-Murcia, Á.; Fernandez-Lafuente, R.; Rodrigues, R. C. Potential of Different Enzyme Immobilization Strategies to Improve Enzyme Performance. *Advanced Synthesis and Catalysis*. 2011, pp 2885–2904. <https://doi.org/10.1002/adsc.201100534>.
- (6) Gomes-Ruffi, C. R.; Cunha, R. H. da; Almeida, E. L.; Chang, Y. K.; Steel, C. J. Effect of the Emulsifier Sodium Stearoyl Lactylate and of the Enzyme Maltogenic Amylase on the Quality of Pan Bread during Storage. *LWT* **2012**, *49* (1), 96–101. <https://doi.org/10.1016/j.lwt.2012.04.014>.
- (7) Jaros, D.; Partschefeld, C.; Henle, T.; Rohm, H. Transglutaminase in Dairy Products: Chemistry, Physics, Applications. *J. Texture Stud.* **2006**, *37* (2), 113–155. <https://doi.org/10.1111/j.1745-4603.2006.00042.x>.

- (8) Ismail, B.; Nielsen, S. S. Invited Review: Plasmin Protease in Milk: Current Knowledge and Relevance to Dairy Industry. *J. Dairy Sci.* **2010**, *93* (11), 4999–5009.
<https://doi.org/10.3168/JDS.2010-3122>.
- (9) Bai, Y.; Huang, H.; Meng, K.; Shi, P.; Yang, P.; Luo, H.; Luo, C.; Feng, Y.; Zhang, W.; Yao, B. Identification of an Acidic α -Amylase from *Alicyclobacillus* Sp. A4 and Assessment of Its Application in the Starch Industry. *Food Chem.* **2012**, *131* (4), 1473–1478. <https://doi.org/10.1016/j.foodchem.2011.10.036>.
- (10) Schückel, J.; Matura, A.; van Pée, K.-H. One-Copper Laccase-Related Enzyme from *Marasmius* Sp.: Purification, Characterization and Bleaching of Textile Dyes. *Enzyme Microb. Technol.* **2011**, *48* (3), 278–284.
<https://doi.org/10.1016/J.ENZMICTEC.2010.12.002>.
- (11) Hakala, T. K.; Liitiä, T.; Suurnäkki, A. Enzyme-Aided Alkaline Extraction of Oligosaccharides and Polymeric Xylan from Hardwood Kraft Pulp. *Carbohydr. Polym.* **2013**, *93* (1), 102–108. <https://doi.org/10.1016/J.CARBPOL.2012.05.013>.
- (12) Subba Rao, C.; Sathish, T.; Ravichandra, P.; Prakasham, R. S. Characterization of Thermo- and Detergent Stable Serine Protease from Isolated *Bacillus Circulans* and Evaluation of Eco-Friendly Applications. *Process Biochem.* **2009**, *44* (3), 262–268.
<https://doi.org/10.1016/j.procbio.2008.10.022>.
- (13) Soldatkin, O. O.; Kucherenko, I. S.; Pyeshkova, V. M.; Kukla, A. L.; Jaffrezic-Renault, N.; El'skaya, A. V.; Dzyadevych, S. V.; Soldatkin, A. P. Novel Conductometric Biosensor Based on Three-Enzyme System for Selective Determination of Heavy Metal Ions. *Bioelectrochemistry* **2012**, *83*, 25–30.
<https://doi.org/10.1016/J.BIOELECHEM.2011.08.001>.

- (14) Apetrei, I. M.; Rodriguez-Mendez, M. L.; Apetrei, C.; de Saja, J. A. Enzyme Sensor Based on Carbon Nanotubes/Cobalt(II) Phthalocyanine and Tyrosinase Used in Pharmaceutical Analysis. *Sensors Actuators B Chem.* **2013**, *177*, 138–144. <https://doi.org/10.1016/j.snb.2012.10.131>.
- (15) Das, R.; Ghosh, S.; Bhattacharjee, C. Enzyme Membrane Reactor in Isolation of Antioxidative Peptides from Oil Industry Waste: A Comparison with Non-Peptidic Antioxidants. *LWT* **2012**, *47* (2), 238–245. <https://doi.org/10.1016/j.lwt.2012.01.011>.
- (16) Atadashi, I. M.; Aroua, M. K.; Aziz, A. A. High Quality Biodiesel and Its Diesel Engine Application: A Review. *Renew. Sustain. Energy Rev.* *14*, 1999–2008. <https://doi.org/10.1016/j.rser.2010.03.020>.
- (17) Luo, K.; Yang, Q.; Yu, J.; Li, X.; Yang, G.; Xie, B.; Yang, F.; Zheng, W.; Zeng, G. Combined Effect of Sodium Dodecyl Sulfate and Enzyme on Waste Activated Sludge Hydrolysis and Acidification. *Bioresour. Technol.* **2011**, *102* (14), 7103–7110. <https://doi.org/10.1016/J.BIORTECH.2011.04.023>.
- (18) Tonini, D.; Astrup, T. Life-Cycle Assessment of a Waste Refinery Process for Enzymatic Treatment of Municipal Solid Waste. *Waste Manag.* **2012**, *32* (1), 165–176. <https://doi.org/10.1016/J.WASMAN.2011.07.027>.
- (19) Tong, Z.; Qingxiang, Z.; Hui, H.; Qin, L.; Yi, Z. Removal of Toxic Phenol and 4-Chlorophenol from Waste Water by Horseradish Peroxidase. *Chemosphere* **1997**, *34* (4), 893–903. [https://doi.org/10.1016/S0045-6535\(97\)00015-5](https://doi.org/10.1016/S0045-6535(97)00015-5).

- (20) van de Velde, F.; Lourenço, N. D.; Pinheiro, H. M.; Bakker, M. Carrageenan: A Food-Grade and Biocompatible Support for Immobilisation Techniques. *Adv. Synth. Catal.* **2002**, *344* (8), 815–835. [https://doi.org/10.1002/1615-4169\(200209\)344:8<815::AID-ADSC815>3.0.CO;2-H](https://doi.org/10.1002/1615-4169(200209)344:8<815::AID-ADSC815>3.0.CO;2-H).
- (21) Kress, J.; Zanaletti, R.; Amour, A.; Ladlow, M.; Frey, J. G.; Bradley, M. Enzyme Accessibility and Solid Supports: Which Molecular Weight Enzymes Can Be Used on Solid Supports? An Investigation Using Confocal Raman Microscopy. *Chem. - A Eur. J.* **2002**, *8* (16), 3769. [https://doi.org/10.1002/1521-3765\(20020816\)8:16<3769::AID-CHEM3769>3.0.CO;2-V](https://doi.org/10.1002/1521-3765(20020816)8:16<3769::AID-CHEM3769>3.0.CO;2-V).
- (22) Villeneuve, P.; Muderhwa, J. M.; Graille, J.; Haas, M. J. Customizing Lipases for Biocatalysis: A Survey of Chemical, Physical and Molecular Biological Approaches. *J. Mol. Catal. - B Enzym.* **2000**, *9*, 113–148. [https://doi.org/10.1016/S1381-1177\(99\)00107-1](https://doi.org/10.1016/S1381-1177(99)00107-1).
- (23) Pessela, B. C. C.; Dellamora-Ortiz, G.; Betancor, L.; Fuentes, M.; Guisán, J. M.; Fernandez-Lafuente, R. Modulation of the Catalytic Properties of Multimeric β -Galactosidase from *E. Coli* by Using Different Immobilization Protocols. *Enzyme Microb. Technol.* **2007**, *40* (2), 310–315. <https://doi.org/10.1016/j.enzmictec.2006.04.015>.
- (24) Hiep Nguyen, H.; Kim, M. An Overview of Techniques in Enzyme Immobilization. *Appl. Sci. Conver. Technol* **2017**, *26* (6), 157–163. <https://doi.org/10.5757/ASCT.2017.26.6.157>.
- (25) Öztürk, B. Immobilization of Lipase from *Candida Rugosa* on Hydrophobic and Hydrophilic Supports, Izmir Institute of Technology, 2001.

- (26) Soleimani, M.; Khani, A.; Najafzadeh, K. α -Amylase Immobilization on the Silica Nanoparticles for Cleaning Performance towards Starch Soils in Laundry Detergents. *J. Mol. Catal. B Enzym.* **2012**, *74* (1–2), 1–5. <https://doi.org/10.1016/j.molcatb.2011.07.011>.
- (27) Guisan, J. M. Immobilization of Enzymes as the 21st Century Begins. In *Immobilization of enzymes and cells*; Guisan JM, Ed.; Humana Press Inc: New Jersey, 2006; pp 1–13. https://doi.org/10.1007/978-1-59745-053-9_1.
- (28) Won, K.; Kim, S.; Kim, K.-J.; Park, H. W.; Moon, S.-J. Optimization of Lipase Entrapment in Ca-Alginate Gel Beads. *Process Biochem.* **2005**, *40* (6), 2149–2154. <https://doi.org/10.1016/j.procbio.2004.08.014>.
- (29) Klotzbach, T. L.; Watt, M.; Ansari, Y.; Minter, S. D. Improving the Microenvironment for Enzyme Immobilization at Electrodes by Hydrophobically Modifying Chitosan and Nafion® Polymers. *J. Memb. Sci.* **2008**, *311* (1–2), 81–88. <https://doi.org/10.1016/J.MEMSCI.2007.11.043>.
- (30) Mohamad, N. R.; Marzuki, N. H. C.; Buang, N. A.; Huyop, F.; Wahab, R. A. An Overview of Technologies for Immobilization of Enzymes and Surface Analysis Techniques for Immobilized Enzymes. *Biotechnology and Biotechnological Equipment*. Diagnosis Press Limited. 2015, pp 205–220. <https://doi.org/10.1080/13102818.2015.1008192>.
- (31) Sheldon, R. A. Cross-Linked Enzyme Aggregates (CLEA®s): Stable and Recyclable Biocatalysts. *Biochem. Soc. Trans.* **2007**, *35* (6), 1583–1587. <https://doi.org/10.1042/BST0351583>.
- (32) Hanefeld, U.; Gardossi, L.; Magner, E. Understanding Enzyme Immobilisation. *Chem. Soc. Rev.* **2009**, *38* (2), 453–468. <https://doi.org/10.1039/B711564B>.

- (33) Velasco-Lozano, S.; López-Gallego, F.; Mateos-Díaz, J. C.; Favela-Torres, E. Cross-Linked Enzyme Aggregates (CLEA) in Enzyme Improvement – a Review. *Biocatalysis* **2016**, *1*, 166–177. <https://doi.org/10.1515/boca-2015-0012>.
- (34) Sheldon, R. A. Cross-Linked Enzyme Aggregates as Industrial Biocatalysts. *Org. Process Res. Dev.* **2011**, *15* (1), 213–223. <https://doi.org/10.1021/op100289f>.
- (35) Sheldon, R. A.; van Pelt, S. Enzyme Immobilisation in Biocatalysis: Why, What and How. *Chem. Soc. Rev.* **2013**, *42* (15), 6223–6235. <https://doi.org/10.1039/C3CS60075K>.
- (36) Górecka, E.; Jastrzębska, M. Immobilization Techniques and Biopolymer Carriers. *Biotechnol. Food Sci.* **2011**, *Vol. 75* (nr 1), 65–86.
- (37) Tischer, W.; Kasche, V. Immobilized Enzymes: Crystals or Carriers? *Trends Biotechnol.* **1999**, *17* (8), 326–335. [https://doi.org/10.1016/S0167-7799\(99\)01322-0](https://doi.org/10.1016/S0167-7799(99)01322-0).
- (38) Alagöz, D.; Tükel, S. S.; Yildirim, D. Enantioselective Synthesis of Various Cyanohydrins Using Covalently Immobilized Preparations of Hydroxynitrile Lyase from *Prunus Dulcis*. *Appl. Biochem. Biotechnol.* **2015**, *177* (6), 1348–1363. <https://doi.org/10.1007/s12010-015-1819-4>.
- (39) Buchholz, K.; Klein, J. Characterization of Immobilized Biocatalysts. *Methods Enzymol.* **1987**, *135*, 3–30.
- (40) Li, S.; Hu, J.; Liu, B. Use of Chemically Modified PMMA Microspheres for Enzyme Immobilization. *BioSystems* **2004**, *77* (1–3), 25–32. <https://doi.org/10.1016/j.biosystems.2004.03.001>.
- (41) Foresti, M. L.; Ferreira, M. L. Chitosan-Immobilized Lipases for the Catalysis of Fatty Acid Esterifications. *Enzyme Microb. Technol.* **2007**, *40* (4), 769–777. <https://doi.org/10.1016/J.ENZMICTEC.2006.06.009>.

- (42) de Lathouder, K. M.; van Benthem, D. T. J.; Wallin, S. A.; Mateo, C.; Lafuente, R. F.; Guisan, J. M.; Kapteijn, F.; Moulijn, J. A. Polyethyleneimine (PEI) Functionalized Ceramic Monoliths as Enzyme Carriers: Preparation and Performance. *J. Mol. Catal. B Enzym.* **2008**, *50* (1), 20–27. <https://doi.org/10.1016/j.molcatb.2007.09.016>.
- (43) Kim, M. Il; Ham, H. O.; Oh, S.-D.; Park, H. G.; Chang, H. N.; Choi, S.-H. Immobilization of *Mucor Javanicus* Lipase on Effectively Functionalized Silica Nanoparticles. *J. Mol. Catal. B Enzym.* **2006**, *39* (1–4), 62–68. <https://doi.org/10.1016/J.MOLCATB.2006.01.028>.
- (44) Guncheva, M.; Dimitrov, M.; Zhiryakova, D. Novel Nanostructured Tin Dioxide as Promising Carrier for *Candida Rugosa* Lipase. *Process Biochem.* **2011**, *46* (11), 2170–2177. <https://doi.org/10.1016/J.PROCBIO.2011.08.020>.
- (45) Suh, W. H.; Suslick, K. S.; Stucky, G. D.; Suh, Y.-H. Nanotechnology, Nanotoxicology, and Neuroscience. *Prog. Neurobiol.* **2009**, *87* (3), 133–170. <https://doi.org/10.1016/J.PNEUROBIO.2008.09.009>.
- (46) Hartmann, M.; Kostrov, X. Immobilization of Enzymes on Porous Silicas – Benefits and Challenges. *Chem. Soc. Rev.* **2013**, *42* (15), 6277–6289. <https://doi.org/10.1039/c3cs60021a>.
- (47) Granmayeh Rad, A.; Abbasi, H.; Afzali, M. H. Gold Nanoparticles: Synthesising, Characterizing and Reviewing Novel Application in Recent Years. *Phys. Procedia* **2011**, *22*, 203–208. <https://doi.org/10.1016/j.phpro.2011.11.032>.
- (48) Ansari, S. A.; Husain, Q. Potential Applications of Enzymes Immobilized on/in Nano Materials: A Review. *Biotechnol. Adv.* **2012**, *30* (3), 512–523. <https://doi.org/10.1016/j.biotechadv.2011.09.00>.

- (49) Cipolatti, E. P.; Silva, M. J. A.; Klein, M.; Feddern, V.; Feltes, M. M. C.; Oliveira, J. V.; Ninow, J. L.; De Oliveira, D. Current Status and Trends in Enzymatic Nanoimmobilization. *J. Mol. Catal. B Enzym.* **2014**, *99*, 56–67. <https://doi.org/10.1016/j.molcatb.2013.10.019>.
- (50) Khan, I.; Saeed, K.; Khan, I. Nanoparticles: Properties, Applications and Toxicities. *Arab. J. Chem.* **2019**, *12* (7), 908–931. <https://doi.org/10.1016/j.arabjc.2017.05.011>.
- (51) Mody, V. V.; Siwale, R.; Singh, A.; Mody, H. R. Introduction to Metallic Nanoparticles. *J. Pharm. Bioallied Sci.* **2010**, *2* (4), 282–289. <https://doi.org/10.4103/0975-7406.72127>.
- (52) Zou, X.; Conradsson, T.; Klingstedt, M.; Dadachov, M. S.; O’Keeffe, M. A Mesoporous Germanium Oxide with Crystalline Pore Walls and Its Chiral Derivative. *Nature* **2005**, *437* (7059), 716–719. <https://doi.org/10.1038/nature04097>.
- (53) Buse, J.; El-Aneed, A. Properties, Engineering and Applications of Lipid-Based Nanoparticle Drug-Delivery Systems: Current Research and Advances. *Nanomedicine* **2010**, *5* (8), 1237–1260. <https://doi.org/10.2217/nnm.10.107>.
- (54) Dykman, L.; Khlebtsov, N. Gold Nanoparticles in Biomedical Applications: Recent Advances and Perspectives. *Chem. Soc. Rev* **2012**, *41* (6), 2256–2282. <https://doi.org/10.1039/c1cs15166e>.
- (55) Faulk, W. P.; Taylor, G. An Immunocolloid Method for the Electron Microscope. *Immunochemistry* **1971**, *8* (11), 1081–1083. [https://doi.org/10.1016/0019-2791\(71\)90496-4](https://doi.org/10.1016/0019-2791(71)90496-4).
- (56) Sau, T. K.; Rogach, A. L.; Jäckel, F.; Klar, T. A.; Feldmann, J. Properties and Applications of Colloidal Nonspherical Noble Metal Nanoparticles. *Adv. Mater.* **2010**, *22* (16), 1805–1825. <https://doi.org/10.1002/adma.200902557>.

- (57) Hu, M.; Chen, J.; Li, Z.-Y.; Au, L.; Hartland, G. V.; Li, X.; Marquez, M.; Xia, Y. Gold Nanostructures: Engineering Their Plasmonic Properties for Biomedical Applications. *Chem. Soc. Rev.* **2006**, *35* (11), 1084. <https://doi.org/10.1039/b517615h>.
- (58) Khlebtsov, N.; Dykman, L. Biodistribution and Toxicity of Engineered Gold Nanoparticles: A Review of in Vitro and in Vivo Studies. *Chem. Soc. Rev.* **2011**, *40* (3), 1647–1671. <https://doi.org/10.1039/C0CS00018C>.
- (59) Murphy, C. J.; Gole, A. M.; Stone, J. W.; Sisco, P. N.; Alkilany, A. M.; Goldsmith, E. C.; Baxter, S. C. Gold Nanoparticles in Biology: Beyond Toxicity to Cellular Imaging. *Acc. Chem. Res.* **2008**, *41* (12), 1721–1730. <https://doi.org/10.1021/ar800035u>.
- (60) Jain, P. K.; Lee, K. S.; El-Sayed, I. H.; El-Sayed, M. A. Calculated Absorption and Scattering Properties of Gold Nanoparticles of Different Size, Shape, and Composition: Applications in Biological Imaging and Biomedicine. *J. Phys. Chem. B* **2006**, *110* (14), 7238–7248. <https://doi.org/10.1021/jp057170o>.
- (61) Eustis, S.; El-Sayed, M. A. Why Gold Nanoparticles Are More Precious than Pretty Gold: Noble Metal Surface Plasmon Resonance and Its Enhancement of the Radiative and Nonradiative Properties of Nanocrystals of Different Shapes. *Chem. Soc. Rev.* **2006**, *35* (3), 209–217. <https://doi.org/10.1039/B514191E>.
- (62) Link, S.; El-Sayed, M. A. Size and Temperature Dependence of the Plasmon Absorption of Colloidal Gold Nanoparticles. *J. Phys. Chem. B* **1999**, *103* (21), 4212–4217. <https://doi.org/10.1021/jp984796o>.

- (63) Templeton, A. C.; Pietron, J. J.; Murray, R. W.; Mulvaney, P. Solvent Refractive Index and Core Charge Influences on the Surface Plasmon Absorbance of Alkanethiolate Monolayer-Protected Gold Clusters. *J. Phys. Chem. B* **2000**, *104* (3), 564–570. <https://doi.org/10.1021/jp991889c>.
- (64) Yeh, Y. C.; Creran, B.; Rotello, V. M. Gold Nanoparticles: Preparation, Properties, and Applications in Bionanotechnology. *Nanoscale* **2012**, *4* (6), 1871–1880. <https://doi.org/10.1039/c1nr11188d>.
- (65) Kim, Y.; Ko, S. M.; Nam, J.-M. ChemInform Abstract: Protein-Nanoparticle Interaction-Induced Changes in Protein Structure and Aggregation. *ChemInform* **2016**, *47* (36). <https://doi.org/10.1002/chin.201636247>.
- (66) Murphy, C. J.; Gole, A. M.; Hunyadi, S. E.; Orendorff, C. J. One-Dimensional Colloidal Gold and Silver Nanostructures. *Inorg. Chem.* **2006**, *45* (19), 7544–7554. <https://doi.org/10.1021/ic0519382>.
- (67) Sean Norman, R.; Stone, J. W.; Gole, A.; Murphy, C. J.; Sabo-Attwood, T. L. Targeted Photothermal Lysis of the Pathogenic Bacteria, *Pseudomonas Aeruginosa*, with Gold Nanorods. *Nano Lett.* **2008**, *8* (1), 302–306. <https://doi.org/10.1021/nl0727056>.
- (68) Murphy, C. J.; Sau, T. K.; Gole, A. M.; Orendorff, C. J.; Gao, J.; Gou, L.; Hunyadi, S. E.; Li, T. Anisotropic Metal Nanoparticles: Synthesis, Assembly, and Optical Applications. *J. Phys. Chem. B* **2005**, *109* (29), 13857–13870. <https://doi.org/10.1021/jp0516846>.
- (69) Murphy, C. J.; Gole, A. M.; Hunyadi, S. E.; Stone, J. W.; Sisco, P. N.; Alkilany, A.; Kinard, B. E.; Hankins, P. Chemical Sensing and Imaging with Metallic Nanorods. *Chem. Commun.* **2002**, *8* (5), 544–557. <https://doi.org/10.1039/b711069c>.

- (70) Thomas, K. G.; Barazzouk, S.; Ipe, B. I.; Joseph, S. T. S.; Kamat, P. V. Uniaxial Plasmon Coupling through Longitudinal Self-Assembly of Gold Nanorods. *J. Phys. Chem. B* **2004**, *108* (35), 13066–13068. <https://doi.org/10.1021/jp049167v>.
- (71) Chen, C. C.; Lin, Y. P.; Wang, C. W.; Tzeng, H. C.; Wu, C. H.; Chen, Y. C.; Chen, C. P.; Chen, L. C.; Wu, Y. C. DNA-Gold Nanorod Conjugates for Remote Control of Localized Gene Expression by near Infrared Irradiation. *J. Am. Chem. Soc.* **2006**, *128* (11), 3709–3715. <https://doi.org/10.1021/ja0570180>.
- (72) Huang, X.; El-Sayed, I. H.; Qian, W.; El-Sayed, M. A. Cancer Cell Imaging and Photothermal Therapy in the Near-Infrared Region by Using Gold Nanorods. *J. Am. Chem. Soc.* **2006**, *128* (6), 2115–2120. <https://doi.org/10.1021/ja057254a>.
- (73) Slowing, I. I.; Vivero-Escoto, J. L.; Wu, C.-W.; Lin, V. S.-Y. Mesoporous Silica Nanoparticles as Controlled Release Drug Delivery and Gene Transfection Carriers. *Adv. Drug Deliv. Rev.* **2008**, *60* (11), 1278–1288. <https://doi.org/10.1016/J.ADDR.2008.03.012>.
- (74) Barbé, C.; Bartlett, J.; Kong, L.; Finnie, K.; Lin, H. Q.; Larkin, M.; Calleja, S.; Bush, A.; Calleja, G. Silica Particles: A Novel Drug-Delivery System. *Adv. Mater.* **2004**, *16* (21), 1959–1966. <https://doi.org/10.1002/adma.200400771>.
- (75) Benezra, M.; Penate-Medina, O.; Zanzonico, P. B.; Schaer, D.; Ow, H.; Burns, A.; DeStanchina, E.; Longo, V.; Herz, E.; Iyer, S.; et al. Multimodal Silica Nanoparticles Are Effective Cancer-Targeted Probes in a Model of Human Melanoma. *J. Clin. Invest.* **2011**, *121* (7), 2768–2780. <https://doi.org/10.1172/JCI45600>.

- (76) Bradbury, M. S.; Phillips, E.; Montero, P. H.; Cheal, S. M.; Stambuk, H.; Durack, J. C.; Sofocleous, C. T.; Meester, R. J. C.; Wiesner, U.; Patel, S. Clinically-Translated Silica Nanoparticles as Dual-Modality Cancer-Targeted Probes for Image-Guided Surgery and Interventions. *Integr. Biol. (Camb)*. **2013**, *5* (1), 74–86.
<https://doi.org/10.1039/c2ib20174g>.
- (77) Tang, L.; Cheng, J. Nonporous Silica Nanoparticles for Nanomedicine Application. *Nano Today* **2013**, *8* (3), 290–312.
- (78) Betancor, L.; Luckarift, H. R. Bioinspired Enzyme Encapsulation for Biocatalysis. *Trends Biotechnol.* **2008**, *26* (10), 566–572. <https://doi.org/10.1016/J.TIBTECH.2008.06.009>.
- (79) Zhao, F.; Hou, T.; Wang, J.; Jiang, Y.; Huang, S.; Wang, Q.; Xian, M.; Mu, X. Immobilization of Proline-Specific Endoprotease on Nonporous Silica Nanoparticles Functionalized with Amino Group. *Bioprocess Biosyst. Eng.* **2017**, *40* (1), 1–7.
<https://doi.org/10.1007/s00449-016-1669-7>.
- (80) Saptarshi, S. R.; Duschl, A.; Lopata, A. L. Interaction of Nanoparticles with Proteins: Relation to Bio-Reactivity of the Nanoparticle. *J. Nanobiotechnology* **2013**, *11* (1), 26.
<https://doi.org/10.1186/1477-3155-11-26>.
- (81) Gunawan, C.; Lim, M.; Marquis, C. P.; Amal, R. Nanoparticle–Protein Corona Complexes Govern the Biological Fates and Functions of Nanoparticles. *J. Mater. Chem. B* **2014**, *2* (15), 2060–2083. <https://doi.org/10.1039/c3tb21526a>.
- (82) Oberlin, A.; Endo, M.; Koyama, T. Filamentous Growth of Carbon through Benzene Decomposition. *J. Cryst. Growth* **1976**, *32* (3), 335–349. [https://doi.org/10.1016/0022-0248\(76\)90115-9](https://doi.org/10.1016/0022-0248(76)90115-9).

- (83) Endo, M.; Hayashi, T.; Kim, Y. A.; Muramatsu, H. Development and Application of Carbon Nanotubes. *Jpn. J. Appl. Phys.* **2006**, *45* (6 A), 4883–4892.
<https://doi.org/10.1143/JJAP.45.4883>.
- (84) Iijima, S. Helical Microtubules of Graphitic Carbon. *Nature* **1991**, *354* (6348), 56–58.
<https://doi.org/10.1038/354056a0>.
- (85) Rassaei L. Assembly and Characterization of Nanomaterials into Thin Film Electroanalysis, Doctoral dissertation, University of Kuopio, Kuopio, 2008.
- (86) Treacy, M. M. J.; Ebbesen, T. W.; Gibson, J. M. Exceptionally High Young's Modulus Observed for Individual Carbon Nanotubes. *Nature* **1996**, *381*, 678–680.
<https://doi.org/https://doi.org/10.1038/381678a0>.
- (87) Putzbach, W.; Ronkainen, N. J. Immobilization Techniques in the Fabrication of Nanomaterial-Based Electrochemical Biosensors: A Review. *Sensors (Switzerland)* **2013**, *13* (4), 4811–4840. <https://doi.org/10.3390/s130404811>.
- (88) De Volder, M. F. L.; Tawfick, S. H.; Baughman, R. H.; Hart, A. J. Carbon Nanotubes: Present and Future Commercial Applications. *Science (80-.)*. **2013**, *339* (6119), 535–539.
<https://doi.org/10.1126/science.1222453>.
- (89) Peng, B.; Locascio, M.; Zapol, P.; Li, S.; Mielke, S. L.; Schatz, G. C.; Espinosa, H. D. Measurements of Near-Ultimate Strength for Multiwalled Carbon Nanotubes and Irradiation-Induced Crosslinking Improvements. *Nat. Nanotechnol.* **2008**, *3* (10), 626–631. <https://doi.org/10.1038/nnano.2008.211>.
- (90) Wei, B. Q.; Vajtai, R.; Ajayan, P. M. Reliability and Current Carrying Capacity of Carbon Nanotubes. *Appl. Phys. Lett.* **2001**, *79* (8), 1172–1174. <https://doi.org/10.1063/1.1396632>.

- (91) Varadan, V. K.; Vinoy, K. J. (Kalarickaparambil J.; Gopalakrishnan, S. *Smart Material Systems and MEMS : Design and Development Methodologies*; John Wiley & Sons, 2006.
- (92) Pop, E.; Mann, D.; Wang, Q.; Goodson, K.; Dai, H. Thermal Conductance of an Individual Single-Wall Carbon Nanotube above Room Temperature. *Nano Lett.* **2006**, *6* (1), 96–100. <https://doi.org/10.1021/nl052145f>.
- (93) Wang, J. Carbon-Nanotube Based Electrochemical Biosensors: A Review. *Electroanalysis* **2005**, *17* (1), 7–14. <https://doi.org/https://doi.org/10.1002/elan.200403113>.
- (94) Snow, E. S.; Perkins, F. K.; Houser, E. J.; Badescu, S. C.; Reinecke, T. L. Chemical Detection with a Single-Walled Carbon Nanotube Capacitor. *Science* **2005**, *307* (5717), 1942–1945. <https://doi.org/10.1126/science.1109128>.
- (95) Esser, B.; Schnorr, J. M.; Swager, T. M. Selective Detection of Ethylene Gas Using Carbon Nanotube-Based Devices: Utility in Determination of Fruit Ripeness. *Angew. Chemie Int. Ed.* **2012**, *51* (23), 5752–5756. <https://doi.org/10.1002/anie.201201042>.
- (96) Qu, L.; Dai, L.; Stone, M.; Xia, Z.; Zhong, L. W. Carbon Nanotube Arrays with Strong Shear Binding-on and Easy Normal Lifting-Off. *Science* **2008**, *322* (5899), 238–242. <https://doi.org/10.1126/science.1159503>.
- (97) Xu, M.; Futaba, D. N.; Yamada, T.; Yumura, M.; Hata, K. Carbon Nanotubes with Temperature-Invariant Viscoelasticity from -196° to 1000°C. *Science* **2010**, *330* (6009), 1364–1368. <https://doi.org/10.1126/science.1194865>.
- (98) Ren, L.; Pint, C. L.; Booshehri, L. G.; Rice, W. D.; Wang, X.; Hilton, D. J.; Takeya, K.; Kawayama, I.; Tonouchi, M.; Hauge, R. H.; et al. Carbon Nanotube Terahertz Polarizer. *Nano Lett.* **2009**, *9* (7), 2610–2613. <https://doi.org/10.1021/nl900815s>.

- (99) Aliev, A. E.; Oh, J.; Kozlov, M. E.; Kuznetsov, A. A.; Fang, S.; Fonseca, A. F.; Ovalle, R.; Lima, M. D.; Haque, M. H.; Gartstein, Y. N.; et al. Giant-Stroke, Superelastic Carbon Nanotube Aerogel Muscles. *Science* **2009**, *323* (5921), 1575–1578.
<https://doi.org/10.1126/science.1168312>.
- (100) Lima, M. D.; Li, N.; De Andrade, M. J.; Fang, S.; Oh, J.; Spinks, G. M.; Kozlov, M. E.; Haines, C. S.; Suh, D.; Foroughi, J.; et al. Electrically, Chemically, and Photonically Powered Torsional and Tensile Actuation of Hybrid Carbon Nanotube Yarn Muscles. *Science* **2012**, *338* (6109), 928–932. <https://doi.org/10.1126/science.1226762>.
- (101) Mizuno, K.; Ishii, J.; Kishida, H.; Hayamizu, Y.; Yasuda, S.; Futaba, D. N.; Yumura, M.; Hata, K. A Black Body Absorber from Vertically Aligned Single-Walled Carbon Nanotubes. *Proc. Natl. Acad. Sci. U. S. A.* **2009**, *106* (15), 6044–6047.
<https://doi.org/10.1073/pnas.0900155106>.
- (102) Xiao, L.; Chen, Z.; Feng, C.; Liu, L.; Bai, Z.-Q.; Wang, Y.; Qian, L.; Zhang, Y.; Li, Q.; Jiang, K.; et al. Flexible, Stretchable, Transparent Carbon Nanotube Thin Film Loudspeakers. <https://doi.org/10.1021/nl802750z>.
- (103) Kam, N. W. S.; Jessop, T. C.; Wender, P. A.; Dai, H. Nanotube Molecular Transporters: Internalization of Carbon Nanotube–Protein Conjugates into Mammalian Cells. *J. Am. Chem. Soc.* **2004**, *126* (22), 6850–6851. <https://doi.org/10.1021/ja0486059>.
- (104) Asuri, P.; Karajanagi, S. S.; Yang, H.; Yim, T. J.; Kane, R. S.; Dordick, J. S. Increasing Protein Stability through Control of the Nanoscale Environment. *Langmuir* **2006**, *22* (13), 5833–5836. <https://doi.org/10.1021/la0528450>.

- (105) Neupane, S.; Patnode, K.; Li, H.; Baryeh, K.; Liu, G.; Hu, J.; Chen, B.; Pan, Y.; Yang, Z. Enhancing Enzyme Immobilization on Carbon Nanotubes via Metal-Organic Frameworks for Large-Substrate Biocatalysis. *ACS Appl. Mater. Interfaces* **2019**, *11* (12), 12133–12141. <https://doi.org/10.1021/acsami.9b01077>.
- (106) Niccoli, M.; Oliva, R.; Castronuovo, G. Cyclodextrin–Protein Interaction as Inhibiting Factor against Aggregation. *J. Therm. Anal. Calorim.* **2017**, *127* (2), 1491–1499. <https://doi.org/10.1007/s10973-016-5736-8>.
- (107) Lakowicz, J. R. Protein Fluorescence BT - Principles of Fluorescence Spectroscopy; Lakowicz, J. R., Ed.; Springer US: Boston, MA, 2006; pp 529–575. https://doi.org/10.1007/978-0-387-46312-4_16.
- (108) Johnson, B. J.; Russ Algar, W.; Malanoski, A. P.; Ancona, M. G.; Medintz, I. L. Understanding Enzymatic Acceleration at Nanoparticle Interfaces: Approaches and Challenges. *Nano Today*. Elsevier B.V. 2014, pp 102–131. <https://doi.org/10.1016/j.nantod.2014.02.005>.
- (109) Baugh, L.; Weidner, T.; Baio, J. E.; Nguyen, P. C. T.; Gamble, L. J.; Stayton, P. S.; Castner, D. G. Probing the Orientation of Surface-Immobilized Protein G B1 Using ToF-SIMS, Sum Frequency Generation, and NEXAFS Spectroscopy. *Langmuir* **2010**, *26* (21), 16434–16441. <https://doi.org/10.1021/la1007389>.
- (110) Karlsson, M.; Carlsson, U. Protein Adsorption Orientation in the Light of Fluorescent Probes: Mapping of the Interaction between Site-Directly Labeled Human Carbonic Anhydrase II and Silica Nanoparticles. *Biophys. J.* **2005**, *88* (5), 3536–3544. <https://doi.org/10.1529/biophysj.104.054809>.

- (111) Calzolari, L.; Franchini, F.; Gilliland, D.; Rossi, F. Protein–Nanoparticle Interaction: Identification of the Ubiquitin–Gold Nanoparticle Interaction Site. *Nano Lett.* **2010**, *10* (8), 3101–3105. <https://doi.org/10.1021/nl101746v>.
- (112) Zanzoni, S.; Pedroni, M.; D’Onofrio, M.; Speghini, A.; Assfalg, M. Paramagnetic Nanoparticles Leave Their Mark on Nuclear Spins of Transiently Adsorbed Proteins. *J. Am. Chem. Soc.* **2016**, *138* (1), 72–75. <https://doi.org/10.1021/jacs.5b11582>.
- (113) Chittur, K. K. FTIR/ATR for Protein Adsorption to Biomaterial Surfaces. *Biomaterials* **1998**, *19* (4–5), 357–369. [https://doi.org/10.1016/S0142-9612\(97\)00223-8](https://doi.org/10.1016/S0142-9612(97)00223-8).
- (114) Schartner, J.; Güldenhaupt, J.; Mei, B.; Rögner, M.; Muhler, M.; Gerwert, K.; Köttling, C. Universal Method for Protein Immobilization on Chemically Functionalized Germanium Investigated by ATR-FTIR Difference Spectroscopy. *J. Am. Chem. Soc.* **2013**, *135* (10), 4079–4087. <https://doi.org/10.1021/ja400253p>.
- (115) Holman, J.; Ye, S.; Neivandt, D. J.; Davies, P. B. Studying Nanoparticle-Induced Structural Changes within Fatty Acid Multilayer Films Using Sum Frequency Generation Vibrational Spectroscopy. *J. Am. Chem. Soc.* **2004**, *126* (44), 14322–14323. <https://doi.org/10.1021/ja046954x>.
- (116) Ceccon, A.; Tugarinov, V.; Bax, A.; Clore, G. M. Global Dynamics and Exchange Kinetics of a Protein on the Surface of Nanoparticles Revealed by Relaxation-Based Solution Nmr Spectroscopy. *J. Am. Chem. Soc.* **2016**, *138* (18), 5789–5792. <https://doi.org/10.1021/jacs.6b02654>.
- (117) Columbus, L.; Kálai, T.; Jekö, J.; Hideg, K.; Hubbell, W. L. Molecular Motion of Spin Labeled Side Chains in α -Helices: Analysis by Variation of Side Chain Structure†. *Biochemistry* **2001**, *40* (13), 3828–3846. <https://doi.org/10.1021/BI002645H>.

- (118) Columbus, L.; Hubbell, W. L. A New Spin on Protein Dynamics. *Trends Biochem. Sci.* **2002**, *27* (6), 288–295. [https://doi.org/10.1016/S0968-0004\(02\)02095-9](https://doi.org/10.1016/S0968-0004(02)02095-9).
- (119) Todd, A. P.; Cong, J.; Levinthal, F.; Levinthal, C.; Hubbell, W. L. Site-Directed Mutagenesis of Colicin E1 Provides Specific Attachment Sites for Spin Labels Whose Spectra Are Sensitive to Local Conformation. *Proteins Struct. Funct. Genet.* **1989**, *6* (3), 294–305. <https://doi.org/10.1002/prot.340060312>.
- (120) Altenbach, C.; López, C. J.; Hideg, K.; Hubbell, W. L. Chapter Three- Exploring Structure, Dynamics, and Topology of Nitroxide Spin-Labeled Proteins Using Continuous-Wave Electron Paramagnetic Resonance Spectroscopy. In *Methods in Enzymology*; Academic Press, 2015; Vol. 564, pp 59–100. <https://doi.org/10.1016/BS.MIE.2015.08.006>.
- (121) Neupane, S.; Pan, Y.; Takalkar, S.; Bentz, K.; Farmakes, J.; Xu, Y.; Chen, B.; Liu, G.; Qian, S. Y.; Yang, Z. Probing the Aggregation Mechanism of Gold Nanoparticles Triggered by a Globular Protein. *J. Phys. Chem. C* **2017**, *121* (2), 1377–1386. <https://doi.org/10.1021/acs.jpcc.6b11963>.
- (122) Fleissner, M. R.; Bridges, M. D.; Brooks, E. K.; Cascio, D.; Kálai, T.; Hideg, K.; Hubbell, W. L. Structure and Dynamics of a Conformationally Constrained Nitroxide Side Chain and Applications in EPR Spectroscopy. *Proc. Natl. Acad. Sci. U. S. A.* **2011**, *108* (39), 16241–16246. <https://doi.org/10.1073/pnas.1111420108>.
- (123) López, C. J.; Oga, S.; Hubbell, W. L. Mapping Molecular Flexibility of Proteins with Site-Directed Spin Labeling: A Case Study of Myoglobin. *Biochemistry* **2012**, *51* (33), 6568–6583. <https://doi.org/10.1021/bi3005686>.

- (124) Lerch, M. Touring the Conformational Landscape of Proteins with High-Pressure SDSL EPR Spectroscopy, University of California, 2015.
- (125) Klug, C. S.; Feix, J. B. Methods and Applications of Site-Directed Spin Labeling EPR Spectroscopy. *Methods Cell Biol.* **2008**, *84*, 617–658. [https://doi.org/10.1016/S0091-679X\(07\)84020-9](https://doi.org/10.1016/S0091-679X(07)84020-9).
- (126) López, C. J.; Fleissner, M. R.; Brooks, E. K.; Hubbell, W. L. Stationary-Phase EPR for Exploring Protein Structure, Conformation, and Dynamics in Spin-Labeled Proteins. *Biochemistry* **2014**, *53*, 7067–7075. <https://doi.org/10.1021/bi5011128>.
- (127) Mchaourab, H. S.; Lietzow, M. A.; Hideg, K.; Hubbell, W. L. Motion of Spin-Labeled Side Chains in T4 Lysozyme. Correlation with Protein Structure and Dynamics. *Biochemistry* **1996**, *35* (24), 7692–7704. <https://doi.org/10.1021/bi960482k>.
- (128) Mchaourab, H. S.; Kálai, T.; Hideg, K.; Hubbell, W. L. Motion of Spin-Labeled Side Chains in T4 Lysozyme: Effect of Side Chain Structure. *Biochemistry* **1999**, *38* (10), 2947–2955. <https://doi.org/10.1021/bi9826310>.
- (129) Columbus, L.; Hubbell, W. L. Mapping Backbone Dynamics in Solution with Site-Directed Spin Labeling: GCN4-58 BZip Free and Bound to DNA. *Biochemistry* **2004**, *43* (23), 7273–7287. <https://doi.org/10.1021/bi0497906>.
- (130) Mahmoudi, M.; Lynch, I.; Ejtehadi, M. R.; Monopoli, M. P.; Bombelli, F. B.; Laurent, S. Protein-Nanoparticle Interactions: Opportunities and Challenges. *Chem. Rev* **2011**, *111* (9), 5610–5637. <https://doi.org/10.1021/cr100440g>.
- (131) Cheng, Y.; Morshed, R. A.; Auffinger, B.; Tobias, A. L.; Lesniak, M. S. Multifunctional Nanoparticles for Brain Tumor Imaging and Therapy. *Adv. Drug Deliv. Rev.* **2014**, *66*, 42–57. <https://doi.org/10.1016/j.addr.2013.09.006>.

- (132) Dastagiri Reddy, Y.; Dhachinamoorthi, D.; Chandra Sekhar, K. B. A Brief Review on Polymeric Nanoparticles for Drug Delivery and Targeting. *J. Med. Pharm. Innov.* **2015**, *2* (7), 19–32.
- (133) Tiwari, P.; Vig, K.; Dennis, V.; Singh, S.; Tiwari, P. M.; Vig, K.; Dennis, V. A.; Singh, S. R. Functionalized Gold Nanoparticles and Their Biomedical Applications. *Nanomaterials* **2011**, *1* (1), 31–63. <https://doi.org/10.3390/nano1010031>.
- (134) Fadeel, B.; Garcia-Bennett, A. E. Better Safe than Sorry: Understanding the Toxicological Properties of Inorganic Nanoparticles Manufactured for Biomedical Applications. *Adv. Drug Deliv. Rev.* **2010**, *62* (3), 362–374. <https://doi.org/10.1016/J.ADDR.2009.11.008>.
- (135) De, M.; Ghosh, P. S.; Rotello, V. M. Applications of Nanoparticles in Biology. *Adv. Mater.* **2008**, *20* (22), 4225–4241. <https://doi.org/10.1002/adma.200703183>.
- (136) Alkilany, A. M.; Lohse, S. E.; Murphy, C. J. The Gold Standard: Gold Nanoparticle Libraries To Understand the Nano–Bio Interface. *Acc. Chem. Res.* **2013**, *46* (3), 650–661. <https://doi.org/10.1021/ar300015b>.
- (137) Delehanty, J. B.; Boeneman, K.; Bradburne, C. E.; Robertson, K.; Bongard, J. E.; Medintz, I. L. Peptides for Specific Intracellular Delivery and Targeting of Nanoparticles: Implications for Developing Nanoparticle-Mediated Drug Delivery. *Ther. Deliv.* **2010**, *1* (3), 411–433. <https://doi.org/10.4155/tde.10.27>.
- (138) Giljohann, D. A.; Seferos, D. S.; Daniel, W. L.; Massich, M. D.; Patel, P. C.; Mirkin, C. A. Gold Nanoparticles for Biology and Medicine. *Angew. Chemie Int. Ed.* **2010**, *49* (19), 3280–3294. <https://doi.org/10.1002/anie.200904359>.

- (139) Petros, R. A.; DeSimone, J. M. Strategies in the Design of Nanoparticles for Therapeutic Applications. *Nat. Rev. Drug Discov.* **2010**, *9* (8), 615–627.
<https://doi.org/10.1038/nrd2591>.
- (140) Shi, J.; Votruba, A. R.; Farokhzad, O. C.; Langer, R. Nanotechnology in Drug Delivery and Tissue Engineering: From Discovery to Applications. **2010**.
<https://doi.org/10.1021/nl102184c>.
- (141) Donnelly, J. J.; Wahren, B.; Liu, M. A.; Robinson, H. L.; Barber, B. H. DNA Vaccines: Progress and Challenges. *J. Immunol.* **2005**, *175* (2), 633–639.
<https://doi.org/10.4049/jimmunol.175.2.633>.
- (142) Pissuwan, D.; Niidome, T.; Cortie, M. B. The Forthcoming Applications of Gold Nanoparticles in Drug and Gene Delivery Systems. *J. Control. Release* **2011**, *149* (1), 65–71. <https://doi.org/10.1016/J.JCONREL.2009.12.006>.
- (143) Shamaila, S.; Zafar, N.; Riaz, S.; Sharif, R.; Nazir, J.; Naseem, S.; Shamaila, S.; Zafar, N.; Riaz, S.; Sharif, R.; et al. Gold Nanoparticles: An Efficient Antimicrobial Agent against Enteric Bacterial Human Pathogen. *Nanomaterials* **2016**, *6* (4), 71.
<https://doi.org/10.3390/nano6040071>.
- (144) Lazarovits, J.; Chen, Y. Y.; Sykes, E. A.; Chan, W. C. W. Nanoparticle–Blood Interactions: The Implications on Solid Tumour Targeting. *Chem. Commun.* **2015**, *51* (14), 2756–2767. <https://doi.org/10.1039/C4CC07644C>.
- (145) Ge, C.; Tian, J.; Zhao, Y.; Chen, C.; Zhou, R.; Chai, Z. Towards Understanding of Nanoparticle–Protein Corona. *Arch. Toxicol.* **2015**, *89* (4), 519–539.
<https://doi.org/10.1007/s00204-015-1458-0>.

- (146) Lynch, I.; Dawson, K. A. Protein-Nanoparticle Interactions. *Nano Today* **2008**, *3* (1–2), 40–47. [https://doi.org/10.1016/S1748-0132\(08\)70014-8](https://doi.org/10.1016/S1748-0132(08)70014-8).
- (147) Kim, Y.; Ko, S. M.; Nam, J.-M. Protein-Nanoparticle Interaction-Induced Changes in Protein Structure and Aggregation. *Chem. - An Asian J.* **2016**, *11* (13), 1869–1877. <https://doi.org/10.1002/asia.201600236>.
- (148) Yang, T.; Li, Z.; Wang, L.; Guo, C.; Sun, Y. Synthesis, Characterization, and Self-Assembly of Protein Lysozyme Monolayer-Stabilized Gold Nanoparticles. *Langmuir* **2007**, *23* (21), 10533–10538. <https://doi.org/10.1021/la701649z>.
- (149) Sanpui, P.; Paul, A.; Chattopadhyay, A. Theranostic Potential of Gold Nanoparticle-Protein Agglomerates. *Nanoscale* **2015**, *7* (44), 18411–18423. <https://doi.org/10.1039/C5NR05805H>.
- (150) Dominguez-Medina, S.; Kisley, L.; Tauzin, L. J.; Hoggard, A.; Shuang, B.; Swarnapali, A.; Indrasekara, D. S.; Chen, S.; Wang, L.-Y.; Derry, P. J.; et al. Adsorption and Unfolding of a Single Protein Triggers Nanoparticle Aggregation. *ACS Nano* **2016**, *10* (2), 2103–2112. <https://doi.org/10.1021/acsnano.5b06439>.
- (151) Zhang, D.; Neumann, O.; Wang, H.; Yuwono, V. M.; Barhoumi, A.; Perham, M.; Hartgerink, J. D.; Wittung-Stafshede, P.; Halas, N. J. Gold Nanoparticles Can Induce the Formation of Protein-Based Aggregates at Physiological PH. *Nano Lett.* **2009**, *9* (2), 666–671. <https://doi.org/10.1021/nl803054h>.
- (152) Shang, L.; Wang, Y.; Jiang, J.; Dong, S. PH-Dependent Protein Conformational Changes in Albumin:Gold Nanoparticle Bioconjugates: A Spectroscopic Study. *Langmuir* **2007**, *23* (5), 2714–2721. <https://doi.org/10.1021/la062064e>.

- (153) Jiang, X.; Jiang, J.; Jin, Y.; Wang, E.; Dong, S. Effect of Colloidal Gold Size on the Conformational Changes of Adsorbed Cytochrome c: Probing by Circular Dichroism, UV-Visible, and Infrared Spectroscopy. *Biomacromolecules* **2005**, *6* (1), 46–53. <https://doi.org/10.1021/bm049744l>.
- (154) Liao, Y. H.; Chang, Y. J.; Yoshiike, Y.; Chang, Y. C.; Chen, Y. R. Negatively Charged Gold Nanoparticles Inhibit Alzheimer's Amyloid- β Fibrillization, Induce Fibril Dissociation, and Mitigate Neurotoxicity. *Small* **2012**, *8* (23), 3631–3639. <https://doi.org/10.1002/smll.201201068>.
- (155) Araya, E.; Olmedo, I.; Bastus, N. G.; Guerrero, S.; Puentes, V. F.; Giralt, E.; Kogan, M. J. Gold Nanoparticles and Microwave Irradiation Inhibit Beta-Amyloid Amyloidogenesis. *Nanoscale Res. Lett.* **2008**, *3* (11), 435–443. <https://doi.org/10.1007/s11671-008-9178-5>.
- (156) Wagner, S. C.; Roskamp, M.; Pallerla, M.; Araghi, R. R.; Schlecht, S.; Kocsch, B. Nanoparticle-Induced Folding and Fibril Formation of Coiled-Coil-Based Model Peptides. *Small* **2010**, *6* (12), 1321–1328. <https://doi.org/10.1002/smll.200902067>.
- (157) Abad, J. M.; Mertens, S. F. L.; Pita, M.; Fernández, V. M.; Schiffrin, D. J. Functionalization of Thioctic Acid-Capped Gold Nanoparticles for Specific Immobilization of Histidine-Tagged Proteins. *J. Am. Chem. Soc.* **2005**, *127* (15), 5689–5694. <https://doi.org/10.1021/ja042717i>.
- (158) Singh, R. K.; Tiwari, M. K.; Singh, R.; Lee, J. K. From Protein Engineering to Immobilization: Promising Strategies for the Upgrade of Industrial Enzymes. *Int. J. Mol. Sci.* **2013**, *14* (1), 1232–1277. <https://doi.org/10.3390/ijms14011232>.

- (159) Datta, S.; Christena, L. R.; Rajaram, Y. R. S. Enzyme Immobilization: An Overview on Techniques and Support Materials. *3 Biotech* **2013**, *3* (1), 1–9.
<https://doi.org/10.1007/s13205-012-0071-7>.
- (160) Seo, M. H.; Han, J.; Jin, Z.; Lee, D. W.; Park, H. S.; Kim, H. S. Controlled and Oriented Immobilization of Protein by Site-Specific Incorporation of Unnatural Amino Acid. *Anal. Chem.* **2011**, *83* (8), 2841–2845. <https://doi.org/10.1021/ac103334b>.
- (161) Jia, H.; Zhu, G.; Wang, P. Catalytic Behaviors of Enzymes Attached to Nanoparticles: The Effect of Particle Mobility. *Biotechnol. Bioeng.* **2003**, *84* (4), 406–414.
<https://doi.org/10.1002/bit.10781>.
- (162) Li, L.; Mu, Q.; Zhang, B.; Yan, B. Analytical Strategies for Detecting Nanoparticle–Protein Interactions. *Analyst* **2010**, *135* (7), 1519–1530.
<https://doi.org/10.1039/c0an00075b>.
- (163) Mchaourab, H. S.; Steed, P. R.; Kazmier, K. Toward the Fourth Dimension of Membrane Protein Structure: Insight into Dynamics from Spin-Labeling EPR Spectroscopy. *Structure* **2011**, *19* (11), 1549–1561. <https://doi.org/10.1016/J.STR.2011.10.009>.
- (164) Cafiso, D. S. Identifying and Quantitating Conformational Exchange in Membrane Proteins Using Site-Directed Spin Labeling. *Acc. Chem. Res.* **2014**, *47*, 3102–3109.
<https://doi.org/10.1021/ar500228s>.
- (165) Kawasaki, K.; Yin, J.-J.; Subczynski, W. K.; Hyde, J. S.; Kusumi, A. Pulse EPR Detection of Lipid Exchange between Protein-Rich Raft and Bulk Domains in the Membrane: Methodology Development and Its Application to Studies of Influenza Viral Membrane. *Biophys. J.* **2001**, *80* (2), 738–748. [https://doi.org/10.1016/S0006-3495\(01\)76053-5](https://doi.org/10.1016/S0006-3495(01)76053-5).

- (166) Pornsuwan, S.; Bird, G.; Schafmeister, C. E.; Saxena, S. Flexibility and Lengths of Bis-Peptide Nanostructures by Electron Spin Resonance. *J. Am. Chem. Soc.* **2006**, *128* (12), 3876–3877. <https://doi.org/10.1021/ja058143e>.
- (167) Godt, A.; Schulte, M.; Zimmermann, H.; Jeschke, G. How Flexible Are Poly(Para-Phenyleneethynylene)S? *Angew. Chemie Int. Ed.* **2006**, *45* (45), 7560–7564. <https://doi.org/10.1002/anie.200602807>.
- (168) Doll, A.; Qi, M.; Wili, N.; Pribitzer, S.; Godt, A.; Jeschke, G. Gd(III)–Gd(III) Distance Measurements with Chirp Pump Pulses. *J. Magn. Reson.* **2015**, *259*, 153–162. <https://doi.org/10.1016/J.JMR.2015.08.010>.
- (169) Turner, A. L.; Braide, O.; Mills, F. D.; Fanucci, G. E.; Long, J. R. Residue Specific Partitioning of KL4 into Phospholipid Bilayers. *Biochim. Biophys. Acta* **2014**, *1838* (12), 3212–3219. <https://doi.org/10.1016/J.BBAMEM.2014.09.006>.
- (170) Fanucci, G. E.; Cafiso, D. S. Recent Advances and Applications of Site-Directed Spin Labeling. *Curr. Opin. Struct. Biol.* **2006**, *16* (5), 644–653. <https://doi.org/10.1016/J.SBI.2006.08.008>.
- (171) DeBerg, H. A.; Brzovic, P. S.; Flynn, G. E.; Zagotta, W. N.; Stoll, S. Structure and Energetics of Allosteric Regulation of HCN2 Ion Channels by Cyclic Nucleotides. *J. Biol. Chem.* **2016**, *291* (1), 371–381. <https://doi.org/10.1074/jbc.M115.696450>.
- (172) Yang, Z.; Kurpiewski, M. R.; Ji, M.; Townsend, J. E.; Mehta, P.; Jen-Jacobson, L.; Saxena, S. ESR Spectroscopy Identifies Inhibitory Cu²⁺ Sites in a DNA-Modifying Enzyme to Reveal Determinants of Catalytic Specificity. *Proc. Natl. Acad. Sci.* **2012**, *109* (17), E993–E1000. <https://doi.org/10.1073/pnas.1200733109>.

- (173) Zhang, X.; Lee, S. W.; Zhao, L.; Xia, T.; Qin, P. Z. Conformational Distributions at the N-Peptide/BoxB RNA Interface Studied Using Site-Directed Spin Labeling. *RNA* **2010**, *16* (12), 2474–2483. <https://doi.org/10.1261/rna.2360610>.
- (174) Vazquez Reyes, C.; Tangprasertchai, N. S.; Yogesha, S. D.; Nguyen, R. H.; Zhang, X.; Rajan, R.; Qin, P. Z. Nucleic Acid-Dependent Conformational Changes in CRISPR–Cas9 Revealed by Site-Directed Spin Labeling. *Cell Biochem. Biophys.* **2017**, *75* (2), 203–210. <https://doi.org/10.1007/s12013-016-0738-5>.
- (175) Ling, S.; Wang, W.; Yu, L.; Peng, J.; Cai, X.; Xiong, Y.; Hayati, Z.; Zhang, L.; Zhang, Z.; Song, L.; et al. Structure of an E. Coli Integral Membrane Sulfurtransferase and Its Structural Transition upon SCN– Binding Defined by EPR-Based Hybrid Method. *Sci. Rep.* **2016**, *6* (1), 20025. <https://doi.org/10.1038/srep20025>.
- (176) Ji, M.; Ruthstein, S.; Saxena, S. Paramagnetic Metal Ions in Pulsed ESR Distance Distribution Measurements. *Acc. Chem. Res.* **2014**, *47* (2), 688–695. <https://doi.org/10.1021/ar400245z>.
- (177) Hubbell, W. L.; López, C. J.; Altenbach, C.; Yang, Z. Technological Advances in Site-Directed Spin Labeling of Proteins. *Curr. Opin. Struct. Biol.* **2013**, *23* (5), 725–733. <https://doi.org/10.1016/J.SBI.2013.06.008>.
- (178) Ionita, P.; Volkov, A.; Jeschke, G.; Chechik, V. Lateral Diffusion of Thiol Ligands on the Surface of Au Nanoparticles: An Electron Paramagnetic Resonance Study. *Anal. Chem.* **2005**, *105* (2), 95–106. <https://doi.org/10.1021/ac071266s>.

- (179) Chang, J.; Taylor, R. D.; Davidson, R. A.; Sharmah, A.; Guo, T. Electron Paramagnetic Resonance Spectroscopy Investigation of Radical Production by Gold Nanoparticles in Aqueous Solutions Under X-Ray Irradiation. *J. Phys. Chem. A* **2016**, *120*, 2815–2823. <https://doi.org/10.1021/acs.jpca.6b01755>.
- (180) He, W.; Liu, Y.; Wamer, W. G.; Yin, J.-J. Electron Spin Resonance Spectroscopy for the Study of Nanomaterial-Mediated Generation of Reactive Oxygen Species. *J. Food Drug Anal.* **2014**, *22* (1), 49–63. <https://doi.org/10.1016/J.JFDA.2014.01.004>.
- (181) Grütter, M. G.; Matthews, B. W. Amino Acid Substitutions Far from the Active Site of Bacteriophage T4 Lysozyme Reduce Catalytic Activity and Suggest That the C-Terminal Lobe of the Enzyme Participates in Substrate Binding. *J. Mol. Biol.* **1982**, *154* (3), 525–535. [https://doi.org/10.1016/S0022-2836\(82\)80011-9](https://doi.org/10.1016/S0022-2836(82)80011-9).
- (182) Bower, C. K.; Xu, Q.; McGuire, J. Activity Losses among T4 Lysozyme Variants after Adsorption to Colloidal Silica. *Biotechnol. Bioeng.* **1998**, *58* (6), 658–662. [https://doi.org/10.1002/\(SICI\)1097-0290\(19980620\)58:6<658::AID-BIT13>3.0.CO;2-3](https://doi.org/10.1002/(SICI)1097-0290(19980620)58:6<658::AID-BIT13>3.0.CO;2-3).
- (183) McCoy, J.; Hubbell, W. L. High-Pressure EPR Reveals Conformational Equilibria and Volumetric Properties of Spin-Labeled Proteins. *Proc. Natl. Acad. Sci. U. S. A.* **2011**, *108* (4), 1331–1336. <https://doi.org/10.1073/pnas.1017877108>.
- (184) Yadav, I.; Aswal, V. K.; Kohlbrecher, J. Size-Dependent Interaction of Silica Nanoparticles with Lysozyme and Bovine Serum Albumin Proteins. *Phys. Rev. E* **2016**, *93* (5), 052601. <https://doi.org/10.1103/PhysRevE.93.052601>.

- (185) Yang, Z.; Jiménez, G.; Osés, J.-O.; Lópezlópez, C. J.; Bridges, M. D.; Houk, K. N.; Hubbell, W. L. Long-Range Distance Measurements in Proteins at Physiological Temperatures Using Saturation Recovery EPR Spectroscopy. *J. Am. Chem. Soc.* **2014**, *136*, 15356–15365. <https://doi.org/10.1021/ja5083206>.
- (186) López, C. J.; Fleissner, M. R.; Guo, Z.; Kusnetzow, A. K.; Hubbell, W. L. Osmolyte Perturbation Reveals Conformational Equilibria in Spin-Labeled Proteins. *Protein Sci.* **2009**, *18* (8), 1637–1652. <https://doi.org/10.1002/pro.180>.
- (187) Fleissner, M. R.; Brustad, E. M.; Kalai, T.; Altenbach, C.; Cascio, D.; Peters, F. B.; Hideg, K.; Peuker, S.; Schultz, P. G.; Hubbell, W. L. Site-Directed Spin Labeling of a Genetically Encoded Unnatural Amino Acid. *Proc. Natl. Acad. Sci.* **2009**, *106* (51), 21637–21642. <https://doi.org/10.1073/pnas.0912009106>.
- (188) Matsumura, M.; Wozniak, J. A.; Dao-Pin, S.; Matthews, B. W. Structural Studies of Mutants of T4 Lysozyme That Alter Hydrophobic Stabilization. *J. Biol. Chem.* **1989**, *264* (27), 16059–16066. <https://doi.org/10.2210/pdb3lzm/pdb>.
- (189) Grabar, K. C.; Freeman, R. G.; Hommer, M. B.; Natan, M. J. Preparation and Characterization of Au Colloid Monolayers. *Anal. Chem.* **1995**, *67* (4), 735–743. <https://doi.org/10.1021/ac00100a008>.
- (190) Haiss, W.; Thanh, N. T. K.; Aveyard, J.; Fernig, D. G. Determination of Size and Concentration of Gold Nanoparticles from UV–Vis Spectra. *Anal. Chem.* **2007**, *79* (11), 4215–4221. <https://doi.org/10.1021/AC0702084>.

- (191) Bower, C. K.; Sananikone, S.; Bothwell, M. K.; McGuire, J. Activity Losses among T4 Lysozyme Charge Variants after Adsorption to Colloidal Silica. *Biotechnol. Bioeng.* **1999**, *64* (3), 373–376. [https://doi.org/10.1002/\(SICI\)1097-0290\(19990805\)64:3<373::AID-BIT14>3.0.CO;2-J](https://doi.org/10.1002/(SICI)1097-0290(19990805)64:3<373::AID-BIT14>3.0.CO;2-J).
- (192) Guo, Z.; Cascio, D.; Hideg, K.; Hubbell, W. L. Structural Determinants of Nitroxide Motion in Spin-Labeled Proteins: Solvent-Exposed Sites in Helix B of T4 Lysozyme. *Protein Sci.* **2008**, *17* (2), 228–239. <https://doi.org/10.1110/ps.073174008>.
- (193) Langen, R.; Oh, K. J.; Cascio, D.; Hubbell, W. L. Crystal Structures of Spin Labeled T4 Lysozyme Mutants: Implications for the Interpretation of EPR Spectra in Terms of Structure. *Biochemistry* **2000**, *39* (29), 8396–8405.
- (194) Mchaourab, H. S.; Oh, K. J.; Fang, C. J.; Hubbell, W. L. Conformation of T4 Lysozyme in Solution. Hinge-Bending Motion and the Substrate-Induced Conformational Transition Studied by Site-Directed Spin Labeling. *Biochemistry* **1997**, *36* (2), 307–316. <https://doi.org/10.1021/bi962114m>.
- (195) Xue, Y.; Li, X.; Li, H.; Zhang, W. Quantifying Thiol-Gold Interactions towards the Efficient Strength Control. *Nat. Commun.* **2014**, *5* (1), 4348. <https://doi.org/10.1038/ncomms5348>.
- (196) Vangala, K.; Ameer, F.; Salomon, G.; Le, V.; Lewis, E.; Yu, L.; Liu, D.; Zhang, D. Studying Protein and Gold Nanoparticle Interaction Using Organothiols as Molecular Probes. *J. Phys. Chem. C* **2012**, *116*, 3645–3652. <https://doi.org/10.1021/jp2107318>.

- (197) Siriwardana, K.; Wang, A.; Vangala, K.; Fitzkee, N.; Zhang, D. Probing the Effects of Cysteine Residues on Protein Adsorption onto Gold Nanoparticles Using Wild-Type and Mutated GB3 Proteins. *Langmuir* **2013**, *29* (35), 10990–10996. <https://doi.org/10.1021/la402239h>.
- (198) Rao, C. N. R.; Kulkarni, G. U.; Thomas, P. J.; Edwards, P. P. Metal Nanoparticles and Their Assemblies. *Chem. Soc. Rev.* **2000**, *29* (1), 27–35. <https://doi.org/10.1039/a904518j>.
- (199) Capeletti, L. B.; De Oliveira, L. F.; Gonçalves, K. D. A.; De Oliveira, J. F. A.; Saito, Â.; Kobarg, J.; Santos, J. H. Z. Dos; Cardoso, M. B. Tailored Silica-Antibiotic Nanoparticles: Overcoming Bacterial Resistance with Low Cytotoxicity. *Langmuir* **2014**, *30* (25), 7456–7464. <https://doi.org/10.1021/la4046435>.
- (200) Dong, L.; Li, M.; Zhang, S.; Li, J.; Shen, G.; Tu, Y.; Zhu, J.; Tao, J. Cytotoxicity of BSA-Stabilized Gold Nanoclusters: In Vitro and In Vivo Study. *Small* **2015**, *11* (21), 2571–2581. <https://doi.org/10.1002/smll.201403481>.
- (201) Lynch, I.; Salvati, A.; Dawson, K. A. What Does the Cell See? *Nat. Nanotechnol.* **2009**, *4* (9), 546–547. <https://doi.org/10.1038/nnano.2009.248>.
- (202) Bock, L. C.; Griffin, L. C.; Latham, J. A.; Vermaas, E. H.; Toole, J. J. Selection of Single-Stranded DNA Molecules That Bind and Inhibit Human Thrombin. *Nature* **1992**, *355* (6360), 564–566. <https://doi.org/10.1038/355564a0>.
- (203) Russo Krauss, I.; Merlino, A.; Randazzo, A.; Novellino, E.; Mazzarella, L.; Sica, F. High-Resolution Structures of Two Complexes between Thrombin and Thrombin-Binding Aptamer Shed Light on the Role of Cations in the Aptamer Inhibitory Activity. *Nucleic Acids Res.* **2012**, *40* (16), 8119–8128. <https://doi.org/10.1093/nar/gks512>.

- (204) Bharti, B.; Meissner, J.; Findenegg, G. H. Aggregation of Silica Nanoparticles Directed by Adsorption of Lysozyme. **2011**, *27*, 9823–9833. <https://doi.org/10.1021/la201898v>.
- (205) Bharti, B.; Meissner, J.; Klapp, S. H. L.; Findenegg, G. H. Bridging Interactions of Proteins with Silica Nanoparticles: The Influence of PH, Ionic Strength and Protein Concentration. *Soft Matter* **2014**, *10* (5), 718–728. <https://doi.org/10.1039/C3SM52401A>.
- (206) Gerber, A.; Bundschuh, M.; Klingelhofer, D.; Groneberg, D. A. Gold Nanoparticles: Recent Aspects for Human Toxicology. *J. Occup. Med. Toxicol.* **2013**, *8* (1), 32. <https://doi.org/10.1186/1745-6673-8-32>.
- (207) Albanese, A.; Chan, W. C. W. Effect of Gold Nanoparticle Aggregation on Cell Uptake and Toxicity. *ACS Nano* **2011**, *5* (7), 5478–5489. <https://doi.org/10.1021/nn2007496>.
- (208) Fratoddi, I.; Venditti, I.; Cametti, C.; Russo, M. V. How Toxic Are Gold Nanoparticles? The State-of-the-Art. *Nano Res.* **2015**, *8* (6), 1771–1799. <https://doi.org/10.1007/s12274-014-0697-3>.
- (209) Alkilany, A. M.; Murphy, C. J. Toxicity and Cellular Uptake of Gold Nanoparticles: What We Have Learned so Far? *J. Nanoparticle Res.* **2010**, *12* (7), 2313–2333. <https://doi.org/10.1007/s11051-010-9911-8>.
- (210) Song, Y.; Li, X.; Du, X. Exposure to Nanoparticles Is Related to Pleural Effusion, Pulmonary Fibrosis and Granuloma. *Eur. Respir. J.* **2009**, *34* (3), 559–567. <https://doi.org/10.1183/09031936.00178308>.
- (211) Cox, A.; Venkatachalam, P.; Sahi, S.; Sharma, N. Silver and Titanium Dioxide Nanoparticle Toxicity in Plants: A Review of Current Research. *Plant Physiol. Biochem.* **2016**, *107*, 147–163. <https://doi.org/10.1016/j.plaphy.2016.05.022>.

- (212) Adhya, S.; Merrill, C. R.; Biswas, B. Therapeutic and Prophylactic Applications of Bacteriophage Components in Modern Medicine. *Cold Spring Harb. Perspect. Med.* **2014**, *4* (1), a012518. <https://doi.org/10.1101/CSHPERSPECT.A012518>.
- (213) Cooper, C. A.; Maga, E. A.; Murray, J. D. Production of Human Lactoferrin and Lysozyme in the Milk of Transgenic Dairy Animals: Past, Present, and Future. *Transgenic Res.* **2015**, *24* (4), 605–614. <https://doi.org/10.1007/s11248-015-9885-5>.
- (214) Brinchmann, M. F. Immune Relevant Molecules Identified in the Skin Mucus of Fish Using -Omics Technologies. *Mol. Biosyst.* **2016**, *12* (7), 2056–2063. <https://doi.org/10.1039/C5MB00890E>.
- (215) Zhang, S.; Lu, H.; Lu, Y. Enhanced Stability and Chemical Resistance of a New Nanoscale Biocatalyst for Accelerating CO₂ Absorption into a Carbonate Solution. *Environ. Sci. Technol.* **2013**, *47* (23), 13882–13888. <https://doi.org/10.1021/es4031744>.
- (216) Ravera, M.; Gabano, E.; Zanellato, I.; Perin, E.; Arrais, A.; Osella, D. Functionalized Nonporous Silica Nanoparticles as Carriers for Pt(IV) Anticancer Prodrugs. *Dalt. Trans.* **2016**, *45* (43), 17233–17240. <https://doi.org/10.1039/C6DT03133A>.
- (217) Xu, Z.; Liu, S.; Kang, Y.; Wang, M. Glutathione- and PH-Responsive Nonporous Silica Prodrug Nanoparticles for Controlled Release and Cancer Therapy. *Nanoscale* **2015**, *7* (13), 5859–5868. <https://doi.org/10.1039/C5NR00297D>.
- (218) Tarn, D.; Ashley, C. E.; Xue, M.; Carnes, E. C.; Zink, J. I.; Jeffrey Brinker, C. Mesoporous Silica Nanoparticle Nanocarriers: Biofunctionality and Biocompatibility. *J. Acc. Chem. Res.* **2012**, *46*, 792–801. <https://doi.org/10.1021/ar3000986>.

- (219) Yang, Z.; Liu, Y.; Borbat, P.; Zweier, J. L.; Freed, J. H.; Hubbell, W. L. Pulsed ESR Dipolar Spectroscopy for Distance Measurements in Immobilized Spin Labeled Proteins in Liquid Solution. *J. Am. Chem. Soc* **2012**, *134*, 9950–9952.
<https://doi.org/10.1021/ja303791p>.
- (220) Pan, H.; Qin, M.; Meng, W.; Cao, Y.; Wang, W. How Do Proteins Unfold upon Adsorption on Nanoparticle Surfaces? *Langmuir* **2012**, *28*, 12779–12787.
<https://doi.org/10.1021/la302258k>.
- (221) Treuel, L.; Brandholt, S.; Maffre, P.; Wiegele, S.; Shang, L.; Nienhaus, G. U. Impact of Protein Modification on the Protein Corona on Nanoparticles and Nanoparticle–Cell Interactions. *ACS Nano* **2013**, *8*, 503–513. <https://doi.org/10.1021/nn405019v>.
- (222) Mortensen, N. P.; Hurst, G. B.; Wang, W.; Foster, C. M.; Nallathamby, P. D.; Retterer, S. T. Dynamic Development of the Protein Corona on Silica Nanoparticles: Composition and Role in Toxicity. *Nanoscale* **2013**, *5* (14), 6372. <https://doi.org/10.1039/c3nr33280b>.
- (223) Huang, R.; Carney, R. P.; Stellacci, F.; Lau, B. L. T. Protein–Nanoparticle Interactions: The Effects of Surface Compositional and Structural Heterogeneity Are Scale Dependent. *Nanoscale* **2013**, *5* (15), 6928. <https://doi.org/10.1039/c3nr02117c>.
- (224) Casals, E.; Pfaller, T.; Duschl, A.; Oostingh, G. J.; Puntès, V. Time Evolution of the Nanoparticle Protein Corona. *ACS Nano* **2010**, *4*, 3623–3632.
<https://doi.org/10.1021/nn901372t>.
- (225) Borbat, P. P.; Freed, J. H. Structural Information from Spin-Labels and Intrinsic Paramagnetic Centers in the Biosciences. In *Structure and Bonding*; Timmel, C. R., Harmer, J., Eds.; Springer: Heidelberg, Germany. New York, USA, 2014; pp 1–82.
https://doi.org/10.1007/430_2011_62.

- (226) Jeschke, G. DEER Distance Measurements on Proteins. *Annu. Rev. Phys. Chem.* **2012**, *63* (1), 419–446. <https://doi.org/10.1146/annurev-physchem-032511-143716>.
- (227) Yang, Z.; Bridges, M.; Lerch, M. T.; Altenbach, C.; Hubbell, W. L. *Saturation Recovery EPR and Nitroxide Spin Labeling for Exploring Structure and Dynamics in Proteins*; Academic Press, 2015; Vol. 564. <https://doi.org/10.1016/BS.MIE.2015.07.016>.
- (228) Stöber, W.; Fink, A.; Bohn, E. Controlled Growth of Monodisperse Silica Spheres in the Micron Size Range. *J. Colloid Interface Sci.* **1968**, *26* (1), 62–69. [https://doi.org/10.1016/0021-9797\(68\)90272-5](https://doi.org/10.1016/0021-9797(68)90272-5).
- (229) Hubbell, W. L.; Altenbach, C. Investigation of Structure and Dynamics in Membrane Proteins Using Site-Directed Spin Labeling. *Curr. Opin. Struct. Biol.* **1994**, *4* (4), 566–573. [https://doi.org/10.1016/S0959-440X\(94\)90219-4](https://doi.org/10.1016/S0959-440X(94)90219-4).
- (230) Larsen, R. G.; Singel, D. J. Double Electron–Electron Resonance Spin–Echo Modulation: Spectroscopic Measurement of Electron Spin Pair Separations in Orientationally Disordered Solids. *J. Chem. Phys.* **1993**, *98* (7), 5134–5146. <https://doi.org/10.1063/1.464916>.
- (231) Borbat, P. P.; Freed, J. H. Measuring Distances by Pulsed Dipolar ESR Spectroscopy: Spin-Labeled Histidine Kinases. In *Methods in Enzymology*; Academic Press, 2007; Vol. 423, pp 52–116. [https://doi.org/10.1016/S0076-6879\(07\)23003-4](https://doi.org/10.1016/S0076-6879(07)23003-4).
- (232) López, C. J.; Yang, Z.; Altenbach, C.; Hubbell, W. L. Conformational Selection and Adaptation to Ligand Binding in T4 Lysozyme Cavity Mutants. *Proc. Natl. Acad. Sci. U. S. A.* **2013**, *110* (46), E4306–15. <https://doi.org/10.1073/pnas.1318754110>.

- (233) Vigderman, L.; Khanal, B. P.; Zubarev, E. R. Functional Gold Nanorods: Synthesis, Self-Assembly, and Sensing Applications. *Adv. Mater.* **2012**, *24* (36), 4811–4841.
<https://doi.org/10.1002/adma.201201690>.
- (234) Kennedy, L. C.; Bickford, L. R.; Lewinski, N. A.; Coughlin, A. J.; Hu, Y.; Day, E. S.; West, J. L.; Drezek, R. A. A New Era for Cancer Treatment: Gold-Nanoparticle-Mediated Thermal Therapies. *Small* **2011**, *7* (2), 169–183. <https://doi.org/10.1002/sml.201000134>.
- (235) Stone, J.; Jackson, S.; Wright, D. Biological Applications of Gold Nanorods. *Wiley Interdiscip. Rev. Nanomedicine Nanobiotechnology* **2011**, *3* (1), 100–109.
<https://doi.org/10.1002/wnan.120>.
- (236) Yavuz, M. S.; Cheng, Y.; Chen, J.; Cobley, C. M.; Zhang, Q.; Rycenga, M.; Xie, J.; Kim, C.; Song, K. H.; Schwartz, A. G.; et al. Gold Nanocages Covered by Smart Polymers for Controlled Release with Near-Infrared Light. *Nat. Mater.* **2009**, *8* (12), 935–939.
<https://doi.org/10.1038/nmat2564>.
- (237) Rana, S.; Bajaj, A.; Mout, R.; Rotello, V. M. Monolayer Coated Gold Nanoparticles for Delivery Applications. *Adv. Drug Deliv. Rev.* **2012**, *64* (2), 200–216.
<https://doi.org/10.1016/J.ADDR.2011.08.006>.
- (238) Yang, X.; Yang, M.; Pang, B.; Vara, M.; Xia, Y. Gold Nanomaterials at Work in Biomedicine. *Chem. Rev.* **2015**, *115* (19), 10410–10488.
<https://doi.org/10.1021/acs.chemrev.5b00193>.
- (239) Ghosh, P.; Han, G.; De, M.; Kim, C. K. Gold Nanoparticles in Delivery Applications. *Adv. Drug Deliv. Rev.* **2008**, *60* (11), 1307–1315.
<https://doi.org/10.1016/J.ADDR.2008.03.016>.

- (240) Peer, D.; Karp, J. M.; Hong, S.; Farokhzad, O. C.; Margalit, R.; Langer, R. Nanocarriers as an Emerging Platform for Cancer Therapy. *Nat. Nanotechnol.* **2007**, *2* (12), 751–760. <https://doi.org/10.1038/nnano.2007.387>.
- (241) Elghanian, R.; Storhoff, J. J.; Mucic, R. C.; Letsinger, R. L.; Mirkin, C. A. Selective Colorimetric Detection of Polynucleotides Based on the Distance-Dependent Optical Properties of Gold Nanoparticles. *Science* **1997**, *277* (5329), 1078–1081. <https://doi.org/10.1126/SCIENCE.277.5329.1078>.
- (242) Kelly, K. L.; Coronado, E.; Zhao, L. L.; Schatz, G. C. The Optical Properties of Metal Nanoparticles: The Influence of Size, Shape, and Dielectric Environment. **2003**. <https://doi.org/10.1021/jp026731y>.
- (243) Huang, X.; Neretina, S.; El-Sayed, M. A. Gold Nanorods: From Synthesis and Properties to Biological and Biomedical Applications. *Adv. Mater.* **2009**, *21* (48), 4880–4910. <https://doi.org/10.1002/adma.200802789>.
- (244) Sperling, R. A.; Parak, W. J. Surface Modification, Functionalization and Bioconjugation of Colloidal Inorganic Nanoparticles. *Philos. Trans. R. Soc. A Math. Phys. Eng. Sci.* **2010**, *368* (1915), 1333–1383. <https://doi.org/10.1098/rsta.2009.0273>.
- (245) Alkilany, A. M.; Abulateefeh, S. R.; Mills, K. K.; Yaseen, A. I. B.; Hamaly, M. A.; Alkhatib, H. S.; Aiedeh, K. M.; Stone, J. W. Colloidal Stability of Citrate and Mercaptoacetic Acid Capped Gold Nanoparticles upon Lyophilization: Effect of Capping Ligand Attachment and Type of Cryoprotectants. *Langmuir* **2014**, *30*, 13799–13808. <https://doi.org/10.1021/la504000v>.

- (246) Khandelia, R.; Jaiswal, A.; Ghosh, S. S.; Chattopadhyay, A. Gold Nanoparticle-Protein Agglomerates as Versatile Nanocarriers for Drug Delivery. *Small* **2013**, *9* (20), 3494–3505. <https://doi.org/10.1002/smll.201203095>.
- (247) Hou, W.; Xia, F.; Alfranca, G.; Yan, H.; Zhi, X.; Liu, Y.; Peng, C.; Zhang, C.; de la Fuente, J. M.; Cui, D. Nanoparticles for Multi-Modality Cancer Diagnosis: Simple Protocol for Self-Assembly of Gold Nanoclusters Mediated by Gadolinium Ions. *Biomaterials* **2017**, *120*, 103–114. <https://doi.org/10.1016/J.BIOMATERIALS.2016.12.027>.
- (248) Sykes, E. A.; Dai, Q.; Sarsons, C. D.; Chen, J.; Rocheleau, J. V.; Hwang, D. M.; Zheng, G.; Cramb, D. T.; Rinker, K. D.; Chan, W. C. W. Tailoring Nanoparticle Designs to Target Cancer Based on Tumor Pathophysiology. *Proc. Natl. Acad. Sci.* **2016**, *113* (9), E1142–E1151. <https://doi.org/10.1073/pnas.1521265113>.
- (249) Cheng, Y.; Samia, A. C.; Meyers, J. D.; Panagopoulos, I.; Fei, B.; Burda, C. Highly Efficient Drug Delivery with Gold Nanoparticle Vectors for *in Vivo* Photodynamic Therapy of Cancer. *J. Am. Chem. Soc.* **2008**, *130* (32), 10643–10647. <https://doi.org/10.1021/ja801631c>.
- (250) Nam, J.; Won, N.; Jin, H.; Chung, H.; Kim, S. PH-Induced Aggregation of Gold Nanoparticles for Photothermal Cancer Therapy. *J. Am. Chem. Soc.* **2009**, *131* (38), 13639–13645. <https://doi.org/10.1021/ja902062j>.
- (251) Zhao, W.; Brook, M. A.; Li, Y. Design of Gold Nanoparticle-Based Colorimetric Biosensing Assays. *ChemBioChem* **2008**, *9* (15), 2363–2371. <https://doi.org/10.1002/cbic.200800282>.

- (252) Biju, V. Chemical Modifications and Bioconjugate Reactions of Nanomaterials for Sensing, Imaging, Drug Delivery and Therapy. *Chem. Soc. Rev.* **2014**, *43* (3), 744–764. <https://doi.org/10.1039/C3CS60273G>.
- (253) Liu, J.; Yi, L. A Colorimetric Lead Biosensor Using DNAzyme-Directed Assembly of Gold Nanoparticles. *J. Am. Chem. Soc.* **2003**, *125* (22), 6642–6643. <https://doi.org/10.1021/JA034775U>.
- (254) Walkey, C. D.; Olsen, J. B.; Guo, H.; Emili, A.; Chan, W. C. W. Nanoparticle Size and Surface Chemistry Determine Serum Protein Adsorption and Macrophage Uptake. *J. Am. Chem. Soc.* **2012**, *134* (4), 2139–2147. <https://doi.org/10.1021/ja2084338>.
- (255) Liu, J.; Peng, Q. Protein-Gold Nanoparticle Interactions and Their Possible Impact on Biomedical Applications. *Acta Biomater.* **2017**, *55*, 13–27. <https://doi.org/10.1016/J.ACTBIO.2017.03.055>.
- (256) Kah, J. C. Y.; Chen, J.; Zubieta, A.; Hamad-Schifferli, K. Exploiting the Protein Corona around Gold Nanorods for Loading and Triggered Release. *ACS Nano* **2012**, *6* (8), 6730–6740. <https://doi.org/10.1021/nn301389c>.
- (257) Alkilany, A. M.; Thompson, L. B.; Boulos, S. P.; Sisco, P. N.; Murphy, C. J. Gold Nanorods: Their Potential for Photothermal Therapeutics and Drug Delivery, Tempered by the Complexity of Their Biological Interactions. *Adv. Drug Deliv. Rev.* **2012**, *64* (2), 190–199. <https://doi.org/10.1016/J.ADDR.2011.03.005>.
- (258) Liu, J.; Lu, Y. Preparation of Aptamer-Linked Gold Nanoparticle Purple Aggregates for Colorimetric Sensing of Analytes. *Nat. Protoc.* **2006**, *1* (1), 246–252. <https://doi.org/10.1038/nprot.2006.38>.

- (259) Thanh, N. T. K.; Rosenzweig, Z. Development of an Aggregation-Based Immunoassay for Anti-Protein A Using Gold Nanoparticles. *Anal. Chem* **2002**, *74*, 1624–1628.
<https://doi.org/10.1021/AC011127P>.
- (260) Dreaden, E. C.; Austin, L. A.; Mackey, M. A.; El-Sayed, M. A. Size Matters: Gold Nanoparticles in Targeted Cancer Drug Delivery. *Ther. Deliv.* **2012**, *3* (4), 457–478.
<https://doi.org/10.4155/tde.12.21>.
- (261) Patra, H. K.; Dasgupta, A. K.; Sarkar, S.; Biswas, I.; Chattopadhyay, A. Dual Role of Nanoparticles as Drug Carrier and Drug. *Cancer Nanotechnol.* **2011**, *2* (1–6), 37–47.
<https://doi.org/10.1007/s12645-010-0011-3>.
- (262) Jazayeri, M. H.; Amani, H.; Pourfatollah, A. A.; Pazoki-Toroudi, H.; Sedighimoghaddam, B. Various Methods of Gold Nanoparticles (GNPs) Conjugation to Antibodies. *Sens. Bio-Sensing Res.* **2016**, *9*, 17–22. <https://doi.org/10.1016/J.SBSR.2016.04.002>.
- (263) Wang, F.; Wang, Y.-C.; Dou, S.; Xiong, M.-H.; Sun, T.-M.; Wang, J. Doxorubicin-Tethered Responsive Gold Nanoparticles Facilitate Intracellular Drug Delivery for Overcoming Multidrug Resistance in Cancer Cells. *ACS Nano* **2011**, *5* (5), 3679–3692.
<https://doi.org/10.1021/nn200007z>.
- (264) Sato, K.; Hosokawa, K.; Maeda, M. Rapid Aggregation of Gold Nanoparticles Induced by Non-Cross-Linking DNA Hybridization. *J. Am. Chem. Soc* **2003**, *125*, 8102–8103.
<https://doi.org/10.1021/JA034876S>.
- (265) Thaddeus J. Norman, J. .; Christian D. Grant; Donny Magana, and; Zhang*, J. Z.; Liu, J.; and, D. C.; Bridges, F.; Buuren, A. Van. Near Infrared Optical Absorption of Gold Nanoparticle Aggregates. **2002**. <https://doi.org/10.1021/JP0204197>.

- (266) Su, K.-H.; Wei, Q.-H.; Zhang, X.; Mock, J. J.; Smith, D. R.; Schultz, S. Interparticle Coupling Effects on Plasmon Resonances of Nanogold Particles. *NANO Lett.* **2003**, *3*, 1087–1090. <https://doi.org/10.1021/NL034197F>.
- (267) Song, Y.; Wei, W.; Qu, X. Colorimetric Biosensing Using Smart Materials. *Adv. Mater.* **2011**, *23* (37), 4215–4236. <https://doi.org/10.1002/adma.201101853>.
- (268) Kahn, C. R.; Baird, K. L.; Jarrett, D. B.; Flier, J. S. Direct Demonstration That Receptor Crosslinking or Aggregation Is Important in Insulin Action. *Proc. Natl. Acad. Sci. U. S. A.* **1978**, *75* (9), 4209–4213. <https://doi.org/10.1073/pnas.75.9.4209>.
- (269) Gole, A.; Murphy, C. J. Biotin-Streptavidin-Induced Aggregation of Gold Nanorods: Tuning Rod-Rod Orientation. *Langmuir* **2005**, *21*, 10756–10762. <https://doi.org/10.1021/la0512704>.
- (270) Zhao, W.; Lam, J. C. F.; Chiuman, W.; Brook, M. A.; Li, Y. Enzymatic Cleavage of Nucleic Acids on Gold Nanoparticles: A Generic Platform for Facile Colorimetric Biosensors. *Small* **2008**, *4* (6), 810–816. <https://doi.org/10.1002/smll.200700757>.
- (271) Lee, J. H.; Wang, Z.; Liu, J.; Lu, Y. Highly Sensitive and Selective Colorimetric Sensors for Uranyl (UO_2^{2+}): Development and Comparison of Labeled and Label-Free DNAzyme-Gold Nanoparticle Systems. *J. Am. Chem. Soc.* **2008**, *130*, 14217–14226. <https://doi.org/10.1021/ja803607z>.
- (272) Saha, K.; Agasti, S. S.; Kim, C.; Li, X.; Rotello, V. M. Gold Nanoparticles in Chemical and Biological Sensing. *Chem. Rev.* **2012**, *112* (5), 2739–2779. <https://doi.org/10.1021/cr2001178>.

- (273) Xu, X.; Ying, Y.; Li, Y. One-Step and Label-Free Detection of Alpha-Fetoprotein Based on Aggregation of Gold Nanorods. *Sensors Actuators B Chem.* **2012**, *175*, 194–200. <https://doi.org/10.1016/J.SNB.2012.04.091>.
- (274) Park, J.-W.; Shumaker-Parry, J. S. Structural Study of Citrate Layers on Gold Nanoparticles: Role of Intermolecular Interactions in Stabilizing Nanoparticles. *J. Am. Chem. Soc.* **2014**, *136* (5), 1907–1921. <https://doi.org/10.1021/ja4097384>.
- (275) Grzelczak, M.; Pérez-Juste, J.; Mulvaney, P.; Liz-Marzán, L. M. Shape Control in Gold Nanoparticle Synthesis. *Chem. Soc. Rev.* **2008**, *37* (9), 1783. <https://doi.org/10.1039/b711490g>.
- (276) Zhang, Y.; Wen, S.; Zhao, L.; Li, D.; Liu, C.; Jiang, W.; Gao, X.; Gu, W.; Ma, N.; Zhao, J.; et al. Ultrastable Polyethyleneimine-Stabilized Gold Nanoparticles Modified with Polyethylene Glycol for Blood Pool, Lymph Node and Tumor CT Imaging. *Nanoscale* **2016**, *8* (10), 5567–5577. <https://doi.org/10.1039/C5NR07955A>.
- (277) Schuetze, B.; Mayer, C.; Loza, K.; Gocyla, M.; Heggen, M.; Epple, M. Conjugation of Thiol-Terminated Molecules to Ultrasmall 2 Nm-Gold Nanoparticles Leads to Remarkably Complex ¹H-NMR Spectra. *J. Mater. Chem. B* **2016**, *4* (12), 2179–2189. <https://doi.org/10.1039/C5TB02443A>.
- (278) Zhang, H.; Zhou, Z.; Yang, B.; Gao, M. The Influence of Carboxyl Groups on the Photoluminescence of Mercaptocarboxylic Acid-Stabilized CdTe Nanoparticles. *J. Phys. Chem. B* **2002**, *107* (1), 8–13. <https://doi.org/10.1021/JP025910C>.

- (279) Shenawi, S.; Jaber, N.; Almog, J.; Mandler, D. A Novel Approach to Fingerprint Visualization on Paper Using Nanotechnology: Reversing the Appearance by Tailoring the Gold Nanoparticles' Capping Ligands. *Chem. Commun.* **2013**, *49* (35), 3688–3690. <https://doi.org/10.1039/c3cc41610k>.
- (280) Negishi, Y. .; Tsukuda, T. One-Pot Preparation of Subnanometer-Sized Gold Clusters via Reduction and Stabilization by Meso-2,3-Dimercaptosuccinic Acid. *J. Am. Chem. Soc* **2003**, *125*, 4046–4047. <https://doi.org/10.1021/JA0297483>.
- (281) Kouassi, G. K.; Wang, P.; Sreevatan, S.; Irudayaraj, J. Aptamer-Mediated Magnetic and Gold-Coated Magnetic Nanoparticles as Detection Assay for Prion Protein Assessment. *Biotechnol. Prog.* **2007**, *0* (0), 0–0. <https://doi.org/10.1021/bp0602101>.
- (282) Cui, M.; Liu, R.; Deng, Z.; Ge, G.; Liu, Y.; Xie, L. Quantitative Study of Protein Coronas on Gold Nanoparticles with Different Surface Modifications. *Nano Res.* **2014**, *7* (3), 345–352. <https://doi.org/10.1007/s12274-013-0400-0>.
- (283) Yang, P.-H.; Sun, X.; Chiu, J.-F.; Sun, H.; He, Q.-Y. †. Transferrin-Mediated Gold Nanoparticle Cellular Uptake. *Bioconjug. Chem.* **2005**, *16*, 494–496. <https://doi.org/10.1021/BC049775D>.
- (284) Zhang, F.; Lees, E.; Amin, F.; RiveraGil, P.; Yang, F.; Mulvaney, P.; Parak, W. J. Polymer-Coated Nanoparticles: A Universal Tool for Biolabelling Experiments. *Small* **2011**, *7* (22), 3113–3127. <https://doi.org/10.1002/sml.201100608>.

- (285) Yanli Liu; Mathew K. Shipton; Joseph Ryan; Eric D. Kaufman; Stefan Franzen, * and; Feldheim*, D. L. Synthesis, Stability, and Cellular Internalization of Gold Nanoparticles Containing Mixed Peptide–Poly(Ethylene Glycol) Monolayers. *Anal. Chem.* **2007**, *79*, 2221–2229. <https://doi.org/10.1021/AC061578F>.
- (286) Otsuka, H.; Nagasaki, Y.; Kataoka, K. PEGylated Nanoparticles for Biological and Pharmaceutical Applications. *Adv. Drug Deliv. Rev.* **2012**, *64*, 246–255. <https://doi.org/10.1016/J.ADDR.2012.09.022>.
- (287) Feng, J.-J.; Zhao, G.; Xu, J.-J.; Chen, H.-Y. Direct Electrochemistry and Electrocatalysis of Heme Proteins Immobilized on Gold Nanoparticles Stabilized by Chitosan. *Anal. Biochem.* **2005**, *342* (2), 280–286. <https://doi.org/10.1016/J.AB.2005.04.040>.
- (288) Phadtare, S.; Kumar, A.; Vinod, V. P.; Dash, C.; Palaskar, D. V.; Rao, M.; Shukla, P. G.; Sivaram, S.; Sastry, M. Direct Assembly of Gold Nanoparticle “Shells” on Polyurethane Microsphere “Cores” and Their Application as Enzyme Immobilization Templates. *Chem. Mater.* **2003**, *15*, 1944–1949. <https://doi.org/10.1021/CM020784A>.
- (289) Mahmoud, K. A.; Lam, E.; Hrapovic, S.; Luong, J. H. T. Preparation of Well-Dispersed Gold/Magnetite Nanoparticles Embedded on Cellulose Nanocrystals for Efficient Immobilization of Papain Enzyme. *ACS Appl. Mater. Interfaces* **2013**, *5* (11), 4978–4985. <https://doi.org/10.1021/am4007534>.
- (290) Gagner, J. E.; Lopez, M. D.; Dordick, J. S.; Siegel, R. W. Effect of Gold Nanoparticle Morphology on Adsorbed Protein Structure and Function. *Biomaterials* **2011**, *32* (29), 7241–7252. <https://doi.org/10.1016/J.BIOMATERIALS.2011.05.091>.

- (291) Pan, Y.; Neupane, S.; Farmakes, J.; Bridges, M.; Froberg, J.; Rao, J.; Qian, S. Y.; Liu, G.; Choi, Y.; Yang, Z. Probing the Structural Basis and Adsorption Mechanism of an Enzyme on Nano-Sized Protein Carriers. *Nanoscale* **2017**, *9* (10), 3512–3523.
- (292) Nikoobakht, B.; El-Sayed, M. A. Preparation and Growth Mechanism of Gold Nanorods (NRs) Using Seed-Mediated Growth Method. *Chem. Mater.* **2003**, *15*, 1957–1962.
<https://doi.org/10.1021/CM020732L>.
- (293) Budil, D. E.; Lee, S.; Saxena, S.; Freed, J. H. Nonlinear-Least-Squares Analysis of Slow-Motion EPR Spectra in One and Two Dimensions Using a Modified Levenberg–Marquardt Algorithm. *J. Magn. Reson. Ser. A* **1996**, *120* (2), 155–189.
<https://doi.org/10.1006/JMRA.1996.0113>.
- (294) Gerd H. Woehrle; Brown, L. O.; Hutchison, J. E. Thiol-Functionalized, 1.5-Nm Gold Nanoparticles through Ligand Exchange Reactions: Scope and Mechanism of Ligand Exchange. *J. Am. Chem. Soc* **2005**, *127*, 2172–2183. <https://doi.org/10.1021/JA0457718>.
- (295) Liang, M.; Lin, I.-C.; Whittaker, M. R.; Minchin, R. F.; Monteiro, M. J.; Toth, I. Cellular Uptake of Densely Packed Polymer Coatings on Gold Nanoparticles. *ACS Nano* **2010**, *4* (1), 403–413. <https://doi.org/10.1021/nn9011237>.
- (296) Bokseveld, M.; Blanchard, N.; Jaffal, A.; Chevolot, Y.; Monnier, V. Shape-Selective Purification of Gold Nanorods with Low Aspect Ratio Using a Simple Centrifugation Method. *Gold Bull.* **2017**, *50* (1), 69–76. <https://doi.org/10.1007/s13404-017-0197-9i>.
- (297) Wen, H.-Y.; Dong, H.-Q.; Xie, W.; Li, Y.-Y.; Wang, K.; Pauletti, G. M.; Shi, D.-L. Rapidly Disassembling Nanomicelles with Disulfide-Linked PEG Shells for Glutathione-Mediated Intracellular Drug Delivery. *Chem. Commun.* **2011**, *47* (12), 3550.
<https://doi.org/10.1039/c0cc04983b>.

- (298) Yu, M.; Zhou, C.; Liu, J.; Hankins, J. D.; Zheng, J. Luminescent Gold Nanoparticles with PH-Dependent Membrane Adsorption. *J. Am. Chem. Soc.* **2011**, *133* (29), 11014–11017. <https://doi.org/10.1021/ja201930p>.
- (299) Jv, Y.; Li, B.; Cao, R. Positively-Charged Gold Nanoparticles as Peroxidase Mimic and Their Application in Hydrogen Peroxide and Glucose Detection. *Chem. Commun.* **2010**, *46* (42), 8017–8019. <https://doi.org/10.1039/c0cc02698k>.
- (300) Yuan, Y.; Ding, D.; Li, K.; Liu, J.; Liu, B. Tumor-Responsive Fluorescent Light-up Probe Based on a Gold Nanoparticle/Conjugated Polyelectrolyte Hybrid. *Small* **2014**, *10* (10), 1967–1975. <https://doi.org/10.1002/sml.201302765>.
- (301) Larson, T. A.; Joshi, P. P.; Sokolov, K. Preventing Protein Adsorption and Macrophage Uptake of Gold Nanoparticles *via* a Hydrophobic Shield. *ACS Nano* **2012**, *6* (10), 9182–9190. <https://doi.org/10.1021/nn3035155>.
- (302) Leng, W.; Pati, P.; Vikesland, P. J. Room Temperature Seed Mediated Growth of Gold Nanoparticles: Mechanistic Investigations and Life Cycle Assessment. *Environ. Sci. Nano* **2015**, *2* (5), 440–453. <https://doi.org/10.1039/C5EN00026B>.
- (303) Ulman, A. Formation and Structure of Self-Assembled Monolayers. *Chem. Rev* **1996**, *96*, 1533–1554. <https://doi.org/10.1021/CR9502357>.
- (304) Love, J. C.; Estroff, L. A.; Kriebel, J. K.; Nuzzo, R. G.; Whitesides, G. M. Self-Assembled Monolayers of Thiolates on Metals as a Form of Nanotechnology. *Chem. Rev* **2005**, *105*, 1103–1170. <https://doi.org/10.1021/CR0300789>.

- (305) Abouhmad, A.; Dishisha, T.; Amin, M. A.; Hatti-Kaul, R. Immobilization to Positively Charged Cellulose Nanocrystals Enhances the Antibacterial Activity and Stability of Hen Egg White and T4 Lysozyme. *Biomacromolecules* **2017**, *18* (5), 1600–1608.
<https://doi.org/10.1021/acs.biomac.7b00219>.
- (306) Luckarift, H. R.; Dickerson, M. B.; Sandhage, K. H.; Spain, J. C. Rapid, Room-Temperature Synthesis of Antibacterial Bionanocomposites of Lysozyme with Amorphous Silica or Titania. *Small* **2006**, *2* (5), 640–643.
<https://doi.org/10.1002/sml.200500376>.
- (307) Kiristi, M.; Singh, V. V.; Esteban-Fernández de Ávila, B.; Uygun, M.; Soto, F.; Aktaş Uygun, D.; Wang, J. Lysozyme-Based Antibacterial Nanomotors. *ACS Nano* **2015**, *9* (9), 9252–9259. <https://doi.org/10.1021/acsnano.5b04142>.
- (308) Di Cosimo, R.; Mc Auliffe, J.; Poulou, A. J.; Bohlmann, G. Industrial Use of Immobilized Enzymes. *Chem. Soc. Rev.* **2013**, *42* (15), 6437–6474.
<https://doi.org/10.1039/c3cs35506c>.
- (309) Barbosa, O.; Ortiz, C.; Berenguer-Murcia, Á.; Torres, R.; Rodrigues, R. C.; Fernandez-Lafuente, R. Strategies for the One-Step Immobilization-Purification of Enzymes as Industrial Biocatalysts. *Biotechnol. Adv.* **2015**, *33* (5), 435–456.
<https://doi.org/10.1016/j.biotechadv.2015.03.006>.
- (310) Zhang, Y.; Ge, J.; Liu, Z. Enhanced Activity of Immobilized or Chemically Modified Enzymes. *ACS Catal.* **2015**, *5* (8), 4503–4513. <https://doi.org/10.1021/acscatal.5b00996>.
- (311) Liese, A.; Hilterhaus, L. Evaluation of Immobilized Enzymes for Industrial Applications. *Chem. Soc. Rev.* **2013**, *42* (15), 6236. <https://doi.org/10.1039/c3cs35511j>.

- (312) Rodrigues, R. C.; Ortiz, C.; Berenguer-Murcia, Á.; Torres, R.; Fernández-Lafuente, R. Modifying Enzyme Activity and Selectivity by Immobilization. *Chem. Soc. Rev.* **2013**, *42* (15), 6290–6307. <https://doi.org/10.1039/C2CS35231A>.
- (313) Laurent, N.; Haddoub, R.; Flitsch, S. L. Enzyme Catalysis on Solid Surfaces. *Trends Biotechnol.* **2008**, *26* (6), 328–337. <https://doi.org/10.1016/J.TIBTECH.2008.03.003>.
- (314) Doonan, C.; Riccò, R.; Liang, K.; Bradshaw, D.; Falcaro, P. Metal–Organic Frameworks at the Biointerface: Synthetic Strategies and Applications. *Acc. Chem. Res.* **2017**, *50* (6), 1423–1432. <https://doi.org/10.1021/acs.accounts.7b00090>.
- (315) Lian, X.; Fang, Y.; Joseph, E.; Wang, Q.; Li, J.; Banerjee, S.; Lollar, C.; Wang, X.; Zhou, H.-C. Enzyme–MOF (Metal–Organic Framework) Composites. *Chem. Soc. Rev.* **2017**, *46* (11), 3386–3401. <https://doi.org/10.1039/C7CS00058H>.
- (316) Majewski, M. B.; Howarth, A. J.; Li, P.; Wasielewski, M. R.; Hupp, J. T.; Farha, O. K. Enzyme Encapsulation in Metal–Organic Frameworks for Applications in Catalysis. *CrystEngComm* **2017**, *19* (29), 4082–4091. <https://doi.org/10.1039/C7CE00022G>.
- (317) Gkaniatsou, E.; Sicard, C.; Ricoux, R.; Mahy, J.-P.; Steunou, N.; Serre, C. Metal–Organic Frameworks: A Novel Host Platform for Enzymatic Catalysis and Detection. *Mater. Horizons* **2017**, *4* (1), 55–63. <https://doi.org/10.1039/C6MH00312E>.
- (318) Rana, S.; Yeh, Y.-C.; Rotello, V. M. Engineering the Nanoparticle–Protein Interface: Applications and Possibilities. *Curr. Opin. Chem. Biol.* **2010**, *14* (6), 828–834. <https://doi.org/10.1016/J.CBPA.2010.10.001>.
- (319) Sun, T.; Zhang, Y. S.; Pang, B.; Hyun, D. C.; Yang, M.; Xia, Y. Engineered Nanoparticles for Drug Delivery in Cancer Therapy. *Angew. Chemie Int. Ed.* **2014**, *53* (46), n/a-n/a. <https://doi.org/10.1002/anie.201403036>.

- (320) Wang, A. Z.; Gu, F.; Zhang, L.; Chan, J. M.; Radovic-Moreno, A.; Shaikh, M. R.; Farokhzad, O. C. Biofunctionalized Targeted Nanoparticles for Therapeutic Applications. *Expert Opin. Biol. Ther.* **2008**, *8* (8), 1063–1070.
<https://doi.org/10.1517/14712598.8.8.1063>.
- (321) Magner, E. Immobilisation of Enzymes on Mesoporous Silicate Materials. *Chem. Soc. Rev.* **2013**, *42* (15), 6213–6222. <https://doi.org/10.1039/c2cs35450k>.
- (322) Vellard, M. The Enzyme as Drug: Application of Enzymes as Pharmaceuticals. *Curr. Opin. Biotechnol.* **2003**, *14* (4), 444–450. [https://doi.org/10.1016/S0958-1669\(03\)00092-2](https://doi.org/10.1016/S0958-1669(03)00092-2).
- (323) Besteman, K.; Lee, J. O.; Wiertz, F. G. M.; Heering, H. A.; Dekker, C. Enzyme-Coated Carbon Nanotubes as Single-Molecule Biosensors. *Nano Lett.* **2003**, *3* (6), 727–730.
<https://doi.org/10.1021/nl034139u>.
- (324) Sun, H.; Zhou, Y.; Ren, J.; Qu, X. Carbon Nanozymes: Enzymatic Properties, Catalytic Mechanism, and Applications. *Angew. Chemie Int. Ed.* **2018**, *57* (30), 9224–9237.
<https://doi.org/10.1002/anie.201712469>.
- (325) Lalaoui, N.; David, R.; Jamet, H.; Holzinger, M.; Le Goff, A.; Cosnier, S. Hosting Adamantane in the Substrate Pocket of Laccase: Direct Bioelectrocatalytic Reduction of O₂ on Functionalized Carbon Nanotubes. *ACS Catal.* **2016**, *6* (7), 4259–4264.
<https://doi.org/10.1021/acscatal.6b00797>.
- (326) Gentil, S.; Che Mansor, S. M.; Jamet, H.; Cosnier, S.; Cavazza, C.; Le Goff, A. Oriented Immobilization of [NiFeSe] Hydrogenases on Covalently and Noncovalently Functionalized Carbon Nanotubes for H₂/Air Enzymatic Fuel Cells. *ACS Catal.* **2018**, *8* (5), 3957–3964. <https://doi.org/10.1021/acscatal.8b00708>.

- (327) Smirnova, E. A.; Gusev, A. A.; Zaitseva, O. N.; Lazareva, E. M.; Onishchenko, G. E.; Kuznetsova, E. V.; Tkachev, A. G.; Feofanov, A. V.; Kirpichnikov, M. P. Multi-Walled Carbon Nanotubes Penetrate into Plant Cells and Affect the Growth of *Onobrychis Arenaria* Seedlings. *Acta Naturae* **2011**, 3 (1), 99.
- (328) Liu, Q.; Chen, B.; Wang, Q.; Shi, X.; Xiao, Z.; Lin, J.; Fang, X. Carbon Nanotubes as Molecular Transporters for Walled Plant Cells. *Nano Lett.* **2009**, 9 (3), 1007–1010. <https://doi.org/10.1021/nl803083u>.
- (329) Rusmini, F.; Zhong, Z.; Feijen, J. Protein Immobilization Strategies for Protein Biochips. *Biomacromolecules* **2007**, 8, 1775–1789. <https://doi.org/10.1021/BM061197B>.
- (330) Wong, L. S.; Khan, F.; Micklefield, J. Selective Covalent Protein Immobilization: Strategies and Applications. *Chem. Rev.* **2009**, 109 (9), 4025–4053. <https://doi.org/10.1021/cr8004668>.
- (331) Saifuddin, N.; Raziah, A. Z.; Junizah, A. R. Carbon Nanotubes: A Review on Structure and Their Interaction with Proteins. *J. Chem.* **2013**, 2013, 1–18. <https://doi.org/10.1155/2013/676815>.
- (332) Zhao, X.; Hao, F.; Lu, D.; Liu, W.; Zhou, Q.; Jiang, G. Influence of the Surface Functional Group Density on the Carbon-Nanotube-Induced α -Chymotrypsin Structure and Activity Alterations. *ACS Appl. Mater. Interfaces* **2015**, 7 (33), 18880–18890. <https://doi.org/10.1021/acsami.5b05895>.
- (333) Antonucci, A.; Kupis-Rozmysłowicz, J.; Boghossian, A. A. Noncovalent Protein and Peptide Functionalization of Single-Walled Carbon Nanotubes for Biodelivery and Optical Sensing Applications. *ACS Appl. Mater. Interfaces* **2017**, 9 (13), 11321–11331. <https://doi.org/10.1021/acsami.7b00810>.

- (334) Davis, T. A.; Holland, L. A. Peptide Probe for Multiwalled Carbon Nanotubes: Electrophoretic Assessment of the Binding Interface and Evaluation of Surface Functionalization. *ACS Appl. Mater. Interfaces* **2018**, *10* (13), 11311–11318. <https://doi.org/10.1021/acsami.8b00022>.
- (335) Karajanagi, S. S.; Vertegel, A. A.; Kane, R. S.; Dordick, J. S. Structure and Function of Enzymes Adsorbed onto Single-Walled Carbon Nanotubes. *Langmuir* **2004**, *20*, 11594–11599. <https://doi.org/10.1021/LA047994H>.
- (336) Feng, D.; Liu, T.-F.; Su, J.; Bosch, M.; Wei, Z.; Wan, W.; Yuan, D.; Chen, Y.-P.; Wang, X.; Wang, K.; et al. Stable Metal-Organic Frameworks Containing Single-Molecule Traps for Enzyme Encapsulation. *Nat. Commun.* **2015**, *6* (1), 5979. <https://doi.org/10.1038/ncomms6979>.
- (337) Lykourinou, V.; Chen, Y.; Wang, X.-S.; Meng, L.; Hoang, T.; Ming, L.-J.; Musselman, R. L.; Ma, S. Immobilization of MP-11 into a Mesoporous Metal–Organic Framework, MP-11@mesoMOF: A New Platform for Enzymatic Catalysis. *J. Am. Chem. Soc.* **2011**, *133* (27), 10382–10385. <https://doi.org/10.1021/ja2038003>.
- (338) Shieh, F.-K.; Wang, S.-C.; Yen, C.-I.; Wu, C.-C.; Dutta, S.; Chou, L.-Y.; Morabito, J. V.; Hu, P.; Hsu, M.-H.; Wu, K. C.-W.; et al. Imparting Functionality to Biocatalysts via Embedding Enzymes into Nanoporous Materials by a *de Novo* Approach: Size-Selective Sheltering of Catalase in Metal–Organic Framework Microcrystals. *J. Am. Chem. Soc.* **2015**, *137* (13), 4276–4279. <https://doi.org/10.1021/ja513058h>.
- (339) Wang, H.-S. Metal–Organic Frameworks for Biosensing and Bioimaging Applications. *Coord. Chem. Rev.* **2017**, *349*, 139–155. <https://doi.org/10.1016/J.CCR.2017.08.015>.

- (340) Chen, L.; Luque, R.; Li, Y. Controllable Design of Tunable Nanostructures inside Metal–Organic Frameworks. *Chem. Soc. Rev.* **2017**, *46* (15), 4614–4630.
<https://doi.org/10.1039/C6CS00537C>.
- (341) Mehta, J.; Bhardwaj, N.; Bhardwaj, S. K.; Kim, K.-H.; Deep, A. Recent Advances in Enzyme Immobilization Techniques: Metal–Organic Frameworks as Novel Substrates. *Coord. Chem. Rev.* **2016**, *322*, 30–40. <https://doi.org/10.1016/J.CCR.2016.05.007>.
- (342) Furukawa, H.; Cordova, K. E.; O’Keeffe, M.; Yaghi, O. M. The Chemistry and Applications of Metal–Organic Frameworks. *Science (80-.)*. **2013**, *341* (6149), 1230444.
<https://doi.org/10.1126/science.1230444>.
- (343) Furukawa, H.; Müller, U.; Yaghi, O. M. “Heterogeneity within Order” in Metal–Organic Frameworks. *Angew. Chemie Int. Ed.* **2015**, *54* (11), 3417–3430.
<https://doi.org/10.1002/anie.201410252>.
- (344) Gole, B.; Stepanenko, V.; Rager, S.; Grüne, M.; Medina, D. D.; Bein, T.; Würthner, F.; Beuerle, F. Microtubular Self-Assembly of Covalent Organic Frameworks. *Angew. Chemie Int. Ed.* **2018**, *57* (3), 846–850. <https://doi.org/10.1002/anie.201708526>.
- (345) Lyu, F.; Zhang, Y.; Zare, R. N.; Ge, J.; Liu, Z. One-Pot Synthesis of Protein-Embedded Metal–Organic Frameworks with Enhanced Biological Activities. *Nano Lett.* **2014**, *14* (10), 5761–5765. <https://doi.org/10.1021/nl5026419>.
- (346) Pan, Y.; Li, H.; Farmakes, J.; Xiao, F.; Chen, B.; Ma, S.; Yang, Z. How Do Enzymes Orient When Trapped on Metal–Organic Framework (MOF) Surfaces? *J. Am. Chem. Soc.* **2018**, *140* (47), 16032–16036. <https://doi.org/10.1021/jacs.8b09257>.

- (347) Sun, C.-Y.; Qin, C.; Wang, X.-L.; Yang, G.-S.; Shao, K.-Z.; Lan, Y.-Q.; Su, Z.-M.; Huang, P.; Wang, C.-G.; Wang, E.-B. Zeolitic Imidazolate Framework-8 as Efficient PH-Sensitive Drug Delivery Vehicle. *Dalt. Trans.* **2012**, *41* (23), 6906.
<https://doi.org/10.1039/c2dt30357d>.
- (348) Neupane, S.; Pan, Y.; Li, H.; Patnode, K.; Farmakes, J.; Liu, G.; Yang, Z. Engineering Protein–Gold Nanoparticle/Nanorod Complexation via Surface Modification for Protein Immobilization and Potential Therapeutic Applications. *ACS Appl. Nano Mater.* **2018**, *1* (8), 4053–4063. <https://doi.org/10.1021/acsanm.8b00839>.
- (349) Song, Y.; Shen, Y.; Gong, C.; Chen, J.; Xu, M.; Wang, L.; Wang, L. A Novel Glucose Biosensor Based on Tb@Mesoporous Metal-Organic Frameworks/Carbon Nanotube Nanocomposites. *ChemElectroChem* **2017**, *4* (6), 1457–1462.
<https://doi.org/10.1002/celec.201600895>.
- (350) Bernfeld, P. Amylases, α and β . *Methods Enzymol.* **1955**, *1*, 149–158.
[https://doi.org/10.1016/0076-6879\(55\)01021-5](https://doi.org/10.1016/0076-6879(55)01021-5).
- (351) Pavlidis, I. V.; Tsoufis, T.; Enotiadis, A.; Gournis, D.; Stamatis, H. Functionalized Multi-Wall Carbon Nanotubes for Lipase Immobilization. *Adv. Eng. Mater.* **2010**, *12* (5), B179–B183. <https://doi.org/10.1002/adem.200980021>.
- (352) Schneider, C. A.; Rasband, W. S.; Eliceiri, K. W. NIH Image to ImageJ: 25 Years of Image Analysis. *Nat. Methods* **2012**, *9* (7), 671–675. <https://doi.org/10.1038/nmeth.2089>.
- (353) Nepal, D.; Geckeler, K. E. PH-Sensitive Dispersion and Debundling of Single-Walled Carbon Nanotubes: Lysozyme as a Tool. *Small* **2006**, *2* (3), 406–412.
<https://doi.org/10.1002/sml.200500351>.

- (354) Matsuura, K.; Saito, T.; Okazaki, T.; Ohshima, S.; Yumura, M.; Iijima, S. Selectivity of Water-Soluble Proteins in Single-Walled Carbon Nanotube Dispersions. *Chem. Phys. Lett.* **2006**, *429* (4–6), 497–502. <https://doi.org/10.1016/J.CPLETT.2006.08.044>.
- (355) Lee-Huang, S.; Huang, P. L.; Sun, Y.; Huang, P. L.; Kung, H. F.; Blithe, D. L.; Chen, H. C. Lysozyme and RNases as Anti-HIV Components in Beta-Core Preparations of Human Chorionic Gonadotropin. *Proc. Natl. Acad. Sci. U. S. A.* **1999**, *96* (6), 2678–2681. <https://doi.org/10.1073/pnas.96.6.2678>.
- (356) Xie, S.; Qiu, L.; Cui, L.; Liu, H.; Sun, Y.; Liang, H.; Ding, D.; He, L.; Liu, H.; Zhang, J.; et al. Reversible and Quantitative Photoregulation of Target Proteins. *Chem* **2017**, *3* (6), 1021–1035. <https://doi.org/10.1016/J.CHEMPR.2017.11.008>.
- (357) Wang, Q.; Zhang, X.; Huang, L.; Zhang, Z.; Dong, S. GOx@ZIF-8(NiPd) Nanoflower: An Artificial Enzyme System for Tandem Catalysis. *Angew. Chemie Int. Ed.* **2017**, *56* (50), 16082–16085. <https://doi.org/10.1002/anie.201710418>.
- (358) Harding, J. H.; Duffy, D. M.; Sushko, M. L.; Rodger, P. M.; Quigley, D.; Elliott, J. A. Computational Techniques at the Organic–Inorganic Interface in Biomineralization. *Chem. Rev.* **2008**, *108* (11), 4823–4854. <https://doi.org/10.1021/cr078278y>.
- (359) Pan, Y.; Heryadi, D.; Zhou, F.; Zhao, L.; Lestari, G.; Su, H.; Lai, Z. Tuning the Crystal Morphology and Size of Zeolitic Imidazolate Framework-8 in Aqueous Solution by Surfactants. *CrystEngComm* **2011**, *13* (23), 6937. <https://doi.org/10.1039/c1ce05780d>.
- (360) Monteiro De Souza, P. APPLICATION OF MICROBIAL-AMYLASE IN INDUSTRY-A REVIEW. *Brazilian J. Microbiol.* **2010**, *41*, 850–861.

- (361) Kandra, L. α -Amylases of Medical and Industrial Importance. *J. Mol. Struct. THEOCHEM* **2003**, 666–667, 487–498. <https://doi.org/10.1016/j.theochem.2003.08.073>.
- (362) Gupta, R.; Gigras, P.; Mohapatra, H.; Goswami, V. K.; Chauhan, B. Microbial α -Amylases: A Biotechnological Perspective. *Process Biochem.* **2003**, 38 (11), 1599–1616. [https://doi.org/10.1016/S0032-9592\(03\)00053-0](https://doi.org/10.1016/S0032-9592(03)00053-0).
- (363) Mehta, D.; Satyanarayana, T. Bacterial and Archaeal α -Amylases: Diversity and Amelioration of the Desirable Characteristics for Industrial Applications. *Front. Microbiol.* **2016**, 7, 1129. <https://doi.org/10.3389/fmicb.2016.01129>.
- (364) Kusnetzow, A. K.; Altenbach, C.; Hubbell, W. L. Conformational States and Dynamics of Rhodopsin in Micelles and Bilayers. *Biochemistry* **2006**, 45 (17), 5538–5550. <https://doi.org/10.1021/bi060101v>.

APPENDIX. EPR SPECTRAL SIMULATION

The CW EPR spectra were fit using the software developed by Dr. Altenbach and Prof. Hubbell at UCLA (<http://www.biochemistry.ucla.edu/biochem/Faculty/Hubbell/>). This program was essentially the MOMD model of the NSLS program established by Freed and co-workers.²⁹³ In our case, the MOMD model includes three coordinate frames to describe the internal motion of the nitroxide spin label in a hybrid. First, the molecular frame which is consistent with the magnetic tensor (g- and hyperfine-tensor) frame (x_M , y_M , z_M). The z_M is defined as to be along with the nitroxide p orbital; the x_M is parallel with the NO bond axis; the y_M follows a right-handed coordinate system. Second, the principle frame of the rotational diffusion tensor (x_R , y_R , z_R), which usually deviate from the molecular frame. Although in principle three Euler angles are required to correlate the two frames, experiences from spectral simulations indicated that only the β_D , the angle between z_R and z_M (Figure A1), is important for simulations. Third, the coordinate frame describing the diffusion of the spin label on the attached hybrid, the director frame, (x_D , y_D , z_D). A good approximation/simplification is to allow the spin label to rotate/move freely within a cone (Figure A1). This also leads to simplifying the rotational diffusion tensor R, wherein the axial symmetry can be assumed. The angle between z_D and z_R is defined as θ .

According to Budil et al, a restoring (ordering) potential (U) is appropriate to describe the extent of spatial constrains of the spin label within the “cone”. The restoring potential $U(\theta) = -1/2k_B T c_0^2 (3\cos^2\theta - 1) + \text{H.O.T.}$, where c_0^2 is a scaling coefficient and H.O.T. represents higher order terms as defined in the literature.²⁹³ In our simulations, only the dominant term and the first H.O.T. term was involved, the coefficients of which are C_{20} and C_{22} in our simulations, respectively.

For describing the nitroxide side chains on a hybrid subject to the above ordering potential, the director frame is fixed. The existence of the restoring potential results in an anisotropic motion and can be characterized by the order parameter $S = -1/2\langle (3\cos^2\theta - 1) \rangle$, where the brackets indicate spatial average. For an individual hybrid molecule, z_D forms an angle ψ with respect to the external magnetic field. To obtain the final spectrum corresponding to an isotropic distribution of protein orientations, the spectra are summed over ψ .

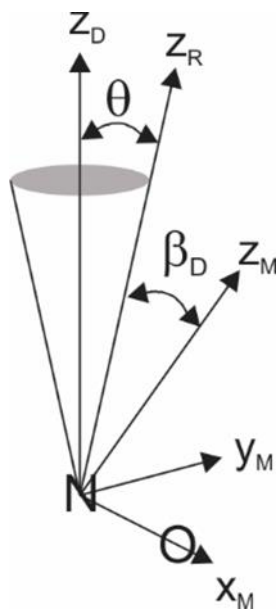


Figure A1. Definition of the three coordinate systems (Z_D , Z_R , and Z_M) related to the MOMD model used in our simulations.

The starting values for the diagonal values of the g and hyperfine (A) tensors were: $g_{xx} = 2.0078$, $g_{yy} = 2.0058$, $g_{zz} = 2.0022$ and $A_{xx} = 6.2$ G, $A_{yy} = 5.9$ G, $A_{zz} = 37.0$ G.³⁶⁴ The rotational correlation rates were described by the rotational diffusion tensor. For simplicity, symmetric motion is assumed, and this assumption was found to provide reasonably good fit to the data. The mean rotational diffusion constant is defined as R .²⁹³ The average effective correlation time is computed as $\tau_c = 1/(6\langle R \rangle)$. Spatial ordering of the diffusion tensor is accounted for by the order parameters, S_{20} and S_{22} , computed from the C_{20} and C_{22} coefficients of the ordering

potential which was varied in fitting.²⁹³ The tilt of the diffusion tensor with respect to the molecular axis of the nitroxide is specified by the Euler angles (α_D , β_D , γ_D). For axially symmetric motion ($R_x = R_y$), only β_D and γ_D need be specified. For z-axis anisotropic motion, the diffusion tilt was fixed at $\beta_D = 36^\circ$, $\gamma_D = 0^\circ$.¹¹⁷

The R_s , C_{20} , and C_{22} parameters were varied in the simulations to fit the selected data. During fitting, the center peak area was weighted as 50% of the rest of the spectrum, in order to better fit the low and high field regions, which are more sensitive to the rate and order. After a good fit was obtained, the diagonal elements of the A and g tensors were varied slightly to obtain the best fit shown in Figure A2. The fitting parameters are listed in Tables A1 -A4.

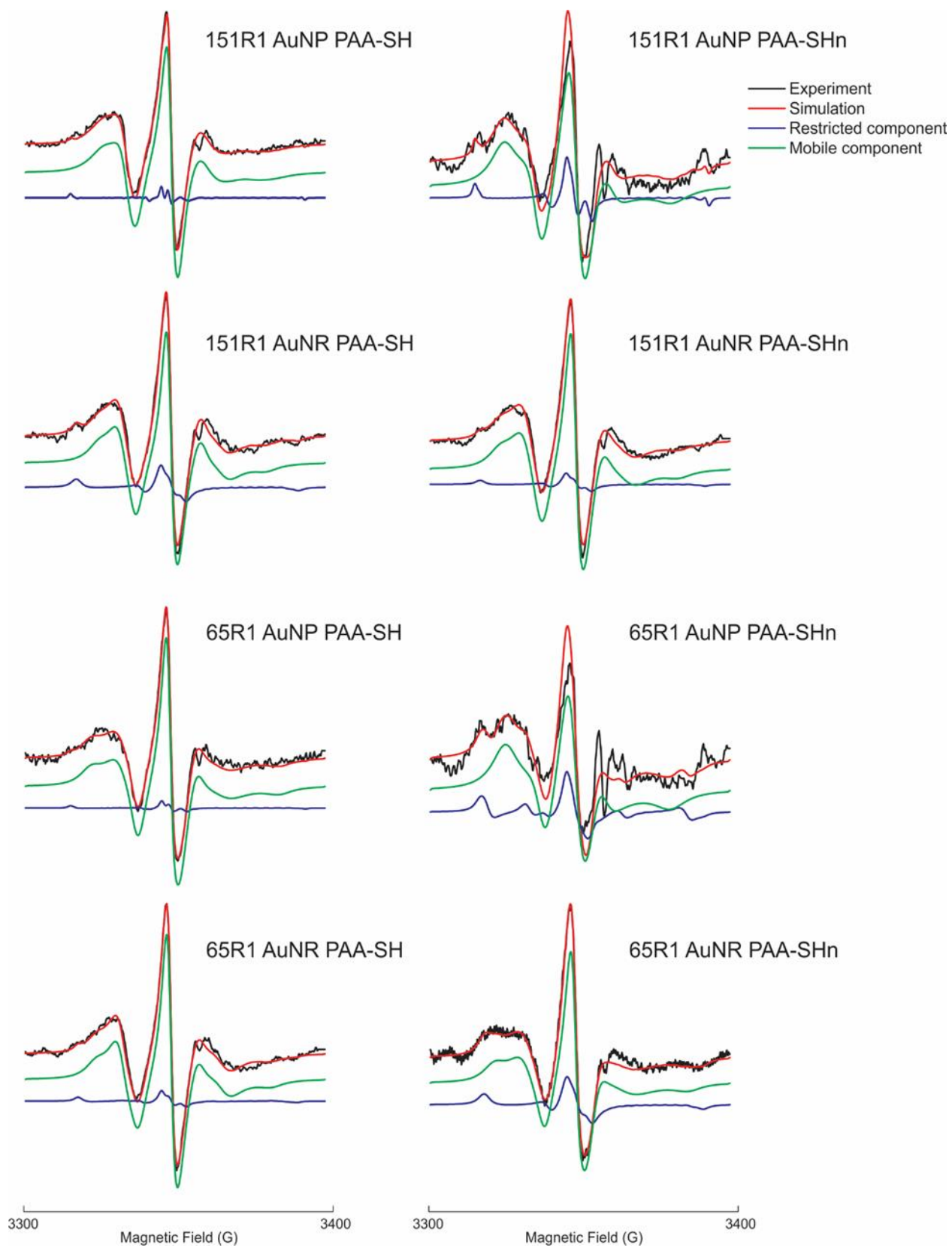


Figure A2. Simulations of key spectra discussed in Chapter 4.

Table A1. The fitting parameters for 151R1 on PAA-SH and PAA-(SH)_n coated AuNPs and AuNRs. The restricted component is indicated by “res”; the less restricted component is indicated by “m”. The uncertainties in population is +/-2-4 %.

Mutant	AuNP PAA-SH	AuNP PAA-(SH)_n	AuNR PAA-SH	AuNR PAA-(SH)_n
$R_{z, \text{res}}$	5.8	5.8	5.8	5.8
τ_C (ns)	260 ns	260 ns	260 ns	260 ns
$R_{z, \text{m}}$	7.92	8.0	8.1	8.11
τ_C (ns)	2 ns	1.6 ns	1.3 ns	1.3 ns
$R_{2, \text{res}}$	1.29	1.3	-2.32	-1.6
$R_{2, \text{m}}$	0.21	0.16	-1.56	-1.13
$C_{20, \text{res}}$	32	32	32	35
S_{20}	0.9	0.9	0.9	0.9
$C_{22, \text{res}}$	-34	-33	-35	-38
S_{22}				
$C_{20, \text{m}}$	-11	-30	-21	-22
S_{20}	-0.4	-0.5	-0.45	-0.45
$C_{22, \text{m}}$	0.36	0.75	0.68	0.54
S_{22}				
Population _{res}	5 %	11 %	12 %	9 %
χ^2	9e-5	7e-5	4.3e-5	3.4e-5

Table A2. The fitting parameters for 65R1 on PAA-SH and PAA-(SH)_n coated AuNPs and AuNRs. The restricted component is indicated by “res”; the less restricted component is indicated by “m”. The uncertainties in population is +/-2-4 %.

Mutant	AuNP PAA-SH	AuNP PAA-(SH) _n	AuNR PAA-SH	AuNR PAA-(SH) _n
R _{z, res}	5.8	5.8	5.68	5.8
τ _C	260 ns	260 ns	260 ns	260 ns
R _{z, m}	8.11	8.31	8.1	7.98
τ _C	1.3 ns	0.8 ns	1.3 ns	2 ns
R _{2, res}	-0.45	-1	-1.16	-0.44
R _{2, m}	-1	-0.47	-1.23	-0.82
C _{20, res}	32	27	32	39
S ₂₀	0.9	0.9	0.9	0.9
C _{22, res}	-37	-34	-37	-42
S ₂₂				
C _{20, m}	-22	-25	-21	-24
S ₂₀	-0.45	-0.45	-0.45	-0.45
C _{22, m}	0.58	1.22	0.51	0.46
S ₂₂				
Population _{res}	4 %	20 %	9 %	21 %
χ ²	7e-5	9e-5	3e-5	3e-6

Table A3. EPR fitting parameters for 4 spin labeled mutants adsorbed to CNTs. Note that 65R1 and 151R1 did not yield converged fitting results due to the high heterogeneity of enzyme binding mode on these two sites.

Mutant	44R1	72R1	118R1	131R1
R _{z, im}	5.97	5.87	5.95	5.83
R _{z, m}	7.88	7.86	7.9	7.9
R _{2, im}	1.15	0.72	1.22	1.42
R _{2, m}	-0.64	-0.38	-0.39	-0.44
C _{20, im}	42.7	38.9	31.7	43.3
C _{22, im}	-43.2	-43.3	-43	-43.7
C _{20, m}	-16	-16	-17	-17.4
C _{22, m}	5.04	4.69	4.82	5.00
Population _{im}	29.9%	37.1%	30.0%	22.4%
Population _m	70.1%	62.9%	70.0%	77.6%
χ ²	2.7e-5	2.6e-5	3.6e-5	6.93e-5

Table A4. EPR fitting parameters for the 6 spin labeled mutants adsorbed to CNT-ZIF. Grey indicates mutants that have more mobile component and are more exposable to the solvent.

Mutant	44R1	65R1	72R1	118R1	131R1	151R1
R _{z, im}	5.97	5.95	5.93	5.84	5.88	6.03
R _{z, m}	7.93	7.91	7.82	7.81	7.85	7.82
R _{2, im}	1.13	0.92	0.62	1.10	0.98	0.66
R _{2, m}	-0.51	-0.71	-0.7	-0.8	-0.57	-0.57
C _{20, im}	45.3	42.3	41.6	42	42.7	43.7
C _{22, im}	-45.6	-45.3	-46	-47	-47.4	-46.1
C _{20, m}	-17.8	-18.7	-17.5	-19.7	-20.5	-22.4
C _{22, m}	4.51	4.61	4.98	4.91	5.45	5.3
Population _i m	38.7%	40.6%	62.1%	42.6%	55.2%	54.8%
Population m	61.3%	59.4%	37.9%	57.3%	44.8%	45.2%
χ^2	2.51e ⁻⁵	1.09e ⁻⁵	1.7e ⁻⁵	2.0e ⁻⁵	3.27e ⁻⁵	6.47e ⁻⁵